Understanding Viscoelastic Behavior of Drug Carriers and Fabrication of Microdevice for Cancer Therapeutic Applications

A thesis submitted in
fulfillment of the requirements
for the award of the degree of

Doctor of Philosophy

by

Niraj Kr Prasad
Roll No.: 186103103

under the guidance of

Prof. Amaresh Dalal & **Prof. Siddhartha Sankar Ghosh**

Department of Mechanical Engineering
Indian Institute of Technology Guwahati
Guwahati - 781039, India
June, 2024

CERTIFICATE

It is certified that the work contained in the thesis entitled **"Understanding Viscoelastic Behavior of Drug Carriers and Fabrication of Microdevice for Cancer Therapeutic Applications"**, by **Niraj Kr Prasad (Roll No. 186103103)** has been carried out under our supervision and that this work has not been submitted elsewhere for a degree.

(Amaresh Dalal)
Professor
Department of Mechanical Engineering
Indian Institute of Technology Guwahati

(Siddhartha Sankar Ghosh)
Professor
Department of Biosciences & Bioengineering
Indian Institute of Technology Guwahati

June, 2024

DECLARATION

I, hereby declare that I am the sole author of the thesis entitled **"Understanding Viscoelastic Behavior of Drug Carriers and Fabrication of Microdevice for Cancer Therapeutic Applications"**. To the best of my knowledge, this thesis contains no information previously published by any other person except where due acknowledgment has been given. This thesis contains no information that has been accepted as part of the requirements of any other academic degree or non-degree program.

This is a original copy of the thesis after incorporating final revisions.

(Niraj Kr Prasad)
(Roll No. 186103103)

June, 2024

Dedicated to ***Maa*** & ***Papa***

Acknowledgments

Humans have evolved to have certain necessary traits to survive and thrive, including the ability to cooperate and contribute. Thus, it is axiomatic to say that one can achieve anything without the support and contributions of significant individuals associated with them. Similarly, the journey of research that I embarked upon would only have come to the destination of completion with valuable inputs and support from exceptional individuals. I am sincerely thankful to them. I want to dedicate this moment to express my gratitude to those special individuals who helped me during my PhD journey at the Indian Institute of Technology Guwahati.

I express my sincere gratitude to my supervisors *Prof. Amaresh Dalal* and *Prof. Siddhartha Sankar Ghosh*, for their invaluable guidance during this thesis study. Their altruistic contributions and omnipresence have lessened the weight of this arduous task by greatly assisting in completing the dissertation. They have always been so gracious as to overcome my mistakes, provide a favorable research environment, and help me look on the bright side. I appreciate their unending assistance in utilizing all of the lab facilities and for introducing me to colleagues from *Anupravaha lab* and *SS Ghosh lab* with excellent scientific understanding. I feel fortunate to have had the opportunity to work under their guidance.

I express my heartfelt gratitude to *Prof. Gautam Biswas* of the *Department of Mechanical Engineering, Indian Institute of Technology Kanpur* for his invaluable contributions, which significantly led to the foundation of this thesis. I had the good fortune to have his mentoring from the start of my doctorate; his words of wisdom enabled me to advance as a research scholar personally and professionally. I would also like to thank *Prof. Pranab Mondal* of *Department of Mechanical Engineering, Indian Institute of Technology Guwahati* for enabling me to access the lab equipment of his lab *Microfluidics lab*. I am extremely grateful to *Prof. Vinayak Kulkarni*, the chairman of my doctoral committee, for his insightful suggestions on experimental and numerical methodology that greatly led to the development of the thesis. I express my gratitude to the other members of my doctoral committee, *Dr. Gavara Madhusudhana*, *Dr. Vinodh Bandaru*, and *Prof. Tapas Kumar Mandal* for their equally insightful and helpful feedback on my work.

I had the opportunity to meet and interact with excellent seniors, colleagues, and friends. I am extremely grateful to *Dr. Binita Nath* for introducing me to the intricacies involved in carrying out a microfluidics experiment. I would also like to thank *Dr. Manash Pratim Borthakur* for giving invaluable insights into

the numerical solver that enabled me to carry out my numerical study. I also convey my sincere gratitude to *Dr. Bhaskarjyoti Sarma* for providing constant mentorship throughout my PhD journey. To carry out interdisciplinary research, it is essential to harness support from the experts in that field. *Dr. Rajib Shome* is the individual whose valuable knowledge and collaboration motivated me to carry out my research with nanocarriers. I sincerely acknowledge the support I got from *Dr. Santanu Kumar Das* throughout my thesis work that assured me of an uninterrupted progressive flow in completing my objectives. I dearly treasure my discussions with *Rupresha* that helped me refine my views on science-related topics and other important aspects. I will fondly remember the time spent with *Dheeraj*, as I deeply admire his attitude of being kind and calm in difficult situations. I heartily remember the cheerful memories I had with *Dr. Kaustabh Chaterjee* and *Abhijit* during our everyday fun-filled evening tea break. In an absolute true sense, my journey in IIT Guwahati became interesting and joyful because of my friends *Tanuj*, *Chandan*, *Rohit*, *Brijesh*, *Bikramjyoti*, *Risabh*, *Alok*, *Ashok*, *Pranab*, *Dr. Nitesh Kumar*, *Biswajyoti*. The journey would not have been memorable without the presence of these individuals. I would also like to thank *Dr. Plaboni Sen* and *Arisha* for being the kind individuals who were always ready to clear my doubts regarding nanovesicles and cancer cells. I am extremely grateful for the support I received from the individuals associated with *cleanroom* facilities of the Centre for Nanotechnology, IIT Guwahati, for providing me with a state-of-the-art facility for fabricating microchannels. I would also like to acknowledge the excellent time I had while working with *Akash*, *Rahul Yadav*, *Somashekhar*, *Rahul Suklabaidya*, *Harish*, *Anubhav*, *Niraj*, *Akshat*, *Biswajit Animesh*, and *Pradeep*.

Without a strong and caring base, nothing can rise. I am nothing that could never have grown without support and love from my *maa* and *papa*. Until now, *maa* and *papa*'s happiness has been a significant source of my happiness. I commit my journey to honoring their sacrifices at every stage of my life. I want to express my deep love and gratitude to my *bhaiya* for always supporting me and giving wise advice when needed. Above all, it is essential to live a journey with fun and joy; I would like to convey my sincere gratitude to my *bhabhi* and infinite love to my *niece* for bringing that joy in a somewhat occasional stressful journey.

A constant throughout my journey is starting and ending my day with the name of **Mahakal**, and it will always remain like that for the rest of my life. A source of infinite energy *om namah shivaya* is always there to help me understand the deeper meaning of everything.

Abstract

Flow-through constricted microchannels are essential in engineering applications like inkjet printing, droplet microfluidics, and biomedical engineering. It is believed that a microfluidic-based study can address one of the most serious concerns of the present world: targeted cancer therapeutics. One of the most crucial aspects of achieving targeted cancer therapy is to design an efficient drug carrier that can act as a guided agent for killing cancer cells at the cancer site. Although efficient and advantageous, circulation instability, less biodegradation, and poor bioavailability of some nanocarriers raise concerns about long-term application in cancer treatment. Additionally, the margination and adhesion of these drug carriers towards the microchannel wall is another problem that needs to be resolved. This limitation also restricts its use in microfluidic devices for cancer therapeutic applications. It has been reported that soft and deformable drug carriers can overcome margination and adhesion and successfully flow through constricted microcapillaries. Better bio-compatibility and longer circulation time can be achieved using natural rather than synthetic drug carriers. Thus, in the present thesis, a sincere attempt was made to synthesize these carriers and to assess and quantify the flow behavior and deformation while moving through the constricted microchannel. Along with this, significant insights were gathered by developing a computational model of these drug carriers. Studying droplet flow through microconfinement is believed to significantly explain the flow dynamics of cancer cells, biological molecules, and drug carriers through blood vessels.

The particles mentioned above possess viscous and elastic behavior and are examined under special polymeric fluids. These fluids exhibit complex mechanical behavior consisting of a long chain of polymer molecules with distinct orientations. Thus, a viscoelastic drop model can be a suitable computational model of these carriers, as it proved to be a successful model for cells and drug carriers. The viscoelastic drop model can gather information about the deformation behavior of cells, drug carriers, and even drug particles moving via microcapillaries inside the human body. Furthermore, a drop breakup study could provide better design guidance for nanocarriers that deliver on-demand burst drug releases at specific cancer sites.

Considering these aspects, an investigation was carried out on the deformation and breakup of a shear-thinning Finitely Extensible Nonlinear Elastic−Peterlin (FENE-P) drop moving through the constricted microchannel. The study revealed

results that were somewhat tough to obtain through an experimental study. The two-phase viscoelastic drop-Newtonian matrix system simulations were performed on an open-source solver, Basilisk. The solvent viscosity ratio could affect drop deformation even at unity Deborah number when it flows through narrower confinement. Furthermore, the viscosity ratio and Deborah number are crucial parameters that can manipulate drop deformation under confinement. However, it was observed that a change in capillary number plays a pivotal role in variations in drop deformation. In the furtherance of the study, the effect of solvent viscosity ratio and capillary number on the viscoelastic normal stress difference distribution inside viscoelastic drop inside the microchannel of different confinements was also carried. The viscoelastic normal stress difference grew inside drop when surface tension forces are altered. The increase in drop deformation at a higher capillary number reduces the strain rate inside the drop. Thus, the viscoelastic stresses inside the drop grow slowly at higher *Ca*. The observations suggested that viscoelastic stresses get convected faster in the flow direction during stress relaxation inside drop at a higher capillary number. Additionally, the contour plots of the square of the average polymer extension for the viscoelastic drop were deciphered. The average polymer extension at the drop interface was lesser for higher capillary numbers. In the continuation of the study, the drop breakup was observed when the capillary number was increased. The critical value of the capillary number for drop breakup depended on the variation of Deborah number and viscosity ratios. Interestingly, the critical capillary study revealed that an increased confinement ratio at higher capillary numbers significantly affected drop deformation and breakup. It has been observed that cancer cell breakup happened from its tail end with the formation of two fragments. Thus, FENE-P drop breakup could closely predict such kind of breakup behavior. The finite extensibility of the polymer molecules becomes very important at the droplet breakup time. While undergoing deformation, the dumbbell beads in the FENE-P model extend finitely, causing a localized increase in elastic stress that eventually balances the capillary pressure. The phenomenon plays a vital role in restricting the drop breakup. The absence of elastic stress resistance due to polymer stretching in Newtonian drop makes it more susceptible to break.

In order to achieve a successful transport of drug carriers through the microchannel walls, experimental and numerical investigations were carried out to demonstrate the flow behavior of polymeric and natural drug carriers. For efficient and uninterrupted drug delivery by drug carriers, it should possess the ability to structurally heal after undergoing various stresses. Thus, the self-healing properties of hydrogel particles that underwent migration through a constricted microchannel without

adhering to the channel walls were deciphered. The particles regained their physical structure after undergoing migration. The study revealed self-healing hydrogel nanocarriers' high load-carrying and elastic recovery characteristics. The aggregation of hydrogel particles restricted the decay of nanocarriers. The nanocarriers demonstrated longer retention of Doxorubicin with sustained drug release. The FENE-P drop model of the shear-thinning nanocarriers manifested remarkable insight into particle-squeezing inside microcapillaries. The FENE-P drop model closely predicted the experiment results of the migration of hydrogel drug carriers. However, significant deviations were observed between experimental and numerical results when hydrogel passed through 7 μm width. The numerical results can be further employed to design complex microfluidic devices for studying drug delivery through brain capillaries, blood-brain barrier, and other intricate human body areas. The flow behavior and deformation of the cellular nanovesicles through branches of contraction/expansion microchannels designed to mimic the human blood capillary networks were also observed. An earlier study observed that nanovesicles could transport through the polymer matrix network to mimic the extra-cellular matrix. They reported that the combination of stress relaxation and matrix stiffness deformed the nanovesicles, which squeezed through the microchannels. However, the study failed to consider the lack of mechanical strength, which resulted in the nanovesicle accumulation. Also, their study could not provide a relative quantification of the nanovesicle deformities. Therefore, the present study attempted to prove the relative quantification of the nanovesicle deformities, which was a gap in their research. Hydrogel carriers showed better structural healing and mechanical strength than nanovesicles, while nanovesicles are more bio-compatible than hydrogel carriers. It has to be noted that both carriers showed sufficient deformation for successful squeezing through 7 μm microchannel.

Along with drug carriers, drug particles themselves are nanoparticles. Thus, drugs themselves tend to agglomerate, marginate, and adhere to channel walls. Thus, similar to hydrogel and nanovesicles, experiments were carried out for a commercial drug, Protein-bound Paclitaxel, Paclicad. Considering this, an investigation was done to discern the transport of a commercially available chemotherapeutic drug, Paclicad, inside a constricted microchannel. The particles were reported to transport without aggregation up to the flow rate of 50 μl/hr. However, the particle aggregation was observed at higher flow rates, causing capillary obstruction at a flow rate of 100 μl/hr. The experiment results demonstrated that shear rate is primarily responsible for particle aggregation. Even in the advection-dominating flow regime, aggregated particles in the flow field might result in a tortuous particle trajectory. It was also observed that the particle mobility decreased when the chan-

nel's cross-section varied. Additionally, the FENE-P drop model for the Paclicad particles was proposed. The viscoelastic and Newtonian models closely predicted the experiment's outcomes; however, the viscoelastic drop model demonstrated superior deformation and elastic recovery. The study provided valuable insight into the transport of a commercial drug inside an extremely confined flow that mimics a situation similar to that of human blood capillaries. A good surface treatment strategy should be adopted to avoid drug agglomeration at higher flow rates.

The understanding from the experimental and numerical investigation on drug carriers and particles was used to fabricate a microfluidic platform for drug uptake study on MCF-7 cells. Estimating drug uptake by cells in vitro is widely determined in a static environment or centrifuge. Such an uptake study cannot give a correct estimation of drug uptake on cells as drug uptake by cells happens when both drug and cells are in movement. Considering these aspects, the microchannels were fabricated to decipher the drug uptake on breast cancer cells (MCF-7 cells) when they flow through conditions similar to the blood capillary network. The drug uptake in the channel with bifurcations of varying width was observed to be 1.17 times higher than the static condition. At the same time, the drug uptake in a channel with multiple curves with constant width was 1.78 times higher than the static condition. The inflection region where channel curvature changed caused MCF-7 cells to deform, which may weaken the membrane, thus allowing a better drug uptake by cells. Furthermore, it was observed that the MCF-7 cells showed noticeable deformation at the entry of the bifurcations and the inflection region. The MCF-7 cells also exhibited faster stress relaxation in the region of higher stresses. The foretip and tail end of the cells were observed to move at different speeds during stress relaxation. The fabricated channel is a new and efficient method for assessing cellular uptake of drugs.

Contents

List of Figures

List of Tables

Nomenclature

a	Color function
Bo	Bond number
C	Conformation tensor
c	Drop diameter to constriction ratio
Ca	Capillary number
D	Diameter of the channel
d	Drop diameter
d_a	Drop dimension along major axis
d_b	Drop dimension along minor axis
D_c	Diffusion coefficient
De	Deborah number
Dn	Dean number
d_h	Displacement of hydrogel drug carrier
$\mathbf{F}$	Interfacial surface tension force
F_{C}	Stretch function
h	Height function
$\mathbf{I}$	Unit tensor

k_b	Boltzmann constant
k_n	Knudsen number
L	Ratio of polymer dumbbell length under full extension to its equilibrium length
l	Characteristic length
l_s	Length scale
m	Density ratio
n	Normal to the interface
p	Pressure
$\mathbf{R}$	End to end vector connecting dumbbell Beads
r_c	Radius of curvature
Re	Reynolds number
S	Deformation rate tensor
T	Extra stress tensor
t	Instantaneous time
t_s	Time scale
U	Velocity of the carrier fluid
$\mathbf{u}$	Fluid velocity vector
$u_{avg,particle}$	Particle average velocity
U_m	Maximum interaction potential
V	Average velocity
v_s	Velocity scale
$x(t)$	Axial displacement of the Paclicad particle

Greek Alphabets

α	Numerical coefficient
β	Solvent viscosity ratio
$\dot{\gamma}$	Shear rate
δ	Interfacial delta function
θ	Viscosity ratio
κ	Interfacial curvature
λ	Relaxation time
μ	Dynamic viscosity
μ_p	Polymeric viscosity
μ_s	Solvent viscosity
ν	Kinematic viscosity
ρ	Fluid density
σ	Interfacial tension
τ	Total stress tensor

Abbreviations

CR	Confinement ratio
Cur	Curcumin
DLS	Dynamic light scattering
DMSO	Dimethyl sulfoxide
DNA	Deoxyribonucleic acid
DOX	Doxorubicin
EMT	Epithelial-mesenchymal transition
FBS	Fetal bovine serum
FDA	Food and drug administration

FEM	Finite element method
FENE-P	Finitely extensible non-linearly elastic- Peterlin
FENE-CR	Finitely extensible non-linearly elastic- Chilcott and Rallison
FESEM	Field-emission scanning electron microscope
FETEM	Field-emission transmission electron microscope
HMDS	Hexamethyldisilazane
LB	Lattice Boltzman
MCF	Michigan cancer foundation
MV	Migration velocity
MYC	Mixed Young centered
PBS	Phosphate buffer saline
PDMS	Polydimethylsiloxane
PEG	Polyethylene glycol
PMMA	Polymethyl methacrylate
PVA	Polyvinyl alcohol
PVP	Polyvinyl pyrrolidone
RBC	Red blood cells
RCA	Radio corporation of America
RES	Reticuloendothelial system
RNA	Ribonucleic acid
TEM	Transmission electron microscope
TPZ	Tirapazamine
VOF	Volume of fluid
WBC	White blood cells

Superscripts

$*$	Non-dimensional value
c	Cell centered values
f	Face centered values

Subscripts

$*$	Auxilary field values
1	Carrier fluid medium
2	Drop medium
a	Measured along major axis
b	Measured along minor axis
CR	Critical number
h	Hydrogel drug-carrier
m	Maximum value
n	Time step
s	Solvent
p	Polymer
x	Measured along x-axis
y	Measured along y-axis

1 Introduction

1.1 Introduction

From its emergence to prominence, three decades of research on microfluidics and microfluidic devices proved to be a game changer in bioengineering applications. The faster reaction time in the microfluidic device helps study the behavior of larger bio-molecules, such as DNA, with a lower diffusion coefficient. Lab on-chip devices can perform pathological functions, such as determining blood glucose levels with a small amount of blood. Microchannels also provide a valuable platform for mimicking arteries, veins, capillaries, and human organs. Microfluidic devices' micron and submicron length scales require a small volume of reagents to perform chemical reactions, which can eliminate mouse models for different biomedical research. The present study will be dedicated to a microfluidic-based study on controlled drug delivery in cancer therapeutics.

Microfluidics gives insight into the science and technology of fluid flow in channels with characteristic dimensions of micron length scale. Microfluidics pertains to manipulating, acting, and precisely controlling gaseous and liquid flows through minuscule channels of varying geometrical forms and scientific applications. Microfluidics has often been referred to as a game changer in biological science and industry [1]. Much research has been done recently in microfluidics, with microfluidic-based devices capable of outperforming their traditional counterpart. With the advancements in design and fabrication of such devices, it has become easy to study the phenomenon that was believed to be evasive to the macro scale devices. The development of microfluidics and the capability of such devices to depict complicated phenomena in several areas of fluid dynamics, biological science, and molecular physics is primarily attributed to the furtherance in micro- and nano-fabrication techniques. The introduction of materials like PDMS and PMMA in fabricating microfluidic devices played a vital role in the prominence

of microfluidics. PDMS and PMMA can generate low-cost, pliable, deformable microfluidic structures of intricate shapes with faster design time than traditional silicon-based devices.

Understanding the physics of microfluidics includes studying the fundamental laws and theory of conventional fluid mechanics and changes in its primary function when the same physics is applied to miniature structures with confined flow. Understanding the difference between microfluidics and conventional fluid mechanics applied to macro-scale flows becomes necessary. When the size of a system reduces, the volume-to-surface area ratio decreases, which means surface effects dominate over volumetric effects [2]. So, for a microchannel flow, surface forces like electrostatic, electrodynamic, surface tension, and viscous forces are prominent, and inertia forces are often neglected. Various non-dimensional numbers are often studied better to understand the relative dominance of such forces in microfluidics. The ratio of inertia and viscous force is given by Reynolds number (Re). For microchannel flow, the Reynolds number is typically less than 10, which shows the dominance of viscous force over inertia force. Reynolds number expression is given below in Eq. 1.1.

$$Re = \rho V l / \mu \tag{1.1}$$

It is clear from the expression of the Reynolds number that as the characteristics of the system's length scale decrease, the Reynolds number also decreases. Since the characteristic linear dimension in microfluidics is of the micron and sub-micron scales, the Reynolds number becomes significantly smaller in microchannel flows than in macro-scale flows. As the fundamental study of microfluidics hinges on transport phenomena on micro and nano scales, it becomes essential to know about advection and diffusion and their relative effect on the flow. Peclet number is the dimensionless number, which is the ratio of advective transport to diffusive transport of fluid molecules. Peclet number (Pe) is given by

$$Pe = V l / D_c \tag{1.2}$$

From Eq. 1.2, it can be seen that the Peclet number is significantly small for micro-scale flows, which explains the dominance of diffusion over advection in the transport of molecules in fluids. The dominance of diffusion over advection causes a shorter diffusion time for fluid molecules in systems of smaller dimensions. Eq. 1.3 approximately gives diffusion time in a microfluidic system is [3].

$$t \approx x^2/2D_c \tag{1.3}$$

From Eq. 1.3 it can be seen that

$$t \propto x^2 \tag{1.4}$$

According to Eq. 1.4, as x reduces to micro and nano length, the diffusion time becomes minimal, which causes a quick reaction time for the diffusion of larger molecules across the microfluidic system. The quick response time of microfluidic devices makes these devices prominent in studying the transport of larger biological molecules like DNA with a lower diffusion coefficient.

Other dimensionless numbers that are most commonly used in microfluidic studies are the Capillary number (Ca), Bond number (Bo), and Knudsen number (Kn). The bond number is the ratio of gravity force to surface tension force. Surface tension force is the force by which fluid tends to reduce its surface area and has an affinity to reduce its free energy. In microscale flow, this force tends to dominate over gravity force, which is utilized as a method to drive a microfluidic device without a prime mover. Capillary force is the force by which a fluid can travel through constricted channels and porous material. This force also dominates over gravity forces at the micro scale, which is used in developing Lab on chip health care devices.

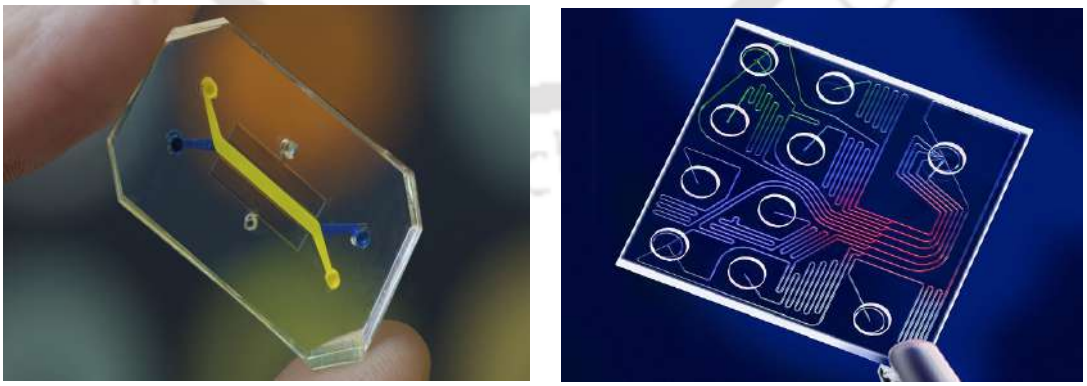

(a) (b)

Figure 1.1: Lab on chip devices, (a) human organ on chip device. *Credit: The Wyss Institute*, (b) lab on chip device. *Credit: Wikipedia*

1.2 Application of microfluidics

Microfluidics finds wide application in biological and chemical studies (Fig. 1.1). With the reduced size, a small volume of liquid reagents is required to perform complicated chemical reactions. For example, in a pathological microfluidic device used for determining blood glucose levels, only a tiny amount of blood is required to monitor the patient's glucose level. The faster reaction time in microfluidic devices helps study the behavior of larger bio-molecules such as DNA with a lower coefficient of diffusion [4]. With a broad spectrum of applications from thermal control of electronic devices, inkjet printing, information technology, and optics to the study of surface chemistry, interfacial physics, and biological analysis, microfluidics has emerged as an interdisciplinary field of science and research.

1.3 Motivation of the study

Microfluidics is often believed to be a game changer in life sciences research and industry. The widespread application of microfluidics has made this field a key area of research. Among numerous applications of microfluidics, the thesis will focus on a microfluidics-based study on targeted cancer therapeutics. Chemotherapy, the most popular treatment of cancer, has adverse side effects, which add to cancer-related morbidity and mortality. Without targeted cancer therapy, chemotherapeutics also kill fast-growing healthy cells like normal blood cells and hair cells. Other side effects of chemotherapeutics include nausea, loss of appetite, higher toxicity, and multi-drug resistance. Controlled and targeted drug delivery is sought to be an efficient way of active and passive targeting of tumor cells. In addition, developing microfluidic devices to assess drug uptake on cancer cells will be an essential advancement in targeted drug delivery. Given this, a literature review was done on previously reported drug carriers, insights into their viscoelastic behavior, and microfluidic devices for controlled drug release and loading.

1.4 Smart drug delivery systems for targeted cancer therapeutics

More than 10 million deaths per year, cancer related deaths are estimated to increase and become 16 million death per year by the year 2040 [5]. Most of the deaths are caused by metastasis, there are other underlying factors which add to this fatal figure. These factors include lack of immediate diagnosis, inefficient drug

treatment, other health complications arising out of cancer treatment. However with current diagnostic devices and treatment strategy, cancer mortality and morbidity is under control but with several other implications. Chemotherapy is the most widely used method for cancer treatment [6, 7], in which chemicals are used for manipulating DNA synthesis and mitosis. As cancer cells grow faster, chemotherapy treatment target faster growing cells, in doing so, other fast growing cells like hair cells, normal blood cells also get killed in chemotherapy [8]. Apart from this other adverse effects of chemotherapy includes loss of apatite, nausea etc. which also add to the higher cancer mortality rate [9]. Due to lack of targeting efficiency in chemotherapy, higher doses are required leading to higher toxicity and eventually leading to multi drug resistance [10–13] . Due to this adverse side effects and low therapeutic efficacy, targeted treatment of cancer cells is desirable for active or passive attack on tumor sites.

Controlled drug delivery by nano carrier is one method of applying drug to the targeted tumor site. Drug carriers, as the name suggests, should be able to deliver anti-cancer drugs, genes and other therapeutics like a laser-guided missile at the concerned tumour site. Nano carriers are coupled with molecules that bind to the overexpressed cancer cell surface receptors. Drug is then released from the carriers by responding to the stimuli based on carrier property. Although efficient and advantageous, circulation instability, less bio degradation and poor bio availability of some of these nano carriers raises concern on the long term application on cancer treatment. Continuous research is required to develop microfluidic based devices for efficient drug delivery to the tumor site. Nano carriers are most likely the better approach for drug delivery application, as it can deal with adverse side effects like toxicity by high selective accumulation on targeted site. High selective accumulation is achieved by passive targeting technique utilizing enhanced permeability and retention effect [14] and active cellular uptake [15]. Active targeting is also achieved by coupling nano carrier containing drug with the molecule that binds to the over expressed receptors on cell surface like a guided missile [16]. Drug is released from the nano carrier by responding to stimuli depending on property of nano carrier [17]. The most potent nano carriers are polymeric nano particles [18–21], liposomes [22, 23], hydrogels [24, 25], dendrimers, micelles, biomacromolecular scaffolds [26] and other inorganic carriers [27] (Fig. 1.2). Though advantageous, circulation instability, less bio degradation and poor bio availability of some of these nano carriers raises concern on their long term application on cancer treatment. Detailed discussion on emergent nano carrier can be found from review of Lombardo et al. [28].

Particles with dimension of the order of 1-100 nm is considered to be nano particles.

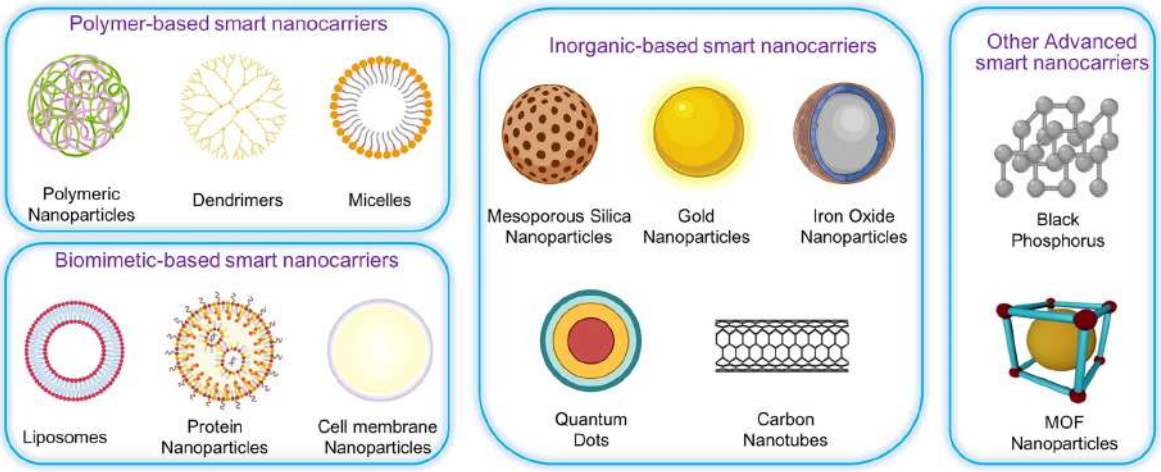

Figure 1.2: Different types of drug carriers [29]

When chemical substance is transported with the use of these nano particles then it is known as nano carriers. Nano particles does not naturally posses the characteristic of a nano carrier, their surface should be modified and functionalized for smart drug delivery application. Nano carrier should not be detected by immune system of body, they should be deposited at the target site only with delivery of correct amount of drug under internal or external stimuli [31, 32]. They should also be able to deliver other material like chemotherapeutic, genetic materials etc. [33].

The controlled drug delivery takes place sequentially in number of steps. Firstly, nano carriers overcome various biological barriers like cleansing by reticuloendothelial system (RES) before reaching the targeted site. The RES causes nano carrier to come out of the circulation, leading to deposition of anti cancer drug on liver, bone marrow or spleen. Abuchowski et al. [34] proposed PEGylation as the solution to overcome RES cleansing process. But PEGylation significantly reduce the drug uptake by cells [35, 36]. This ambiguity was named PEGylation dilemma [37, 38]. Secondly, the nano carrier should be functionalized to differentiate between cancer and healthy cells. The over expressed proteins on cancer cell surface differentiate it physiologically from healthy cells. The nano carriers are conjugated with ligands that bind to targeted cancer cells' overexpressed proteins. Thirdly, a mechanism for effective drug release from the carrier is required after the drug-loaded carrier reaches the targeted cancer site. For this the carriers are treated with several chemical group to make it responsive to any stimulus. Thus, drugs can be released from carrier to targeted site under specific stimulus. A pictorial representation of drug delivery at cancer site is shown in Fig. 1.3.

As microfluidic devices are used extensively in biomedical application, researchers

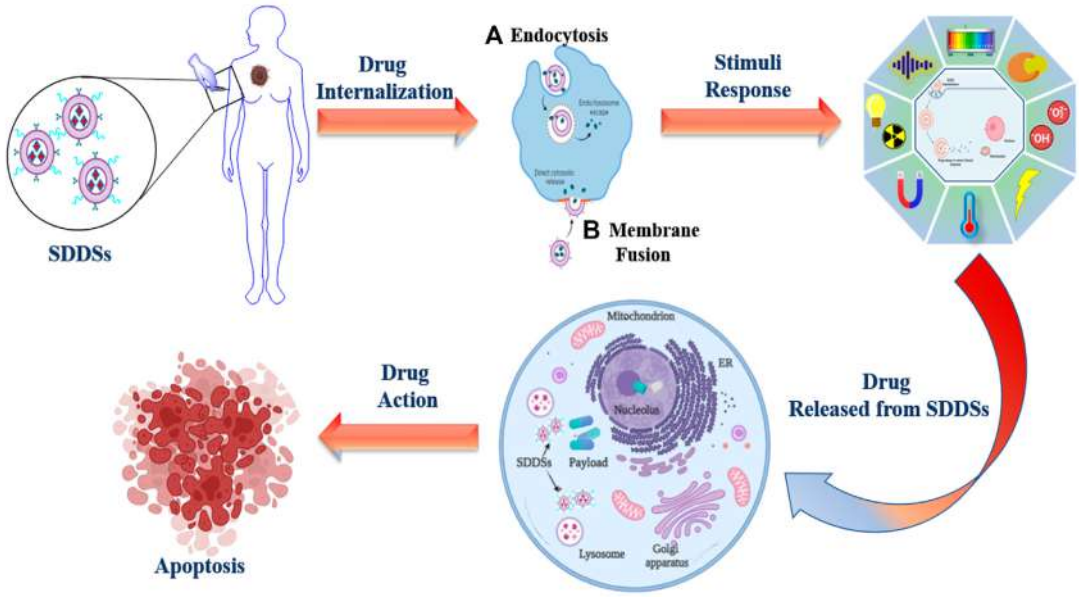

Figure 1.3: Smart drug delivery systems designed for targeted cancer therapeutics [30]

have also begin to explore its use in cancer theronautics and drug delivery application. Control of nano scale properties of microfluidic device for lab on chip application is the main challenge in its development [39]. For example PDMS is most commonly used for microfluidic fabrication, the hydrophobic surface of PDMS suffers unwanted protein adsorption [40]. Flow migration of nano particles undergo margination and adhesion to these channels, which makes flow behavioral study of nano carriers difficult. For efficient drug delivery by nano carrier nano particle must have better circulation and higher cellular uptake. This tendency of nano particles to marginate towards blood vessels wall becomes crucial in micro circulation of nano carriers.

Toy et al. [41] conducted the study to find the effect of nano particle size, shape, density on margination. To mimic the venule or arteriole dimensions, they designed a microfluidic channel of dimensions, 175×100 μm, walls of channel were treated with fibronectin to ensure the active targeting by ligand binding receptor surface. Both adherent and non adherent particles were collected. Lighter non-sphere nanoparticles with large sizes were observed to marginate more rapidly. Among other factors, particles with higher stiffness have a higher tendency for margination [42]. Soft deformable nanoparticles show the least margination and adhesion phenomenon in microcirculation and are best suited for the microfluidic investigation of drug delivery by nanocarriers. Liposomes, hydrogel, and polymeric nanoparticles are the nanocarriers that can deform and show less tendency of margination and adhesion. Hydrogels possess a high range of advantages over other

nanoparticles. Exploration of hydrogel advantage and finding the domain of its application in cancer drug delivery needs a great deal of research.

Made of 3D cross-linked chain of hydrophilic polymers, the hydrogel can hold large amounts of water [43, 44]. This property of hydrogel is utilized for various biomedical purposes, especially in drug delivery applications [45]. Other advantages of hydrogels include higher biocompatibility, tunable biodegradability, porous structure, etc. However low mechanical strength of hydrogel possesses a serious limitation in its application. Research is going on to produce novel synthetic hydrogel to achieve higher mechanical strength and enhanced water retention [46]. Hydrogel can be completely artificially synthesized and sustain adverse conditions like high temperature and high or low pH environment [47]. Adding functional groups to the polymeric chain, the hydrogel can respond to various stimuli like pH, light, heat, magnetic fields, chemical agents, etc. [48, 49]. Chai et al. [50] discussed various methods for preparing synthetic hydrogel for drug delivery application. Development of synthesis mechanism of hydrogel, hydrogel-based nanocarrier can deliver water-soluble drugs [51], hydrophobic drugs [52] etc.

Furthermore, these synthetic nano-carriers are prone to be attacked and eliminated by the innate immune responses of the human body. Therefore, it is necessary to design a drug carrier that can successfully shield itself from metabolism, excretion, and immune clearance [53]. In addition, synthetic drug carriers are susceptible to causing inflammation and cytotoxicity, while artificial liposomes are proven inefficient in cell uptake [54]. Therefore, membrane-derived biomimetic nanovesicles from cancer cells are sought to be the solution to this issue. Besides possessing self-homing capability, these typical biomimetic nanovesicles are characteristically bio-compatible as it is derived from cancer cells [55]. Moreover, retaining its functional characterizations and surface properties confers homing ability to these nanocarriers, enhancing the therapeutic outcome. Furthermore, recent research reveals that the surface protein modification of extracellular vesicles can significantly enhance its targeting efficiency [56].

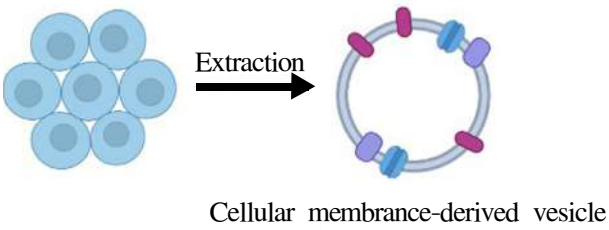

Figure 1.4: Cell membrane-derived vesicle [57]

Extracellular vesicles (Fig. 1.4) are formed and released by cells as secretory exo-

somes to communicate with each other [57]. Extracellular vesicles contain various proteins like extracellular matrix proteins, cell surface receptors, transcription factors, cytosolic signaling protein and microRNAs, RNA transcripts, and pieces of genomic DNA [58]. These characteristics make extracellular vesicles interconnect within cells by cell surface interactions and target-cell modulations and thus can be a potent drug vehicle. Besides, extracellular vesicles derived from dendritic cells can also be used for delivering vaccines [59]. A study in the Kalluri laboratory designed siRNAs to target the mutant protein of pancreatic tumors and then treated them with fibroblast-derived extracellular vesicles [56]. The drug delivery assembly was later administered to the mice, which lived longer and exhibited significant tumor suppression than the untreated mice that died within a short period. The study presented an astounding breakthrough in treating the highly aggressive pancreatic tumor.

Cell membrane-derived nanovesicles are classified based on the parent cells from where they are derived. Based on it, there are plasma-derived extracellular vesicles, bacterium-derived extracellular vesicles, cancer cell-derived extracellular vesicles, adherent cell-derived extracellular vesicles, milk-derived extracellular vesicles, and suspension-cell-derived extracellular vesicles.

In the recent advancement of cancer treatment with extracellular vesicles as a drug carrier, a new subtype called cell membrane-derived nanovesicles is gaining prominence [60]. These nanovesicles are obtained from mechanical extrusion of parent cells [61] that can be used as carrier [62]. Moreover, the efficacy of these nanovesicles can be further enhanced by coating [63] of therapeutic drugs and nanocarriers, respectively. Compared to synthetic nanoparticles, these nanovesicles exhibit better biocompatibility, longer circulation, lesser toxicity, immunogenicity, and inherent targeting potency [64]. In comparison to the normal cell-derived nanovesicles, the tumor-specific nanocarriers are extremely desirable on account of their targeted drug release and minimum off-target toxicities in comparison to the conventional nanocarriers [65]. Recently, the development of biomimetic cell membrane-derived nanocarriers obtained from various cell types has gained much importance. The retention of the intrinsic properties such as surface proteins, receptors, etc., attributed to their ability to evade the immune system, decreased phagocytic uptake, and prolonged circulation [66]. Additionally, the self-homing capabilities of these nanovesicles towards the tumor microenvironment also contribute to their superiority in targeting the tumor in vivo [67]. Apart from membrane-derived vesicles, Bidkar et al. [68] developed a membrane-coated nanocarrier for the codelivery of chemotherapeutic agents along with curcumin (Cur) and tirapazamine (TPZ). Cur and TPZ were constituted with biodegrad-

able poly (lactic-co-glycolic acid) nanoparticles (PLGA NPs). The nanoparticles thus obtained were coated with a red blood cell (RBC) membrane. The nanocarrier developed showed long-term stability, efficient cellular internalization, and bio-compatibility.

Limitations of bio-compatibility, longer circulation, margination, and adhesion of drug carriers can be easily discerned and overcome by using soft-deformable cancer cell membrane-derived vesicles. However, other challenges are yet to be addressed before drug-carrier-based therapy can replace chemotherapy. Some of the major aspects are the high cost of production, ineffective penetration, and premature release. Thorough clinical trials are required to assess the accumulation of nanocarriers and their effect on physiological functions. A thorough study is necessary to decipher the immune responses that are triggered by these drug carriers. In addition, drug carriers can also cause cytotoxicity at the targeted tumor sites. Furthermore, a thorough understanding of how carriers withstand the adverse effects of migration while undergoing absorption, distribution, metabolism, and excretion is also required. Besides, the effects of term applications of these drug carriers are also unknown. However, even with these limitations, few drug-mediated nanomedicines have been approved by the FDA. These nanomedicines are Doxil, PEG-functionalized liposomal doxorubicin, CPX-351, Abraxane, and NBTXR3 Henify are other FDA-approved nanomedicines for the treatment of acute myeloid leukemia.

1.5 Viscoelastic fluid drop model of drug carriers and cells

Cells and drug carriers possess structural and functional integrity. This structural and functional integrity is greatly affected by the mechanical properties of these particles. Any kind of change in mechanical property can depict a change in its functionality. Studying the mechanical behavior of biological cells is of great importance for the detection of various diseases in the human body [69]. Thus, it is needless to say that a mechanical model of cells and drug carriers can solve various mysteries about its mechanical behavior that can not be ascertained by experimental studies. Numerous researchers have put an arduous task into developing various models of cells, while the development of mechanical models of drug carriers is still at a nascent stage. Various models adopted for modeling cells are reviewed by Lim et al. [70] (Fig. 1.5).

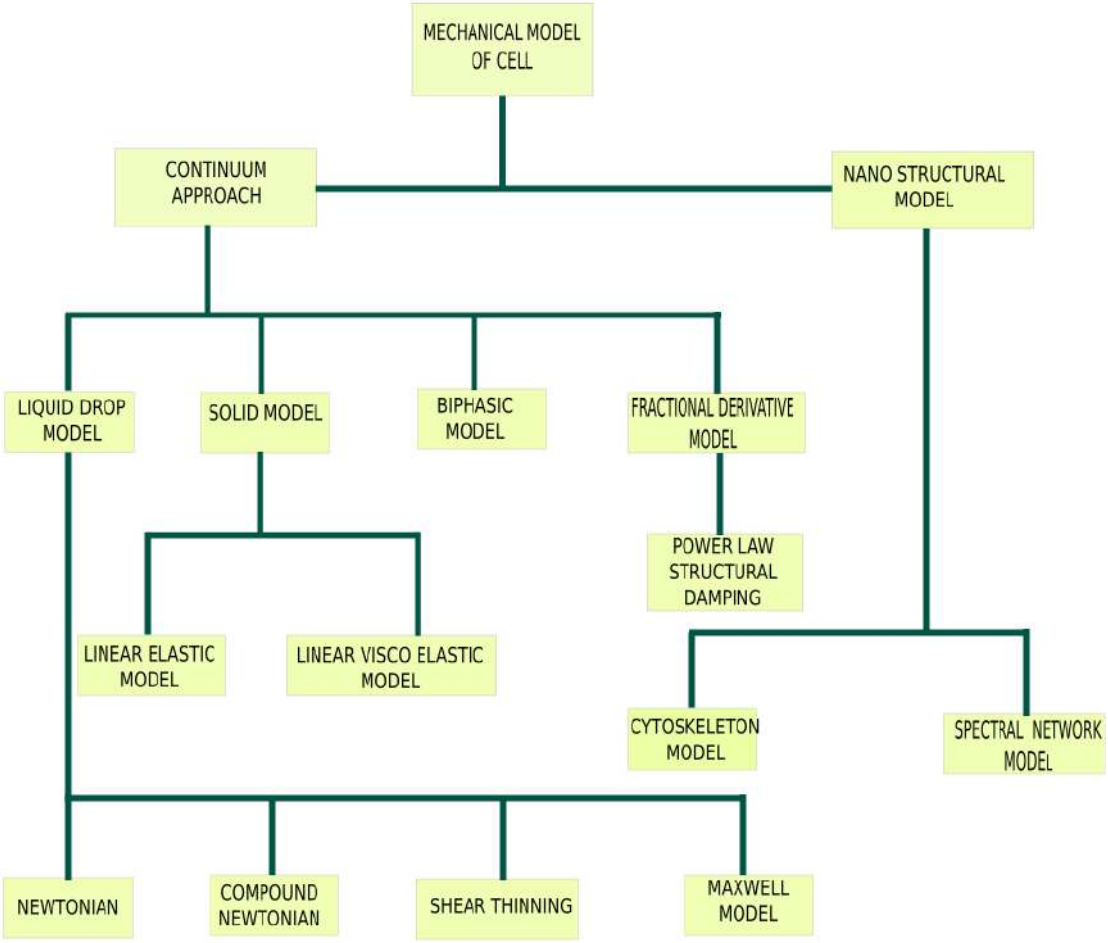

Figure 1.5: An outline of mechanical model of living cell [70]

Living cells behave mostly like liquid drops and acquire a spherical shape when suspended. Yeung et al. [71] simulated the flow of liquid-like cells. They used the Newtonian drop model (Fig. 1.6a), where the interior of the cell is assumed to be homogeneous Newtonian viscous liquid while the cortical portion of the cell was taken as an anisotropic viscous fluid layer. The cell cortex was modeled to have static tension but no bending stress. Interfacial velocity between the cortical layer and the cytoplasmic core was assumed to be continuous. They showed the creep response, γ of Newtonian fluid with viscosity μ, under stress $\tau = 2\mu$. Tran-Son-Tay et al. [72] also applied the Newtonian liquid drop model for studying the recovery of neutrophils subjected to large deformation.

A eukaryotic cell is composed of a cell membrane, cytoplasm, and nucleus. Nucleus makes 21% of cell volume [73]. Also, it is stiffer and more viscous than surrounding cytoplasm [74, 75]. So, a more complex model was required to model the contribution of the nucleus of the cell. Dong et al. [76] and Hochmuth et al. [77] used a three-layer compound droplet model (Fig. 1.6b) to study the more accurate

behavior of cell by taking the contribution of nucleus volume in the model. The computational model consists of a cortex kept under constant tension, a softer cytoplasm with viscosity less than the Newtonian liquid drop model, a nucleus cortex under constant surface tension, and an inner nuclear core with viscosity more than the cytoplasm. The compound model was observed to be the refinement of the Newtonian model, which was more appropriate for predicting the nonlinear behavior of cells that closely relate to the experimental observation. Leong et al. [78] envisaged the Newtonian compound drop model for modeling cell entry into the micro-channel.

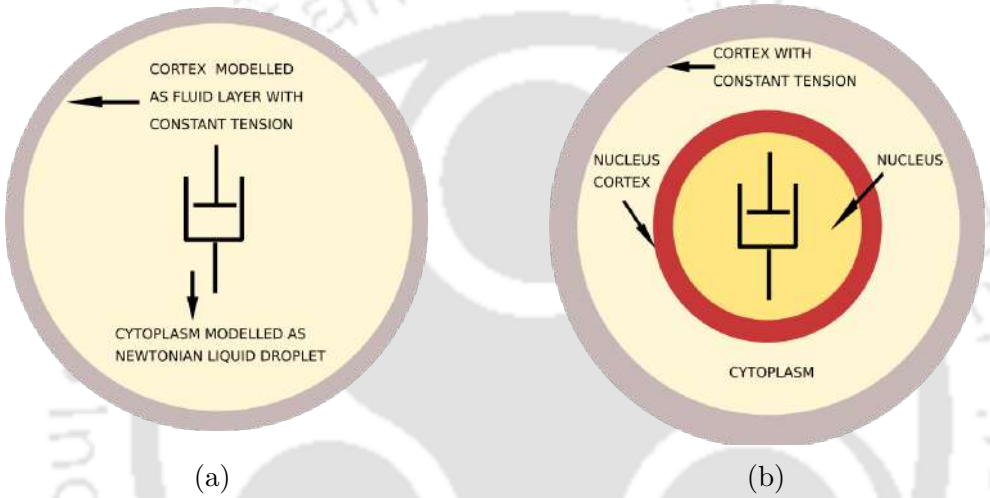

Figure 1.6: Cell liqiuid dropmodel, (a) Newtonian liquid drop model [71], (b) compound Newtonian liquid drop model [77]

A two-dimensional axisymmetric test model was used to study the entry behavior of the cells in a microchannel. Fluid was assumed to be Newtonian and incompressible. Continuity and momentum equations were solved distinctly for both cytoplasm and nucleus. To take the elastic behavior of both the cortex and nucleus, the elastic force was added tangentially to the interface in addition to the normal surface tension force to the interface. They were able to validate the experimental displacement versus time characteristics with the proposed model. Luo et al. [79] also used the Newtonian drop model for their simulation. They used the level set method [80] for interface capturing. A study on Ahmad et al. [81] work can be useful for further information on two-component models of cells.

Though the Newtonian drop model proved to be a more convenient model to predict cell movement, the dependence of apparent cytoplasmic viscosity on shear rate for large deformation was still not explained. Tsai et al. [82] observed constant aspiration speed under constant aspiration pressure with the Newtonian liquid drop model. The behavior was inconsistent with the observed cell acceleration after the whole cell was sucked in. The study suggested a shear-thinning model of cells with

a power law relation between apparent viscosity and shear rate. The model was able to simulate the experiment better than the liquid drop model of Newtonian fluid. The shear thinning model also showed consistent results for polymeric fluids. Wang et al. [83] also used the power law model of cells. They did a simulation to study the cell damage due to mechanical impact in direct cell writing.

Au et al. [84] presented the coarse-grained model circulating tumor clusters migrating through microchannel using a fully coupled Lattice Boltzmann(LB) - immersed boundary method. The deformable particles were modeled considering beads connected with finitely extensible nonlinear elastic (FENE) springs. They showed the effect of the adhesive strength of modeled circulating tumor clusters on their migration through constricted channels.

Other theoretical models include both liquid and solid models of cells. These studies include a study by Raj et al. [85], a finite element model by Mijailovich et al. [86], a two-dimensional FEM model of breast cancer cells by Barber et al. [87]. Other simulation approaches used for solving cell migration behavior were adopted, such as smoothed particle dynamics used by Ye et al. [88] for their simulation, and dissipative particle dynamics approach used by Wang et al. [89]. As the Newtonian and non-Newtonian liquid drop model was believed to give satisfactory results for cells undergoing large deformation, a suggestion for a convenient model for studying the cell behavior of cells undergoing small deformation was required. Dong et al. [90] used the Maxwell liquid drop model for studying small deformation characteristics of Leukocytes. The major difference between the Newtonian model and the Maxwell model is that the Maxwell model contains an elastic element. The model was successful in explaining the elastic rebound behavior of cells. It successfully predicted the visco-elastic nature of the polymeric fluid.

Zhou et al. [91] used both the Viscoelastic drop model and the Newtonian model for the simulation of neutrophil deformation and transport in capillaries. They used a diffused interface model for simulating interfacial phenomena for two-fluid systems. They defined phase field function ϕ for interface construction. The Oldroyd-B model was used to model the viscoelastic cell, and the outer matrix was Newtonian fluid. They studied the viscoelastic effect on the entry time of Neutrophils and deformation characteristics. The simulation showed that with an increase in Deborah number, the entry time of the cell decreases monotonically. Hymel et al. [92] did a simulation to see the effect of bifurcation angle on cell trapping in a Y-junction microchannel. Intracellular interfaces (between cytoplasm and nucleus) and cell surfaces were tracked by the volume of fluid method. The cell cytoplasm was modeled as a single-phase viscoelastic continuum with a Newtonian fluid-like component (cytosol) and polymeric component (cytoskeleton); the polymeric

component (cytoskeleton) contributes to the interfacial cortical tension of the cell, which is the source of viscoelasticity. Giesekus constitutive relation [93] was used to study the viscoelasticity of the cytoskeleton. A similar study was done by Simoncini et al. [94] with the viscoelastic model of a cell.

Viscoelastic fluids are commonly known as polymeric fluids. The name suggests that these fluids possess both viscous and elastic behavior. These fluids are described as elastic fluids due to certain characteristics exhibited by these fluids. One such behavior is having a memory effect. Elastic material needs to have memory to return to its original shape. Thus, fluids with memory are also considered to be an elastic fluid. Polymeric fluids are basically large molecules composed of smaller structural units. These structural units are connected in linear or cross-linked chain-like networks. Most of the biological molecules are made up of different structural units. For example, DNA molecules are made of chains of such structural units that contain genetic information. Furthermore, these polymers have the tendency to remain in different configurational orientations. These orientations usually change due to thermal motions and rotations around the chemical bonds. Due to configurational changes, a wide spectrum of time constants are linked with these polymeric fluids. Thus, these fluids also have a wide spectrum of relaxation times that give partial memory to these fluids. Apart from memory effects, these fluids also exhibit normal stress differences in a shear flow. These normal stress differences effect is not present in Newtonian or non-Newtonian fluids that do not possess elastic behavior. Viscoelastic fluids exhibit extra tension along the streamlines. Thus, these fluids practically exhibit negative normal stress differences along the streamlines. Garner and Nissan [95] studied the rod-climbing effect of polymeric fluids and experimentally demonstrated the normal stress difference effect. In the experiment, it was observed that polymeric solution was able to climb a rotating rod immersed in it. While Newtonian fluid was pushed away from the rotating rod due to the centrifugal effect. It can be deciphered that these fluids exhibited a complex behavior that arises due to the configuration of smaller structural units. Thus, the most important aspect of developing a mechanical model of these fluids is to model the orientations of these polymeric chains.

In the present thesis, kinetic theory-based models to model the configurational orientation of polymeric molecules in the polymer solution were adopted. The model considers an elastic dumbbell where a spring connects two beads suspended in a Newtonian fluid. The maximum extension of polymer molecules decides the elastic dominance in the polymeric fluids. In the dumbbell model, the maximum extensibility of the polymeric beads directs the maximum level of viscoelastic stresses. The model provides a better estimation of dilute polymer solution. The

model may be a linear elastic dumbbell model or a non-linear elastic dumbbell model. In the linear elastic dumbbell model, the dumbbell consists of two identical beads connected by a Hookean spring immersed in a Newtonian solvent. The beads experience hydrodynamic forces exerted by the solvent, Brownian forces due to the random collision of beads with the solvent molecules, and the tension forces due to spring. The cumulative effect of these hydrodynamic forces and tension forces on the dumbbell beads determines the viscoelastic behavior of the fluid. In the present model, the inertia of beads, molecular and chemical interaction between beads and solvent, and gravity are neglected.

In linear elastic dumbbell models such as the Oldroyd-B model, the tension forces on the beads are determined using linear Hookean spring law. It results in the unbounded extension of spring even at a finite extension rate. This limitation causes abnormal extension of polymeric dumbbells under the region of higher stresses. The following limitations are not present in finitely extensible non-linear elastic dumbbell models such as the FENE-P and FENE-Cr models. The FENE-P drop model exhibits a shear-thinning behavior, while the FENE-CR model describes a class of fluids known as Boger fluids; these fluids possess elastic effects and shear rate-independent constant viscosity. Apart from the FENE-CR model, the FENE-P model differs from the Oldroyd-B model regarding the extensibility of the polymer molecules. In the present thesis, the flow of the shear-thinning viscoelastic drop, such as the FENE-P drop, will be discussed.

1.6 Microfluidic devices for controlled drug release and drug uptake study

A great deal of research has been done in recent times in microfluidics that proved microfluidic-based devices are capable of outperforming their traditional counterpart. With the advancements in design and fabrication of such devices, it has now become easy to study the phenomenon, which was believed to be evasive to the macro scale devices. The development of microfluidics and the capability of such devices to depict complicated phenomena in several areas of fluid dynamics, biological science, and molecular physics is largely attributed to the furtherance in micro- and nano-fabrication techniques. The introduction of materials like PDMS and PMMA in the fabrication of microfluidic devices played a key role in the prominence of microfluidics. PDMS and PMMA are capable of generating low-cost, pliable, deformable microfluidic structures of intricate shapes with faster design time than traditional silicon-based devices.

Sustained and controlled administration of drugs is of immense importance in the context of targeted drug delivery in cancer therapeutics. Conventional oral and injectable drug administration treatment involves a first-order drug release kinetic that is unable to achieve a sustained release. As a solution to this, drug delivery microchip is now gaining momentum to shape the future of drug delivery. The drug delivery microchip can be implanted into the concerned site in the human body and can achieve controlled and targeted drug release for a longer period as it follows zero-order release kinetics. Thus, a diffusion-controlled drug release device that can achieve zero-order drug release. In the diffusion-controlled drug delivery microchip, a well serves as a reservoir for the drug particles, and a microchannel filled with biocompatible polymer serves as a diffusion barrier between the drug particles and body fluid. The body fluid will be allowed to infiltrate through a biocompatible polymer-filled channel and reach through the reservoir well filled with drugs. The drug particles then dissolve with body fluid, and the solution flows back through the same channel and gets released into the human body. To optimize the size of the microchip, a drug-loading device will also be fabricated as a part of the drug delivery system. A drug with better loading efficiency on cancer cells will require a lesser volume of the drug reservoir to achieve an efficient drug release. The drug-loading device will be designed to create a chaotic motion that can create a stirring effect for the desired drug loading.

Drug delivery microchips that can be implantable are gaining a great deal of interest in the context of sustained and controlled drug release [96]. Implantable systems with improved bio-compatibility can achieve drug delivery for a longer period. The sustained drug delivery system also reduces the risk of side effects of conventional drug delivery in cancer theranostics. Conventional drug administration, like chemotherapeutics in oral or injectable form, follows a first-order drug release kinetics. In first-order drug release kinetics, the drug concentration in the blood level decreases exponentially after a high initial blood level concentration within a span of the short duration of first drug administration. In the process of such kind of drug administration, there is an increased risk of toxicity, and low therapeutic efficacy is achieved. On the other hand, in zero-order drug release kinetics, the drug concentration in the blood level remains constant after an initial high blood level concentration. Regarding this, several drug delivery systems in the form of pellets, rods, and wafers with biocompatible polymer as matrix [97, 98] have been developed. However, achieving zero-order drug delivery is still not achievable with these systems. Given this, implantable drug delivery devices can be produced to replace the conventional drug delivery system. By the application of microfabrication technology, a microchip can be designed that can accurate

and precise drug release in the human body [99, 100]. The microchip made of soft bio-compatible material can be implanted in the body with less inflammation. For the implant, an incision of the shape and size of the microchip should be made on the human body. The drug delivery can then be achieved by applying an external field like an electric field or magnetic field [101]. The drug release can also be controlled by diffusion or external force like radio frequency [102]. Earlier, a drug delivery assembled with micropump and microchambers on a microchip achieved an accurate and efficient drug release [102]. Ji et al. [103] fabricated a diffusion-controlled soft microfluidic drug delivery device. They suggested that a combination of smaller and longer channel lengths can achieve the onset of drug release from 1 to 4 days and a total drug release period of 55 to 335 days. For the combination of channels of different lengths, they used different reservoirs for each straight channel. Besides, the straight channel reservoir barrier was also used by Lee et al. [99, 100].

Thus, it can be understood a drug-delivery microchip along with a drug-uptake device can bring significant improvement in cancer therapeutics. The development of drug delivery and drug-loading microdevices is still in nascent stages, with a meager amount of research available. Most of the drug-uptake studies on cancer cells are carried out in a still environment or a centrifuge. It can easily be found that these techniques could not accurately predict the amount of drug loaded on the cells. Given such limitations, it is necessary to develop a platform where drug loading on cells or drug carriers can be done when both drug solution and cells or drug carriers are flowing under a mechanical environment similar to the blood vessels network.

1.7 Objectives

Based on a thorough literature review and acknowledging the research gap, the following objectives for the thesis are outlined.

- To develop a viscoelastic drop model for drug carriers. To report the FENE-P drop breakup inside the constricted microchannel. A previous study [104] reported that the effect of solvent viscosity ratio was negligible on drop deformation at the Weissenberg number ($Wi = 1$) when it flows under confinement. Thus, an attempt to examine the effect of solvent viscosity ratio on drop deformation flowing inside confinement at unity Deborah number.
- To investigate the migration of shear-thinning and self-healing hydrogel nano drug carriers in a constricted microchannel of 7 μm diameter, designed to

mimic human blood capillaries. To decipher the drug release and drug loading efficiency of these carriers. Additionally, to perform experiments for quantification and assessment of flow behavior and deformation of cancer cell-membrane-derived nanovesicles flowing inside branches of the microchannel and micro blockages.

- To investigate the transport of a commercial drug, protein-bound Paclitaxel, Paclicad through a mechanically adverse environment inside a constricted microchannel. Desai et al. [105] suggested that albumin-bound paclitaxel of average size 130 nm shows less tendency of capillary obstruction. Although commercially approved, the transport mechanism of such drugs inside micro-capillaries is still not known. Thus, experimental investigations will be done to explore the transport tendency of this commercial drug.

- To fabricate a microchannel for a complete assessment of intravenous drug uptake on breast cancer cells (MCF-7). The microchannel will be designed to mimic the complex network structure of blood capillaries.

1.8 Thesis outline

A brief introduction to the thesis subject is discussed in the present chapter. The chapter presented discussions on the basic concepts of microfluidics, detailed literature on smart drug delivery by drug carriers, the development of a numerical model of cells, and the fabrication of a drug-release microchannel. In the later section of the chapter, the objectives of the thesis are presented based on the research gap found after the literature review. In Chapter 2, the various methodologies adopted for carrying out the studies are discussed in detail. In the chapter, various experimental techniques required for particle preparation, characterization, and transport tracking are discussed. The chapter also provides a detailed discussion of the steps and equipment involved in microchannel fabrication by photolithography. Furthermore, a thorough discussion of numerical techniques and governing equations involved in the study is presented. The chapter presented the formulation of the viscoelastic drop and Newtonian matrix model. A detailed discussion on solver *Basilisk* is also discussed in the chapter. In Chapter 3, a detailed study on the deformation and breakup of shear-thinning FENE-P drop is carried out. The effect of solvent viscosity ratio, confinement ratio, capillary number, and viscosity ratio on drop deformation was studied. The variation of viscoelastic normal stress difference distribution inside a drop undergoing deformation inside a constricted microchannel with sudden entry and exit is also discussed. The drop breakup and

variation of critical capillary number with Deborah number and viscosity ratio are also discussed. In the fourth chapter, the transport behavior of synthetic and natural drug carriers flowing under a microchannel of 7 μm thickness is discussed. The discussion on the synthesis, flow behavior, and quantification of deformation of synthetic drug carriers (hydrogel) and natural drug carriers (nanovesicles) is done. In the chapter, a viscoelastic drop model of hydrogel drug carriers is also developed, and a comparison of experimental and computational results is made. After a study on the transport behavior of two kinds of drug carriers, the study is then extended to the drug itself in Chapter 5. The investigation of the transport behavior of the commercial anti-cancer drug practiced inside a microchannel of 7 μm is discussed. In Chapter 6, drug uptake on breast cancer cells is deciphered. The drug uptake study is carried out in a microchannel of two configurations that can nearly replicate the blood capillary network. In the end, conclusions and the future extension of the thesis are discussed in Chapter 7.

2

Experimental and numerical methods

The present thesis will explore the transport behavior of particles, mainly drug carriers and cells, through constricted microchannels. In the quest for this exploration, various experimental and numerical techniques were applied for visualization and prediction of the transport behavior of the above-mentioned particles. The first possibility was to explore the preparation of deformable particles that can adjust and structurally heal themselves while flowing through adverse constrictions. Thus, suitable protocols to synthesize hydrogel drug carriers and breast cancer cells with viscous and elastic behavior were selected. The next step was to capture and visualize the flow of these particles using proper experimental techniques. The visualization of particles and cell flow was primarily done in bright field mode, while the particle and cell characterization was done in fluorescence mode. As the particles and cells moved very fast in the minute constricted channels and did not have a self-fluorescence property, an efficient light source to get discrete excitation and emission of fluorescence could not be achieved. Thus, it needed to adopt very sophisticated microchannel fabrication techniques to visualize the flow of particles and cells through the constricted channel. Thus, considerable effort was put into understanding and gaining expertise in photolithography techniques. Numerous microchannels of delicate designs were self-fabricated using the in-house cleanroom facility of the Centre for Nano Technology of the Indian Institute of Technology Guwahati. Furthermore, getting more profound insights into particle behavior and internal morphological changes can only sometimes be captured in experiments, primarily due to the unavailability of sophisticated experimental facilities. Thus, a significant effort was made to prepare a numerical model of these particles and cells with viscous and elastic behavior. Thus, in the present chapter, an elaborate discussion regarding the methods and protocols for particle synthesis, characterization, experiment procedure, microfabrication, and numerical modeling will be discussed.

2.1 Experimental methods

The discussions in the section include protocols adopted for drug carrier and cell synthesis, characterization of particles and cells, experimental procedure and types of equipment, and microchannel fabrication by photolithography.

2.1.1 Synthesis of drug carrier particles and cancer cell culture

The protocols followed for the synthesis of hydrogel drug carriers, nanovesicle extraction, sample preparation of Paclicad particles, and breast cancer cell secretion are discussed in this section.

2.1.1.1 Synthesis of hydrogel

The hydrogel was synthesized by physical crosslinking of PVA and PVP as reported by Banerjee et al. [106]. PVA, PVP, and phosphate-buffered saline were purchased from Sigma Aldrich, USA. Briefly, the PVA and PVP were mixed in a ratio of (70: 30 w/w) and stirred in the solution for 24 h at 95 °C. The mixture was then incubated at -80 °C for 12 h, and afterward, the frozen mixture was allowed to melt at room temperature. This freeze-thaw cycle was repeated six times to facilitate the crosslinking between PVA and PVP, forming a hydrogel. The resultant mixture was centrifuged and washed thrice with deionized water to remove unreacted molecules. The resultant particles are dissolved in deionized water to get the sample solution for the experiments.

2.1.1.2 Paclicad sample preparation

The injectable protein-bound Paclitaxel, Paclicad, was acquired commercially from Cadilla Pharmaceuticals Ltd. The experiment solution was prepared by dissolving 10 mg of the solute into 2 ml of water. The solution concentration was mentioned in the guidelines provided by the manufacturer. The solution was mixed with blue-colored dye and was washed thoroughly to remove the specks of dirt and chemical additives. Dye was added to produce a contrast between drug particles and carrier fluid to successfully track the drug particles in bright field mode.

2.1.1.3 Nanovesicles extraction

The nanovesicles were extruded from MCF7 cell membranes through a 0.8 μm pore-sized membrane, followed by a 0.2 μm pore-size membrane. The obtained nanovesicles were washed in PBS solution by centrifugation (20,000×g) [107]. The centrifuged pellet was resuspended in 1X PBS and stored in 20 °C. The prepared nanovesicles were later characterized using a Field Emission Electron Microscope and Dynamic Light Scattering (DLS). Moreover, nanovesicles were drop-casted on aluminum foil and dried for the FESEM (Sigma 300, Carl Zeiss AG, Jena, Germany) study. The hydrodynamic diameter and surface charge distribution of nanovesicles were analyzed in a DLS zeta sizer (Zetasizer Nano series, Malvern Instruments Ltd, Malvern, UK).

2.1.1.4 Cell lines and culture condition

Breast cancer cell line MCF7 was purchased from the National Centre of Cell Science (Pune, India). It was maintained and cultured in Dulbecco's Modified Eagle's medium-high glucose supplemented with L-glutamine, sodium pyruvate, sodium bicarbonate (Sigma Aldrich) 10 % fetal bovine serum (FBS) (Gibco, USA),100 μ/mL and 100 μg/mL. Penicillin and Streptomycin, respectively (Thermo Fisher Scientific, USA) under humidified air condition comprising 5 % CO_2 at 37 °C. The chemotherapeutic fluorescent drug Doxorubicin was acquired commercially from Cadilla Pharmaceuticals Ltd. The experiment solution was prepared by dissolving dox powder in DMSO. The solution working concentration used was 10 micromolars. The cells were dissolved in 1X PBS and mixed with Doxorubicin for further analysis.

2.1.2 Characterization of particles and cells

2.1.2.1 Dynamic light scattering study

The hydrodynamic diameter of the hydrogel, Paclicad particles, and nanovesicles was measured using a dynamic light scattering analyzer (Malvern Zetasizer Nano ZS-90). Measurements were recorded while keeping the sample in PBS buffer at 25 °C.

2.1.2.2 Field-Emission Transmission Electron Microscopy analysis

JOEL JAM 2100F TEM with an operating voltage of 200 kV was used for TEM measurement to analyze the size of the hydrogel carriers. Before taking the measurement, 8 μl of hydrogel and Paclicad particles were drop-cast on a carbon-coated copper grid and dried in a desiccator overnight.

2.1.2.3 Field-Emission Scanning Electron Microscopy analysis

FESEM analysis of the hydrogel, Paclicad particles, and nanovesicles were analyzed using JOEL JSM-7610F Schottky Field Emission Scanning Electron Microscope. Sample (20 μl) was drop cast on an aluminum foil-coated glass slide and dried using a desiccator overnight. Samples were coated with gold film using a sputter coater (SC 7620 Mini, Polaron Q Sputter Coater).

2.1.3 Experiment procedure and result analysis

2.1.3.1 Experiment setup

The flow study of migration of hydrogel, Paclicad, nanovesicles, and cancer cells in the microchannel was done in several steps. The microchannel was stationed on the microscope stage at first. Polyethylene-made intramedic semi-rigid tubing with an inner diameter of 0.38 mm and an outer diameter of 1.09 mm was used to connect the flow to the inlet and outlet of the microchannel. A sufficient volume of the sample solution is taken by Eppendorf tube to a syringe, fixed securely with the syringe pump by Harvard apparatus (Fig. 2.1a). The connections to the inlet and outlet of the channel were secured well with close observation. The microscope and pump were switched on by connecting them to the power source. As the syringe pump started to operate, the sample solution began to fill the connecting tube and flow through the microchannel. The average velocity of blood (usually measured in cm/s) generally varies from 0.03 to 40 cm/s as the blood flows through the vena cava, capillaries, and aorta. The experimental sample-bound paclitaxel was allowed to flow passively at a constant flow rate with the help of a syringe pump. The flow of hydrogel, Paclicad, and nanovesicles was observed and recorded by Phantom Miro lab 320 camera (Fig. 2.1b) with a frame rate of 5000 - 21000 fps. The flow of cancer cells for the drug loading device was recorded by Phantom VEO 340 L (Fig. 2.1c) camera at a frame rate of 5000 - 10000 fps. The camera was connected to an inverted microscope Leica DMI 3000M (Fig. 2.1d). The videos were then deconvoluted to obtain images at the required time instants. The schematic of the

experimental setup has been shown in Fig. 2.2.

(a) (b)

(c)

(d)

Figure 2.1: Experimental equipment (a) syringe pump, (b) phantom miro lab 320 high speed camera, (c) phantom VEO 340 L high speed camera, (d) inverted microscope Leica DMI 3000M

2.1.3.2 Migration video analysis

The migration of hydrogel, Paclicad, nanovesicles, and cancer cells was captured by a high-speed camera Phantom LAB miro 320. At first, the transport of

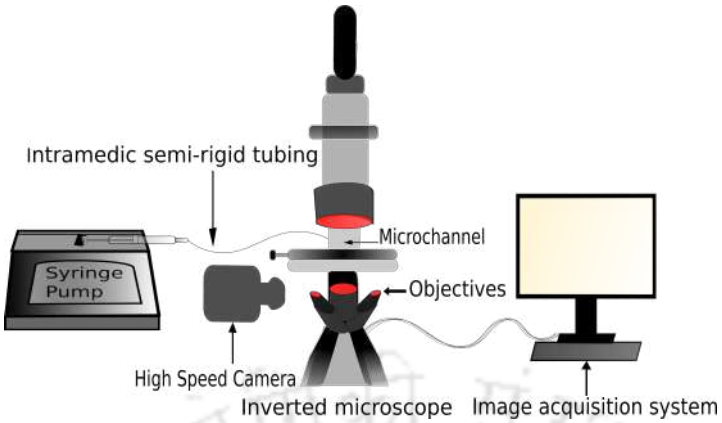

Figure 2.2: Pictorial illustration of the experimental setup with contributing equipments.

hydrogel drug carriers was studied. As hydrogel particles differed in size, the flow behavior of hydrogel particles about the micron-scale size was analyzed. The migration was discerned with the help of an inverted microscope, Leica DMI 3000M. The observation was made in bright field mode with an objective lens with 50x magnification. Considering the time duration of a single observation, the video was captured at a frame rate of 5000 fps with a customized resolution of 1280×400. Advanced image processing controls of Phantom camera controller software were used to analyze the cine files of the captured migration video. Time, distance, and particle size were measured by choosing a reference origin and calibrating the cine files with the experiment variables. After calibration, the distance traversed by the particle can be calculated in terms of frame progression, and the time can be calculated similarly. The size of the particles was determined by edge tracking them by utilizing filters in the image tools of the PCC software cine analysis feature. The transit of the trailing edge leaves the region mentioned above of the microchannel. The transit velocity can be found by

$$\text{Transition Velocity} = \frac{d_h}{t} \tag{2.1}$$

where d_h was the displacement of the hydrogel particle from the point when the leading edge of the particle enters the 7 μm constricted channel to the point when the trailing edge leaves the 7 μm constricted channel measured in time t. A similar approach was used to analyze the displacement profile of Paclicad particles, nanovesicles, and cancer cells. For these cases, time, distance, and particle size measurements were done by choosing a reference origin and calibrating the cine files with the experiment variables. After calibration, the distance traversed by the particle can be calculated in terms of frame progression, and the time can be calculated similarly. The average migration velocity (MV) can be found out by

$$\mathrm{MV} = \frac{x(t+\Delta t) - x(t)}{\Delta t} \tag{2.2}$$

where x was the axial displacement of the particle at time instant t, and Δt was the time interval between the two frames where the measurements were taken.

2.1.3.3 Drug loading and efficiency determination

Doxorubicin was loaded in the hydrogels by incubating hydrogel and doxorubicin in a buffered solution under continuous stirring. Doxorubicin hydrochloride was purchased from Pfizer Ltd. The mixture was centrifuged at 10000 rcf at 4 °C for 10 min. The resultant pellet was collected, washed, and centrifuged thrice to flush out unbound drugs. The supernatant was collected after the first centrifugation to determine the drug loading efficiency. After that, 100 μl of the supernatant was transferred in 96 well plates, excited at 470 nm, and emission was recorded at 595 nm using a multi-well plate reader (Infinite M200 Pro, Tecan, Switzerland). Doxorubicin solution initially used for encapsulation was used as a control. The loading efficiency was calculated using the following relation.

$$\text{Loading efficiency} = \frac{(\text{Dox initially used} - \text{Dox in supernatant})}{\text{Dox initially used}} \times 100\% \tag{2.3}$$

2.1.3.4 Study of drug release profile

To study the drug release profile of the hydrogel, the doxorubicin encapsulated hydrogels were incubated in phosphate buffer saline (PBS; 0.01 mM, pH 7.4) for up to 24 h. After the desired time interval, the sample was centrifuged at 10000 rcf at 4 °C for 10 min, and the supernatant was collected. From there, 100 μl of supernatant was transferred in 96 well plates, and the readings were recorded (excitation: 470 nm and emission: 570 nm) using a multi-well plate reader (Infinite M200 Pro, Tecan, Switzerland). The release profile was calculated using the following relation.

$$\text{Cumulative release} = \frac{\text{Dox initially released in supernatant}}{\text{Dox loaded in hydrogel}} \times 100\% \tag{2.4}$$

2.1.3.5 Mobility and trajectory measurement

The mobility of the particle is defined as the ratio of the particle's average velocity in a region to the carrier fluid velocity in that region. The mobility of the particle

is given by,

$$\text{Mobility} = \frac{u_{\text{avg,particle}}}{U} \tag{2.5}$$

where $u_{avg,particle}$ is the average velocity in the respective region of the microchannel, and U is the carrier fluid velocity in that region.

The particle trajectories were determined using the single particle tracking method of image processing software Phantom Camera Controller. The plots were generated using the Matplotlib package of Python programming.

2.1.3.6 Experiment reproducibility and data information

All experimental results presented in the present thesis are representations of at least three independent experiments, and the results are reproducible. It is also mentioned here that the particle, carries and cells does not always start at the same vertical position during the flow process of different experiments, so the displacement profile is not the exact repetition of the previous experiment; however, the trend is always similar. Given this, the results depicted the trend of displacement for different experimental observations. The displacement profiles were represented with error bands and error bars for the correct representation of deviations in the results.

2.1.4 Fabrication by photolithography

Microchannel fabrication has always been an arduous task from the initial days of research in microfluidics. As mentioned in the thesis review, advances in microfabrication techniques played a crucial role in the prominence of microfluidics. It has shaped many areas of research in the present world. Electronic industries and automobile industries are heavily dependent on microfabrication. An accurate microfabrication technique plays a vital role in shaping the future world. The most critical aspect of microfabrication is achieving dimensional accuracy without particle contaminations, as sometimes microchannel dimensions are smaller than the dust particles in the environment. Most microfabrication steps are performed inside a cleanroom to combat these restrictions. The current section will discuss microchannel preparation using photolithography inside the cleanroom. Apart from photolithography, other prominent microfabrication techniques are laser micro-machining and bio-printing.

Microchannel fabrication through photolithography involves the exposure of ultra-violet rays to a particular kind of chemical known as a photoresist. Photoresists are chemicals that are sensitive to exposure to ultraviolet rays. Photoresists are coated

on a substrate; a silicon wafer (Si wafer) or glass can also be used. The substrate covered with photoresist is then exposed to laser rays to carve the channel pattern. Based on the photoresist type, the coated resist bond will become weak or strong on exposure to laser rays. The photoresist exposes the laser rays according to the required microchannel design. The exposed portion of the photoresist is later removed or retained after immersing the substrate inside a photoresist developer to obtain the final microchannel pattern on the substrate.

2.1.4.1 Substrate preparation

Before photoresist coating, the substrate is cleaned using a standard RCA clean procedure. During his work at Radio Corporation of America, Kern [108] developed this cleaning process for silicon wafers. The cleaning process includes the removal of the organic contaminants, followed by ionic cleaning. The organic contaminants are cleaned by rinsing the Si wafer with DI water. The wafer is then immersed in boiling acetone at 56 °C to remove any metallic contaminations. The substrate is also cleaned with Iso-propyl alcohol for additional particle removal. The ionic cleaning is achieved after immersing the substrate in hydrochloric acid and hydrogen peroxide solution. The process will remove the remaining traces of metallic contaminants. The cleaned substrate is then rinsed with DI water and dried with liquid nitrogen gas. The cleaned substrate is then soft baked over a hot plate for 10 mins at 170 °C before photoresist coating.

2.1.4.2 Photoresist coating

Photoresist coating is most crucial in microchannel fabrication. Uniform photoresist coating is required to attain a uniform microchannel depth. Photoresist coating is completed in several steps based on the type of photoresist used. At first, Hexamethyldisilazane (HMDS) is coated over a thoroughly cleaned Si wafer. HMDS allows easier coating of photoresist on Si wafer. HMDS is poured on a silicon wafer placed on the chuck of the spin coater. A uniform layer of HMDS is formed after spinning at 4000 rpm for 60 s. The HMDS-coated Si wafer is soft-baked at 170 °C for 15 mins. Soft baking removes trapped air bubbles after spin coating. After the successful coating of HMDS, the photoresist is poured on the substrate. The coating procedures for positive and negative photoresists are different. Positive photoresist bonds tend to weaken on exposure to UV rays, resulting in the exposed portion washing out after developing. The resulting channel is later obtained by etching the photoresist's washed-out portion. However, it is the opposite for negative photoresists, where bonds become strong on exposure to UV rays. The

exposed portion of the photoresist only remains after the developing procedure. The resulting channel will be obtained as a bulge over the Si wafer. The most commonly used photoresist is S-1813, while negative photoresists are Su8-2025, Su8-2035, Su8-2050, and Su8-2075. The photoresist coating completes in one step when the substrate with photoresist is rotated at 3500 rpm for 60 s. For negative photoresist, the coating is done in two steps; first, a substrate with negative photoresist is rotated at 500 rpm for 30 s. In the next step, the substrate is again rotated at some given speed for 90 s based on the desired thickness of the photoresist. The speed versus thickness curve for negative photoresist Su8 is shown in Fig. 2.3b. The spin coater used for the present study is a POLOS spin coater (Fig. 2.3a). The final coated substrate is soft-baked before laser exposure. A substrate coated with positive photoresist is soft baked on a hot plate at 130 °C for 2 mins, while for negative photoresist, it is soft baked at 65 °C for 3 mins and 95 °C for 9 mins in succession.

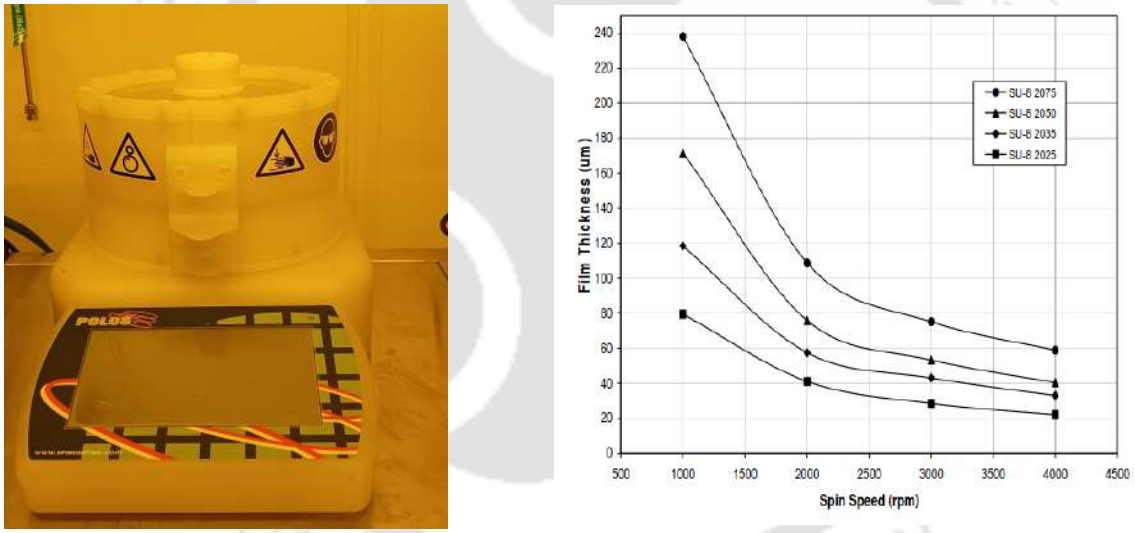

(a) (b)

Figure 2.3: Spin Coater and Data Sheet, (a) POLOS spin coater, (b) speed versus thickness curve for Su8 photoresist (source : www.microchem.com)

2.1.4.3 Contours and fillings for laser writing

For pattern writing on a coated Si wafer, the geometry is first drawn on a software format that is readable to any lithography instrument. Primarily, the geometry is drawn on an open-source software, Klayout, and saved in a .gds file extension. The geometry file is then imported on the Laser Writer software file (KLOE SOFTWARE SUIT), where the commands for contour and filling paths are given. The laser should follow the path to write the pattern on the mask. Ensuring that the laser appropriately starts contouring from its corner is necessary. It is done by

reducing the path geometry in the software. The resulting contour and the filling file saved in the .lwo extension are then imported into the mask writing machine for the final exposure.

2.1.4.4 Laser exposure for final patterning

The Dilase 250 shown in Fig. 2.4 is a direct laser photolithography equipment that materializes the pattern on photoresist by exposing it to a UV laser beam of wavelength 375 nm. The laser beam follows the contour and filling information from the .lwo files on the KLOE software suite. The writing speed and laser modulation are decided on the type of patterns required to obtain. The final exposed substrate is then immersed in a developer solution to acquire the final pattern. During negative photoresist, it has to be immersed in developer and Iso-propyl alcohol for successive times. For negative photoresists, post-exposure soft baking is also required.

Figure 2.4: Dilase 250 laser photolithography

2.1.4.5 Fabrication of microchannels

A representation of a fabricated microchannel is shown in Fig. 2.5a. The imprints of the channel of the design as mentioned above were made on a single Su8 master silicon wafer, prepared in the Centre of Nano Science and Engineering, Department of Indian Institute Of Science Bangalore, India, and Centre for Nanotechnology, Indian Institute of Technology Guwahati. PDMS was used as material for fabricating open microchannels. PDMS solution was prepared by mixing SYLGARD 184 silicone elastomer with a cross-linker in a ratio of 10:1 by weight. The mold was made by carefully placing the nylon ring over the Su8 master on top of aluminum foil. The PDMS solution is then steadily poured over the Su8 master bounded by a nylon ring. The mold was then placed over aluminum foil and was allowed to solidify by baking it in a hot air oven for 1 hour at 90 °C. After PDMS was solidified on the mold, the entire array was allowed to cool at room temperature. The PDMS structure containing an array of integrated channels was removed; the

single channels were later collected by surgical sectioning. Precision holes were made by punching to create an inlet and outlet of the channel. As the channels prepared were open, the top of the channel was sealed by a glass side. The sealing of the open channel with a glass slide by treating it in an oxygen plasma chamber by Harrick Plasma (Fig. 2.5b) for 1 min in a clean environment. To ensure a firm, watertight bonding, the binding surfaces of the open channel and glass side were exposed to high-intensity plasma for 30 s. The final closed channel was thus prepared by fixing the open PDMS channel with the glass slide.

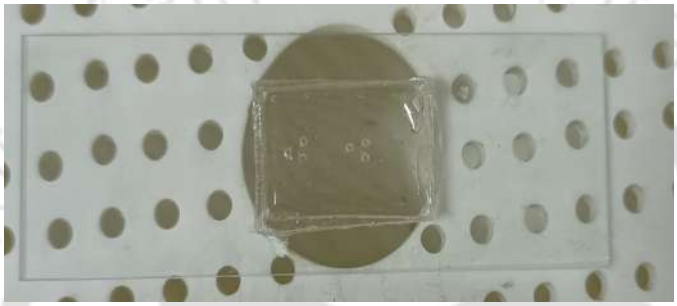

(a)

(b)

Figure 2.5: (a) fabricated microchannel, (b) harrick plasma chamber

2.2 Numerical methods

As mentioned earlier in the chapter, these particles and cells should have both viscous and elastic behavior to flow through the constricted microchannel. Thus, a two-phase viscoelastic drop and matrix system was adopted to produce a computational model. The drop phase was modeled as shear-thinning viscoelastic fluid, while the matrix was treated as Newtonian fluid. The shear-thinning viscoelastic fluid selected for the present study is FENE-P fluid. The reason for selecting FENE-P over other shear-thinning viscoelastic fluids is discussed in section 1.5.

2.2.1 Governing equations and solution methods

Incompressible mass and momentum conservation equations were used as governing equations for the simulation of the two-dimensional, two-phase, drop-matrix system. As the flow of drug carriers and cells inside blood capillaries is not necessarily axisymmetric, 2D simulations were carried out for the present study. The simulation results will serve as a pathway to achieve the broader objective of precisely designing drug delivery systems for attaining burst drug release by nano-carriers inside a constricted mechanical environment. Thus, in this section, the governing equations and methods adopted for solving the equations will be discussed. The simulations were performed on finite volume-based open source solver *Basilisk*. The vectors are represented in bold text, while tensors are represented in standard text in the equations, and the role of gravity is neglected.

$$\nabla \cdot \mathbf{u} = 0 \tag{2.6}$$

$$\rho\left(\frac{\partial \mathbf{u}}{\partial t} + \mathbf{u} \cdot \nabla \mathbf{u}\right) = \nabla \cdot \tau + \mathbf{F} \tag{2.7}$$

$$\tau = -p\mathrm{I} + \mathrm{T} + \mu_s \mathrm{S} \tag{2.8}$$

$$\mathbf{F} = \sigma \kappa \mathbf{n} \delta \tag{2.9}$$

$$\mathrm{S} = \left[\nabla \mathbf{u} + \left(\nabla \mathbf{u}\right)^T\right] \tag{2.10}$$

2.2.2 Two-phase formulation

A color function a was used to track the position of the fluids, where.

$$a = \begin{cases} 1 & \text{fluid 1 (drop phase)} \\ 0 & \text{fluid 2 (matrix phase)} \\ 0 < a < 1 & \text{control volume containing both drop and matrix phases} \end{cases}$$

Eqs. 2.11 and 2.12 gives the densities and viscosities for the two-phase flow. The advection equation of the volume fraction, a is given by Eq. 2.13.

$$\rho\big(a\big) = a\rho_1 + \big(1-a\big)\rho_2 \tag{2.11}$$

$$\mu\big(a\big) = a\mu_1 + \big(1-a\big)\mu_2 \tag{2.12}$$

$$\frac{\partial a}{\partial t} + \nabla \cdot \big(a\mathbf{u}\big) = 0 \tag{2.13}$$

.

A second-order accurate time discretization form was achieved using a staggered time discretization of density, volume fraction, and pressure. The discretized equation is given by,

$$\rho_{n+\frac{1}{2}}\left[\frac{\mathbf{u}_{n+1}-\mathbf{u}_n}{\Delta t}+\mathbf{u}_{n+\frac{1}{2}}\cdot\nabla\mathbf{u}_{n+\frac{1}{2}}\right]=-\nabla\mathbf{p}_{n+\frac{1}{2}}+\nabla\cdot\left[\tau_n+\tau_{n+1}\right]+(\sigma\kappa\delta\mathbf{n})_{n+\frac{1}{2}} \tag{2.14}$$

$$\frac{a_{n+\frac{1}{2}}-a_{n-\frac{1}{2}}}{\Delta t}+\nabla\cdot(a_n\mathbf{u}_n)=0 \tag{2.15}$$

$$\nabla\cdot\mathbf{u}_n=0 \tag{2.16}$$

Furthermore, the equations are discretized using the classical time-splitting projection method [109].

$$\rho_{n+\frac{1}{2}}\left[\frac{\mathbf{u}_*-\mathbf{u}_n}{\Delta t}+\mathbf{u}_{n+\frac{1}{2}}\cdot\nabla\mathbf{u}_{n+\frac{1}{2}}\right]=\nabla\cdot\left[\tau_n+\tau_*\right]+(\sigma\kappa\delta\mathbf{n})_{n+\frac{1}{2}} \tag{2.17}$$

$$\mathbf{u}_{n+1}=\mathbf{u}_*-\frac{\Delta t}{\rho_{n+\frac{1}{2}}}\nabla\mathbf{p}_{n+\frac{1}{2}} \tag{2.18}$$

$$\nabla\cdot\mathbf{u}_{n+1}=0 \tag{2.19}$$

$\mathbf{u}_*$ can be solved from Poisson equation,

$$\nabla\cdot\left[\frac{\Delta t}{\rho_{n+\frac{1}{2}}}\nabla\mathbf{p}_{n+\frac{1}{2}}\right]=\nabla\cdot\mathbf{u}_* \tag{2.20}$$

A second-order unsplit upwind scheme by Bell, Collela, and Glaz was used for the estimation of the advection term $\mathbf{u}_{n+\frac{1}{2}}\cdot\nabla\mathbf{u}_{n+\frac{1}{2}}$ [110]. The scheme is stable for CFL numbers less than 1. The solver adjusts the time step based on the CFL number.

The discretization of the computational domain is done by employing square finite volumes hierarchically organized as a quadtree. The quadtree grid restricts the resolution to powers of two defined in terms of number termed "level". A grid arrangement of two to the power "level" determines the grid resolution of the computational domain. For example, a level of 10 corresponds to 1024 × 1024

grid. The grid arrangement with the drop interface entering the constriction is shown in Fig. 2.6. The variables are collocated at the center of each square (2D) and cubic (3D) discretization finite volume and are estimated as the volume averaged value of the related finite volume. In the first step, spatial discretization of the pressure correction equation (Eq. 2.18) and Poisson equation (Eq. 2.20) using an approximate projection method [111] is done. Solving Eq. 2.17 will give the cell centered velocity field ($\mathbf{u}_*^c$). The auxiliary face-centered value ($\mathbf{u}_*^f$) was then obtained by taking the average of the cell-centered values on all faces of the discretized finite volumes. In the next step, computation of divergence of the auxiliary field from Eq. 2.20 was done for each control volume using finite volume approximation given by Eq. 2.21.

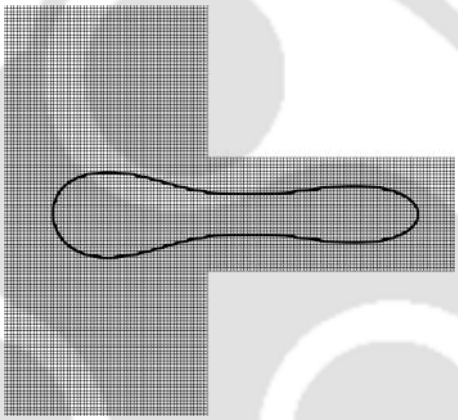

Figure 2.6: Grid arrangement showing drop interface entering into the constriction

$$\nabla \cdot \mathbf{u}_* = \frac{1}{\Delta} \sum_f \mathbf{u}_*^f \cdot \mathbf{n}^f \tag{2.21}$$

.

After solving Eq. 2.21, applying pressure correction is done on the face-centered auxiliary velocity field given by Eq. 2.22.

$$\mathbf{u}_{n+1}^f = \mathbf{u}_*^f - \frac{\Delta t}{\rho^f_{n+\frac{1}{2}}} \nabla^f \mathbf{p}_{n+\frac{1}{2}} \tag{2.22}$$

Similarly, the cell-centered velocity field at time n+1 is obtained by applying cell-centered pressure correction. The equations mentioned above required a proper estimation of face-centered values of density ($\rho^f_{n+\frac{1}{2}}$) or viscosity ($\mu^f_{n+\frac{1}{2}}$) and volume fraction ($c^f_{n+\frac{1}{2}}$) field. The advection of the volume fraction, a (Eq. 2.13), was solved using a piecewise linear geometrical volume of fluid scheme formalized for qaudtreee or octree spatial discretization. The scheme is solved classically in two steps. The steps are interface reconstruction, geometrical flux computation, and

interface advection. The interface is defined by a line in each cell given by Eq. 2.23.

$$\mathbf{m} \cdot \mathbf{x} = \alpha \tag{2.23}$$

α is determined so that the volume of fluid is contained in the cell and the fraction is equal to a. The normal to the interface $\mathbf{m}$ is evaluated by using a Mixed Young Centred (MYC) scheme [112]. In contrast, a direction-split scheme was employed to evaluate volume fraction advection [113].

2.2.3 Surface tension force calculation

The Continuum-Surface-Force/Peskin approach (Eq. 2.9) in the context of the VOF provides a discrete equilibrium between surface tension and pressure gradient. The force estimation requires approximation given by Eq. 2.24.

$$\sigma\kappa\delta_s\mathbf{n} \approx \sigma\kappa\nabla\tilde{\mathbf{a}} \tag{2.24}$$

$$\kappa \approx \nabla \cdot \tilde{\mathbf{n}}, \quad \text{where} \quad \tilde{\mathbf{n}} \equiv \frac{\nabla\tilde{\mathbf{a}}}{|\nabla\tilde{a}|} \tag{2.25}$$

$\tilde{c}$ is the spatially filtered volume fraction field. The discrete equilibrium between surface tension and pressure gradient using CSF approximation is given by Eq. 2.26.

$$-\nabla\mathbf{p}_{n+\frac{1}{2}} + \sigma\kappa(\nabla\mathbf{a})_{n+\frac{1}{2}} = 0 \tag{2.26}$$

The exact discrete equilibrium solution is then given by Eq. 2.27

$$p_{n+\frac{1}{2}} = \sigma\kappa a_{n+\frac{1}{2}} + \text{arbitrary constant} \tag{2.27}$$

In the present scheme, the surface tension forces are estimated on the faces of the discretized volume. Thus, the surface tension force is applied on the auxiliary face-centered velocity field (Eq. 2.28).

$$\mathbf{u}^f_* \leftarrow \mathbf{u}^f_* + \frac{\Delta t \sigma \kappa^f_{n+\frac{1}{2}}}{\rho\left(a^f_{n+\frac{1}{2}}\right)} \nabla^f \mathbf{a}_{n+\frac{1}{2}} \tag{2.28}$$

The cell-centered surface tension force is applied to the auxiliary cell-centered velocity field (Eq. 2.29). The steps are applied before the projection method steps.

$$\mathbf{u}_*^c \leftarrow \mathbf{u}_*^c + \left| \frac{\Delta t \sigma \kappa^f_{n+\frac{1}{2}} \nabla^f \mathbf{a}_{n+\frac{1}{2}}}{\rho\left(a^f_{n+\frac{1}{2}}\right)} \right|^c \tag{2.29}$$

The accuracy of CSF approximation largely depends upon the accuracy of curvature calculation. The curvature of the interface was calculated by estimating the derivative of generalized height functions in a given direction. The curvature was computed as,

$$\kappa = \frac{h_{xx}}{(1+h_x^2)^{\frac{3}{2}}} \tag{2.30}$$

2.2.4 Viscoelastic fluid formulation

The extra stress tensor (T) appearing in Eq. 2.8 is due to the elastic nature of the polymeric fluid. The present thesis adopted kinetic theory-based models to formulate extra stress tensors. The dynamics of the polymeric chains determine the elastic response of a viscoelastic fluid. The significant challenges lie in modeling the dynamics of these polymeric chains. So, modeling this elastic response will also play a substantial role in drop deformation and breakup behavior. The structural configuration of these viscoelastic fluids is determined by conformation tensor (C). Thus, the formulation of viscoelastic stresses regarding conformation tensor (C) will be discussed in this section. The logarithm of the conformation tensor was employed to deal with the instability arising from the development of regions of high stress in a highly elastic flow. The primary variable to deal with was the stress tensor, evaluated by a split scheme proposed by Hao and Pan [114]. The scheme successively solved the upper convective term, the advection term, and the model term (specific to the viscoelastic model selected). Eqs. 2.31, 2.32, and 2.33 gives the constitutive relation for extra stress tensor for FENE-P fluid is given by.

$$\frac{\partial \mathrm{C}}{\partial t} + \nabla \cdot \left(\mathbf{u}\mathrm{C}\right) - \left(\nabla \mathrm{u}\right)^T \cdot \mathrm{C} - \mathrm{C} \cdot \nabla \mathbf{u} = -\frac{1}{\lambda}\left(F_{\mathrm{C}}\mathrm{C} - \mathrm{I}\right) \tag{2.31}$$

$$F_{\mathrm{C}} = \frac{1}{1 - \frac{\mathrm{trace(C)}}{L^2}} \tag{2.32}$$

$$\mathrm{T} = \frac{\mu_p}{\lambda}\left(F_{\mathrm{C}}\mathrm{C} - \mathrm{I}\right) \tag{2.33}$$

The conformation tensor is calculated by the ensemble average of the dyadic product of end-to-end vector $\mathbf{R}$. F_{C} is the stretch function, and L is defined as the ratio of the length of a polymer dumbbell under full extension to its equilibrium length. The trace of the conformation tensor given by Eq. 2.35 is determined as

the mean square of the dumbbell length.

$$\mathrm{C} = \left\langle \mathbf{RR} \right\rangle \tag{2.34}$$

$$\mathrm{trace(C)} = \mathrm{R}^2 \tag{2.35}$$

2.2.5 Validation of numerical formulation

The simulations were performed on an open-source solver, Basilisk. The simulations in the present thesis were performed at grid levels 11, 10, and 9, and the results were compared to ascertain the grid resolution for the present study. The deformation results at levels 11 and 10 matched closely, while minimal deviation was observed at level 9 (Fig. 2.7). The grid independence tests were performed for simulation results (Fig. 2.7a and Fig. 2.7b). After the grid comparison results and to ensure sharp interface capturing, the simulations were performed on level 10. The present grid resolution also enabled a smooth drop entry into the constriction region of the microchannel. The grid arrangement with the drop interface entering the constriction is shown in Fig. 2.6. The default domain in the solver is a square; the required geometry is achieved by masking the non-domain part.

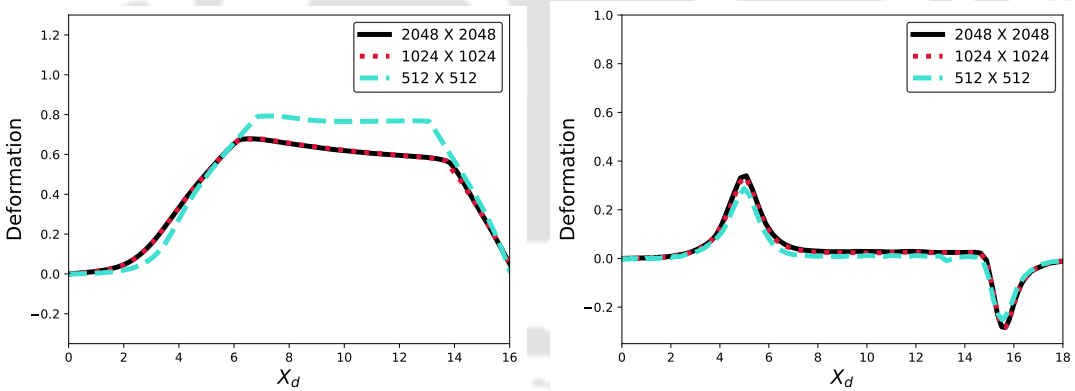

(a) (b)

Figure 2.7: (a) comparison of deformation results obtained from simulations with grid resolutions of 512 × 512, 1024 × 1024, 2048 × 2048 at $\beta = 0.6$, $Ca = 0.1$, $c = 0.5$, $CR = 6$, $Re = 2$, $De = 1$, $m = 1$, and $\theta = 1$, (b) comparison of deformation results obtained from simulations with grid resolutions of 512 × 512, 1024 × 1024, 2048 × 2048 at $\beta = 0.6$, $Ca = 0.3$, $c = 1$, $CR = 3$, $Re = 2$, $De = 1$, $m = 1$, $\theta = 1$

To validate the reliability of the present numerical method, our numerical results were compared with the deformation of a Newtonian drop in the Newtonian matrix ($CR = 5$) by Chung et al. [115] (Fig. 2.8a). Our results closely matched their results, while a minute deviation was observed in predicting the maximum deformation under the constricted portion of the microchannel. The close comparison between

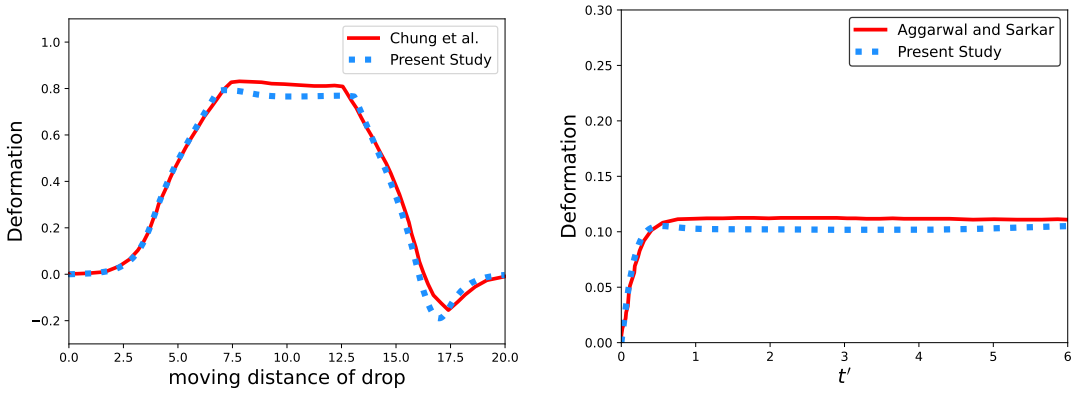

(a) (b)

Figure 2.8: Validation of present study with previous studies (a) comparison of present numerical study with a study on deformation of Newtonian drop in the Newtonian matrix under 5:1:5 contraction/expansion channel by Chung et al. [115] at $Ca = 1$, $\theta = 1$ and $d = 70$, (b) comparison of present numerical study with study on deformation of Oldroyd-B drop under steady shear by Aggarwal and Sarkar [116] at $Re = 0.1$, $Ca = 0.1$, $De = 2.0$

the results validates the reliability of the current simulation results. Furthermore, the present numerical model closely matched the results of Aggarwal and Sarkar [116] for Oldroyd-B drop deforming under simple shear with minute deviation (Fig. 2.8b). Codes were incorporated for constitutive equations of Oldroyd-B in our present numerical framework for carrying out the validation study.

3

Understanding deformation and breakup tendency of shear-thinning viscoelastic drop in constricted microchannels

The study of drop deformation in response to various stresses has long piqued the interest of several academics. The deformation behavior of cells, drug carriers, and even drug particles moving via microcapillaries inside the human body can be modeled using a viscoelastic drop model. A drop breakup study can also provide better design guidance for nanocarriers that deliver on-demand burst drug releases at specific cancer sites. Thus, an attempt was made to investigate the deformation and breakup of a shear-thinning Finitely Extensible Nonlinear Elastic—Peterlin (FENE-P) drop moving through the constricted microchannel. The computational simulation suggested that drop deformation and breakup can be manipulated with variable parameters like channel confinement, Deborah number, solvent viscosity ratio, viscosity ratio, and capillary number. In another study, an attempt was made to find the critical capillary number to initiate drop breakup. Observations from the present study will give valuable insights into the deformation and breakup patterns of drug carriers inside constricted microcapillaries. The two-phase viscoelastic drop-Newtonian matrix system simulations were performed on an open-source solver, Basilisk.

3.1 Introduction

Flow-through constricted microchannels are essential in engineering applications like inkjet printing, droplet microfluidics, and biomedical engineering [117]. Flow dynamics of cancer cells, biological molecules, and drug carriers through blood vessels can be significantly explained by studying droplet flow through micro

confinement [118]. The particles mentioned above possess viscous and elastic behavior and are examined under special polymeric fluids. These fluids exhibit complex mechanical behavior consisting of a long chain of polymer molecules with distinct orientations. These attributes allow polymeric fluids to find essential applications in paints, stabilizers for emulsion, biochemical molecules, polymers, and plastic industries. Researchers used the viscoelastic behavior of polymeric fluids to model human cells [119], drug carriers, and anti-cancer drugs flowing through constricted microchannels. Furthermore, the viscoelastic drop model also provided fruitful insights into understanding the complex phenomenon of cell trapping in the Y junction microchannel [92].

Thus, an attempt was made to study the computational research dedicated to understanding the parameters that govern the deformation and breakup behavior of viscoelastic drops in different geometries. Modeling and simulating viscoelastic drop flow through constricted passage exhibits complex mechanical behavior [120]. Initial studies by Yue et al. [121] and Aggarwal and Sarkar [116] suggested the deformation of polymeric drops initially decreases and then increases with viscoelasticity. Ramaswamy and Leal [122] reported that viscoelastic drop in the Newtonian matrix shows minor deformation while deformation is enhanced in the opposite case. Furthermore, studies have also been conducted on the deformation of viscoelastic drop flowing through microchannels with sudden contraction/expansion [123]. The effect of parameters like a capillary number, viscosity ratio, and Deborah number on drop deformation was reported for viscoelastic-Newtonian, Newtonian-viscoelastic, and viscoelastic-viscoelastic drop-matrix systems by Chung et al. [115, 124]. They further observed the deformation and breakup dynamics of drop passing through obstruction in confined flow [125]. Izbassarov and Muradoglu [104] studied the effect of solvent viscosity ratio on deformation of FENE-CR drop in sudden contraction/expansion channel. They suggested that the solvent viscosity ratio's effect on the viscoelastic drop's deformation is negligible at the unity Weissenberg number. Furthermore, the deformation tendency of FENE-CR drop flowing through channels with complex geometries was also reported by Zolfaghari et al. [126]. They suggested that viscoelasticity decreases droplet mobility by inhibiting deformation. Zhou et al. [127] observed that viscoelasticity in drop and matrix could facilitate and oppose drop deformation depending on the drop-to-matrix viscosity ratio and capillary number.

Apart from microchannel flow, several studies reported the deformation and breakup of viscoelastic Oldroyd-B drop and FENE-P drop [128] under steady shear. Aggarwal and Sarkar [116] used a front-tracking finite difference method to study the deformation of Oldroyd-B drop in the Newtonian matrix under steady shear.

They also suggested an ordinary differential equation model deciphering the role of Deborah number, capillary number, and solvent viscosity ratio on drop deformation. The effect of the high capillary number on droplet breakup was also reported experimentally by Li and Sundararaj [129], where drop deforms under flow direction and vorticity direction. Further, they also studied the effect of matrix viscoelasticity on the deformation of Newtonian drop, where matrix viscoelasticity seemed to promote the drop breakup [130]. In the study's furtherance, the viscosity ratio's effect on the deformation of viscoelastic drop under steady shear was also reported by Mukherjee and Sarkar [131]. Besides, along with these parameters, drop size was registered to affect the drop breakup undergoing deformation under simple shear [132].

Based on a thorough literature review, the objectives of the current chapter were structured to address these interlinked problems. As reported in a previous study [104], the effect of solvent viscosity ratio was observed to be negligible on drop deformation at the Weissenberg number ($Wi = 1$) when it flows under confinement. To get better insights into this, the effect of solvent viscosity ratio on drop deformation flowing inside confinement at unity Deborah number was studied. Poole [133] suggested that the Weissenberg number is equivalent to the Deborah number when one length and time scale determines the flow dynamics. A single-length scale determines the flow dynamics in the present problem. Thus, simulation at the unity Deborah number can be equivalent to the unity Weissenberg number. Immense research is going on to achieve active burst drug release by nanocarriers at targeted cancer sites. The burst release can be achieved by dissociating the nanocarrier assembly at the tumor site [134]. Thus, an attempt was made to report the FENE-P drop breakup inside the constricted microchannel to model such nanocarriers.

3.2 Computational domain

The computational domain for the present study is represented by constricted microchannels with confinement ratios ($CR = \frac{D_1}{D_2}$) of 6 and 3, as shown in Fig. 3.1. The subscripts 1 and 2 denote the drop and matrix phase, respectively. The drop was given an initial position at a distance of $5D_2$ from the left wall of the microchannel, as shown in Fig. 3.1. Incompressible mass and momentum conservation equations can be written for the present two-dimensional, two-phase, drop-matrix system. The drop phase is modeled as FENE-P viscoelastic fluid, while the matrix is treated as Newtonian fluid. The FENE-P drop, shear-thinning, can be modeled to design nano-carriers to achieve active burst drug release at the

targeted tumor site. As the flow of these nano-carriers inside blood capillaries is not necessarily axisymmetric, 2D simulations were performed for the present study. The simulation results will serve as a pathway to achieve the broader objective of precisely designing drug delivery systems for attaining burst drug release by nano-carriers inside a constricted mechanical environment. The vectors are represented in bold text, while tensors are represented in standard text in the equations, and the role of gravity is neglected.

$$m = \frac{\rho_1}{\rho_2}, \quad \theta = \frac{\mu_1}{\mu_2}, \quad c = \frac{d}{D_2}, \quad CR = \frac{D_1}{D_2} \tag{3.1}$$

Where 1 and 2 are the indices to signify properties of fluid 1 and 2, d is the drop diameter. The deformation is calculated by,

$$\text{Deformation} = \frac{d_a - d_b}{d_a + d_b} \tag{3.2}$$

where d_a and d_b are the drop dimensions along its major and minor axis. The deformation parameter is plotted against a parameter X_d, defined as an axial distance of the drop centroid from the initial position. Values of parameters selected for studying deformation in the present study were, $Re = 2$, $Ca = 0.1$, $De = 1$, $m = 1$, $\theta = 1$, $L = 5$.

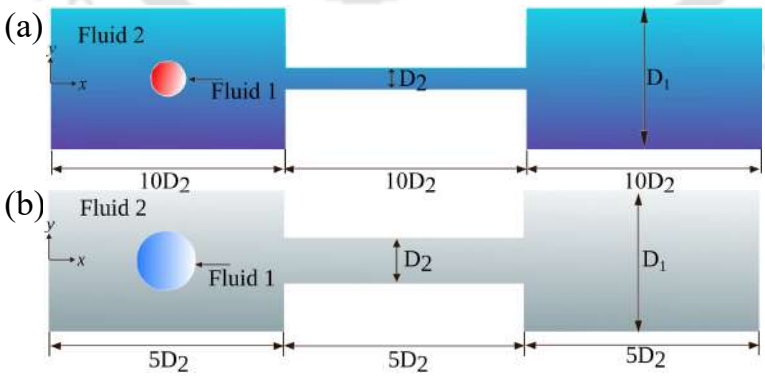

Figure 3.1: Computational Domain showing the initial position of viscoelastic drop in the channel of (a) $CR = 6$, (b) $CR = 3$

3.3 Results and discussion

3.3.1 Boundary conditions

A uniform axial inlet velocity condition is applied at the inlet wall. The value of uniform velocity is taken as $V = 1$.

$$u_x = V,\ u_y = 0, \tag{3.3}$$

The walls at the top and bottom boundaries are no-slip and no-penetration walls

$$u_x = 0,\ u_y = 0, \tag{3.4}$$

while a constant pressure outlet boundary condition at the right boundary is applied

$$p = 0 \tag{3.5}$$

Neumann boundary conditions for viscoelastic stresses for all boundaries at t= 0 were applied

$$\partial_x \mathrm{T}_{xx} = 0,\ \partial_y \mathrm{T}_{yy} = 0 \tag{3.6}$$

As mentioned in the previous section, the volume of fluid (VOF) approach was adopted to simulate two-phase flow with the equations involving advection of a (Eq. 2.13). A piecewise linear geometrical volume of the fluid scheme was adopted for interfacial reconstruction and geometrical flux computation, and interface advection. The interface is defined by a line in each cell given by Eq. 2.23. where $\mathbf{x}$ is the position vector, $\mathbf{m}$ is normal to the interface α is the intercept that ensures the volume of fluid contained in the cell is equal to the volume fraction a. The normal to the interface, $\mathbf{m}$, is evaluated by using Mixed Young Centred (MYC) scheme [112], while a direction-split scheme was employed to assess volume fraction advection. Equation 2.9, represents the Continuum-Surface-Force/Peskin approach in the context of VOF that provides discrete equilibrium between surface tension and pressure gradient. The curvature of the interface is calculated by estimating the derivatives of a generalized height function (h) in a given direction. The curvature is computed according to the relation given in Eq. 2.30

In the previous chapter (Chapter 2), the constitutive relation for the extra stress tensor of the viscoelastic fluid (Eq. 2.32, 2.34, 2.35) was discussed. The logarithm of the conformation tensor is employed to deal with the instability arising due to the development of regions of high stress in a highly elastic flow. The primary variable is the stress tensor, evaluated by the split scheme proposed by Hao and

Pan [114]. The scheme successfully solves the upper convective, advection, and model term (specific to the viscoelastic model selected).

As mentioned earlier, an attempt was made to decipher the deformation and breakup tendency of FENE-P drop when it migrates through a constricted microchannel of different confinements. As previously stated, viscoelastic drop deformation at unity Weissenberg number varies negligibly with solvent viscosity ratio [135]. An attempt to study the deformation at Deborah number equal to 1, equivalent to the unity Weissenberg number, was made in the present study. For a more detailed investigation, an investigation was done on the drop deformation of different diameters under microchannel with varying confinement ratios (CR). A study was also done to comprehend how a change in capillary number and viscosity ratio affects drop deformation. For the drop breakup study, a study was done to find the variation of critical capillary number with significant parameters like De, θ, and CR that can be required to achieve an on-demand drop breakup. All the results obtained in this Chapter were obtained by computational study.

3.3.2 Effect of channel confinement and solvent viscosity ratio

An extensive study was done to find the drop deformation variations with solvent viscosity ratios at $De = 1$. The study was done when drop migrates through the channels with different confinement ratios. The deformation of drops with different diameters was observed to get deeper insights. The deformation variations were plotted at four β values ($\beta = 0.11, 0.5, 0.6, 0.9$) flowing through microchannel as shown in (Fig. 3.2) and (Fig. 3.3) respectively. The β values were selected to see the deformation of drops with higher to lower contribution of polymeric viscosity inside drops. The deformation parameter shown in the plots is defined in Eq. 3.2, where d_a and d_b are the drop dimensions along its major and minor axis. At first, an attempt was made to observe the deformation inside a microchannel with $CR = 3$, as shown in Fig. 3.2. As the drop enters the constricted region of the microchannel, the d_a increases and causes a sudden increase in the deformation parameter. The sudden peaks in the deformation parameter in the flow direction represent the overshoot. The sudden overshoot of the deformation parameter at the constricted channel entry was least for the drop with a higher diameter ($c = 1.5$) (Fig. 3.2d), while it was highest for a drop with a lesser diameter ($c = 0.5$) (Fig. 3.2a). In the constriction region, a drop with a smaller diameter ($c = 0.5$) attains its initial shape when the wall effect ceases while migrating through the constricted region. The drops with higher diameters ($c = 1$,1.25, 1.5) exhibited

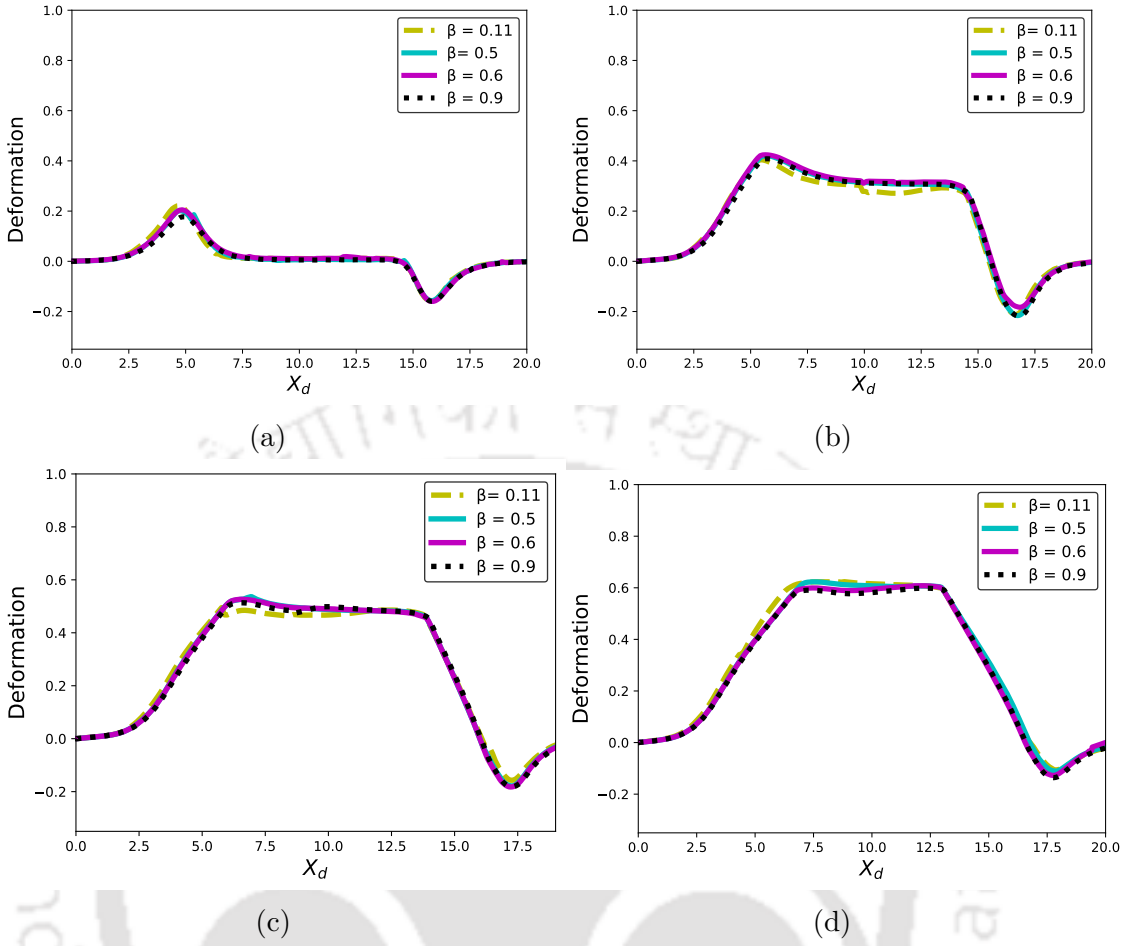

Figure 3.2: Plot showing the deformation of drops of different diameters (a) c = 0.5, (b) c = 1, (c) c = 1.25, (d) c = 1.5 for different β values (β = 0.11, 0.5, 0.6, 0.9) flowing through constricted microchannel of CR = 3 at Re = 2, Ca = 0.1, De = 1, m = 1, θ = 1

higher deformation parameters in the constriction region. Furthermore, at the exit, a sudden decrease in the deformation was observed as the drop underwent deformation in the cross-flow direction. The overshoot at the exit of the constriction region was observed in all cases. The larger drops also seemed to regain their original shape slowly compared to the smaller drops when the stresses were removed. The deformation of the drop was observed to vary insignificantly with the change in β values for the present cases (Fig. 3.2).

Interestingly, the deformation results differed when the confinement ratio was increased to 6 (Fig. 3.3). A higher overshoot of deformation parameters at the entry and exit of the microchannel was deciphered in the present case. Although, the deformation of the smaller drop (c= 0.5) (Fig. 3.3a) did not vary with the solvent viscosity ratio (β). However, the deformation for drops with similar or higher diameter than the constriction width (c = 1, 1.25, 1.5) was reported to increase with the increase of solvent viscosity ratios (Fig. 3.3b, Fig. 3.3c, Fig.

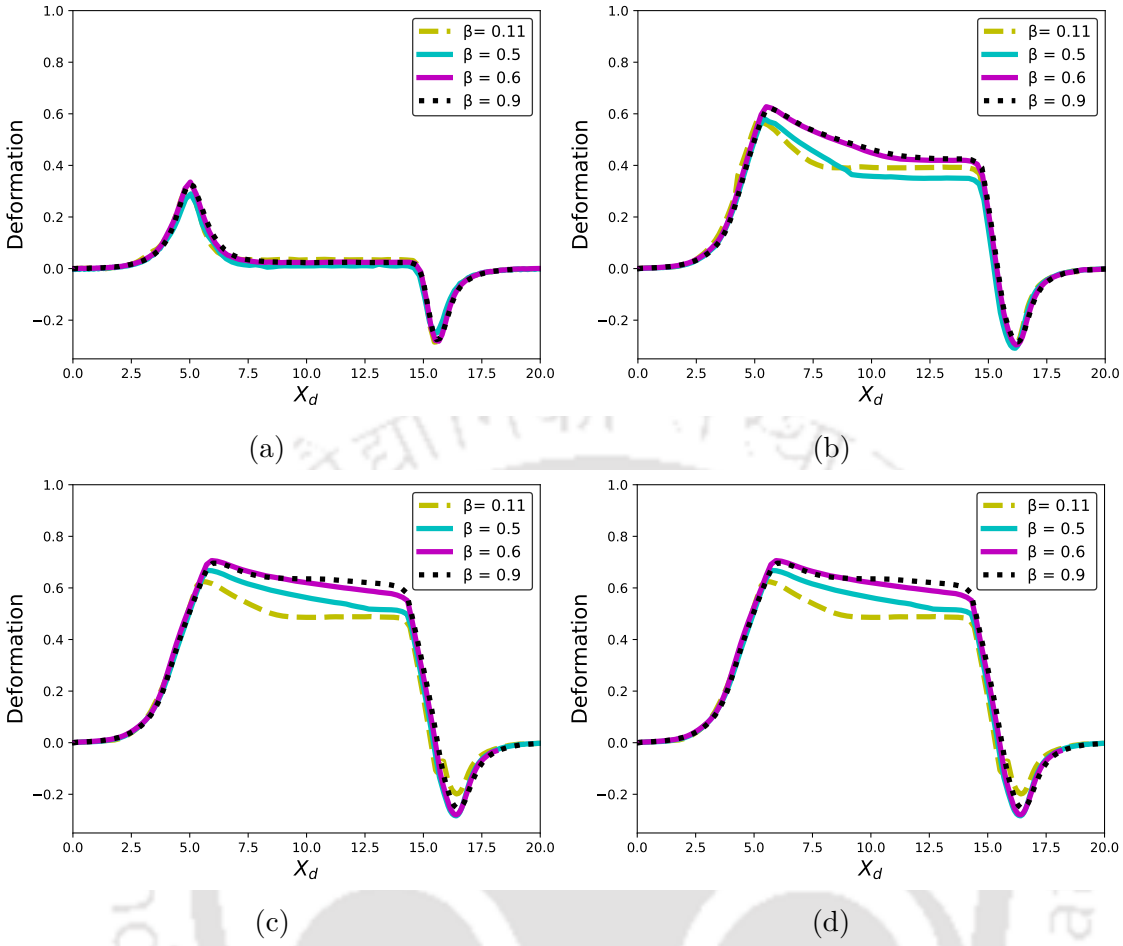

Figure 3.3: Plot showing the deformation of drops of different diameters (a) $c = 0.5$ (b) $c = 1$, (c) $c = 1.25$, (d) $c = 1.5$ for different β values ($\beta = 0.11$, 0.5, 0.6, 0.9) flowing through constricted microchannel of $CR = 6$ at $Re = 2$, $Ca = 0.1$, $De = 1$, $m = 1$, $\theta = 1$

3.3d). The value of the deformation parameter was observed to be most for $\beta = 0.6$ and 0.9 with negligible variation between the two values, while it was least for $\beta = 0.11$. The increase in the deformation parameter with β was significant for β values up to $\beta = 0.6$. The deformation parameter varied insignificantly for $\beta \geq 0.6$. Furthermore, the deformation in the non-constriction region did not seem to vary with β. The observation showed that the deformation of larger drops under extremely tight confinement could be controlled by altering the fluid's polymer viscosity even at a unity Deborah number.

In the furtherance of the study, viscoelastic normal stress difference distribution inside the drop, as it migrates through different sections of the microchannel, was reported. As reported earlier, the drop deformation was observed to vary with β under the microchannel with a higher confinement ratio. The viscoelastic normal stress difference distribution and shape evolution of viscoelastic drop was reported at different timestamps inside the microchannel of $CR = 6$. Viscoelastic normal

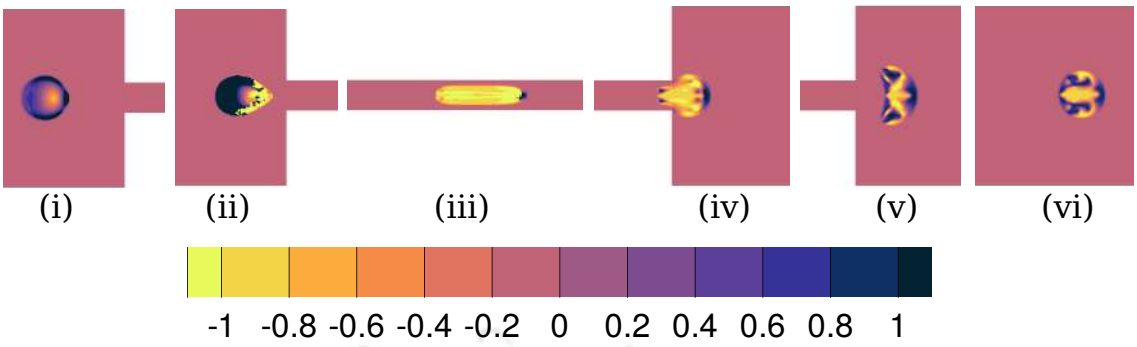

Figure 3.4: Contours of viscoelastic normal stress difference, T_{xx} - T_{yy} inside drop migrating through microchannel of $CR = 6$ at timestamps (i) $t^* = 0.05$, (ii) $t^* = 0.07$, (iii) $t^* = 0.1$, (iv) $t^* = 0.12$, (v) $t^* = 0.13$, (vi) $t^* = 0.17$ at $c = 1.5$, $\beta = 0.11$, $Re = 2$, $Ca = 0.1$, $De = 1$, $m = 1$, $\theta = 1$

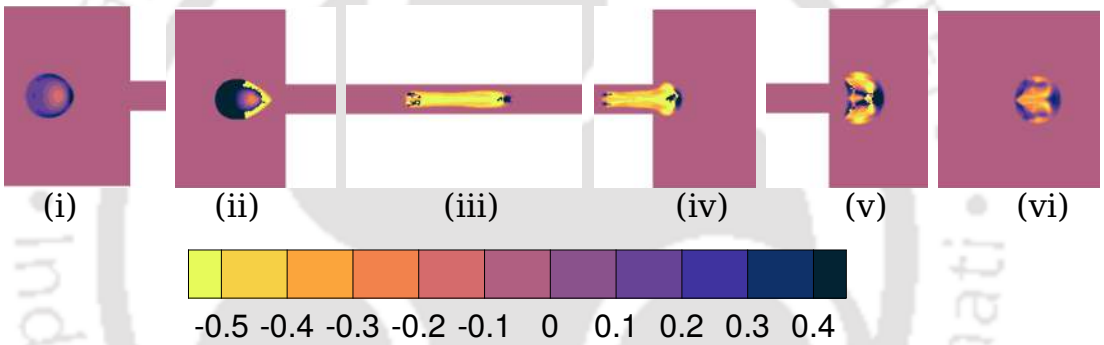

Figure 3.5: Contours of viscoelastic normal stress difference, T_{xx} - T_{yy} inside drop migrating through microchannel of $CR = 6$ at timestamps (i) $t^* = 0.05$, (ii) $t^* = 0.07$, (iii) $t^* = 0.1$, (iv) $t^* = 0.12$, (v) $t^* = 0.13$, (vi) $t^* = 0.17$ at $c = 1.5$, $\beta = 0.6$, $Re = 2$, $Ca = 0.1$, $De = 1$, $m = 1$, $\theta = 1$

stress difference distribution was discerned at $\beta = 0.11$ and 0.6 to ascertain the development of viscoelastic normal stress difference inside the drop with different polymeric viscosity contributions. Initially, the viscoelastic normal stress difference was observed to be prominent and develop around the drop interfaces when the drop started moving towards the constricted portion of the channel at $t^* = 0.05$ (Fig. 3.4(i) and Fig. 3.5(i)). The normal stress difference distribution was more prominent for $\beta = 0.11$ case than $\beta = 0.6$ case. As the drop moved further, the higher viscoelastic normal stress difference was distributed around the drop's tail portion. In contrast, negative distribution around the drop interface was observed at the fore tip of the drop at $t^* = 0.07$ (Fig. 3.4(ii) and Fig.3.5(ii)). The distribution was observed to be more uniform for $\beta = 0.6$ cases (Fig. 3.5(ii)) Negative value of normal stress difference signifies additional tension along the flow direction. Thus, as the drop begins to move through the constricted channel, the foretip of

the drop experiences a higher strain rate that causes the development of negative viscoelastic stresses, which in turn causes the foretip of the drop to stretch. As the drop moves further, the presence of negative normal stress difference was observed to be prominent inside the significant portion of the drop at $t^* = 0.1$ (Fig. 3.4(iii) and Fig. 3.5(iii)). Although, a higher positive viscoelastic normal stress difference was observed at the fore tip of the drop for $\beta = 0.11$ (Fig. 3.4(iii)) case that caused the drop to get pull inward and resist further interface stretching. The positive normal stress difference was observed at both the fore and tail end of the drop for $\beta = 0.6$ case (Fig. 3.5(iii)), indicating stress development due to larger interface stretching. At the exit of the constriction region, viscoelastic stress distribution at the fore tip of the drop becomes more prominent (Fig. 3.4(iv) and Fig. 3.5(iv)). A higher viscoelastic normal stress difference at the fore tip of the drop for $\beta = 0.11$ (Fig. 3.4(iv)) case causes the front portion to bulge more with lesser interfacial stretching than $\beta = 0.6$ cases (Fig. 3.5(iv)). Interesting observations were made when the drop completely migrated out through the constriction. As the strain rate inside the drop decreases, the major portion of the drop interface occupies a higher positive normal stress difference for $\beta = 0.11$ case (Fig. 3.4(v)). The observation signified a faster stress relaxation response of the drop with lesser β values. As the drop moves further, it tries to regain its initial shape. Even after complete structural healing of the drop, the viscoelastic normal stress difference distribution inside it completely differed from its initial stress distribution (Fig. 3.4(vi) and Fig. 3.5(vi)). The observation successfully represented the stress hysteresis phenomenon inside a viscoelastic drop.

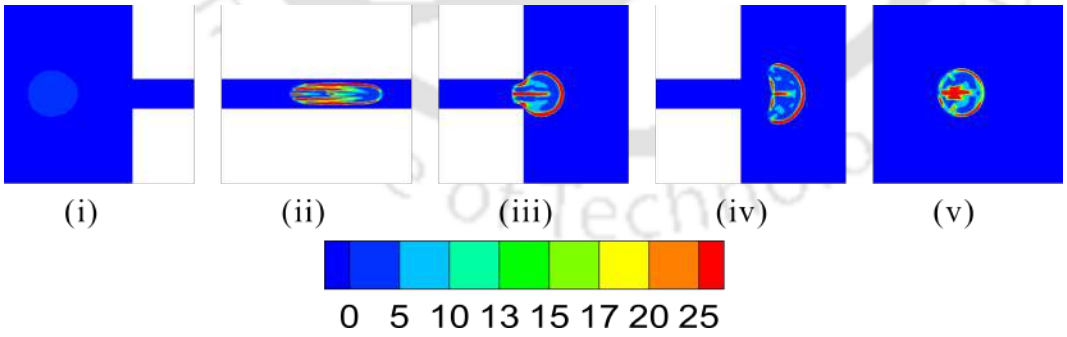

Figure 3.6: Contours of mean square of polymer extension (trace(C)) inside drop migrating through microchannel of $CR = 6$ at timestamps (i) $t^* = 0.05$,(ii) $t^* = 0.1$, (iii) $t^* = 0.12$, (iv) $t^* = 0.13$, (v) $t^* = 0.17$ at $c = 1.5$, $\beta = 0.11$, $Re = 2$, $Ca = 0.1$, $De = 1$, $m = 1$, $\theta = 1$

In viscoelastic drop internal orientation of polymeric molecules directs the elastic behavior of the drop. The extension of the dumbbell beads when a viscoelastic drop is subjected to a higher strain rate results in a localized increase in elastic stresses. This localized increase in elastic stresses and stress hysteresis is a significant reason

behind the resulting asymmetric stress distribution inside the viscoelastic drop shown in Fig. 3.4 and Fig. 3.5. Again these polymer dumbbell extensions will be more prominent for concentrated polymer solutions. Polymeric fluid with lesser β values corresponds to the concentrated polymeric solution, representing the more contribution of polymeric viscosity. Thus, the contours of the square of average polymer extension (trace(C)) for viscoelastic drop at $\beta = 0.11$ and $\beta = 0.6$ (Fig. 3.6 and Fig. 3.7) were plotted. The average polymer extension was observed to be more at the drop interface inside the constricted region of the microchannel at t^*= 0.1 (Fig. 3.6(ii) and Fig. 3.7(ii)). The average polymer extension was observed to be higher at the drop interface for β=0.11 case at all timestamps (Fig. 3.6). Interestingly, an increase in polymer extension was observed at the tail end of the drop when the drop exited through the constricted channel at t^*= 0.12 for both β=0.11 and β=0.6 cases (Fig. 3.6(iii) and Fig. 3.7(iii)). Furthermore, the average polymer extension was observed to slightly cease from the interface as the drop moves further in the exit region of constricted microchannel at t^*= 0.13 and 0.17 (Fig. 3.6(iv) and Fig. 3.6(v)). The average polymer extension on drop interface was lesser for $\beta = 0.6$ case (Fig. 3.7). A higher polymer extension at the interface was observed at the fore tip of the drop inside the constriction region at $t^* = 0.1$ for $\beta = 0.6$ case (Fig. 3.7(ii)). At the exit of the constriction region drop exhibited lesser polymer extension at the interface at time $t^* = 0.13$ and t^* = 0.17 (Fig. 3.7(iv) and Fig. 3.7(v)). Thus, viscoelastic drop with lesser β value undergoes higher polymer extension that causes an increase in elastic stresses to resist deformation at a higher strain rate inside a confined microchannel. Again, it was also discerned that viscoelastic drops with lesser β values exhibit faster stress relaxation.

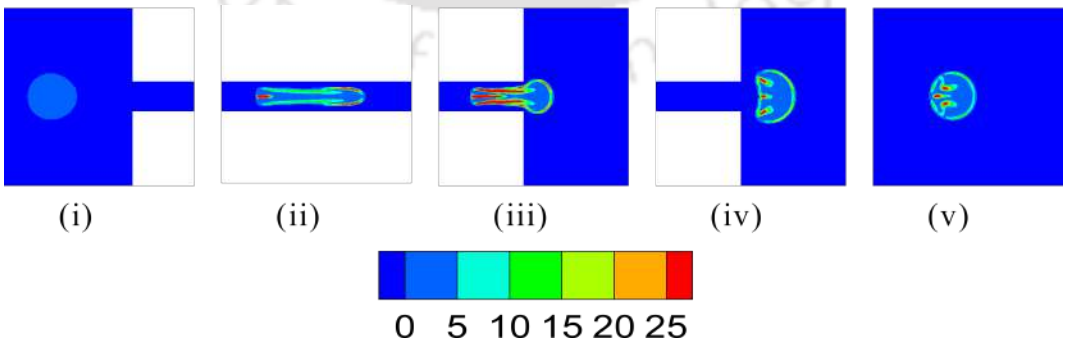

Figure 3.7: Contours of mean square of polymer extension (trace(C)) inside drop migrating through microchannel of $CR = 6$ at timestamps (i) $t^* = 0.05$,(ii) $t^* = 0.1$, (iii) $t^* = 0.12$, (iv) $t^* = 0.13$, (v) $t^* = 0.17$ at $c = 1.5$, $\beta = 0.6$, $Re = 2$, $Ca = 0.1$, $De = 1$, $m = 1$, $\theta = 1$

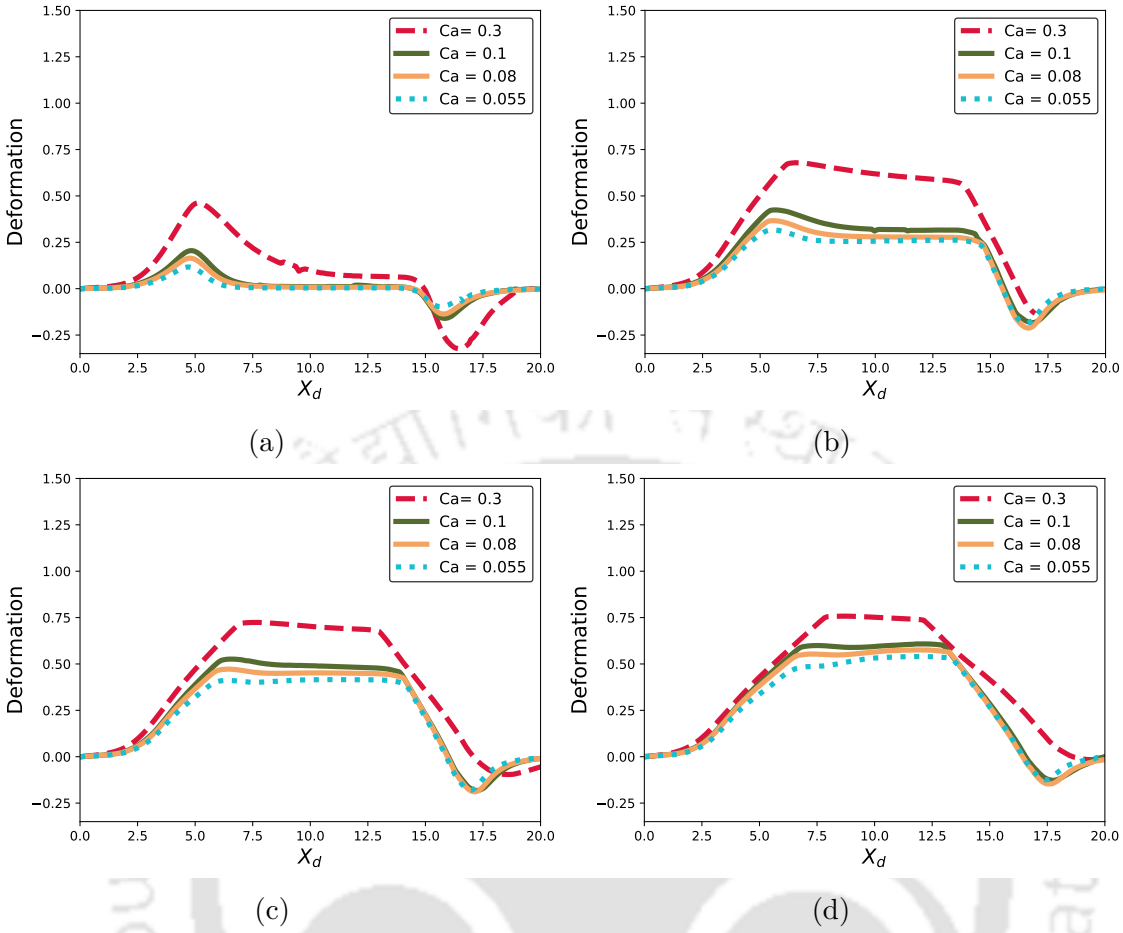

Figure 3.8: Plots showing the deformation of drops of different diameters (a) $c = 0.5$ (b) $c = 1$, (c) $c = 1.25$, (d) $c = 1.5$ for different capillary numbers ($Ca = 0.3$, 0.1, 0.08, 0.055) flowing through microchannel of $CR = 3$ at $Re = 2$, $De = 1$, $m = 1$, $\theta = 1$

3.3.3 Effect of capillary number

In the furtherance of the study, the effect of capillary number ($Ca = 0.055$, 0.08, 0.1, 0.3) on the deformation of a drop of different diameters $CR = 3$ (Fig. 3.8) and 6 (Fig. 3.9) was studied. The effect of Ca on drop deformation followed a similar pattern when drop migrates through both confinements ($CR = 3$ and 6). However, the values of the deformation parameter were observed to be more in $CR = 6$ (Fig. 3.9) than $CR = 3$ (Fig. 3.8). The deformation seemed to vary significantly with Ca, where deformation seemed to increase with the increase in Ca. A higher overshoot of the deformation parameter at both entry and exit was observed for a drop with a smaller diameter ($c = 0.5$) (Fig. 3.8a and Fig. 3.9a) at $Ca = 0.3$. The deformation seemed to vary slightly with other capillary number values ($Ca = 0.1$, 0.08, and 0.055) for smaller droplets ($c = 0.5$). As seen in Fig. 3.8b and Fig. 3.9b, the deformation increased with Ca for drops with a diameter equal to the constriction width ($c = 1$). The observation trend remained similar with the drop

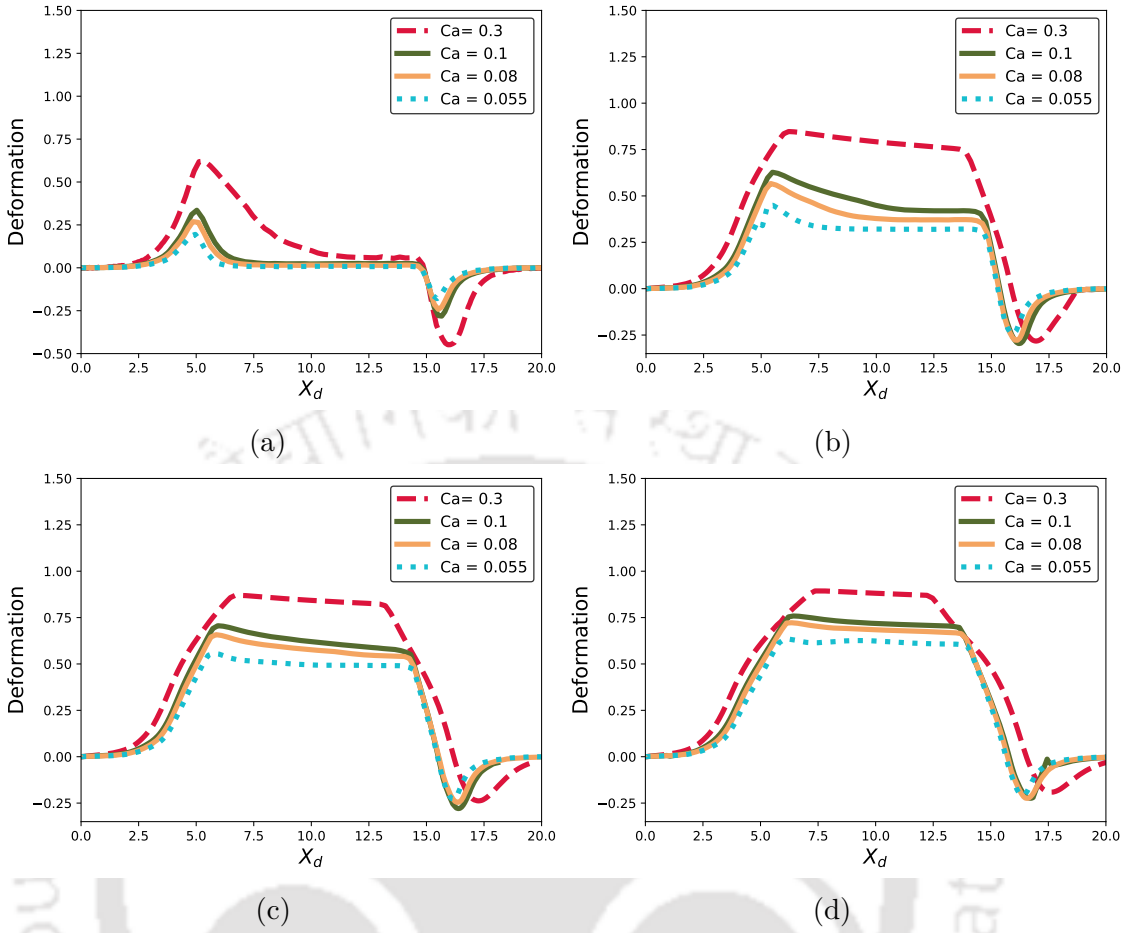

Figure 3.9: Plots showing the deformation of drops of different diameters (a) $c = 0.5$ (b) $c = 1$, (c) $c = 1.25$, (d) $c = 1.5$ for different capillary numbers ($Ca = 0.3$, 0.1, 0.08, 0.055) flowing through microchannel of $CR = 6$ at $Re = 2$, $De = 1$, $m = 1$, $\theta = 1$

of higher diameters ($c = 1.25$ and 1.5) for both confinement ratio cases (Fig. 3.8c, Fig. 3.8d, Fig. 3.9c, and Fig. 3.9d), where a significant deformation was noticed at $Ca = 0.3$.

As mentioned earlier, the drop underwent higher deformation at a higher Capillary number. The deformation was further amplified for a larger drop ($c = 1.5$) inside the constricted section of the channel. Thus, studies were carried out to investigate the effect of capillary number on the viscoelastic normal stress difference distribution and shape evolution of viscoelastic drop of larger diameter at different timestamps inside the microchannel of $CR = 6$. Viscoelastic stress distribution was discerned at $Ca = 0.055$ and 0.3 to determine how viscoelastic normal stress difference grows inside drop when surface tension forces are altered. Initially, the positive viscoelastic normal stress difference was observed to develop around the drop interfaces when the drop starts moving at $t^* = 0.05$ (Fig. 3.10(i) and Fig. 3.11(i)). With further drop movement, the higher positive viscoelastic normal stress

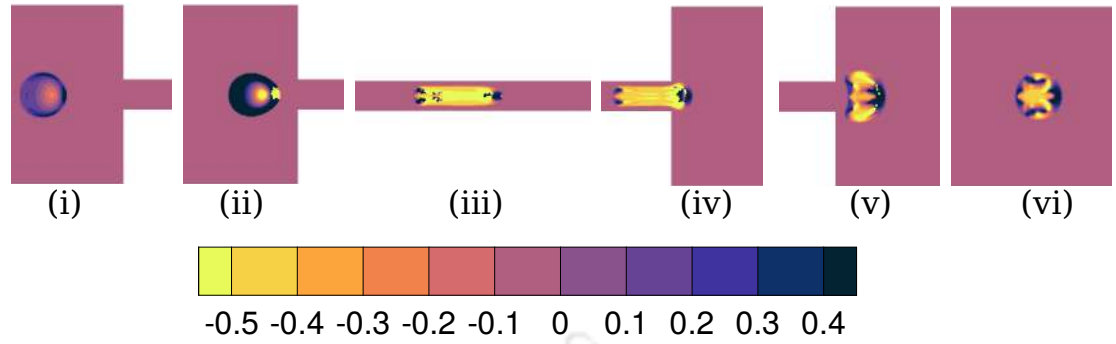

Figure 3.10: Contours of viscoelastic normal stress difference, T_{xx} - T_{yy} inside drop migrating through microchannel of $CR = 6$ at timestamps (i) $t^* = 0.05$, (ii) $t^* = 0.07$, (iii) $t^* = 0.1$, (iv) $t^* = 0.12$, (v) $t^* = 0.13$, (vi) $t^* = 0.17$ at $c = 1.5$, $\beta = 0.6$, $Re = 2$, $Ca = 0.055$, $De = 1$, $m = 1$, $\theta = 1$

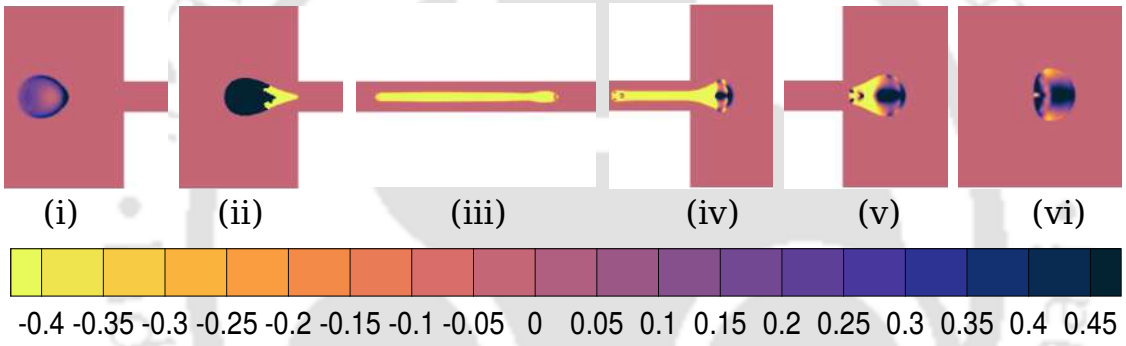

Figure 3.11: Contours of viscoelastic normal stress difference, T_{xx} - T_{yy} inside drop migrating through microchannel of $CR = 6$ at timestamps (i) $t^* = 0.05$, (ii) $t^* = 0.07$, (iii) $t^* = 0.1$, (iv) $t^* = 0.12$, (v) $t^* = 0.13$, (vi) $t^* = 0.17$ at $c = 1.5$, $\beta = 0.6$, $Re = 2$, $Ca = 0.3$, $De = 1$, $m = 1$, $\theta = 1$

difference was distributed around the drop's tail portion. In contrast, negative distribution around the drop interface was observed at the fore tip of the drop t^* = 0.07 (Fig. 3.10(ii) and Fig. 3.11(ii)). Interestingly, the distribution of positive viscoelastic stress difference at the drop's tail end was confined at the drop interface at Ca = 0.055 cases (Fig. 3.10(ii)) while it was distributed throughout the drop's tail at Ca = 0.3 cases (Fig. 3.11(ii)). The negative value of normal stress difference at the drop fore tip was prominent for $Ca = 0.3$ case, causing the drop front portion to stretch. With further movement of drop inside constricted microchannel, viscoelastic stresses get convected, causing prominence of negative normal stress difference distribution inside the significant portion of the drop at $t^* = 0.1$ ((Fig. 3.10(iii) and Fig. 3.11(iii)). However, a higher positive viscoelastic normal stress difference was observed at the fore tip and tail end of the drop for $Ca = 0.055$ (Fig. 3.10(iii)) case that caused the drop to resist deformation. In contrast, the absence of positive normal stress difference distribution for $Ca = 0.3$ caused the drop to get

stretched significantly (Fig. 3.11(iii)). The increase in drop deformation at a higher capillary number reduces the strain rate inside the drop. Thus, the viscoelastic stresses inside the drop grow slowly at higher Ca. Therefore, the drop underwent higher deformation at a higher capillary number due to reduced surface tension forces. At the exit of the constriction region, the appearance of positive viscoelastic normal stress distribution at the fore tip of the drop was observed at $t^* = 0.12$ (Fig. 3.10(iv) and Fig. 3.11(iv)). A higher viscoelastic normal stress difference at the fore tip and tail end of the drop for $Ca = 0.055$ (Fig. 3.10(iv)) case causes the front portion to bulge with lesser stretching of drop tail. The extension of the drop tail was observed to be most prominent for $Ca = 0.3$ case due to less noticeable positive viscoelastic stress distribution at the drop tail portion (Fig. 3.11(iv)). A significant difference in drop shape for the two cases was observed when the drop exited completely from the constricted portion of the microchannel at $t^* = 0.13$ (Fig. 3.10(v) and Fig. 3.11(v)) The terminal ends of the drop interface occupies a higher positive normal stress difference for $Ca = 0.055$ cases (Fig. 3.10(v)) causing the drop to stretch in crossflow direction. At the same time, positive normal stress was observed to be distributed primarily on the front portion of the drop for $Ca = 0.3$ cases, causing the drop to bulge in the direction of flow (Fig. 3.10(v)). The observation suggested that viscoelastic stresses get convected faster in the flow direction during stress relaxation inside drop at a higher capillary number. It was also observed that drops were able to attain initial shape at $t^* = 0.17$ for $Ca = 0.055$ cases (Fig. 3.10(vi)) while drop remained deformed at $t^* = 0.17$ for $Ca = 0.3$ cases (Fig. 3.11(vi)). The deformed shape of drop at $t^* = 0.17$ for $Ca = 0.3$ case was evident from the presence of higher positive normal stress difference inside drop (Fig. 3.11(vi)). The prominence of normal stress difference signifies the tendency of a drop to continue restricting deformation in the crossflow direction.

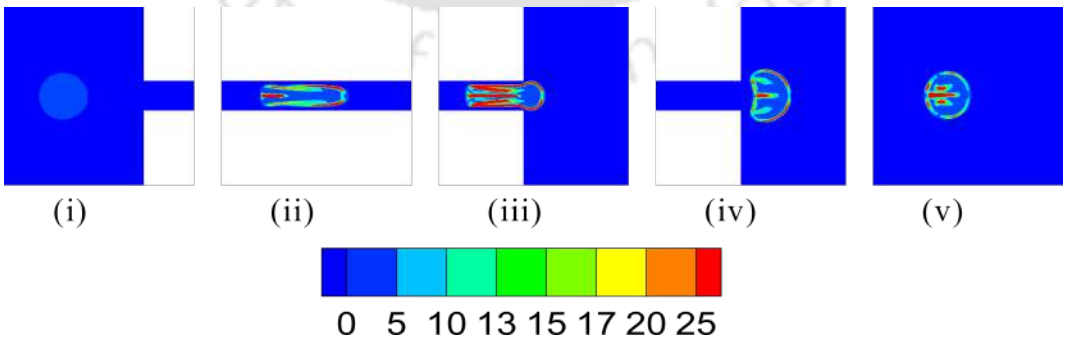

Figure 3.12: Contours of mean square of polymer extension (trace(C)) inside drop migrating through microchannel with $CR = 6$ at timestamps (i) $t^* = 0.05$, (ii) $t^* = 0.1$, (iii) $t^* = 0.12$, (iv) $t^* = 0.13$, (v) $t^* = 0.17$ at $c = 1.5$, β,= 0.6, $Re = 2$, $Ca = 0.055$, $De = 1$, $m = 1$, $\theta = 1$

The contours of the square of average polymer extension (trace(C)) for viscoelastic

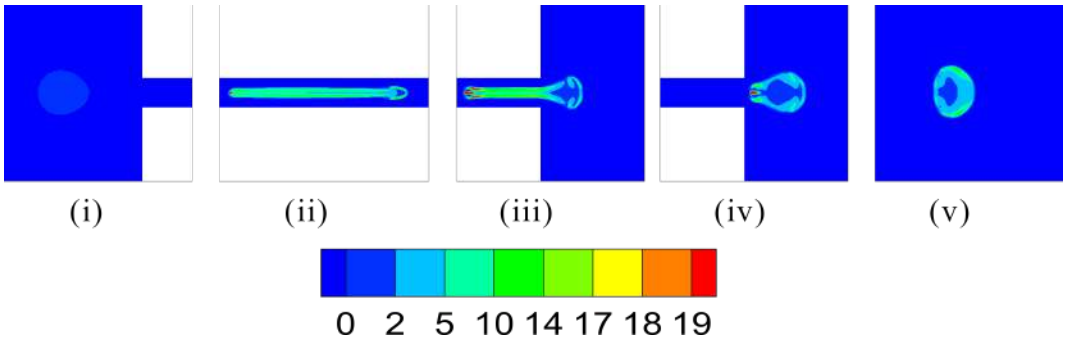

Figure 3.13: Contours of mean square of polymer extension (trace(C)) inside drop migrating through microchannel with $CR = 6$ at timestamps (i) $t^* = 0.05$, (ii) $t^* = 0.1$, (iii) $t^* = 0.12$, (iv) $t^* = 0.13$, (v) $t^* = 0.17$ at $c = 1.5$, β,= 0.6, $Re = 2$, $Ca = 0.3$, $De = 1$, $m = 1$, $\theta = 1$

drop at Ca= 0.055 and Ca= 0.3 (Fig. 3.12(i) and Fig. 3.13(i)) were plotted. The average polymer extension was observed to be more at the drop interface for $Ca = 0.055$ inside the constricted region of the microchannel at t^*= 0.1 (Fig. 3.12(ii)). The average polymer extension was higher in the rear portion of the drop than in the foretip of the drop. As a result, the front end of the drop appeared to be bulging at t^*= 0.1 (Fig. 3.13(ii)) for $Ca = 0.3$ case. Average polymer extension was observed to be higher at the tail end of the drop when the drop exited through the constricted channel at t^*= 0.12 for both $Ca = 0.055$ and $Ca = 0.3$ cases (Fig. 3.12(iii) and Fig. 3.13(iii)). The average polymer extension was observed to cease from the interface as the drop moves further in the exit region of constricted microchannel at t^*= 0.13 and 0.17 for $Ca = 0.055$ cases (Fig. 3.12(iv) and Fig. 3.12(v)). However, the observation of higher average polymer extension at the fore tip and the tail end of the drop was still observed at t^*= 0.13 (Fig. 3.12(iv)). The average polymer extension at the drop interface was lesser for $Ca = 0.3$ cases throughout the migration. The difference in shape evolution of drop in the expansion region of the microchannel for two cases was evident from the contours of trace(C).

3.3.4 Effect of viscosity ratio (θ)

An attempt was made to study the effect of viscosity ratio (θ) on the deformation of viscoelastic drop. Like earlier cases, the deformation of drops of different diameters at $\theta = 0.5$, 1, 5, and 10 (Fig. 3.14) were deciphered. In contrast to previous cases, the droplet exhibited non-monotonic behavior with a variation of θ. The deformation behavior was similar for θ lesser than 1 and θ greater than 10 cases. The observation suggested a significant deviation of deformation behavior when viscosity ratios become greater than 1. Although a higher overshoot

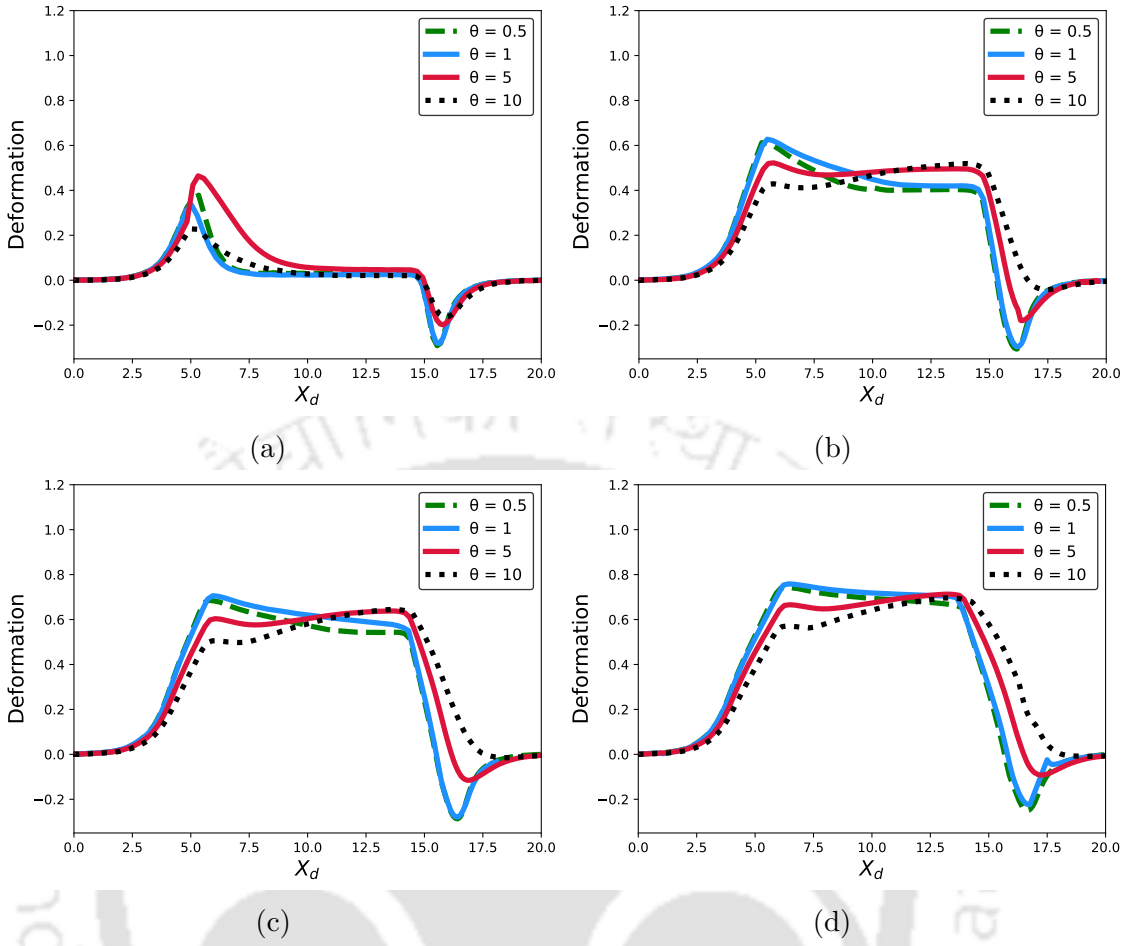

Figure 3.14: Plot showing the deformation of drops of different diameters (a) $c = 0.5$ (b) $c = 1$, (c) $c = 1.25$, (d) $c = 1.5$ for different θ values ($\theta = 0.5$, 1, 5 and 10) flowing through the constricted microchannel with $CR = 6$ at $Re = 2$, $Ca = 0.1$, $De = 1$, $m = 1$, $\beta = 0.6$

of drop deformation of smaller drop (Fig. 3.14a) was observed at the inlet of the constricted channel for $\theta = 5$ case. Furthermore, the maximum value of the deformation parameter was observed to shift towards the exit of the constricted channel with an increase in θ values (Fig. 3.14b, Fig. 3.14c, and Fig. 3.14d). The observation suggested that a viscous drop tries to resist deformation when it is subjected to a sudden increase in strain rate at the entry of the constriction. However, the drop eventually gets elongated under the continuous effect of a higher strain. Furthermore, drop deformation in the cross-flow direction at the exit of constriction was also discerned at $\theta = 10$ cases. In the furtherance of the study, the development of viscoelastic normal stress difference inside a larger drop at $\theta = 0.5$ and 10 (Fig. 3.15 and Fig. 3.16) was studied. The viscoelastic stress distribution inside drop for $\theta = 0.5$ case followed a similar pattern to $\theta = 1$ case explained in the earlier section (Fig. 3.5). In contrast, the viscoelastic normal stress difference distribution for $\theta = 10$ cases at different timestamps of drop

migration was completely different from previous cases. The negative viscoelastic stress difference distribution inside the drop increased with the strain rate inside the drop. The absence of positive viscoelastic normal stress difference in the fore tip and tail end of the drop resulted in extensible stretching of the rear end of the drop at $t^* = 0.1$ and $t^* = 0.12$ (Fig. 3.16(iii) and Fig. 3.16(iv)). Furthermore, prominent development of positive normal stress difference was deciphered at the front end of the drop at $t^* = 0.13$ (Fig. 3.16(v)), which later developed uniformly inside the drop at $t^* = 0.17$ (Fig. 3.16(vi)). Interestingly, the viscoelastic stress distribution inside at $t^* = 0.17$ seemed to be closer to the initial stress distribution at $t^* = 0.05$ (Fig. 3.16(i)). The observation suggested a reduced stress hysteresis tendency of a higher viscous drop.

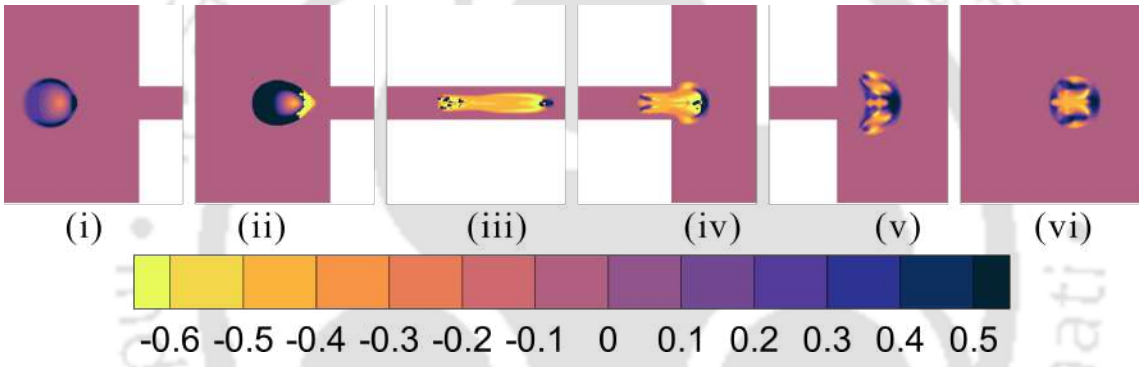

Figure 3.15: Contours of viscoelastic normal stress difference, T_{xx} - T_{yy} inside drop migrating through microchannel with $CR = 6$ at time stamps (i) $t^* = 0.05$, (ii) $t^* = 0.07$, (iii) $t^* = 0.1$, (iv) $t^* = 0.12$, (v) $t^* = 0.13$, (vi) $t^* = 0.17$ at $c = 1.5$, $\beta = 0.6$, $Re = 2$, $Ca = 0.1$, $De = 1$, $m = 1$, $\theta = 0.5$

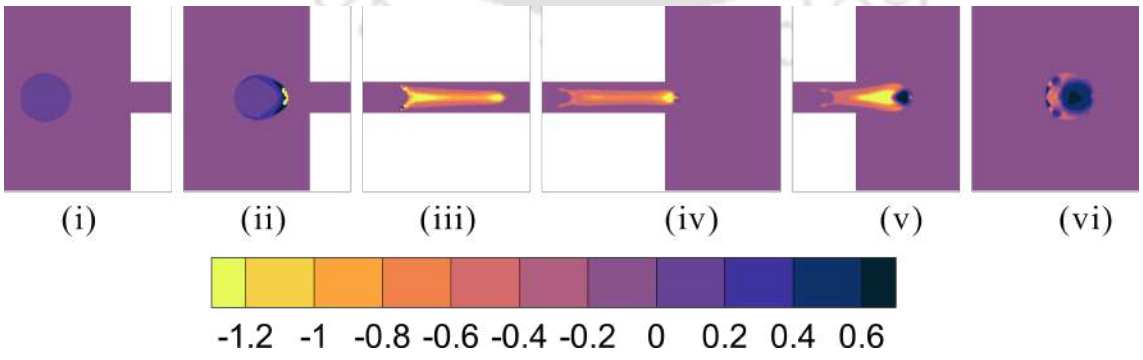

Figure 3.16: Contours of viscoelastic normal stress difference, T_{xx} - T_{yy} inside drop migrating through microchannel of $CR = 6$ at time stamps (i) $t^* = 0.05$, (ii) $t^* = 0.07$, (iii) $t^* = 0.1$, (iv) $t^* = 0.12$, (v) $t^* = 0.13$, (vi) $t^* = 0.17$ at $c = 1.5$, $\beta = 0.6$, $Re = 2$, $Ca = 0.1$, $De = 1$, $m = 1$, $\theta = 10$

3.3.5 Drop breakup assessment

As noted earlier, channel confinement, solvent viscosity ratio, and capillary number significantly impact drop deformation. Therefore, an extensive study was done to track the droplet breakup tendency and examine the parameters that influence the breakup. Interestingly, drop breakup was observed at lesser confinement of $CR = 3$, while the drop was able to restrict breakup while migrating through higher confinement ($CR = 6$). Wall effects in higher confinement result in closed flow streamlines that stabilize drop by promoting higher deformation [136, 137]. Thus, the drop is less prone to break in channels with higher confinement. However, it can be noted that the effect of Deborah number on drop deformation has still not yet been studied. Thus, before carrying out the drop breakup study, the effect of Deborah number on drop deformation migrating through the channel of CR = 3 was studied. As mentioned earlier, the drop is more prone to break up inside a channel with a lesser confinement ratio. Thus, the deformation behavior inside the microchannel of $CR = 3$ was investigated in this section.

The drop deformation behavior under the effect of varying Deborah number (De) is shown in Fig. 3.17. The deformation was studied for the drop of different diameters ($c = 0.5$, 1, 1.25, 1.5) at different Deborah numbers ($De = 0.1$, 1, 10, 50) at $Ca = 0.1$, $Re = 2$, $\beta = 0.11$. The observations suggested a slight variation in drop deformation with an increase in De. However, an observational decrease in drop deformation in the constricted region of the microchannel was discerned for a larger drop ($c = 1.5$) at $De = 50$ (Fig. 3.17d). Although drop deformation may vary insignificantly with the Deborah number De variation, the observations may be attributed to the lower capillary number ($Ca = 0.1$) chosen for present cases. In order to get further insights, the plots were made showing contours of viscoelastic normal stress difference distribution inside drop deforming under varying conditions of Deborah number ($De = 0.1$ and 50) represented in Fig. 3.18 and Fig. 3.19 respectively. The viscoelastic normal stress difference distribution growth was plotted at timestamps $t^* = 0.05$, $t^* = 0.07$, $t^* = 0.12$, $t^* = 0.17$, $t^* = 0.19$, $t^* = 0.25$. The stress distribution growth with time was observed to be similar for $De = 0.1$ and $De = 50$ cases (Fig. 3.18 and Fig. 3.19), with some distinguishable changes at entry and exit of the constricted microchannel at timestamps $t^* = 0.07$ and $t^* = 0.17$. Negative viscoelastic stress difference was distributed more prominently around the interface of the drop front portion at $De = 50$ cases (Fig. 3.19(ii)), indicating drop stretch is not only confined to the fore tip as observed in $De = 0.1$ case. The observations may suggest that drop deformation may depend on Deborah number at other values of parameters like Ca and θ.

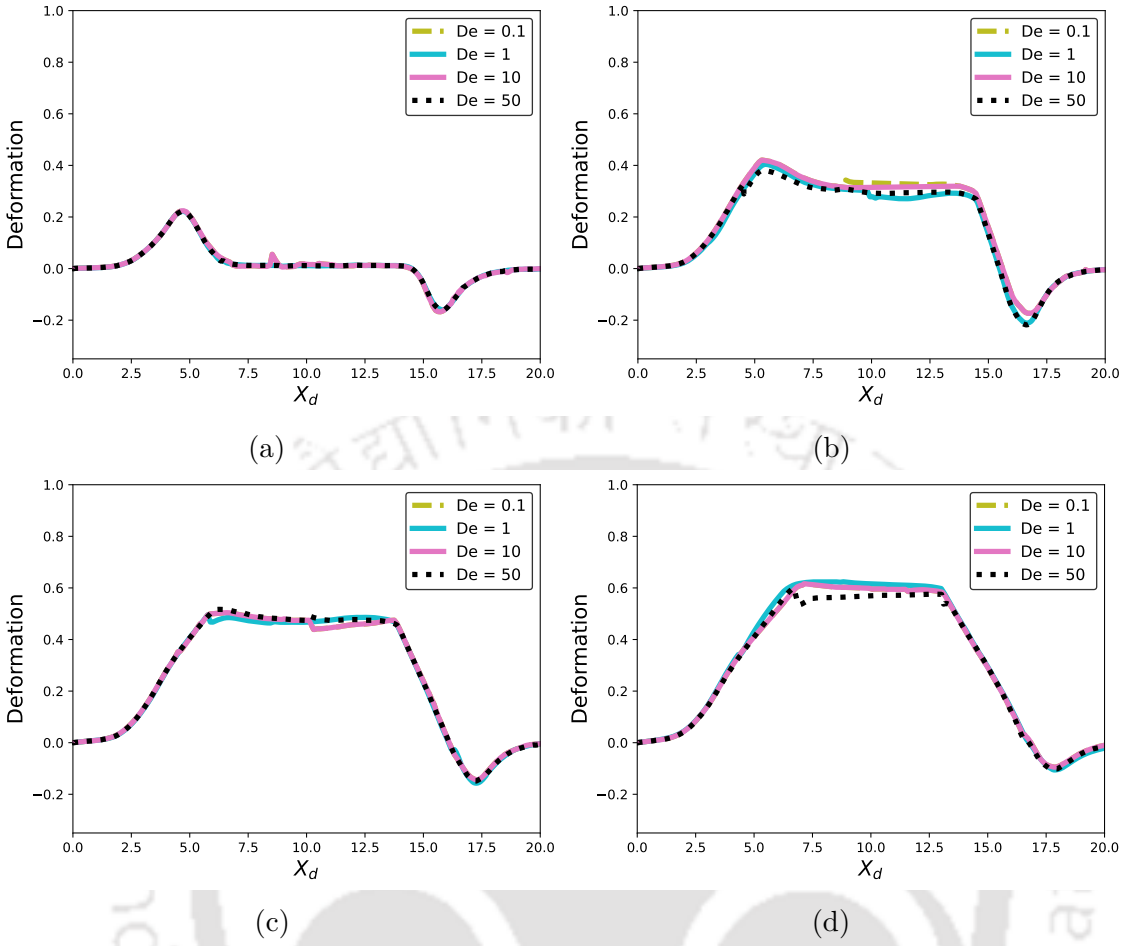

Figure 3.17: Plot showing the deformation of drops of different diameters (a) $c = 0.5$ (b) $c = 1$, (c) $c = 1.25$, (d) $c = 1.5$ for different De values ($De = 0.1$, 1, 10 and 50) flowing through a constricted microchannel with $CR = 3$ at $Re = 2$, $Ca = 0.1$, $\theta = 1$, $m = 1$, $\beta = 0.11$

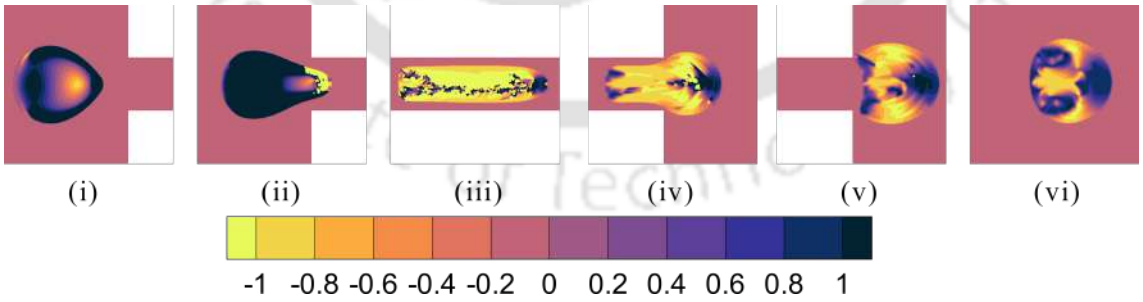

Figure 3.18: Contours of viscoelastic normal stress difference, T_{xx} - T_{yy} inside drop migrating through microchannel with $CR = 3$ at time stamps (i) $t^* = 0.05$, (ii) $t^* = 0.07$, (iii) $t^* = 0.12$, (iv) $t^* = 0.17$, (v) $t^* = 0.19$ and (vi) $t^* = 0.25$ at $c = 1.5$, $\beta = 0.11$, $Re = 2$, $Ca = 0.1$, $De = 0.1$, $m = 1$, $\theta = 1$

In the continuation of the study, the drop breakup by increasing Ca and how the critical value of Ca for drop breakup changes with De and θ were observed. Interestingly, the critical capillary study revealed that drop deformation and breakup were significantly affected by an increase in De at higher Ca. The drop

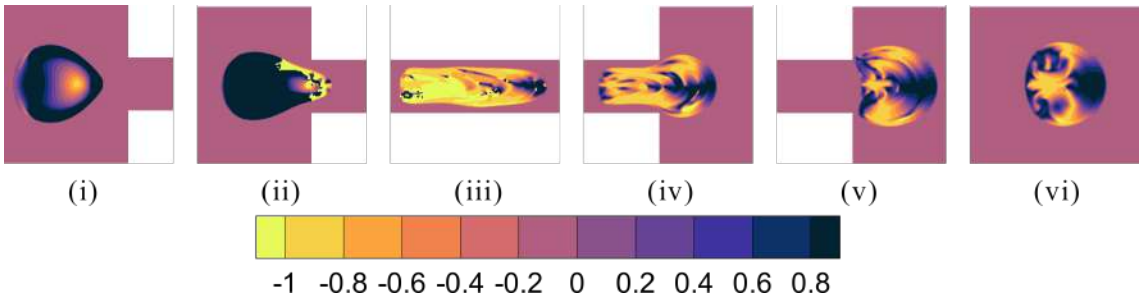

Figure 3.19: Contours of viscoelastic normal stress difference, T_{xx} - T_{yy} inside drop migrating through microchannel with $CR = 3$ at timestamps (i) $t^* = 0.05$, (ii) $t^* = 0.07$, (iii) $t^* = 0.12$, (iv) $t^* = 0.17$, (v) $t^* = 0.19$ and (vi) $t^* = 0.25$ at $c = 1.5$, $\beta = 0.11$, $Re = 2$, $Ca = 0.1$, $De = 50$, $m = 1$, $\theta = 1$

breakup was observed for a larger drop (c = 1.5) at $\beta = 0.11$ and capillary numbers greater than 1. Fig. 3.20a and Fig. 3.20b show the development of viscoelastic normal stress difference inside a larger drop ($c = 1.5$) at $\theta = 1$ and $\theta = 0.5$ respectively. As the drop enters the constricted portion of the microchannel at $t^* = 0.04$, the fore tip of the drop experiences a higher strain rate and elongates. In response to higher strain, a higher positive normal stress difference developed along the interface of the fore tip of the drop (Fig. 3.20a(i) and Fig. 3.20b(i)). The stress development around the drop interface was most prominent for the $\theta = 0.5$ (Fig. 3.20b(i)) case. Drop stretches considerably inside the constricted channel at $t^* = 0.1$ (Fig.3.20a(ii) and Fig. 3.20b(ii)). A negative normal stress difference was observed inside the drop, indicating extra tension in the flow direction. However, a positive viscoelastic normal stress difference at the drop's foretip pulls the drop's front end inward. As a result, the front end of the drop appeared to bulge while the latter portion stretched considerably. With further movement of the drop, the front end of the drop continues to bulge, pulling the major portion of the drop inward towards the front end. In contrast, its tail end becomes thinner as droplets begin to exit from the constricted channel at $t^* = 0.17$ (Fig. 3.20a(iii) and Fig. 3.20b(iii)), the bulging fore tip of the drop experiences a reduced strain rate, while the tail end still experienced higher strain rate. A higher positive viscoelastic stress difference was reported at the front end of the drop, while its absence resulted in a significant thinning of the drop's tail end. As a result of the difference in strain rate and viscoelastic normal stress difference distribution at the foretip and tail end of the drop caused the drop to break from the tail end. Formation of two daughter droplets was observed at the expansion region of the microchannel at $t^* = 0.22$ (Fig. 3.20a(iv) and Fig. 3.20b(iv)). Interestingly, a higher positive normal stress difference was noticed at the tail end of the drop after breakup for $\theta = 0.5$ cases (Fig. 3.20b(v)). The observation suggested higher viscoelastic stress distribution inside less viscous drops after a breakup. Furthermore, a firm bullet shape drop

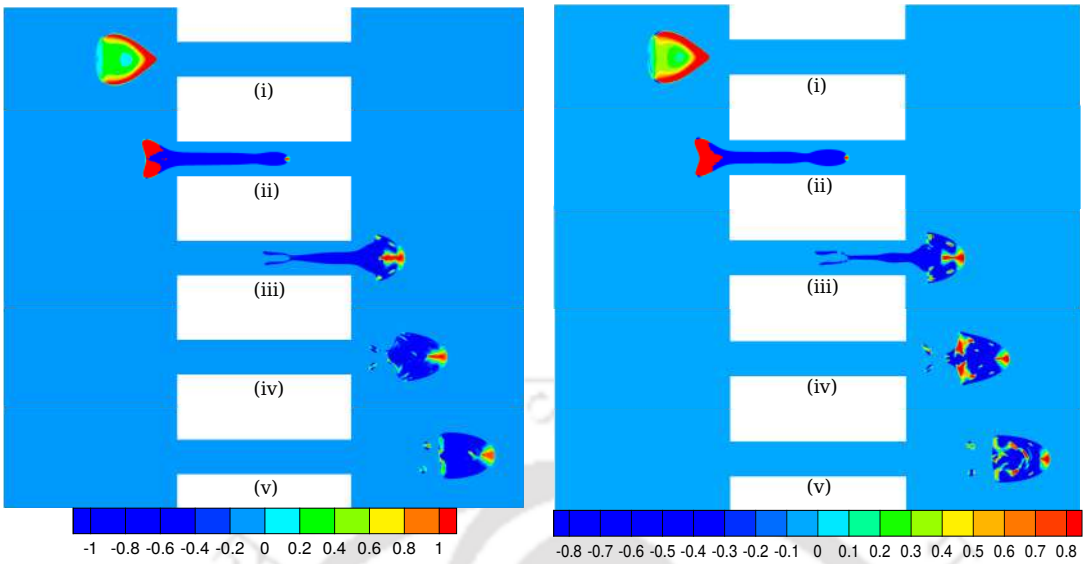

(a) (b)

Figure 3.20: Contours of viscoelastic normal stress difference, T_{xx} - T_{yy} inside drop migrating through microchannel of $CR = 3$ at timestamps (i) $t^* = 0.04$, (ii) $t^* = 0.1$, (iii) $t^* = 0.17$, (iv) $t^* = 0.22$, (vi) $t^* = 0.28$ at (a) $\theta = 1$, (b) $\theta = 0.5$ at $c = 1.5$, $\beta = 0.11$, $Re = 2$, $De = 1$, $m = 1$, $Ca = 1.5$

was observed for $\theta = 1$ case at $t^* = 0.28$ (Fig. 3.20a(v) and Fig. 3.20b(v)). The viscoelastic stress distribution was observed to be more uniform for a higher viscous drop (Fig. 3.20a(v)), while a chaotic distribution was observed inside a less viscous drop (Fig. 3.20a(v)). The observation suggested that a viscoelastic drop with higher viscosity exhibits a better stress relaxation behavior. In addition to the strain rate difference at the terminal ends of the drop, capillary pressure drives the thinning that leads to drop breakup. Elastic stress caused by dumbbell elongation can resist the drop breakup, but the resistance cannot avoid breakup at higher *Ca*. Hooper and Boyd [138] found that for lesser viscosity ratios, the interface becomes unstable under negligible surface tension at higher *Ca*. The breakup in viscoelastic fluid mainly involves elasto-capillary forces [139], where elastic forces restrict drop breakup at lower *Ca*.

Interestingly, a completely different drop breakup behavior was observed for the Oldroyd-B drop under similar flow conditions and parameters applied to the FENE-P drop. The viscoelastic normal stress difference distribution inside Oldroyd-B drop at different timestamps is shown in Fig. 3.21a. In contrast to the FENE-P drop, the breakup of the Oldroyd-B drop was characterized by the formation of a single-daughter droplet from the tail end. The predominance of positive viscoelastic normal stress difference was observed when the drop enters and elongates inside the constricted portion of the channel. A higher positive viscoelastic normal stress difference was deciphered at the drop tail end when it breaks (Fig. 3.21a(iv)).

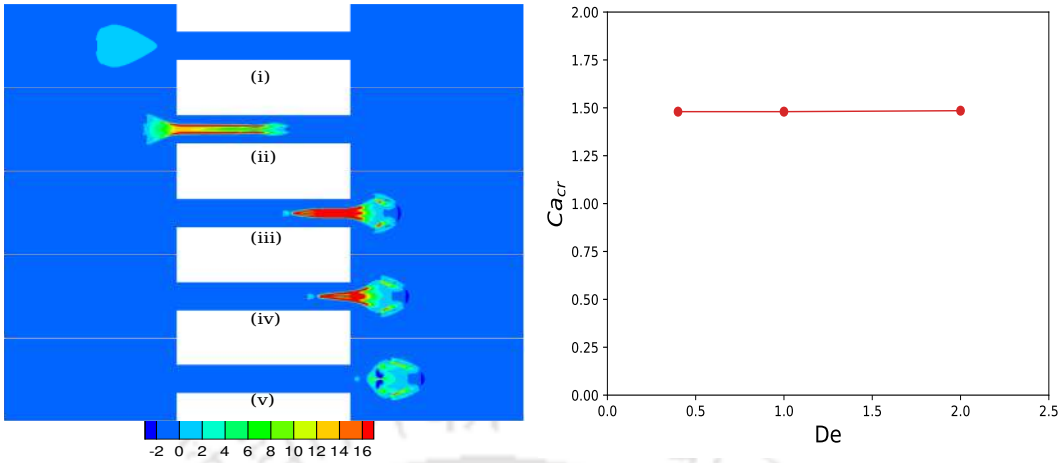

(a) (b)

Figure 3.21: (a) Contours of viscoelastic normal stress difference, T_{xx} - T_{yy} inside an Oldroyd-B drop migrating through microchannel of $CR = 3$ at timestamps (i) $t^* = 0.04$, (ii) $t^* = 0.1$, (iii) $t^* = 0.17$, (iv) $t^* = 0.18$ and (vi) $t^* = 0.2$ at (a) $\theta = 1$ and, $c = 1.5$, $\beta = 0.11$, $Re = 2$, $De = 1$, $m = 1$, $Ca = 1.5$, (b) variation of critical capillary number of Oldroyd-B drop breakup (Ca_{CR}) with De at $\theta = 1$, $CR = 3$, $\beta = 0.11$, $Re = 2$, $m = 1$

Furthermore, the thinning of the drop tail end before the breakup of the Oldroyd-B drop was not as severe as the FENE-P drop. The observation was justified by the development of the higher positive viscoelastic normal stress difference at the drop tail to restrict the significant stretching of the drop at higher Ca. The resulting increase in higher positive viscoelastic normal stress difference during drop breakup may arise from the localized increase in elastic stress arising out of the non-finite extension of the polymeric dumbbell inside the Oldroyd-B drop. However, to put things into perspective, the detachment of cancer cells inside constricted capillary [140] happened from its tail end with the formation of two fragments. Thus, FENE-P drop breakup could closely predict such kind of breakup behavior.

Critical capillary (Ca_{CR}) number for FENE-P drop breakup inside constricted microchannel is not reported earlier. Thus, the Critical capillary number for drop breakup was deciphered for different viscosity ratios (θ) (Fig. 3.22a), Deborah numbers (De) (Fig. 3.22b) and Confinement Ratios (CR) (Fig. 3.22c). The critical parameters were calculated after extensive computation with maximum grid refinement ($\Delta x/D_2 = \Delta y/D_2 = 0.0146$). The critical capillary number was found by performing simulations at different capillary numbers for respective studies. The capillary number at which the outcome of drop breakage was observed was reported to be the critical capillary number for drop breakup. The critical capillary number was reported after acquiring accuracy up to three places of

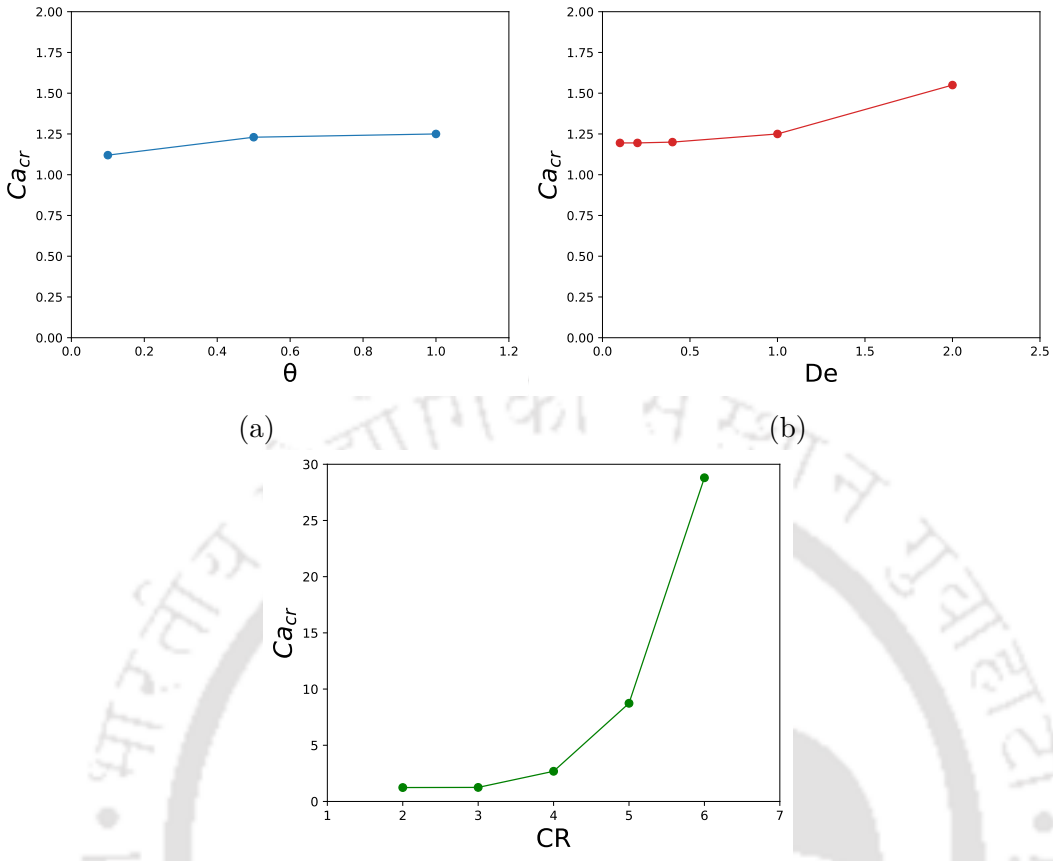

Figure 3.22: Variation of critical capillary number (Ca_{CR}) with (a) θ at $De = 1$, (b) De at $\theta = 1$, (c) CR at $De = 1$ and $\theta = 1$ ($c = 1.5$, $\beta = 0.11$, $Re = 2$, $m = 1$)

decimals. The development of viscoelastic stresses restricts drop breakup; thus, the Ca_{CR} of FENE-P drop was observed to be higher than Newtonian drop [141]. Furthermore, the Ca_{CR} for drop breakup inside a constricted channel was reported to be larger than the Ca_{CR} drop breakup under simple shear [116]. It was found that the critical capillary number varied slightly with the viscosity ratio (θ). As droplet breakup seemed more prominent for $\theta < 1$, the Ca_{CR} value was reported to be higher at higher θ values. At $\theta = 5$, the Ca_{CR} value was found to be 25. Interestingly, the Ca_{CR} varied noticeably when θ values become less than one ($\theta < 1$). In the furtherance of the study, it was observed that Ca_{CR} increased monotonically with Deborah number (Fig. 3.22b). The observation was consistent with the Lerdwijitjarud et al. [142] experimental investigation. A larger variation in Ca_{CR} was observed for a greater Deborah number difference. A significant difference in Ca_{CR} was reported for $De \geq 1$ as shown for $De = 2$ in Fig. 3.22b. The Ca_{CR} varies minutely for De values lesser than 1. In contrast, the Ca_{CR} values for Oldroyd-B drop breakup were observed to remain constant with the variation of Deborah number (Fig. 3.21b). An interesting phenomenon of cavity formation was

observed for Oldroyd-b drop at lower De values at Ca values closer to 1.5. However, this phenomenon will not be discussed, as it is beyond the scope of the present study. Furthermore, the variation of critical capillary number was observed to be more sensitive to channel confinement. The critical capillary number was observed to increase drastically with an increase in confinement ratio, as shown in Fig. 3.22c. The finite extensibility of the polymer molecules becomes very important at the droplet breakup time. While undergoing deformation, the dumbbell beads in the FENE-P model extend finitely [143], causing a localized increase in elastic stress that eventually balances the capillary pressure. The phenomenon plays a vital role in restricting the drop breakup. The absence of elastic stress resistance due to polymer stretching in Newtonian drop makes it more susceptible to break.

Xiao et al. [134] developed a deoxyribonucleic acid (DNA) toehold switch-engineered spherical nucleic acid-templated hydrogel to achieve active burst release of chemotherapeutic drugs at the targeted cancer cells. The active burst release was achieved by dissociating drug carrier assembly by selected adenosine triphosphate (ATP) molecules. It is evident from the previous study that designing a nanocarrier assembly for achieving burst drug release is an arduous task. The present understanding of viscoelastic drop breakup can provide crucial insights into creating nanocarriers to achieve on-demand dissociation for active burst drug release at concerned sites. Proper knowledge of critical capillary number, confinement ratio, and solvent viscosity ratio for FENE-P drop breakup can lead to the fabrication of hydrogel drug carriers.

3.4 Summary

In the study discussed above, the effect of parameters like solvent viscosity ratio (β), capillary number (Ca), viscosity ratio (θ), and channel confinement (CR) on the deformation of FENE-P drop migrating through the microchannel was observed. It was found that deformation depends on solvent viscosity ratio when drop flows through higher confinement even at the unity Deborah number. Drop deformation was observed to get enhanced with the increase in β values. However, the drop with a lesser β value was reported to exhibit faster stress relaxation. Drop showed larger deformation at higher capillary numbers. It was also reported that viscoelastic stress distribution gets convected faster at a higher capillary number when the strain rate inside drop reduces. Drop deformation was observed to vary non-monotonically with an increase in viscosity ratios. The droplet breakup was also studied at higher capillary numbers. The capillary number at which the droplet breakup occurred was termed as critical capillary number. Variations of

critical capillary numbers with Deborah numbers, viscosity ratios, and confinement ratios were also discussed. The critical capillary number increased drastically when the confinement ratio increased. Drop breakup assessment can be utilized to design nanocarrier assembly for on-demand burst release of anti-cancer drugs at the selected site.

4

Migration of synthetic and natural nano-carriers through constricted microchannel

The margination of nano-drug carriers towards the wall of the microcapillaries during movement is an essential issue in therapeutics. A soft and deformable drug carrier can overcome the limitations of margination and wall adhesion. Meanwhile, cancer cell membrane-derived nanovesicles can overcome the limitations of biodegradability and lesser circulation. Thus, shear-thinning and self-healing PVA/PVP-based hydrogel particles were synthesized. Hydrogels are three-dimensional network structures with a high amount of water content, which are ideal for loading water-soluble drugs/molecules. These salient features led us to study PVA/PVP-based shear thinning hydrogel as an ideal drug carrier through capillary constriction. Thus, a blood capillary-sized PDMS microchannel was fabricated with a minimum constriction width of 7 μm over 200 μm. The hydrogel drug carriers regained their original shape and structure after migration. This provided a remarkable insight into the self-healing property of the hydrogel particles. Drug encapsulation and drug release studies determined the drug carrier's therapeutic efficacy. A shear-thinning viscoelastic FENE-P drop model was adopted to delineate the drug carriers' migration behavior numerically. A relaxation time of 850 ms is suggested for better migration prediction of the carriers. Additionally, the migration potential of these nanovesicles through branches of constricted microchannels was observed. The study revealed that these vesicles get aggregated while migrating through microcapillary-sized channels. However, these particles migrated successfully through constricted microchannels without exhibiting channel obstructions and adhesion to the walls. The study's observations will help design cancer cell-derived nanovesicles for drug delivery.

4.1 Introduction

As the name suggests, drug carriers should be able to deliver anti-cancer drugs, genes, and other therapeutics at the concerned tumor site like a laser-guided missile. Nanocarriers are coupled with the molecules that bind to the over-expressed receptors on the cancer cell surface. Drug is then released from the carriers by responding to the stimuli based on carrier property. As mentioned earlier in the review, circulation instability, less biodegradation, and poor bioavailability of some of these nanocarriers raise concerns about the long-term application of cancer treatment. However, there are certain limitations like margination and adhesion of these nanocarriers towards the wall while flowing through constricted capillaries. This limitation also restricts its use in microfluidic devices for cancer therapeutic applications. These carriers also undergo protein adsorption in hydrophobic PDMS-based channels, the tendency which requires control of nano-scale properties of these carriers for microfluidic application [39]. Toy et al. [41] did a study on liposomes to find the solution of margination and adhesion of nanocarriers inside the microchannel. They suggested margination and adhesion in microchannels can be overcome by using soft deformable nanocarriers with surface modifications. Operti et al. [144] designed a microfluidic device to study the effect of particle size of poly(lactic-co-glycolic acid) (PLGA) on their cellular uptake and release property.

Thus, based on previously reported studies, it can be found that soft, deformable, 3D cross-linked hydrophilic polymers, hydrogel particles can be a promising nanocarrier for controlled and efficient drug delivery application [145]. Highly bio-compatible, porous structure, tuneable biodegradable, hydrogel drug carriers can sustain adverse pH environments and high temperatures. Surface-modified hydrogel drug carriers can deliver hydrophilic, hydrophobic, and lipophilic drugs and are responsive to various stimuli like light, heat, pH, magnetic fields, etc. Along with numerous advantages, the low mechanical strength of hydrogel drug carriers limits its application in widespread drug delivery application.

Three-dimensional cross-linked chains of hydrophilic polymers forming soft and deformable hydrogels can hold large amounts of water. These attributes of hydrogel particles find numerous uses in various biomedical purposes, especially as opportune nanocarriers in controlled drug delivery applications for cancer theranostics. Hydrogels can retain their structural wholeness by elastic modulus recovery. As a result, they can deform and arrange themselves to the shape of the surface where it is applied [146]. This transient recovery under relaxation is higher for shear-thinning hydrogels. The shear-thinning behavior of hydrogels assists in injectability through

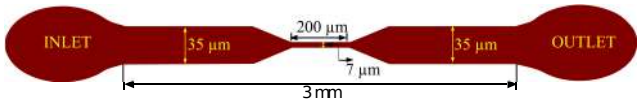

Figure 4.1: Pictorial representation depicting the design of the fabricated microchannel

syringes for convenient drug delivery to the targeted site [147]. Liu and Hsu [148] studied the biomedical application of the self-healing property of hydrogel particles, which explains its ability to repair the structural damages and retention of the original function, while Pang et al. [149] reported the development of shear thinning hydrogel with endoscopic injectability. The self-healing and shear-thinning nature of hydrogel particles can be utilized to produce a potent drug delivery vehicle for anti-cancer drugs. However, due to its low mechanical strength, the hydrogel cannot withstand high loads. As a result, it causes the nanocarrier to decay and flow away from the targeted site. Furthermore, migration of these nanocarriers in microchannels undergoes margination and adhesion towards the channel wall. This tendency limits its use in microfluidic devices attributed to cancer theranostics and drug delivery applications. Furthermore, the hydrophobic surface of PDMS-based microfluidic devices also suffers unwanted protein adsorption, necessitating the control of nanoscale properties of the microfluidic devices for lab-on-chip application. Numerous types of research are attributed to producing novel synthetic hydrogel with lesser limitations, but very few researches are dedicated to determining their mechanical strength in microchannels [46].

Furthermore, issues on bio-compatibility and circulation duration of these synthetic drug carriers always prevail. As mentioned earlier in the review, membrane-derived vesicles can answer this crucial question. The vesicles derived from cancer cell membranes possess tumor-specific antigens and homologous surface adhesion molecules (such as EpCAM, N-cadherin, etc.) that further escalate the fusion of these membranous cellular nanovesicles with the homotypic cancer cells [150]. For example, an RBC membrane functionalized with PLGA-NP (poly(lactic-co-glycolic acid nanoparticle) was one of the first membrane-coated nanovesicles, which exhibited enhanced stability, prolonged circulation, and targeted delivery [151]. Comparetti et al. [152] synthesized cancer cell membrane-derived nanoparticles to transport chemotherapeutics to carcinoma and immunocompetent cells. They found it to be an efficient drug carrier for pancreatic cancer. He et al. [153] developed a cancer cell membrane-based nanovesicle that efficiently delivered immunostimulants to enhance antitumor immune responses. Furthermore, recent research has also revealed that these nanovesicles can be utilized to develop targeting delivery strategies for post-surgery tumor recurrence and metastasis [154]. Besides drug

delivery to cancer sites, nanovesicles are also credited with the oral, transdermal, and tropical delivery of proteins and peptides [155].

Most microfluidic-based studies on nanocarriers were solely dedicated to variations in size and surface properties on the pharmacokinetics characteristics of nanoparticles. Thus, the present study addressed several research voids related to hydrogel and cancer cell-membrane-derived nanovesicles. The mesoscopic hydrodynamic simulations of blood flow carried out by Müller et al. [156] delineated the effect of margination and adhesion of micro- and nanocarriers on drug delivery. However, an investigation involving an experimental study for real-time migration tendency of micro- and nanoparticles in blood capillaries has yet to be explored. Thus, an investigation was done by performing experiments on PVA/PVP-based hydrogel micro/nanocarriers, and a numerical investigation was done by choosing a mathematical model for hydrogels. The migration of hydrogel nano drug carriers in a constricted microchannel of 7 μm diameter, designed to mimic human blood capillaries, was investigated. As drug carriers are subjected to high shear flow inside adverse constriction of blood capillaries, it becomes necessary to track the self-healing nature of the drug carrier, its drug loading potency, and drug release efficiency under such an adverse constricted environment. Thus, hydrogel drug carriers' drug loading and release efficiency in two different pH levels were investigated. Furthermore, the shear thinning behavior of hydrogel particles was examined by performing numerical simulations. A shear-thinning viscoelastic mathematical model was chosen to estimate their flow tendency inside the microchannel better. The computational results obtained from the simulation of a mathematical model of hydrogels were compared with the experimental results. A shear thinning nonlinear viscoelastic model FENE-P [157] was shown to estimate the experimental results appropriately. Lenzini et al. [158] reported that extracellular vesicles perform better than liposomes when escaping stress-relaxing environments. They suggested that extracellular vesicle surface protein provides mechanical stiffness to the target cells. However, they did not consider the hydrodynamic movement of these vesicles. To elucidate it, an attempt was made to study the migration of aggregated nanovesicles through blockages and branched microchannels designed to mimic the network of microcapillaries. The nanovesicles selected for the present experimental study were derived from luminal breast cancer cells, namely MCF-7. Further, it was attempted to get a representation of the displacement profile and quantification of its deformation inside the constricted microchannels.

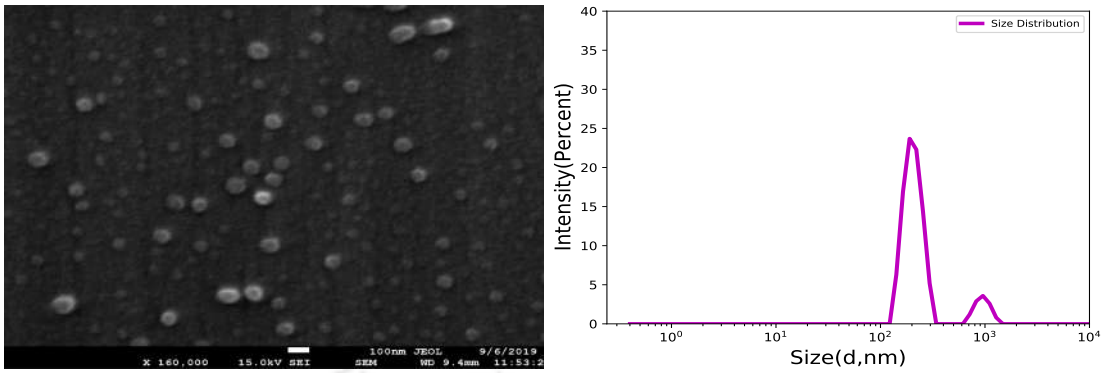

(a) (b)

Figure 4.2: (a) shape and size distribution of hydrogel particles viewed under FESEM, (b) dynamic light scattering study for mean hydrodynamic diameter of hydrogel particles

4.2 Results and discussion

4.2.1 Understanding the self-healing, shear-thinning characteristics and therapeutic efficacy of hydrogel drug carriers migrating through constricted microchannel resembling blood microcapillary

Shear-thinning and self-healing PVA/PVP-based hydrogel particles were synthesized. Hydrogels are three-dimensional network structures with a high amount of water content, which are ideal for loading water-soluble drugs/molecules. Nonetheless, the chemical nature, network morphology, and equilibrium swollen state of hydrogels are responsible for critical parameters such as mechanical strength and internal and external transport. The advantages of PVA/PVP-based hydrogel are high porosity, soft consistency, water solubility, bio-degradability, biocompatibility, non-carcinogenicity and extremely low cytotoxicity [159]. These salient features led us to study PVA/PVP-based shear thinning hydrogel as an ideal drug carrier through capillary constriction. The blood capillary-sized PDMS microchannel was fabricated with a minimum constriction width of 7 μm over 200 μm. The flow speed of 50 μl/hr was taken for migration study, which was by the blood flow speed inside the microcapillary.

4.2.1.1 Characterization of hydrogel particles

The hydrogel synthesis was confirmed by FESEM analysis, which showed that most hydrogels were spherical in shape and monodisperse in nature, as shown in Fig.

4.2b. The average size of the hydrogel was found to be 100 ± 15 nm. The DLS study in Fig. 4.2a depicted the mean hydrodynamic diameter 120 ± 25 nm of the hydrogel, which is suitable for cellular uptake [160]. The increase in size detected in hydrodynamic diameter is due to the hydration process of the hydrogel.

4.2.1.2 Migration of hydrogel particles through constricted microchannel

The experiment was performed with a clean microchannel to ensure no hindrance to micro/nano hydrogel particle flow. The synthesized hydrogel particles were suspended in water with a 0.5 mg/mL concentration and were first washed to remove any possible contaminants. The clean solution was then allowed to pass through the microchannel at the flow rate of 50 μl/h. As the characterization of hydrogel particles showed the particle size varying as 100 ± 15 nm, the hydrodynamic behavior of micro hydrogel particles migrating through the constriction region was captured and analyzed. As these nanoparticles possess high surface energy, they aggregate and behave like particles of larger hydraulic diameters. The aggregated hydrogel particle of diameter 4 μm, as shown in Fig. 4.3a (i-ii), migrates through section of width 35 μm without any indication of margination or adhesion to the wall, which is evident from the soft and hydrophilic nature of the hydrogel particle. The particle, while reaching the inlet of the constriction region of width 7 μm adjusts to the flow and readily enters the constriction region undergoing deformation to adjust to the highly constricted flow as shown in Fig. 4.3a (iii). The particle, owing to its deformable and hydrophilic nature, passed the constriction region at a relatively higher speed with no obstruction and unwanted adhesion, as shown in Fig. 4.3a (iv-v). Hydrogel particles, after leaving the constriction region, tend to regain their original structure, which substantiates that the particle did not lose its self-healing property even after traversing 7 μm thick constricted channel shown in Fig. 4.3a (vi). To study the size dependence of deformation and the self-healing nature of hydrogel particles, the migration of aggregated particles with a relatively higher hydraulic diameter of 9 μm through the same constriction was examined. As shown in Fig. 4.3b (i-vi), the larger deformable hydrogel particles exhibit a similar migrating tendency as shown by smaller particles and tend to repair their original structure after leaving the constriction region. The self-healing property is thus retained for the relatively larger hydrogel particles. Due to their high surface energy, micro/nanoparticles also tend to agglomerate while flowing through microchannels. This limitation was also examined by observing the migration of a group of hydrogel particles. The synthesized hydrogel particles tend to traverse the 35 μm wide region and 7 μm wide constricted region without undergoing

agglomeration again. The aggregated hydrogel particles, as shown in Fig. 4.4 (i-vi), are arranged to avoid re-agglomeration before entering the constriction region. The particles readily pass through the constriction and leave the constriction without re- agglomeration. The drug carrier was observed to possess a remarkable elastic recovery as it withstand the adverse constriction of microchannel.

The high-speed camera videos showed the remarkable ability of hydrogel drug carriers to retain their shape and structure after migrating through the adversely constricted channel. The experimental observations showed astounding proof of hydrogel's tendency to preserve its self-healing nature even in extreme environments. This attribute is crucial for the drug retention of hydrogel drug carriers and confirms it as an efficient drug carrier. As reported earlier, hydrogel possesses weak mechanical strength and can undergo unwanted decay before reaching the tumor site; the present experiment affirms the ability of hydrogel drug carriers to withstand high shear flow without signs of decay. The self-healing nature of larger hydrogel drug carriers was also observed. The synthesized soft hydrogel particles overcame the tendency of wall adhesion to a larger extent and also showed a reduced tendency of aggregated micro- and nanoparticles to undergo re-agglomeration. However, the entry and exit of carriers to the constriction region of the microchannel were well captured by a high-speed camera. However, the migration through the constriction region was slenderly captured. The migration through the constriction region was observed to be very fast owing to the hydrophobic-hydrophilic nature of the PDMS channel wall and hydrogel particle, respectively. The time scale of milliseconds for the capillary migration of the hydrogel drug carriers signifies the circulation of drug carriers in microcapillaries before they reach the concerned tumor site.

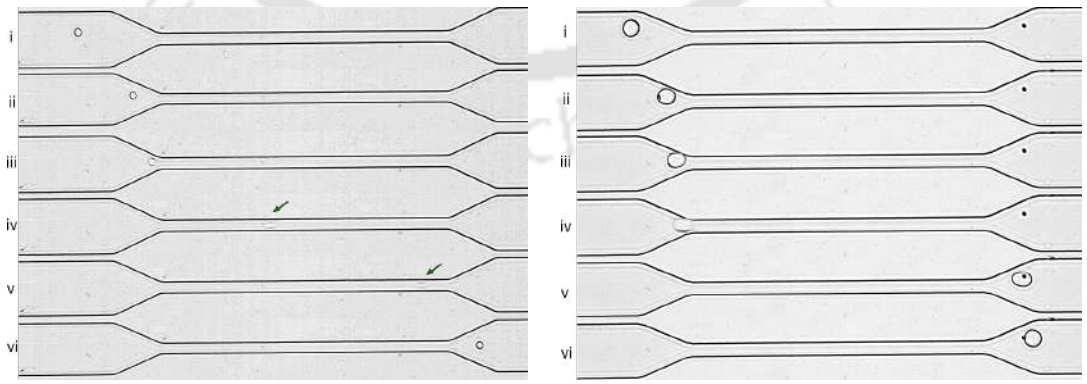

(a) (b)

Figure 4.3: Migration of hydrogel drug carriers imaged by high speed camera, (a) migration of a single hydrogel drug carrier of diameter 4 μm through different regions of microchannel, (b) migration of a single hydrogel drug carrier of diameter 9 μm through different regions of microchannel

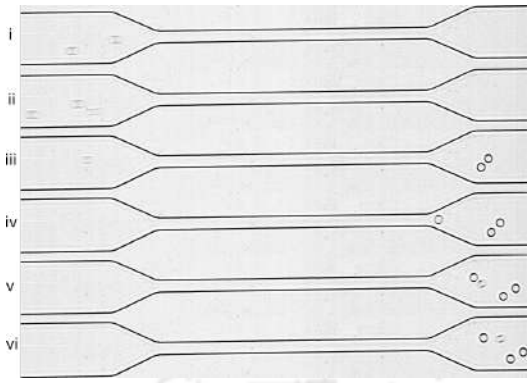

Figure 4.4: Migration of group of hydrogel drug carriers through different regions of microchannel

4.2.1.3 Flow behavior of single hydrogel particle through constricted microchannel

The flow progression of a single hydrogel particle of diameter 4 μm inside a microchannel at different regions is shown in Fig. 4.5a. The portion of the channel selected for studying the migration behavior of hydrogel particles is indicated in Fig 4.5a. The domain of study was divided into different regions. Region I was the 35 μm wide and 38 μm long straight section of the channel, Region II was 34 μm long tapered section of the channel, which was the entry zone for the hydrogel particle; Region III was 7 μm wide and 200 μm long constriction region of channel that mimics the blood capillaries of human blood vessels. Region IV was 34 μm long and was a tapered section and exit region of the hydrogel particles. The last region of the domain was Region V, 35 μm wide and 34 μm long straight section of the channel. The average velocities of 4 μm single hydrogel particles at different regions of the channel were calculated by plotting the displacement of the particle at different instants of time. The extreme left section of Region I was taken as the origin point in position and time for calculating the displacement of the particle. Parameters like displacement, time, particle size, and average velocity were calculated for the particle by using the image-processing utility of Phantom Camera Controlled software for cine analysis. Phantom Miro lab 320 high-speed camera captured the cine file for studying migration. Fig. 4.5b. shows the plot of displacement versus time curve for the single hydrogel nanocarrier of diameter 4 μm. The average velocities of the nanocarrier at different regions were calculated, shown in Fig. 4.5b. The average velocities in Region I – Region V were found to be 0.436 mm/s, 1.093 mm/s, 30 mm/s, 0.764 mm/s and 0.3207 mm/s respectively. The size variation of transit velocity of hydrogel nanocarrier is indicated in the plot shown in Fig. 4.5c. The transit velocity is the average velocity with which the hydrogel nanocarrier traverses the microchannel's Region III (constriction region).

The experimental data was plotted with linear curve feet with a standard error of 4.237 mm/s in transit velocity. The plots are generated using Matplotlib, a plotting library for the Python programming language.

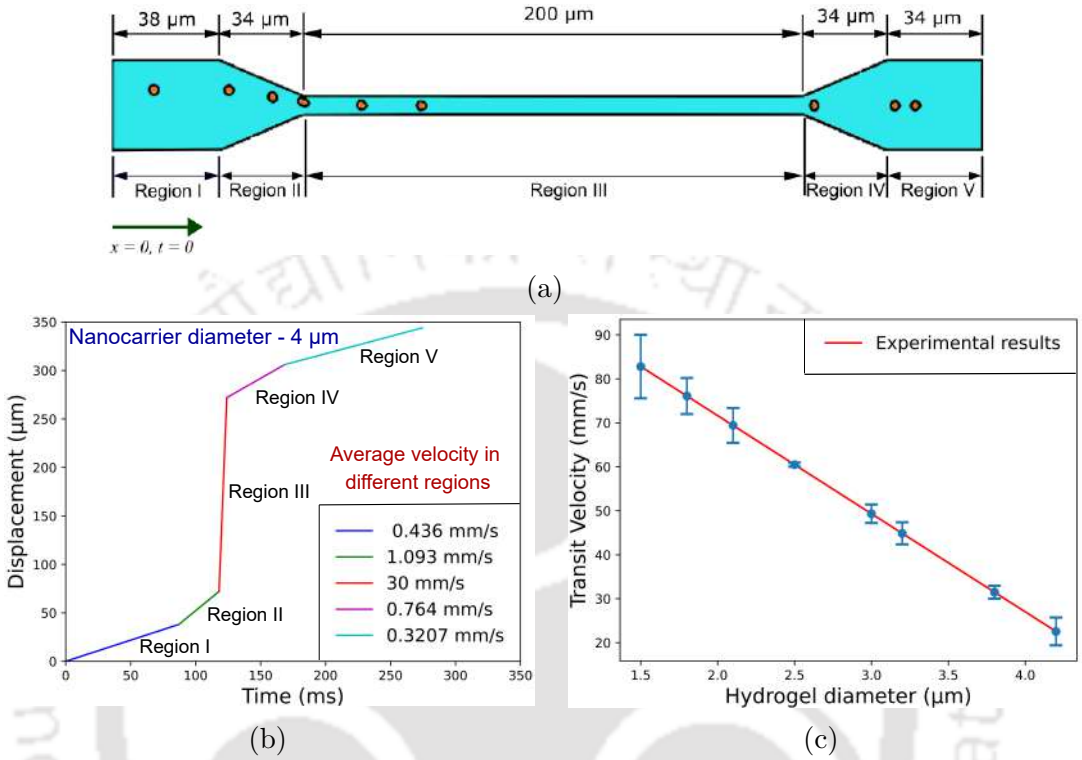

Figure 4.5: (a) Schematic representation of migration of single hydrogel drug carrier of diameter 4 μm through different regions of capillary sized microchannel, (b)experimental resutls of displacement versus time curve for the migration of single hydrogel drug carrier of diameter 4 μm with regions of microchannel marked, (c) variation of transit velocity with different hydrogel drug carriers' diameter

4.2.1.4 Deformation of hydrogel particle at the entry and exit region of constricted microchannel

Deformation of hydrogel particle of diameter 9 µm was calculated at the entry and exit region of the constricted channel as shown in Fig. 4.6. Figure 4.6a shows the deformation of the hydrogel drug carrier along the axial distance in the converging section Region II of the microchannel. The particle tends to show marginal deformation after fully entering into the converging section of the microchannel; the deformation then gradually increases as the particle progresses toward the constricted region. The sharp increase in deformation was seen when the leading edge of the particle entered the constricted region, showing the maximum deformation. The deformation of the hydrogel particle along the diverging section, Region IV, is shown in Fig. 4.6b. The deformation calculation at the exit to

the constricted region is very significant as it showed the self-healing behavior of the hydrogel particle. The particles seemed to show similar deformation at the immediate entry and exit of the constricted microchannel. The particle deformation value gradually decreases in the diverging section with maximum value at the immediate exit of the constriction. The particle deformation sharply decreased as it progressed towards the straight section of the microchannel, eventually reaching a zero value as it approached the exit of the diverging section. The particle regained its original shape after 43 ms of coming out of high shear flow in a constricted microchannel.

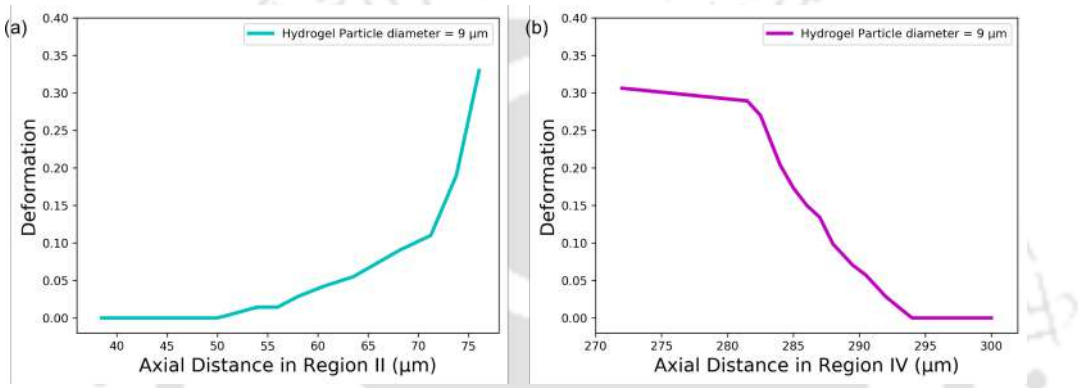

Figure 4.6: Plot showing the experimental results of deformation of a single hydrogel particle of diameter of 9 μm along the axial distance in microchannel, (a) in entry region (Region II), (b) in exit region (Region IV)

The elastic recovery of the hydrogel particles was further examined by calculating its deformation at the entry and exit section of the constricted microchannel. Similar deformation behavior at the immediate entry and exit of the constricted channel was observed. The macro-scale bulk deformation of hydrogel particles is linked with the conformation change of the polymer network in the microscale, and its significant water content makes it less resistant to deformation and even fracture. Hydrogel particles were able to deform and able to withstand high shear without undergoing fracture. The complete regain of shape was obtained after 43 ms when the particle came out of the constricted microchannel.

4.2.1.5 Drug encapsulation and release study of hydrogel drug carrier

The benchmark of an efficient nanocarrier is its ability to encapsulate a high concentration of drug molecules in each such carrier. Essentially, the drug loading efficiency of the hydrogels was determined using fluorescence spectroscopy of excitation at 470 nm and emission at 595 nm. The obtained results indicate that the hydrogel loaded approximately 68.6 % of doxorubicin (with 16.8 µg/mL concentration in the solution containing 1.0 mL hydrogel) within 3 hours (Fig.

4.7a). The nanocarrier is also supposed to release the encapsulated drugs either by a burst release or sustained release, depending on the type of application. The release kinetics of the nanocomposite was assessed using fluorescence spectroscopy. From the time-dependent release profile, it can be observed that approximately 60.6 % drug was released by 12h at pH: 7.4 (Fig. 4.7b). The drug release kinetics was also observed at pH: 4.5 (Fig. 4.8). The intracellular endosomal, lysosomal vesicles and extracellular tumor milieu possess an acidic pH of around 4.5. At the same time, the physiological pH of the human circulatory system is 7.4. The drug release kinetics was assessed at pH 4.5 and 7.4 to mimic both extracellular and intracellular environments. In contrast to the burst drug release observed in the acidic condition, the neutral condition showed sustained drug release.

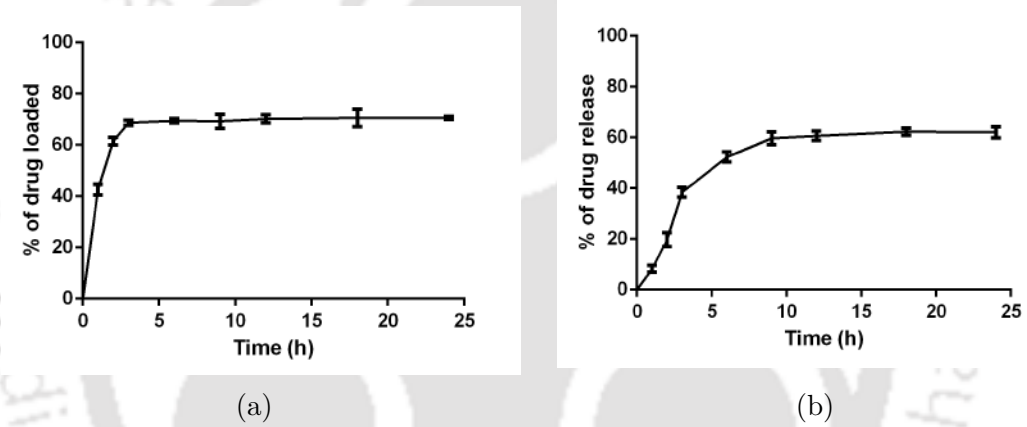

(a) (b)

Figure 4.7: Experimental investigation of drug encapsulation and release study of hydrogel drug carrier, (a) drug loading efficiency of hydrogel carriers, (b) drug release efficiency of hydrogel carriers at pH = 7.7

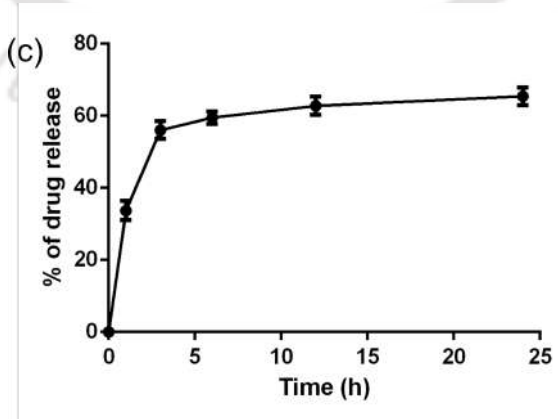

Figure 4.8: Experimental investigation of drug release efficiency of hydrogel carriers at pH = 4.5

The physical properties of hydrogels, particularly their porosity, offer enormous advantages in drug delivery applications such as sustained release of the loaded

drug. A high local concentration of the active pharmaceutical ingredient is retained over a long period via a suitable release mechanism controlled by diffusion, swelling, chemical, or based on some environmental stimuli [161]. As doxorubicin is highly water soluble, it is plausible that the apparent high efficiency could be due to the loading of the molecules on the surface and inside the hydrogel and the strong bonding between –COOH and doxorubicin. This could be due to the hydrophilic nature of the hydrogel with the extensive presence of a hydrogen-bonded interpenetrating network. On the other hand, the slow release of doxorubicin from the hydrogel could be due to the strong interaction between the hydrogel and drug molecule or other parameters like hydration capacity of the hydrogel, pore size, diffusion kinetics in PBS buffer, etc. Besides, the faster drug release in the acidic environment could be attributed to the mutual interaction between doxorubicin and acetate buffer, which enhanced the permeability of the drug. Thus, the shear-thinning hydrogel produced from biocompatible polymer enables minimal invasive injection of the gel into the desired area for local drug delivery and sustained release.

4.2.1.6 Comparison of migration of mathematical model of hydrogel with the experimental results

The shear thinning property, desirable for drug carriers, was examined by performing numerical simulations. Besides, mathematical modeling gives a better understanding of particle squeezing inside the microchannel, which is crucial for drug delivery applications. The viscoelastic drop model used by Hymen et al. [92] for studying cell trapping in Y junction microchannel is believed to be a promising model for understanding the complex behavior of the flow of cells in micro capillaries. The shear-thinning viscoelastic model FENE-P was used to model the present two-phase fluid system. The hydrogel particle was modeled as the FENE-P viscoelastic drop suspended in Newtonian fluid water. A two-dimensional model was used to perform the simulations. The viscoelastic drop of diameter 4 μm was given the initial position by the displacement of the particle observed in the experiment. No slip boundary condition was applied at the channel walls, and inlet velocity was given at $x = 0$ (Fig. 4.9). The interface tracking method, the volume of fluid (VOF) technique, was used to study the interfacial interaction of drop with the outer matrix. The FENE-P model was preferred over the Oldroyd-B model as the former manifests finite extensibility. The computational domain is shown in Fig. 4.9.

The non-dimensional number and parameters involved in the study were Reynolds number(Re), capillary number (Ca), Deborah number (De), Viscosity ratio (θ),

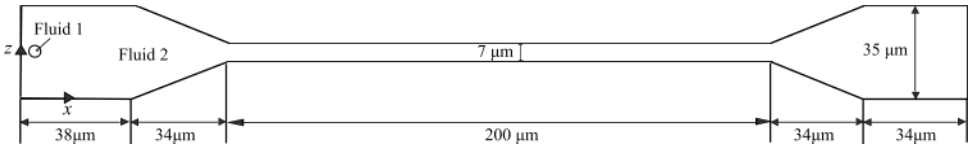

Figure 4.9: Computational domain with initial position of viscoelastic drop for two-phase droplet-matrix system.

solvent viscosity ratio (β), density ratio (m), expressed as,

$$Re = \frac{\rho_2 V D}{\mu},\ Ca = \frac{\mu_2 V}{\sigma},\ De = \frac{\lambda}{T},\ \theta = \frac{\mu_2}{\mu_1}, \beta = \frac{\mu_s}{\mu_s + \mu_p}, m = \frac{\rho_2}{\rho_1} \tag{4.1}$$

where 1 and 2 are the indices to signify properties of fluid 1 and fluid 2. Incompressible mass and momentum conservation equations can be written for the present two-phase drop-matrix system.

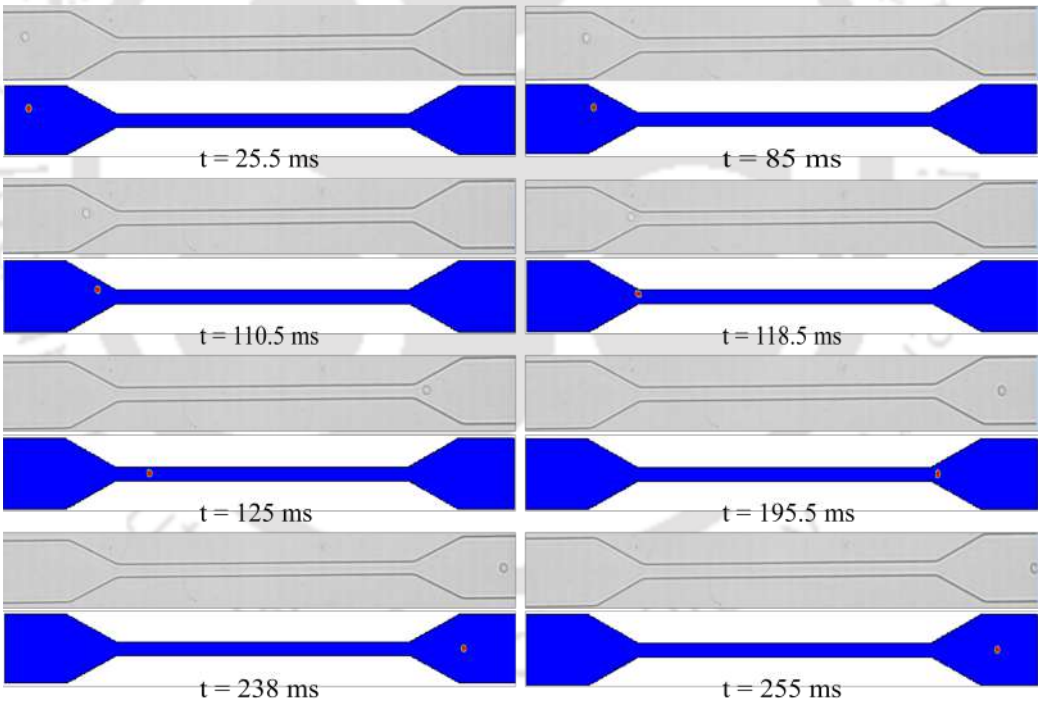

Figure 4.10: Validation map comparing the experimental and numerical results obtained for the migration of hydrogel carrier and modelled hydrogel carrier in microchannel at different instant of times

Figure 4.10 compares the experimental and numerical results obtained for the migration of hydrogel carrier and modeled hydrogel carrier in a microchannel. The comparison was based on the displacement of aggregated hydrogel carrier of diameter 4 μm at different instants of the time. As mentioned earlier, the FENE-P model was used to design a viscoelastic drop model of hydrogel particles. Each

comparison manifested experimental and numerical results of carrier displacement at the same instant. The polymeric time scale is adopted to obtain the dimensional time from the non-dimensional time in the numerical results. The validation was performed by taking a relaxation time of 850 ms for the hydrogel particle.

The modeled hydrogel particle seems to closely follow up the experimental result of the carrier displacement at time instants $t = 25.5$ ms and $t = 85$ ms. The follow-up remains the same at time instant $t = 110.5$ ms with a slight deviation from the experimental result. The modeled hydrogel particle entered the 7 μm constriction region at nearly the same time instant $t = 118.5$ ms. Noticeable deviation in displacement was seen for the modeled hydrogel particle at the time instants $t = 125$ ms and $t = 195.5$ ms. This was where hydrogel carrier particles migrated through the highly constricted region under high shear. The significant deviation and faster migration of hydrogel carrier particles may be attributed to the hydrophobic and hydrophilic nature of the PDMS channel wall and the particle, respectively. This aspect was not considered for the numerical simulations as a no-slip boundary condition was taken for the channel walls. The deviation gradually becomes less at the time instants $t = 238$ ms and $t = 255$ ms for the tapered region and the straight section region of Width 35 μm. Comparison between experimental and numerical results of the displacement versus time curve for a single hydrogel drug carrier of diameter μm is shown in Fig. 4.11.

The two-phase fluid system approach incorporated for modeling the migration of hydrogel drug carriers showed remarkable similarity with the experiment results. The displacement of FENE-P viscoelastic drop flowing in the Newtonian matrix closely followed the displacement progression of hydrogel drug carriers in the microchannel regions till the entry to the 7 μm constriction region. The noticeable deviation could be attributed to the boundary condition used for channel walls in the constriction region. The boundary condition for considering the hydrophobic-hydrophilic nature of PDMS channel wall and hydrogel particle could be useful in reducing the deviation in constriction region [162]. The deviation, however, gradually reduced when the viscoelastic drop left the constriction region. The validation results conclusively established the FENE-P viscoelastic model as a better model for modeling shear-thinning hydrogel particles. Simulation results also predicted a relaxation time of 850 ms for hydrogel particles.

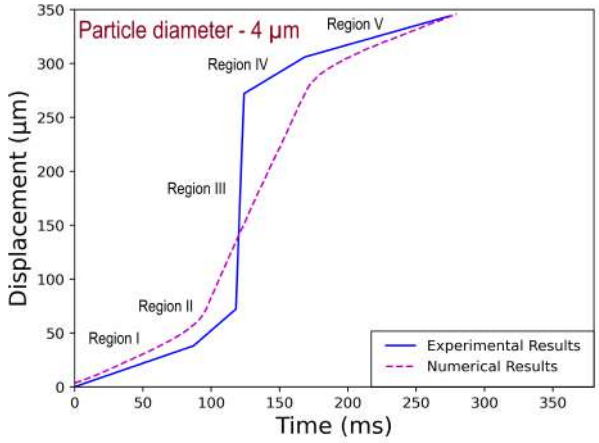

Figure 4.11: Comparison between experimental and numerical results of displacement versus time curve for the migration of single hydrogel drug carrier of diameter 4 μm with regions of microchannel marked

4.2.2 Understanding the migration tendency of cancer cell membrane-derived nanovesicles through network of micron sized channels

Undeniably, an overall understanding of cancer cell-membrane-derived nanovesicles is required to assess the future of nanovesicles-based drug delivery. One less-known aspect is the study on nanovesicle stiffness and how it behaves in the blood capillaries under high stress. As these nanovesicles also experience hydrodynamic stresses because of their flow through the constricted blood capillaries, the stress-healing tendency of nanovesicles may differ in those cases. Furthermore, the nanovesicles are also prone to aggregate due to the size of nano scales. Thus, it becomes essential to study the flow behavior of nanovesicles under micro confinement designed to mimic the branched structures of blood capillaries.

4.2.2.1 Channel design

The schematic shows the microchannel design (Fig. 4.12a). The microchannel's main structure consists of a channel of varying width with a maximum width of 184 μm of 2.85 mm in length. Four square blockages of 30 μm $\times$ 30 μm were introduced in the main passage of the channel to create branches of smaller passages of 15 μm, 12 μm, 10 μm, 12 μm, 15 μm width. The microchannel was further divided into branches of three contraction/expansion channels with sudden entry/exit. The minimum and maximum width of the contraction/expansion channel was 35 μm and 7 μm, respectively. It was prepared using the mask writing method on a silicon wafer to fabricate the microchannel pattern. Molten PDMS (Polydimethylsiloxane)

was then poured on the pattern to attain the desired structure (Fig. 4.12b). The fabrication methods are discussed in detail in Chapter 2.

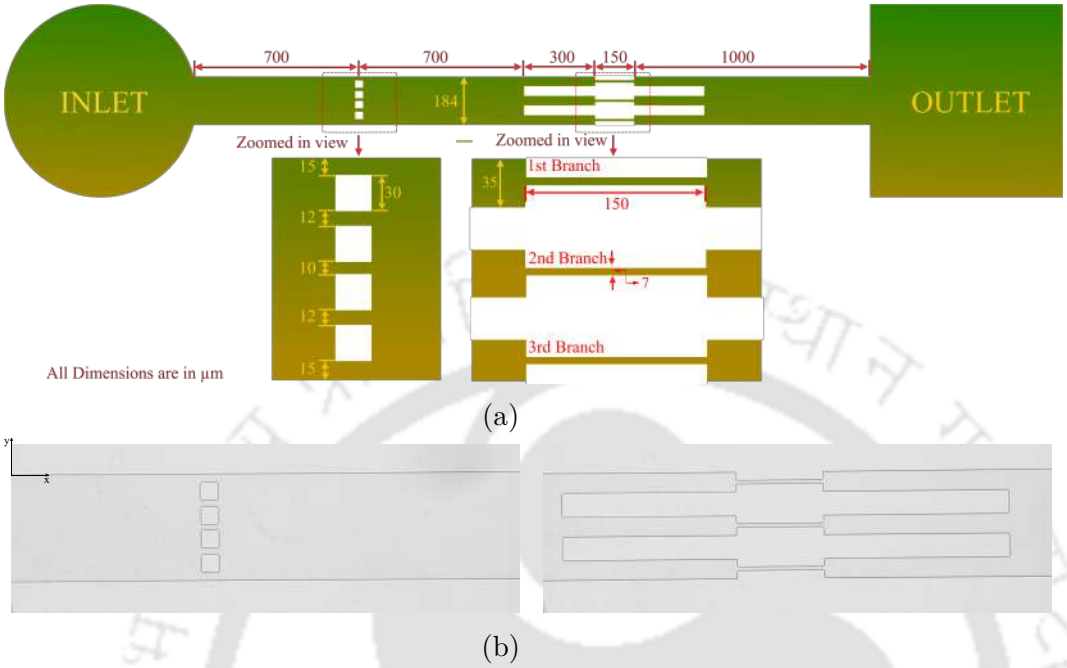

Figure 4.12: (a) Pictorial representation of branched microchannel design, (b) Branched microchannel showing the four square blockages and contraction/expansion microchannel fabricated with PDMS

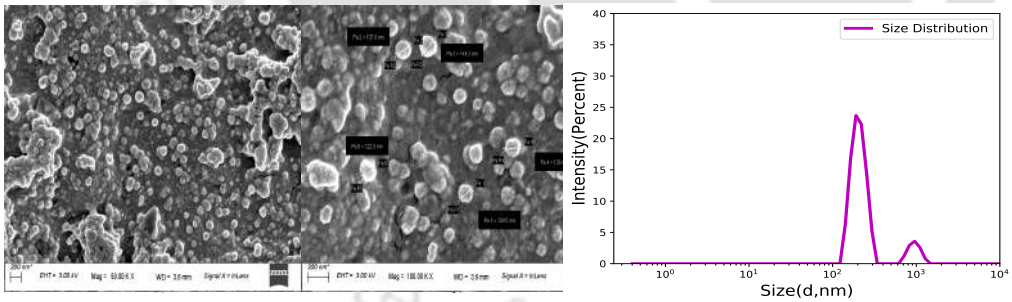

Figure 4.13: (a) Shape and size distribution of nanovesicles observed under Field Emission Scanning Electron Microscope (FESEM), (b) dynamic light scattering (DLS) study for assessment of mean hydraulic diameter of nanovesicles

4.2.2.2 Experimental setup

The microchannel was first placed under the objectives of an inverted microscope (Leica DMI 3000 M). The microchannel inlet and outlet were connected to a polyethylene intramedic semi-rigid tubing of the inner and outer diameters of 0.38 mm and 1.09 mm, respectively. A freshly prepared nanovesicle solution was allowed

to flow through the inlet tube with the help of a syringe pump from the Harvard apparatus. Nanovesicle migration was captured by a high-speed camera (Phantom-MIRO-LAB 320) at frame rates from 5000 fps to 21000 fps. The procedure for particle tracking, video analysis, and microchannel fabrication can be found in our previous studies and is discussed elaborately in Chapter 2.

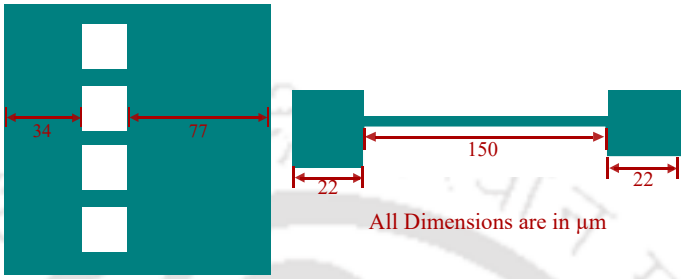

(a)

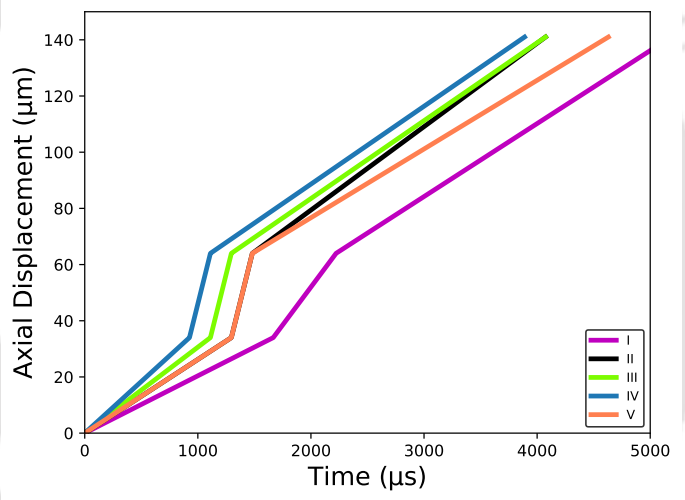

(b)

Figure 4.14: (a) Section of branched microchannel selected for deciphering nanovesicles displacement profile, (b) experimental results of displacement profile of nanovesicles flowing through 4 square blockages

4.2.2.3 Characterization of the membrane-derived nanovesicles

Characterization of nanovesicles was done to discern the distribution, size, and shape of the nanovesicles. Field Emission Scanning Electron Microscope (FESEM) images suggested mono-dispersed and aggregated nanovesicle distribution. The membrane-derived nanovesicles were discretely spherical, with their hydrodynamic diameter varying from 129 nm - 144 nm (Fig. 4.13a). The aggregated distribution of nanovesicles suggested the presence of bigger particles. Further, their size was also studied by dynamic light scattering (DLS). The DLS study suggested the presence of nanovesicles with hydrodynamic diameter varying from 141 nm - 296

nm (Fig. 4.13b) with maximum intensity percentage at a size of 190.1 nm.

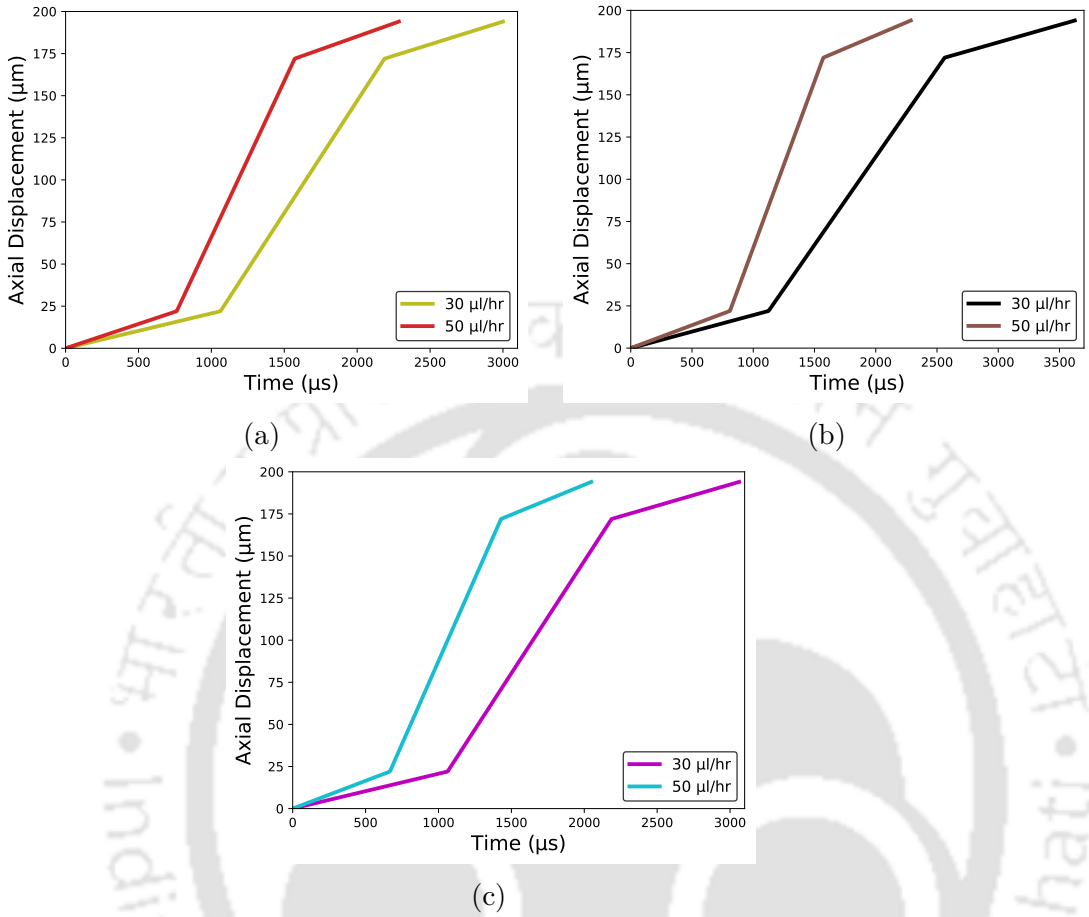

Figure 4.15: Experimental investigation of displacement profile of nanovesicles migrating through (a) 1st branch, (b) 2nd branch, (c) 3rd branch of contraction/expansion channels of 7 μm width

4.2.2.4 Migration of nanovesicles through branched channels

The previous section discussed how nano-particle migration is hindered in the microchannel due to the margination and adhesion tendency of nano-sized particles to the microchannel wall. Moreover, aggregation of nano-particles at higher flow rates also restricts the obstruction-free migration of these particles. Our studies suggested that the pressure-driven nano-particle migration inside constricted microchannels is more complex than typical miniature and macro channels. These tendencies can cause serious complications when nano-carriers flow through micron-sized blood capillaries. It was also observed that the shear-thinning and self-healing nature of hydrogels could undergo adhesion and obstruction-free migration through the 7 μm channel. Therefore, a study was carried out to observe the migration tendency of natural drug carriers like nanovesicles when subjected to microchannel networks.

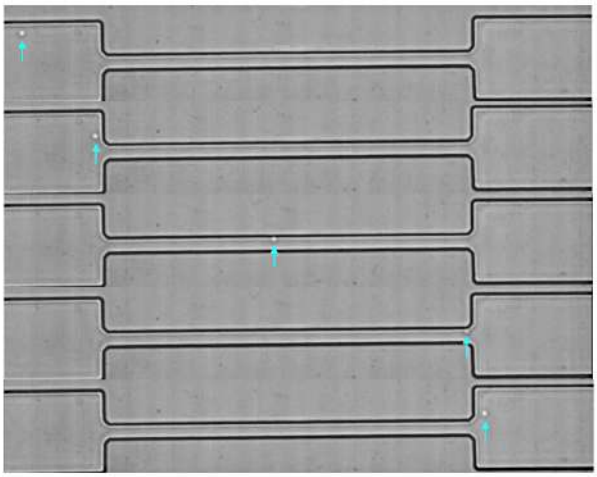

Figure 4.16: High-speed camera visualisation of migration of nanovesicles through contraction/expansion channel of 7 μm width

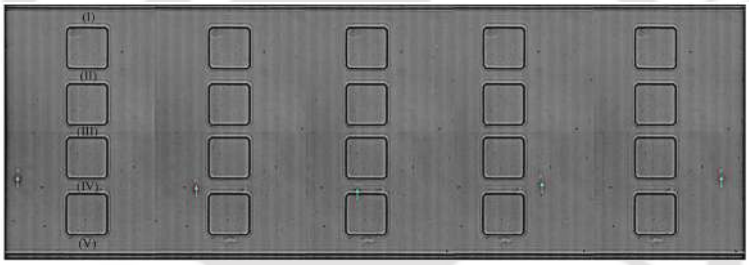

Figure 4.17: High-speed camera visualisation of nanovesicles flowing through micro passage (IV) of 12 μm width

Figure 4.16 shows the migration of spherical aggregated nanovesicles of hydraulic diameter 2.3 μm through the 7 μm channel of contraction/expansion branches of the main channel. The migration shown in Fig. 4.16 was captured at lower flow rates to present the visual representation of nanovesicle migration inside the 7 μm channel. For the present experimental study, the migration was observed at different flow rates like 30 μl/hr and 50 μl/hr to mimic the intravenous blood flow rates [163]. In the experiment, it was observed that these nanovesicles were able to successfully migrate through all the micron-sized passages (Fig. 4.17) and 7 μm contraction/expansion channels (Fig. 4.16).

Moreover, the displacement of these nanovesicles was also tracked through the 5 micro passages formed by 4 square blockages (Fig. 4.1) and through the three contraction/expansion channels of 7 μm constriction channels. The portion of the channel selected for studying the displacement profile is shown in Fig. 4.14a. The 5 micro passages are designated as I, II, III, IV, and V as shown in Fig. 4.17. The three regions of contraction/expansion channel of the width of 7 μm width selected for displacement profile study were designated sections A, B, and C of length 22 μm, 150 μm, and 22 μm, respectively. The nanovesicles appeared to

migrate faster through II, III, and IV micro passages, while a relatively slower migration was observed through micro passages I and V (Fig. 4.14b). The particle migration was slowest through the I micro passage as the blockage was nearer to the wall of the parent microchannel. The nanovesicles exhibit a similar displacement profile while migrating through all the three branches termed as 1st, 2nd, and 3rd branches of 7 μm constriction channels as shown in the plots Fig. 4.15a, Fig. 4.15b and Fig. 4.15c. They were observed to migrate slowly through the 2nd branch of the contraction/expansion channel, which represents the 2nd branch of the main microchannel at a flow rate of 30 μl/hr. At the same time, a similar kind of migration profile was observed for the other two branches nearer to the main microchannel's walls. The migration profile at 50 μl/hr was also observed, where faster migration was observed in the second and third branches of the constricted portion (Section B) of the contraction/expansion channel. The average migration velocity in each section of the contraction/expansion channel is mentioned in Table 4.2 and 4.1 for flow rates of 30 μl/hr and 50 μl/hr. The plots in Fig. 4.15a, b, c represent the mean displacement profile of nanovesicles through three branches. The data and plots in the present study represent displacement profiles of three independent experimental observations. As the measured experimental deviation is slight, deviations from the mean displacement profile are mentioned in Table 4.3 and Table 4.4 instead of showing in plots.

Table 4.1: Average migration velocity of nanovesicles in contraction/expansion channel of constriction 7 mm width at flow rate of 30 μl/hr

Section	1st branch (mm/s)	2nd branch (mm/s)	3rd branch (mm/s)
A	20.706	19.555	20.706
B	133.333	104.3478	133.333
C	27.077	20.70588	25.14286

Table 4.2: Average migration velocity of nanovesicles in contraction/expansion channel of constriction 7 mm width at flow rate of 50 μl/hr

Section	1st branch (mm/s)	2nd branch (mm/s)	3rd branch (mm/s)
A	32.992	27.170	32.992
B	196	196.829	196.829
C	35.530	30.7929	35.5

4.2.2.5 Trajectory of nanovesicles migrating through square blockages

The flow trajectories of the nanovesicles were plotted using a single particle tracking method of image processing software, Phantom Camera Controller (Fig. 4.18).

Table 4.3: Deviation from mean displacement value of nanovesicles in different sections of contraction/expansion channel at flow rate of 30 μl/hr

Section	1st branch (μm)	2nd branch (μm)	3rd branch (μm)
A	$\pm$0.398	$\pm$0.47	$\pm$0.277
B	$\pm$1.0417	$\pm$0.967	$\pm$0.49
C	$\pm$0.308	$\pm$0.398	$\pm$0.4286

Table 4.4: Deviation from mean displacement value of nanovesicles in different sections of contraction/expansion channel at flow rate of 50 μl/hr

Section	1st branch (μm)	2nd branch (μm)	3rd branch (μm)
A	$\pm$0.458	$\pm$0.706	$\pm$0.428
B	$\pm$3.676	$\pm$3.125	$\pm$3.125
C	$\pm$0.9777	$\pm$0.97	$\pm$0.507

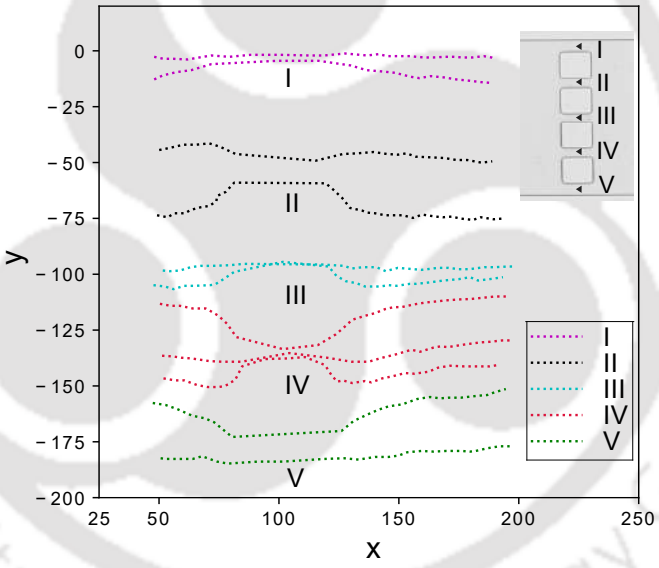

Figure 4.18: Flow trajectories of nanovesicles flowing different square blockages

The flow trajectories were observed at a 30 μl/hr flow rate. More nanovesicles were observed to flow through micro passages between III and IV for a single observation time. Interestingly, nanovesicles were also observed to migrate faster through these micropassages (Fig. 4.14b). Furthermore, nanovesicles exhibited lesser tortuous trajectories, signifying an advection-dominated flow regime. More compact trajectories were observed in nanovesicles migrating through square blockage III in the center. The close trajectories can also be attributed to the narrower width of Region III. Interestingly, nanovesicles were not observed to flow through region V near the wall of the channel. The observations were made for a single observation where nanovesicles were trackable and visible under a microscope with a 50x magnification factor. The observation can be different for

non-aggregated nanovesicles that cannot be captured and observed under bright field mode with the magnification above factor of the microscope. Nanovesicles' trajectories were not captured in the contraction/expansion channel as nanovesicles migrated very fast through the 7 μm constricted channel.

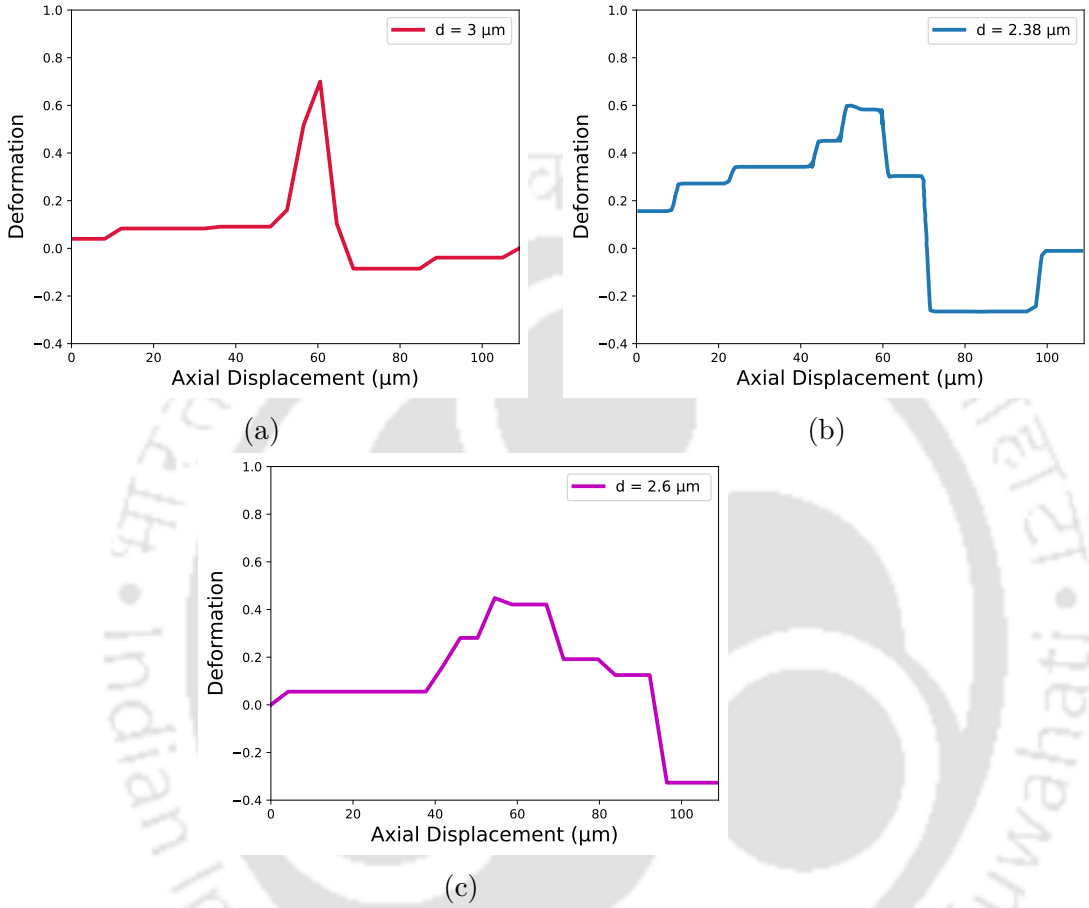

Figure 4.19: (a) Experimental results of deformation profile of nanovesicles flowing through square blockage (I) of width 12 μm, (b) deformation profile of nanovesicles flowing through square blockage (II) of width 12 μm, (c) deformation profile of nanovesicles flowing through square blockage (III) of width 10 μm

4.2.2.6 Deformation of aggregated nanovesicles

In addition, to track the nanovesicles' migration, it was also deciphered how the aggregated nanovesicles deform while migrating through micron-sized flow blockages in the parent microchannel. To study the deformation behavior, the deformation of aggregated nanovesicles of diameter 3 μm (Fig. 4.19a), 2.6 μm (Fig. 4.19c) and 2.38 μm (Fig. 4.19b) were tracked. The aggregated nanovesicles migrated through micropassages I, II, and III. It was observed that nanovesicles could undergo appreciable deformation to migrate successfully through the flow passages of micron size. Maximum deformation was observed for 3 μm aggregated

nanovesicles, while 2.6 μm showed lesser values of the deformation parameter. The maximum and minimum value of deformation parameters is shown in Table. 4.5. The observations suggested that the bigger aggregated nanovesicles exhibit a better tendency to deform. Interestingly, 2.33 μm nanovesicles showed a higher value of deformation parameter than that of 2.6 μm sized nanovesicles. The higher deformation of the smaller nanovesicles was attributed to their faster migration through blockage II than III, as shown in Fig. 4.14b. A more interesting observation was made when these nanovesicles underwent deformation in a transverse direction while coming out of the micro passages. The nanovesicles of 3 μm showed the least deformation, while nanovesicles with 2.33 μm showed maximum deformation in the flow direction at the exit of the micropasasages. The observation suggested that the aggregated nanovesicles showed faster stress recovery and shape-regaining tendency when stresses were removed from them. Furthermore, smaller aggregated nanovesicles required more time to regain the initial shape Fig 4.19. It can also be validated that deformation in the cross-flow direction is higher in regions where nanovesicles showed faster migration. Faster migration of nanovesicles restricted faster elastic recovery. The elastic recovery can be crucial for efficiently delivering drugs by nanovesicles. Delayed shape regain can also lead to premature drug release by these nanovesicles. Nanovesicles are derived from cancer cell membranes and lack structural integrity like other nanocarriers or cells. As a result, they exhibit a limited tendency for elastic recovery, while larger aggregated nanovesicles showed faster elastic recovery. Deformation was calculated by using the relation given below,

$$\text{Deformation} = \frac{x_a - x_b}{x_a + x_b} \tag{4.2}$$

where x_a and x_b are the maximum particle dimensions in x and y directions.

Table 4.5: Maximum and minimum deformation of nanovesicles

Deformation	Blockage I	Blockage II	Blockage III
Maximum	0.6999	0.599	0.448
Minimum	-0.0853	-0.265	-0.3268

4.3 Summary

In the work discussed in this chapter, experimental and numerical investigations to decipher the self-healing properties of hydrogel particles that underwent migration through a constricted microchannel without having adhered to the channel walls. The particles regained their physical structure after undergoing migration. The

study revealed self-healing hydrogel nanocarriers' high load-carrying and elastic recovery characteristics. The aggregation of hydrogel particles restricted the decay of nanocarriers. The nanocarriers demonstrated longer retention of Doxorubicin with sustained drug release. The mathematical model of the shear-thinning nanocarriers manifested remarkable insight into particle-squeezing inside microcapillaries. Additionally, an investigation was done to understand the flow behavior and deformation of the cellular nanovesicles through branches of contraction/expansion microchannels designed to mimic the human blood capillary networks. Thus, the study was done to prove the relative quantification of the nanovesicle deformities, which had not been reported earlier. Hydrogel carriers showed better structural healing and mechanical strength than nanovesicles, while nanovesicles are more bio-compatible than hydrogel carriers. It has to be noted that both carriers showed sufficient deformation for successful squeezing through 7 μm microchannel. The experimental and numerical results can be further employed to design complex microfluidic devices for studying drug delivery through brain capillaries, blood-brain-barrier, and other intricate human body areas.

5

Transport behaviour of commercial anti-cancer drug protein-bound paclitaxel (Paclicad) in blood capillary sized microchannel

Protein-bound Paclitaxel has been developed clinically as one of the most successful chemotherapy drugs for treating various cancers. However, due to their nanoscale properties, these medications may often induce capillary blocking while migrating through minute blood vessels. Considering the detrimental impact of this restriction, the transport of protein-bound Paclitaxel in a 7 μm microchannel mimicking the identical mechanical condition of the blood capillaries was investigated. The chemotherapeutic drug was reported to migrate through a constricted microchannel without obstruction at a solution flow rate of 20 μl/hr – 50 μl/hr. The onset of the agglomerated site was observed at higher flow rates of 70 μl/hr – 90 μl/hr, while complete capillary obstruction was observed at 100 μl/hr. The mobility of the particles was also calculated, and the results suggested that varying cross-sections affect the mobility of the drug particles. The trajectory of the particle migration was observed to be less tortuous at the higher flow rate. However, the tortuous nature increased with agglomerated sites in the flow field. The present experimental results provide better insight into the agglomeration tendency of protein-bound Paclitaxel when it underwent the high shear flow inside a constricted microchannel at higher flow rates. The numerical model could be further employed to model the drug particle migration for more complex intravenous transport of drugs.

5.1 Introduction

The anti-cancer drugs' performance and efficiency depend on the drug's transport in the blood vessel and the penetration of the drug into the tumor site. On

the other hand, the drug's transport mechanism depends on plasma and blood pharmacokinetics [164], pharmacodynamics, and transport properties of drugs. Both convection and diffusion processes carry out the mass transport of drugs across blood vessels and penetration into tissue [165]. The microvascular structure of the tumor also plays a vital role in drug transport in circulation and through extravascular space. The drug's size, charge, lipid solubility, and acid-based characteristics determine the tumor-invading potential. Investigating the transport behavior of commercially available chemotherapy drugs in microcapillaries can give better insights into the unknown attributes of intravenous delivery of drugs. Among the most prominent anti-cancer drugs, Paclitaxel is established as the primary drug for the treatment of metastatic breast cancer [166]. Paclitaxel creates cytotoxicity and mitotic arrest of proliferating tumor cells by hyperstabilization of polymerized microtubules [167]. Being naturally hydrophobic [168], Paclitaxel has poor water solubility, requiring a synthetic solvent for delivery and stabilization. Paclitaxel is constituted with castor oil (cremophor), which significantly reduces Paclitaxel efficiency. Cremophor entraps active drugs in micelles formed in plasma, which significantly disturbs the pharmacokinetics of Paclitaxel. Even increasing the dose of synthetic solvent-based Paclitaxel does not help. Instead, it causes a severe risk of side effects [169]. Besides, the solvent is also toxic, sometimes bringing susceptible reactions [170]. Given such limitations, a solvent-free protein-bound Paclitaxel was commercially approved for metastatic breast cancer [171], melanoma, pancreatic cancer [172], and lung cancer treatment. The protein-bound Paclitaxel shows a significant anti-tumor effect [173], as it significantly reduces toxicity related to cremophor solvent and improves Paclitaxel efficiency [174, 175]. Besides, in most recent advancements, protein-bound Paclitaxel is also used for cancer chemo-immunotherapy [176]. As the protein consists of both polar and non-polar sequences of amino acids, they exhibit amphipathic behavior. The non-polar region can bind the hydrophobic drug Paclitaxel, while the polar region can be favorable for transport in hydrophilic solvents.

Although the protein envelope of Paclitaxel provides efficiency and stabilization to the drug, other complex interactions also arise with the transport of the drug, due to its protein envelope. The complex interactions include protein adsorption to the surface [177] and protein aggregation [178] during intravenous transport of these particles. Protein adsorption is prevalent for both metal [179] and polymer surface [180], so it plays a vital role in theranostics, biochemicals, and surgical processes. Various complex interactions involving different forces can lead to protein adsorption. The forces include electrostatic interaction between charged amino acid side chains and surface [181], hydrogen bonding between amino acids with water

[182], and hydrophobic interactions in hydrophilic medium [183]. Besides, other factors like temperature [184] and the presence of multiple proteins in the same system [185] also influence protein adsorption. Furthermore, protein adsorption can become more crucial in bio-microfluidics-based studies, as the PDMS surface is very prone to protein adsorption, resulting in various complex outcomes. Protein aggregation is also an intricate phenomenon when the protein folds itself to acquire a thermodynamically favorable shape [186]. The phenomenon is influenced by the tendency of a non-polar (hydrophobic) portion of protein to fold itself to avoid the hydrophilic surroundings. The protein aggregation is further aggravated by various environmental factors, like pH, temperature, and oxidative stress [187]. These external factors can be attributed to the changes brought due to mutations [184] or various diseases [188]. Although protein aggregation due to folding will not be prominent with protein-bound Paclitaxel, it's understanding of protein adsorption can give better insight into the intravenous transport of these drug particles and whether this transport is prone to agglomeration inside the adverse mechanical environment of blood capillaries.

Considering studies involving intravenous transport of particles, polydimethylsiloxane-based (PDMS-based) microchannels are the most sought-after devices for replicating human capillaries. Solid PDMS walls are elastic and supposed to be most effective for mimicking human capillaries [189]. PDMS-based microfluidic devices can control the physical parameters like cell elasticity, cell size, pressure, and constriction size prevailing for human cells. Furthermore, the microchannnels are also used previously for other intravenous migration studies [190, 191]. Au et al. [84] studied the migration of clustering tumor cells through capillary-sized vessels modeled as a microchannel; in further study, Nath et al. [140] fabricated a PDMS microchannel to model the migration of HeLa cells during cancer metastasis. In other studies, confined flow migration was also studied for deciphering the drug-resistant behavior of metastatic EMT breast cancer cells [192]. Most of these studies involved the transport of cancer cells and human cells through confined microchannels, but studies involving the migration of drug carriers and drug particles about the size of nano scales are still inadequate. Hazra et al. [193] elucidated the dynamics of microparticle undergoing confined flow in a shear-thinning viscoelastic fluid at low Reynolds number in a 60 μm microchannel for better particle focusing and manipulation in biological fluids. However, an additional aspect needs to be considered while studying nanoparticle transport, as it tends to undergo agglomeration owing to its high surface energy [194]. Aggregated particles in a flow field significantly influence the flow characteristics [195] inside a confined domain. Furthermore, an interfacial jamming of nanoparticles also seemed to cause hindrance to the droplet

transport inside a confined microchannel [196]. In the context of the protein-bound Paclitaxel, owing to its nanoscale size, with the tendency of protein adsorption on PDMS surface [40], make it more susceptible to aggregation in a constricted microfluidic channel, and it needs to be investigated.

As mentioned previously, external environmental factors like pH, temperature, and oxidative stresses can affect protein aggregation and adsorption. However, mechanical confinement's effect on protein aggregation still needs to be studied. Thus, in the present study, the transport of a commercial protein-bound Paclitaxel, Paclicad, undergoing high shear flow through a mechanically adverse environment inside a constricted microchannel will be investigated. A square channel with a width of 7 μm microchannel was fabricated for the study to replicate blood capillaries' mechanical confinement. Landau and Davis [197], in their study for determining conjunctival capillaries of patients with diastolic hypertension, observed the diameter of capillaries lie between 5 – 12 μm and stated that this range could be applied for most of the human capillaries. The microchannel was fabricated using PDMS as a material. The migration was observed at different flow rates to examine whether the increase in flow rate or increasing shear in flow can lead to particle aggregation and, eventually, capillary obstruction. Desai et al. [105] suggested that albumin-bound paclitaxel of average size 130 nm shows less tendency of capillary obstruction. A computational model was also developed to examine the viscoelastic nature of the particle. Although commercially approved, the transport mechanism of such drugs inside microcapillaries still needs to be discovered. For better efficiency, the drug must undergo obstruction-free circulation in micro capillaries.

5.2 Results and discussion

5.2.1 Characterization of Paclicad particles

The hydrodynamic diameter of the Paclicad particles was recorded using a dynamic light scattering analyzer (Malvern Zetasizer Nano ZS-90). Measurements were recorded while keeping the sample in PBS buffer at 25 °C. The zeta potential study was done using Zetasizer by Malvern Panalytical. The measurement was done with the sample solution at 25 °C. JOEL JAM 2100F. TEM with an operating voltage of 200 kV was used to analyze the size of the Paclicad particles. Before taking the measurement, a freshly prepared sample of Paclicad particles was drop-cast on a carbon-coated copper grid and dried in a desiccator overnight. FESEM analysis of the Paclicad particles was carried out using JOEL JSM-7610F Schottky Field

Emission Scanning Electron Microscope. A dirt-free, freshly prepared sample was drop cast on an aluminum foil-coated glass slide and dried using a desiccator overnight. Samples were coated with gold film using a sputter coater (SC 7620 Mini, Polaron Q Sputter Coater). The shape and size distribution of Paclicad particles were observed and confirmed by thorough analysis. The particles were observed to be spherical and monodispersed in nature when viewed under Field Emission Transmission Electron Microscope (FETEM) and Field Emission Scanning Electron Microscope (FESEM), as shown in Fig. 5.1a and Fig. 5.1b, respectively. The particle distribution was also observed under a confocal microscope. The distribution of aggregated Paclicad particles was observed under fluorescent mode (Fig. 5.1c(i)), bright field mode (Fig. 5.1c(ii)) and in merged mode (Fig. 5.1ciii). The mean hydrodynamic diameter of Paclicad particles was deciphered by a Dynamic Light Scattering study (Fig. 5.1d), where the highest intensity was observed for the particles with a hydrodynamic diameter of about 142 nm, while the size distribution range of the particle diameter was from 80 nm - 290 nm. The size distribution of the Paclicad particles was further determined by FESEM and FETEM analysis. The mean hydrodynamic diameter was 132 $\pm$ 30 nm and 138 $\pm$ 40 nm, observed under FETEM and FESEM, respectively. Our size analysis matched the commercial standard size of the protein-bound Paclitaxel, 130 nm. The Zeta potential study suggested that the particles were negatively charged, with zeta potential ranging from -5 mV to -43 mV, with a significant count of the particles showing zeta potential of -27 mv (Fig. 5.1e).

To summarize, characterization revealed the spherical and monodispersed nature of the particles, with their hydrodynamic diameter ranging from 80 nm to 290 nm, which was within the commercial standard size of the protein-bound Paclitaxel. The particles were also observed to be negatively charged, with the zeta potential ranging from -5mV to -43mV. The negative charge on the particles explained the amphipathic nature of the protein surface. The charged surface allows it to be dissolved in a polar hydrophilic solvent, while the non-charged inner core can bind the non-polar hydrophobic drug.

5.2.1.1 Experiment reproducibility and data information

All experimental results presented in the current study are representations of at least three independent experiments, and the results are reproducible. It is also mentioned here that the particle does not always start at the same vertical position during the flow process of different experiments, so the particle displacement profile is not the exact repetition of the previous experiment; however, the trend is always similar. Given this, the present results depicted the trend of particle displacement

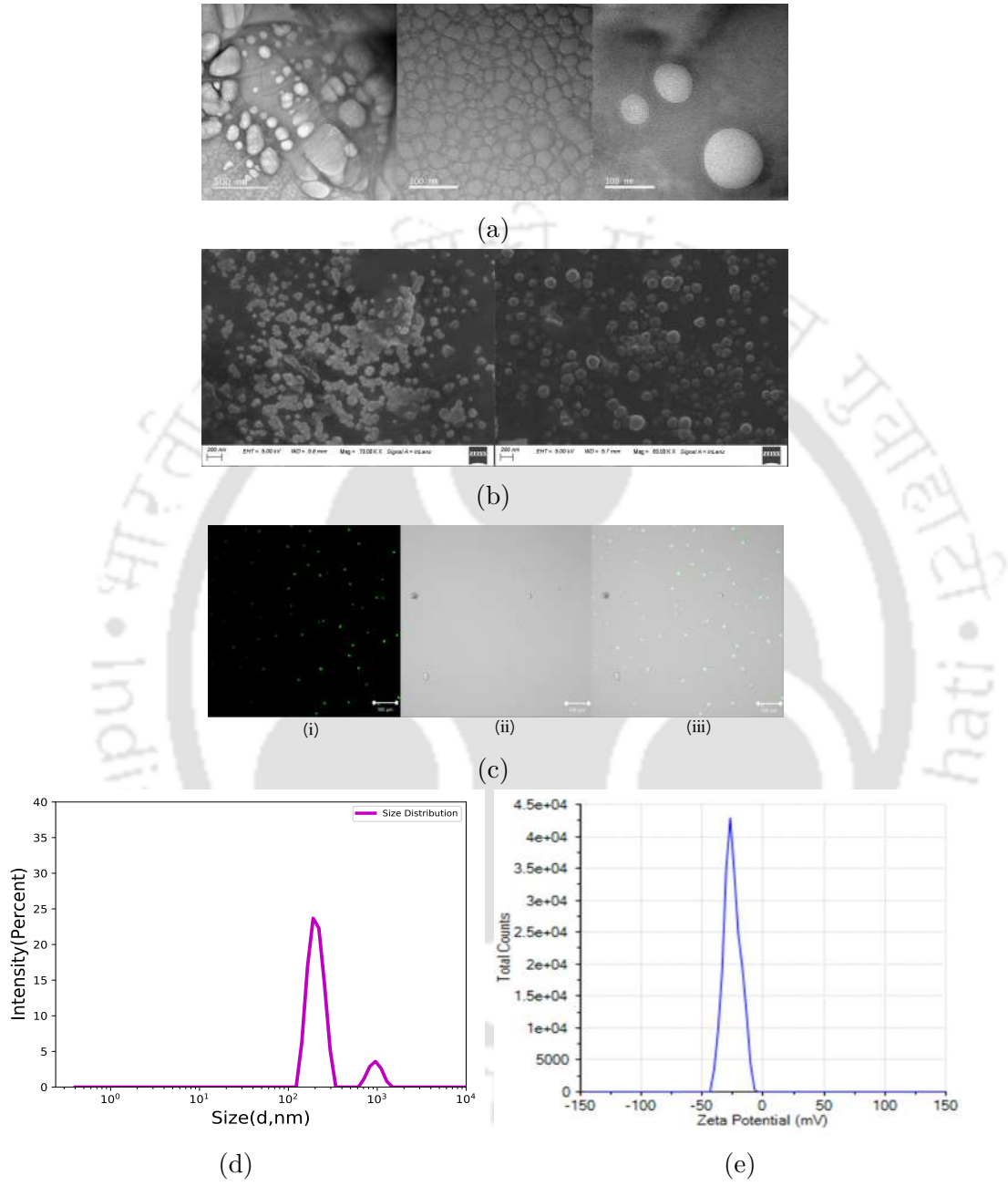

Figure 5.1: Characterization of Paclicad particles, (a) size and distribution of Paclicad particles recorded under Field Emission Transmission Electron Microscope, (b) characterization of Paclicad particles viewed under Field Emisssion Scanning Electron Microscope, (c) confocal microscope images of Paclicad particles (i) fluorescent mode, (ii) bright field mode, (iii) merged mode, (d) size distribution of Paclicad particle measured by Dynamic Light Scattering method, (e) the zeta potential distribution of Paclicad particles by zetasizer

for different experimental observations. The plot (Fig. 5.2d) showed the variation in the particle displacement values, where the displacement is measured from the centerline and near the wall region of the channel. A maximum variation of 9 mm/s in particle velocity was observed in the constricted region (III), while a minimum variation of 6.4 mm/s was observed in the straight section (I). Depending on flow symmetry, the average migration velocity of every particle in different sets of experiments was within the range of values presented for the centerline and near-wall region. Furthermore, the experiments were performed with fresh microchannels to avoid errors in measurement from any trace amount of drugs.

5.2.2 Paclicad particles migrating through 7 μm microchannel

The transport of Paclicad drug particles was studied experimentally in a microchannel of the design shown in Fig. 4.1. The transport behavior of the drug was observed under a microscope, with the objective having a 50x magnification factor. The flow was captured using a high-speed camera at the frame rate of 5000 - 12000 fps. The portion of channel under observation is shown in Fig. 5.2b, which has 34 μm long straight (I) and converging section (II) each, 200 μm extended constriction region (III) of 7 μm width and 34 μm long diverging (IV) and straight section (V) each. The experiment observation section was chosen so as to converge our area of interest to examine the most crucial capillary transport of the drugs. A sample of the nano-constituted drug Paclicad, an injectable protein-bound Paclitaxel, was prepared and allowed to pass through the microchannel. The migration of a small group of Paclicad particles of size 870 nm was captured under a high-speed camera. For a better flow visualization, the migration of a small group of Paclicad particles behaving as a single particle (enclosed in a red circle) through the constricted region of the microchannel is shown in Fig. 5.2a. As the flow actuated with a flow rate of 30 μl/hr, the drug particle seemed to flow through the converging and diverging sections without indicating particle aggregation and adhering to the wall. The flow tendency did not change while undergoing high shear flow in the 7 μm constricted region. As the flow rate was set according to the intravenous flow speed of the blood, the commercial drug did not cause capillary obstruction and successfully migrated through the 30 μl/hr microchannel. The drug's displacement vs time plot with average transition velocity values in each microchannel region is shown in Fig. 5.2c.

The displacement was tracked for a single Paclicad particle passing through the center region of the channel. The axial displacement and migration velocity are

calculated using Eq. 2.2. The displacement vs. time results differed for particles migrating through different vertical distances of the channel. The deviation in displacement vs time plot for the Paclicad particle migrating through the centerline and near wall region is shown in Fig. 5.2d. The displacement vs time characteristics of particles migrating at different vertical positions are expected to lie between the centerline and near wall region.

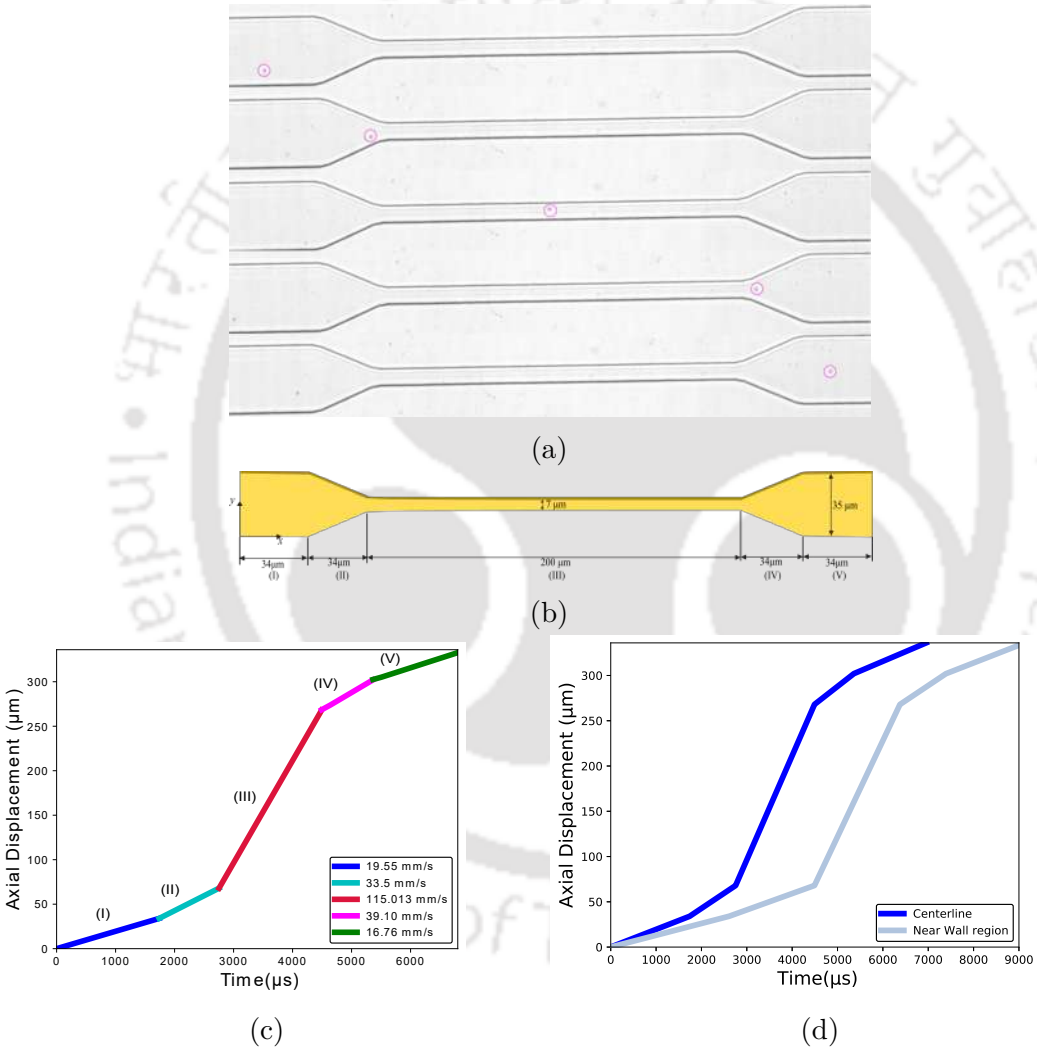

Figure 5.2: Experimental results of (a) migration of a group of Paclicad particles through constricted microchannel at 30 μl/hr captured by High Speed Camera, (b) the portion of the microchannel selected as the domain for the experimental study, (c) displacement versus Time curve for the Paclicad particle migration through different regions of microchannel, (d) plot showing the displacement vs time curve of the Paclicad particle measured at different initial vertical position in microchannel

5.2.3 Migration behavior of Paclicad particles at different flow rates

In order to further examine the flow rate dependency on the migration of Paclicad particles, experimental observation was also made at different flow rates of 20 μl/hr, 50 μl/hr, 70 μl/hr, 90 μl/hr, and 100 μl/hr. The obstruction-free migration behavior at flow rates of 20 μl/hr and 50 μl/hr was observed, and the regime was similar to that explained for 30 μl/hr. However, the emergence of drug aggregation was witnessed at flow rates higher than 50 μl/hr. The outcome of nanoclusters and wall adhering was seen at the exit of the constriction region at the flow rate of 70 μl/hr (Fig. 5.3a). The observed aggregation can significantly obstruct the flow, causing changes in particle flow behavior. As the bulk flow rate increased, the number of aggregated sites also increased in the different regions of the microchannel, finally causing the aggregated site to develop at the entry of 7 μm constricted region, causing complete flow blockage at a flow rate of 100 μl/hr (Fig. 5.3b). Furthermore, aggregated drug particles were also observed to adhere to the channel walls. The blockage in the converging zone was gradually removed under the flow pressure, and aggregated drug particles migrated through the constricted portion. A crucial observation of capillary obstruction by Paclicad drug particles was observed at the increased bulk flow rate.

(a)

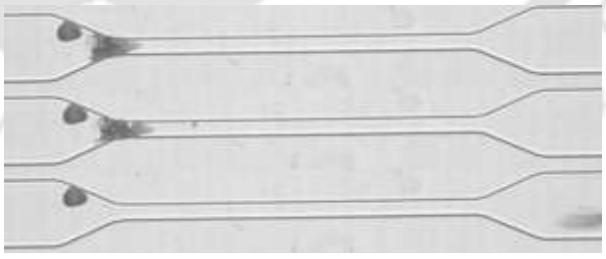

(b)

Figure 5.3: Experimental observation of migration of Paclicad particles and presence of agglomerated sites at different flow rate above 50 μl/hr (a) presence of agglomerated site of Paclicad particles at flow rate of 70 μl/hr, (b) capillary obstruction by agglomerated particles at the flow rates of 100 μl/hr

The displacement vs time plot of the drug particles migrating through the centerline region of the microchannel at different flow rates is shown in Fig. 5.4. The displacement vs. time plots shifted towards the left as the flow rate increased, with the particle undergoing habitual faster migration at a higher flow rate. The

particle migration becomes significantly faster for a flow rate of more than 20 μl/hr as the curve becomes steeper with the flow rate increase. As there were particle aggregated sites at the exit of the constriction region for particle migration at flow rate 70 μl/hr (Fig. 5.3a). Owing to the decrease in available flow area caused by the aggregation site, the particle seemed to migrate very fast through the diverging section (Region IV), as shown with a very steep curve for the respective region in Fig. 5.4. The average velocities of particles migrating through different regions of microchannel at different flow rates are presented in Table 5.1. The displacement vs. time curve at flow rates of 90 μl/hr and 100 μl/hr were not presented as there were events of capillary obstruction at these flow rates.

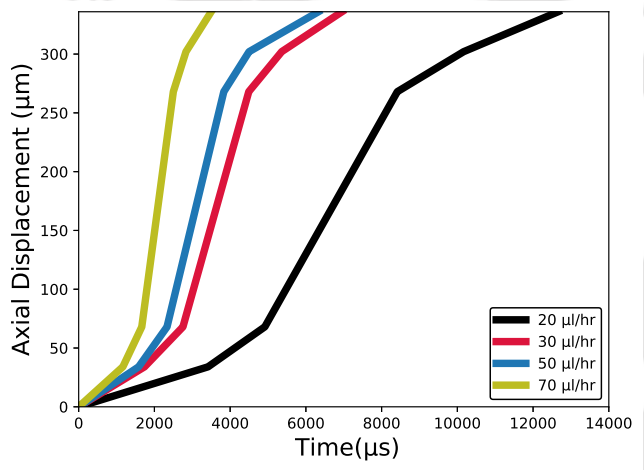

Figure 5.4: Experimental results of displacement versus time curve for Paclicad particle measured for different flow rates

Table 5.1: Average migration velocity of Paclicad particle in different section of microchannel for different flow rates

Flow rate (μl/hr)	I (mm/s)	II (mm/s)	III (mm/s)	IV (mm/s)	V (mm/s)
20	9.952	22.66	57.15	19.43	13.6
30	19.55	33.5	115.013	39.10	16.76
50	21.557	45.3	133.354	51.00	18.00
70	29.14	60	240	102	51.00

The charged surface of Paclicad particles makes the solution stable and provides an unfavorable environment for aggregation. However, even the charge coating makes particles repel each other and restricts aggregation, although Paclicad aggregations were observed when the solution flow rate increased. The experimental observation showed that the particles could restrict the agglomeration and successfully transport through a 7 μm constricted channel at a low solution flow rate of up to 50 μl/hr. However, as the flow rate increases, an outcome of particle agglomeration appears

at a flow rate of around 70 μl/hr. The particle aggregation tendency increased with flow rate, causing capillary obstruction at a flow rate of 100 μl/hr. In addition, the presence of blood cells plays a vital role in the margination and adhesion of microparticles inside blood vessels, as reported by D'Apolito et al. [198, 199]. Furthermore, numerical reports by Muller et al. [156] and Doshi et al. [200] suggested that the shape, size, and geometries also affect the margination of micro and nanoparticles in blood flow. However, for the present study, particular attention was given to only observing the transport of drug particles. Additionally, the effect of mechanical stress on the aggregation of the drug above particles during transport was investigated.

To decipher the aggregation of the protein surface, the interaction between protein surfaces [201] or, more precisely, the interaction between the nanoparticles was explored. The theory of maximum entropy of mixing principle provides a better insight into aggregation distribution of weakly interacting nanoparticles [202]. In this context, a broader explanation for the aggregation of particles in the liquid medium could be given by Derjaguin-Landau-Verway-Overbeek (DLVO) theory [203]. The theory states that the net interaction between the particles is contributed by the van der Waals attraction force and repulsion potential caused by electric double-layer forces between two charged particles. The net interaction energy between the particles is the total of the van der Waals interaction energy and double layer interaction energy. The van der Waals interaction energy can be found out by Hamaker expression [204] and electric double layer interaction energy between two spheres is given by the expression by Bhattacharjee et al. [205]. For the solution to be stable and non-aggregating, a repulsion potential must dominate over the attraction potential. Net interaction energy should not cross the energy barrier for aggregation. The theory is also extended for the interacting particles with rough surface [205]. The theory explains the interaction of particles in the Brownian regime when the dominance of advection and shear rate is not considered. When the particles interact while undergoing transport under shear flow, the shear rate affects the energy barrier. Zaccone et al. [206] studied the effect of shear rate on the potential barrier for two-particle aggregation and gave the relation of rate constant $k_{1,1}$,

$$k_{1,1} = \sqrt{\frac{3\pi\alpha\mu\dot{\gamma}a^3 - U_m''}{k_B T}} e^{-\frac{U_m - 6\pi\alpha\mu\dot{\gamma}a^3}{k_B T}} \tag{5.1}$$

where, U_m is the maximum interaction potential, $\dot{\gamma}$ is the shear rate, α is the numerical coefficient which is for simple shear is $\alpha = \frac{1}{3\pi}$, μ is the dynamic viscosity of the solvent, a is the particle radius, k_b is the Boltzmann constant. The Equation

5.1 is in the form of Arrhenius equation where, $\sqrt{\frac{3\pi\alpha\mu\dot{\gamma}a^3-U_m''}{k_BT}}$ is the frequency factor and $\frac{U_m-6\pi\alpha\mu\dot{\gamma}a^3}{k_BT}$ is the activation energy. It can be found from the given equation that with the increase of shear rate ($\dot{\gamma}$), the activation energy decreases, and the frequency of collision of the particles increases. The increase in shear rate profoundly affects the particle's ability to cross the energy barrier and causes particle aggregation. This explains particle aggregation in the present experiment at a higher flow rate, allowing particles to overcome the energy barrier at the higher shear rate and get aggregated. The following relation can also determine the time required for aggregation to happen,

$$t_a \sim \frac{1}{k_{1,1}} \sim \frac{1}{\sqrt{\frac{3\pi\alpha\mu\dot{\gamma}a^3-U_m''}{k_BT}}} e^{\frac{U_m-6\pi\alpha\mu\dot{\gamma}a^3}{k_BT}} \tag{5.2}$$

From the given equation, it can be found out that aggregation time decreases with the increase in particle radius, so for the larger particle the solution will be stable for the lesser time.

Earlier, Sicignano et el. [207] also reported the effect of shear flow on aggregation of micron size particle as a result of catalytic chemical reaction. They suggested that aggregation was created when the microparticles adhered to wall at relatively higher Reynolds number when frequency of collision of particles increased with the wall surface and that further lead to aggregation of other particles. Although they only reported the study for Reynolds number, 5 and 15. While, it was observed that particles aggregate to each other with or without adhesion to wall, when they undergo high shear flow and the tendency increases with increase in flow rate. Besides, the presence of Red blood cells also influence the shear induced diffusion of microparticles [208], and presence of RBCs tend to slow the shear induced diffusion process as reported by Vahidkhah et al. [209]. But they made the observation under constant shear rate flow, and not under pressure driven flow that actually prevail in blood vessels of human body. In the present study, the flow of blood cells was not considered in order to gain insight into the transport of drug particle only under a pressure driven flow.

The particle aggregation can be controlled and stabilized by using surfactants and macromolecular surface coatings. Nanoparticle aggregation occurs when particle surfaces come in contact with each other and thermodynamic interactions between them cause particles to attach together [210]. Surfactants are adsorbed on nanoparticles surface to prevent aggregation by reducing interfacial energy between particle and solvent [211]. Furthermore, increasing hydrophobicity of the protein surface can restrict the protein aggregation [212]. But the method can

not be effective for polar solvent and increased hydrophibicity can pose additional restrictions other than aggregation.

5.2.4 Mobility and trajectory of the Paclicad particles at different flow rate

In the furtherance of the study, the transport behavior of Paclicad particles was investigated by studying their mobility and trajectories at different flow rates. The particle's mobility determines the particle's proficient movement concerning bulk flow. The present section examined the Paclicad particles' mobility at three different flow rates of 20 μl/hr, 30 μl/hr, and 50 μl/hr. As the flow field was obstructed due to the agglomerated site at a flow rate of 70 μl/hr and the flow rate above it, the mobility was only calculated for these flow rates. Mobility of the Paclicad particles in different regions of the microchannel and at three different flow rates is shown in Fig. 5.5. The mobility of the particle was observed to be less in the converging (Region II) and diverging regions (III) than in the straight regions of the channel, resulting in the zig-zag pattern of mobility for all three flow rates. The mobility values seemed higher for the constriction region (Region III) and exit straight section. (Region V) for flow rate 20 μl/hr and 30 μl/hr and only for constriction region for flow rate 50 μl/hr. The less mobility at the converging and diverging sections provides better insight into the less proficient movement of particles relative to the bulk flow in the region with varying cross-section areas. Furthermore, the mobility values were observed to be less for particle migration at 50 μl/hr; the observation may suggest the early signs of the emergence of particle aggregation that eventually resulted in the formation of aggregated sites at the exit of the constriction region at a flow rate of 70 μl/hr. Table 5.2 shows the mobility values for three flow rates.

Table 5.2: Mobility of Paclicad particles measured for different regions of microchannel for flow rates 20, 30 and 50 μl/hr

Mobility (Region)	20 (μl/hr)	30 (μl/hr)	50 (μl/hr)
I	0.4392	0.575	0.380
II	0.3332	0.32875	0.267
III	0.5075	0.675	0.473
IV	0.279	0.383	0.3
V	0.599	0.599	0.318

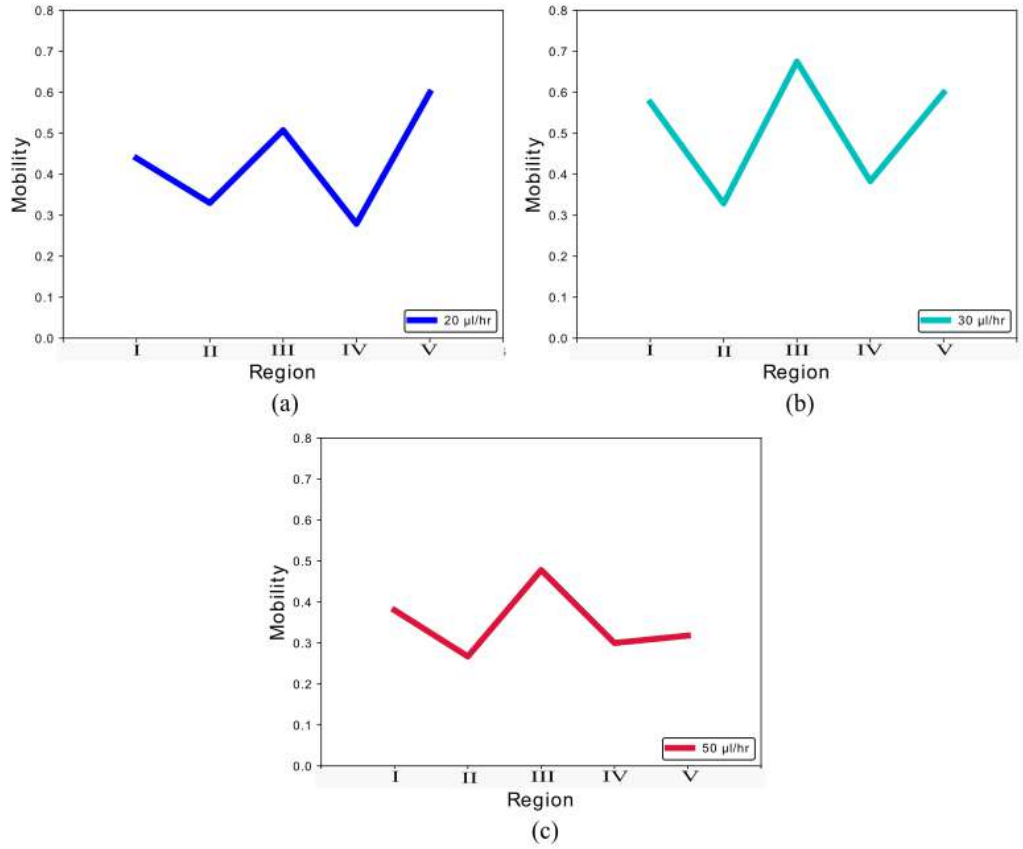

Figure 5.5: Plot showing the experimental results of mobility of Paclicad particles in different regions of microchannel for flow rate, (a) 20 μl/hr, (b) 30 μl/hr , (c) 50 μl/hr.

Considering the 7 μm constriction region as the major checkpoint for flow blockage by particle agglomeration, the trajectory at the regions ahead of the constriction region was studied. The phenomenon happening in that region could be the major reason leading to flow blocking. Thus, trajectories of Paclicad particles at different flow rates were investigated. Figure 5.6 shows the particle trajectory at flow rate 1 μl/hr, 20, μl/hr, 30 μl/hr, 50 μl/hr, 70 μl/hr, and 90 μl/hr in the Regions I and II. The particle trajectory at flow rate 1 μl/hr seemed to be more tortuous in the straight section. At the same time, it was less tortuous for the converging section, and the particle also tended to drift toward the microchannel wall. A similar trajectory was observed for particle migration at 20 μl/hr but with a lesser tortuous trajectory than 1 μl/hr. A relatively straighter trajectory was discerned for a flow rate of 30 μl/hr, but the tendency of wall drifting remained at this flow rate. The tortuous trajectory suggested a diffusion-dominated transport of Paclicad particles at the flow above rates. A significant decrease in tortuous nature was observed at a flow rate of 50 μl/hr, where the particles underwent migration with a straight trajectory without wall drifting tendency. The observation suggested an

advection-dominated transport of the particle at a higher flow rate, resulting in a straighter trajectory of the particles. An emergence of tortuous trajectory was again observed at a higher flow rate of 70 μl/hr, which suggested the disturbance of the flow field due to the appearance of the aggregated site in Region IV at 70 μl/hr. At further increased flow rate, the particle drifting towards the wall also appeared at 90 μl/hr, when aggregated sites appeared more prominent.

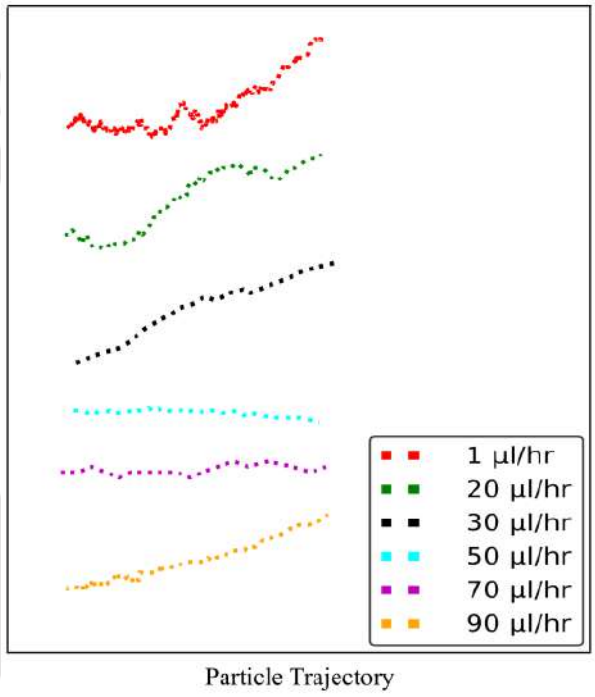

Figure 5.6: Experimental results of paclicad particle trajectory in the regions before 7 μm constriction region recorded at different flow rates.

From the mobility and trajectory study, it was found that the mobility of Paclicad particles was affected by the varying cross-section of the channel in converging and diverging regions. The results suggested that the varying cross-section affected the movement of the particles and suspended fluid differently. Further, the particle mobility is also less for the flow rate of 50 μ l/hr, suggesting the indication of disruption of the flow field attributed to the early aggregation stage. In addition, particle trajectory at different flow rates was also investigated. The trajectory was less tortuous at a higher flow rate due to advection dominance in the transport. However, the trajectory again became tortuous at a further higher flow rate. The tortuosity in the advection dominance regime in the transport was attributed to the presence of aggregated particle sites in the flow field.

5.2.5 Viscoelastic behavior of Paclicad articles

The majority of the particles and bio-molecules, like cells and drugs, flowing inside a human body migrate through a complex network of blood vessels of varying sizes and shapes. It requires better deformability and elastic recovery to undergo successful migration through these complex networks. Considering these aspects, the fluid behavior of the Paclicad particles was investigated by modeling it as a Newtonian and viscoelastic FENE-P drop. The FENE-P viscoelastic model was selected as it is reported to possess a shear-thinning behavior [213, 214], and for the drug particle to successfully migrate through the complex network of blood vessels, it should manifest a shear-thinning nature. A computational model was adopted to discern the viscoelastic behavior of the particle. A FENE-P viscoelastic drop was selected to model the Paclicad drug particles, while Newtonian fluid was chosen to model the carrier fluid. A Newtonian drop model was also adopted to bring out a better comparison. The numerical results from both models were compared with the experimental results of displacement versus time characteristics of the particles. The governing equations and numerical method adopted for the present two-phase viscoelastic drop-Newtonian matrix system are discussed elaborately in Chapter 2. Figure 5.7 compares numerical results obtained from both viscoelastic and Newtonian drop models with experimental results. Figure 5.7a shows the comparison at a 30 μl/hr flow rate. The results from both viscoelastic and Newtonian drop models gave identical results. The drop model matched the particle flow behavior at the regions (Regions I and II). At the same time, a slight deviation was observed at the later portion of the constriction region, where the numerical model underpredicted the experimental results. The drop model shows more deviation at the exit straight region (Region V), where the drop model exhibits slower migration than the experimental result. Overall, the drop model closely matched the migration behavior of Paclicad particles. The results were also compared for the particle migration at a flow rate of 50 μl/hr, as shown in Fig. 5.7b. The viscoelastic and Newtonian drop again showed identical migration results, but a significant deviation was observed between the drop model and experimental results. A relatively lesser deviation was observed between the drop model and the experimental result in the constriction region at a 30 μl/hr flow rate. However, the drop model undergoes slower migration and underpredicted the experimental results mainly at the higher flow rate. The results from the drop model differed from the flow rate variation as the numerical results vary slightly with a change in bulk flow rate.

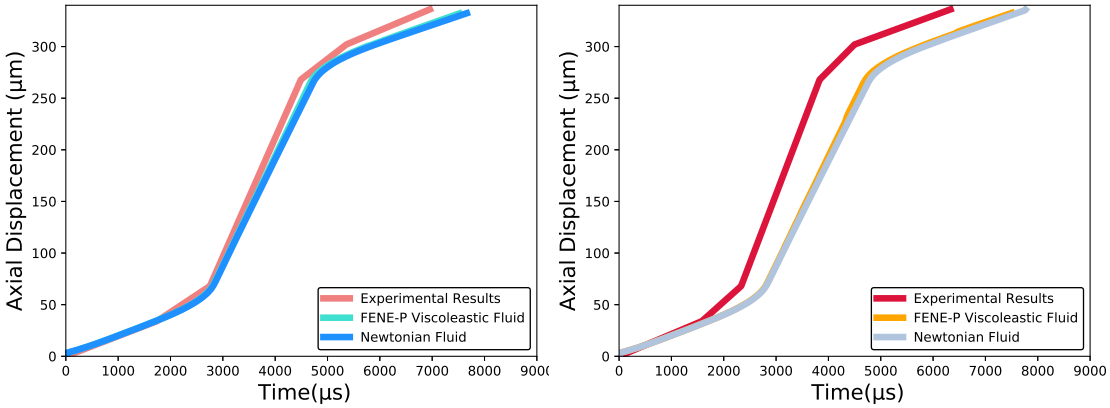

(a) (b)

Figure 5.7: Comparison of migration behavior of mathematical Newtonian and FENE-P drop model with the experimental results of Paclicad particle for two flow rates of (a) 30 μl/hr, (b) 50 μl/hr

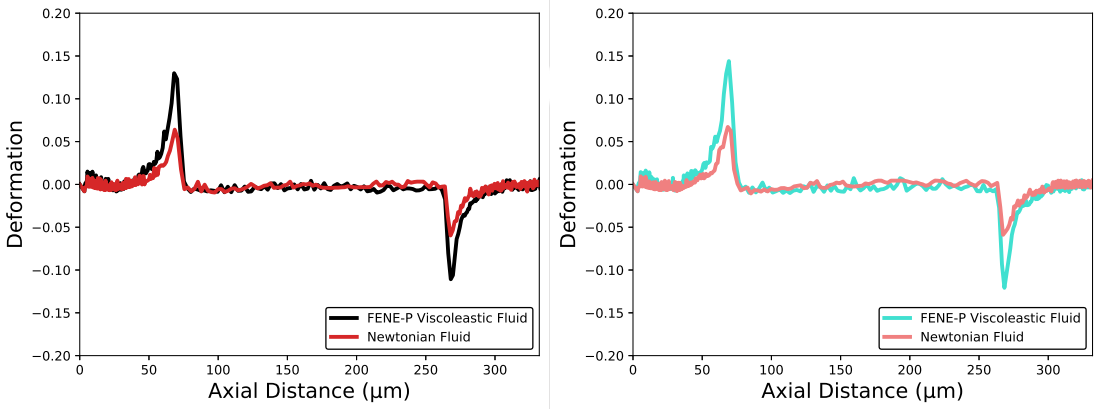

(a) (b)

Figure 5.8: Deformation of drop model of Paclicad particle measured along the axial distance of the microchannel for two flow rates of (a) 30 μl/hr, (b) 50 μl/hr

Table 5.3: Maximum deformation of drop model in Region II and Region IV

Flow rate (μl/hr)	II Newtonian	II FENE-P	IV Newtonian	IV FENE-P
30	0.06742	0.1332	-0.612	-0.113
50	0.06797	0.1464	-0.615	-0.12112

As the migration behavior shown by both Newtonian and FENE-P drop models was observed to be identical for both flow rates, a study on the deformation of the two models was carried out. The deformation behavior by Newtonian and FENE-P drop models was observed to be different, where FENE-P drop was observed to be more deformable than the Newtonian model. The drop deformation was studied for flow rates 30 μl/hr (Fig. 5.8a) and 50 μl/hr (Fig. 5.8b). The drop deformation was negligible in the straight sections of the microchannel, while a significant drop

deformation was noted in the converging and diverging sections of the microchannel. The maximum drop deformation was observed at the entry and exit of the 7 μm constriction region. The negative value of the deformation parameter was observed at the exit of the constriction region, as the particle underwent deformation in the cross-flow direction. Even though the FENE-P drop undergoes larger deformation than the Newtonian model, both models attain initial shape nearly simultaneously, explaining the faster stress relaxation and better elastic recovery of the FENE-P viscoelastic drop. The drop deformation was also observed to vary with a change in flow rate. Drop deformation seemed to increase with the flow rate, indicating dependency of drop deformation on bulk flow rate. The deformation variation with the flow rate was higher for the FENE-P drop, while the deformation of the Newtonian drop showed insignificant variation with the flow rate. The maximum deformation of the two drop model in the converging (Region II) and diverging (IV) region of the microchannel is shown in table 5.3. The method for calculating drop deformation is explained in Chapter 2.

The interface tracking by the VOF method successfully matched the experimental results of Paclicad displacement at the flow rate of 30 μl/hr. At the same time, a significant deviation was observed at a higher flow rate of 50 μl/hr. The result suggested that the numerical model needed more consistent matching of the experimental results at a higher flow rate. The drop migration behavior for Newtonian and FENE-P drops was the same for both flow rates. As the particle size was considerably small compared to the channel width, the wall effect did not come into play during the drop migration. A deviation between Newtonian and viscoelastic models could have been observed under the wall effect, as viscoelastic stresses are prominent near the wall. Furthermore, the deformation of the numerical model of the particles was deciphered. The small particle size compared to the channel width showed negligible deformation in the straight section of the channel. The drop appeared to show a noticeable deformation in the converging and diverging section of the channel, where the maximum deformation was observed at the entry and exit of the 7 μm constricted channel. The FENE-P drop model was reported to show more deformation than the Newtonian drop model. The FENE-P model and Newtonian drop both regained the original shape simultaneously, suggesting the viscoelastic model undergoes faster stress relaxation and manifests better elastic recovery.

Considering deformability and elastic recovery as desirable behavior for the successful migration of drug particles through blood vessels, the FENE-P drop model is a better numerical model than the Newtonian model. Viscoelastic fluids or polymeric fluids are a particular class of fluids where the arrangement and distribu-

tion of polymeric coils in a polymeric solution determine the complex mechanical behavior of the fluid. The isolated arrangement of these polymeric coils favors the independent molecular motion that, in turn, assists the deformation of these fluids. The isolated arrangement of the polymeric coils is more prominent in dilute polymeric solution. So a dilute polymeric solution will manifest a better deformation behaviour. Mathematically, a dilute polymeric fluid can be modeled by a viscoelastic drop with a higher solvent viscosity ratio. In addition, the FENE-P drop model also reported more deformation variation with the change of flow rate in comparison to the Newtonian drop model. The deformation of FENE-P drop was noted to increase with the increase of flow rate, which is also reported in the previous study that suggests an increase of deformation of the viscoelastic drop with an increase in Reynolds number [135].

5.3 Summary

In the present study, a dedicated investigation was carried out on transporting a commercially available chemotherapeutic drug, Paclicad, undergoing high shear flow inside a constricted microchannel. The particles were reported to transport without aggregation up to the flow rate of 50 μl/hr. However, the particle aggregation was observed at higher flow rates, causing capillary obstruction at a flow rate of 100 μl/hr. The experimental observation revealed the dominant role of shear rate in causing particle aggregation. The presence of aggregated particles in the flow field can lead to tortuous particle trajectory even in the advection dominant flow regime. The particle mobility was also discerned to decrease in the presence of varying channel cross-sections. The study provided valuable insight into the transport of a commercial drug inside an extremely confined flow that mimics a situation similar to that of human blood capillaries.

6

A heuristic approach to assess the drug uptake by MCF-7 cells inside a microfluidic channel designed to mimic the blood capillary networks

Estimating drug uptake by cells in vitro is widely determined in a static environment or centrifuge. Such an uptake study cannot give a correct estimation of drug uptake on cells as drug uptake by cells happens when both drug and cells are in movement. Considering these two aspects, microchannels with two different configurations were fabricated to replicate the confinement of the blood capillary network. The microchannels were fabricated to decipher the drug uptake on breast cancer cells (MCF-7 cells) when they flow through conditions similar to the blood capillary network. The drug uptake in Channel A and Channel B was observed to be 1.17 and 1.78 times higher than the conventional method. The inflection region where channel curvature changed caused MCF-7 cells to deform, which may weaken the membrane, thus allowing a better drug uptake by cells. Furthermore, the hydrodynamic effect on cell movement inside the microchannel was also investigated. It was observed that the MCF-7 cells showed noticeable deformation at the entry of the bifurcations and the inflection region. The MCF-7 cells also exhibited faster stress relaxation in the region of higher stresses. The cells' fore tip and tail end were observed to move at different speeds during stress relaxation. The novel microfluidic channel discussed in the study provided a new and efficient platform for the complete assessment of cellular uptake of drugs.

6.1 Introduction

A medicine's therapeutic efficacy largely depends on how well it is absorbed by cells. Substances enter cells through facilitated or simple diffusion [215]. Kell and

Oliver [216] presented a detailed argument on how drugs get into cells and the role of carrier-mediated uptake and bilayer lipoidal diffusion. A drug's ability to be absorbed by cells is either examined using simple diffusion in a static condition or assisted diffusion in a centrifuge [217]. Furthermore, it can be noted that the internalization of nanocarrier by cells follows a different pathway than drug internalization [218]. Endocytosis-related processes cause nanocarriers to be taken up by cells [219]. It has been reported that differences in the sizes of free drugs and nanocarriers can be the reason behind their difference in cellular uptake. Smaller drug molecules are internalized by cells via simple diffusion while nanoparticles are trapped in endosomes during its internalization [220]. Apart from simple diffusion, the cellular uptake of drugs can also be facilitated by applying external chemical stimuli and physical stimuli like ultrasound waves and mechanical fields [221]. However, even with advanced techniques for achieving enhanced cellular uptake of drugs, a correct estimation of drug uptake on cells while undergoing intravenous flow still needs to be discovered. Thus, it becomes essential to ascertain that the study is solely dedicated to quantifying the free drug uptake by cells.

The emergence and prominence of microfluidics have led to advancements in unraveling the fundamental laws governing blood flow inside human blood capillaries. The development of microfabrication techniques has paved a pathway for mimicking blood flow inside blood flows to replicate the clinical environment of various diseases [222]. Replicating blood flow can provide a significant understanding of phenomena like the distribution of drugs and molecules inside the body, transport and attachment of exosomes, cancer cells, biomarkers, and signaling factors. For example, the microfluidic model was used for detecting malaria-infected RBCs at various stages of parasite infection [223]. Furthermore, to reduce the complications arising from inefficient filtration of WBCs during blood transfusion, the margination tendency of WBC was overcome in a microfluidic device [224]. Additionally, a microfluidic device was fabricated to mimic the stenosed arteriolar blood vessels, and it successfully provided constant surveillance during anticoagulation therapy [225]. Moreover, a microfluidic model mimics the blood vascular structure for studying the vaso-occlusive risk in sickle cell diseases. The study also reported that the risk increases with an increase in shear rate [226]. Thus, the microfluidic model for replicating blood vascular structures has immense capabilities in gaining insights into disease prognosis, drug delivery, and therapeutics.

In previously reported studies, the quantification and estimation of drug uptake study on cancer cells either happen in a static environment or a centrifuge. Arguably, neither method must correctly depict the mechanical condition of drug uptake on cells when they migrate through complex blood capillary networks. In actual

intravenous flows, cells are not static or under the constant effect of centrifugal force. Instead, it migrates through various branches of the blood capillary network, experiencing inertial, viscous, surface tension, and dean forces. Thus, considering these aspects, the current work will fabricate microchannels to replicate the blood capillary networks. To achieve this, microchannels of two configurations were fabricated, as shown in Fig. 6.1. A microchannel with several bifurcations of varying width (Channel A) and other microchannel with branches of constant width (Channel B) were fabricated. An attempt to decipher the uptake of Doxorubicin on MCF-7 cells was made when two streams of cells and Doxorubicin were allowed to flow through Channel A and Channel B. Furthermore, an attempt was made to compare drug uptake by cells in static conditions and while flowing through channels via a flow cytometry study. Furthermore, the current study also explored the effect of the flow behavior of MCF-7. All the results presented in this Chapter were obtained by experimental study.

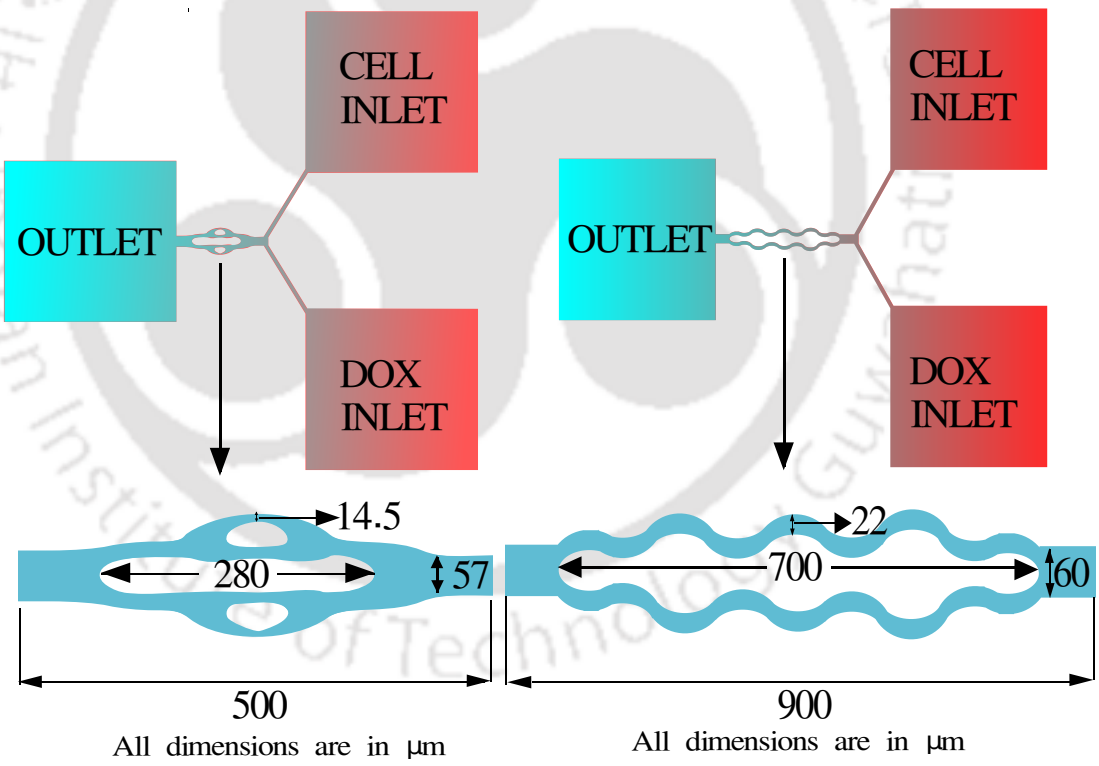

Figure 6.1: Channel design, (a) Channel A, (b) Channel B

6.2 Channel design

Blood capillaries are made of numerous interlinked networks of branch microchannels. Egana et al. [227] visualized the complex blood vascular network where

branches of blood capillaries evolve from branches of other capillaries. Thus, to develop a near identical confinement of blood capillaries, it is important to fabricate this complex interlinked branched microchannel. In a view to replicate this, microchannels with two different configurations Channel A and Channel B were fabricated. Channel A had branches of varying widths while Channel B had branches of constant width. The minimum width of the daughter branch of channel A was 14.5 μm and the minimum width of the parent branch was 60 μm. There was also an intermediate branch for channel A (Fig. 6.1a). The width of the daughter branches of channel B was 22 μm while the width of the parent branch was 57 μm (Fig. 6.1b). One most interesting aspects of the channel design was that it does not obey Murray's law of branching. It has been reported that dermal lymphatic capillaries do not obey Murray's law [228]. Thus, an attempt was made to design a channel to replicate a blood capillary network that does not obey Murray's law. Both the microchannels had separate inlets for the flow of MCF-7 cells and Doxorubicin.

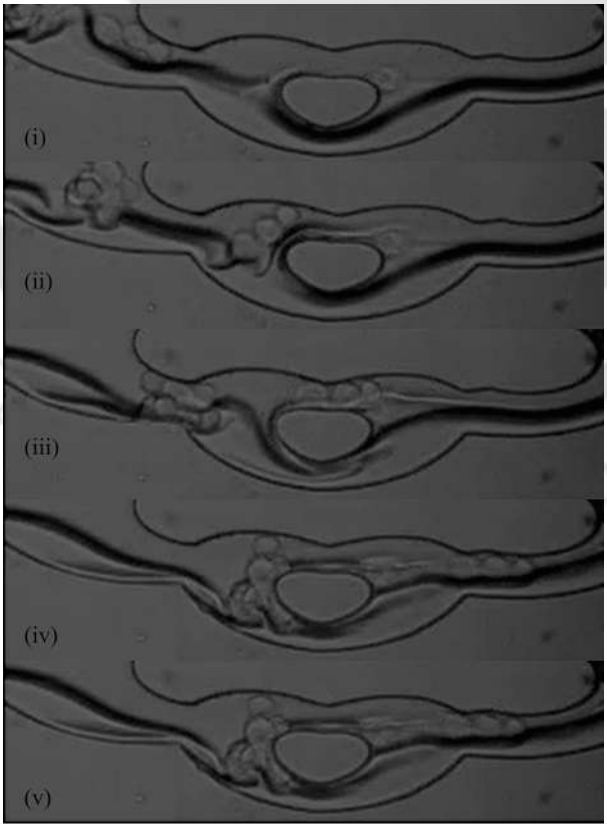

Figure 6.2: High-speed camera visualisation of migration of MCF-7 breast cancer cells through channel of minimum width 14.5 μm (Channel A) mimicking the vascular structure of microcapillaries

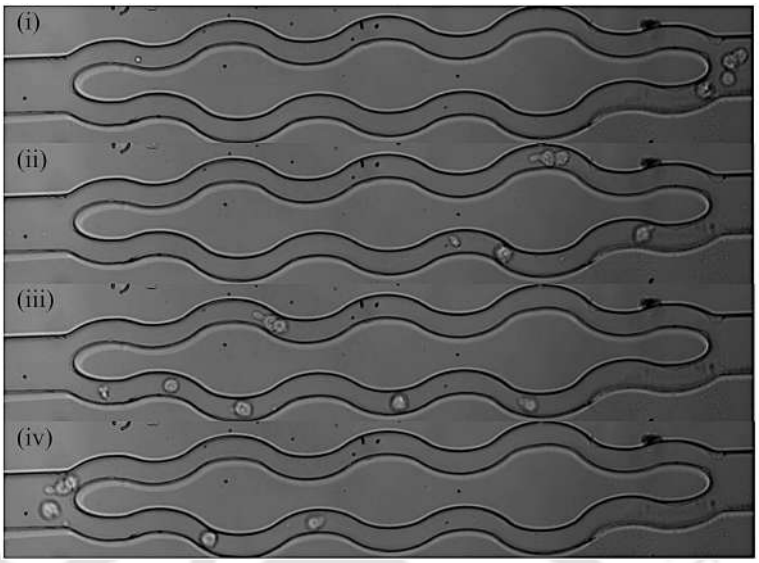

Figure 6.3: High-speed camera visualisation of migration of MCF-7 breast cancer cells through channel of minimum width 22 μm (Channel B) mimicking the vascular structure of microcapillaries

6.3 Results and discussion

6.3.1 Drug uptake on MCF-7 cells

In Chapter 4, the drug-loading efficiency of the hydrogel drug carrier was studied. Although the study can predict a close quantification of drug uptake on cells and drug carriers, the study is always carried out in a static environment. This process is most followed for estimating drug uptake on cells and drug carriers in drug delivery. Another widely followed method for estimating drug uptake on cells is by rotating the solution of drug and cells in a centrifuge. However, it can be argued that drug loading inside blood vessels happens when both drugs and cells are flowing together. Thus, correct estimation of drug uptake on cells cannot be achieved in a static environment and a centrifuge. Thus, an attempt was made to decipher the Doxorubicin uptake on MCF-7 cells when both underwent high shear flow inside branches of Channel A and Channel B. The MCF-7 cells suspended in 1X PBS solution and solution of Doxorubicin were allowed to flow at 50 μl/hr through two inlets shown in Fig. 6.1a, and Fig. 6.1b. The MCF-7 was observed to flow through both daughter branches of channel A (Fig. 6.2) and channel B (Fig. 6.3). The observation presented exciting results as the cells managed to flow readily through both daughter branches even if it does not obey the widely accepted Murray's law. High-speed camera images presented the cells mixing through the Doxorubicin stream for proper Doxorubicin uptake on MCF-7 cells (Fig. 6.2). The images were captured at 30000 fps.

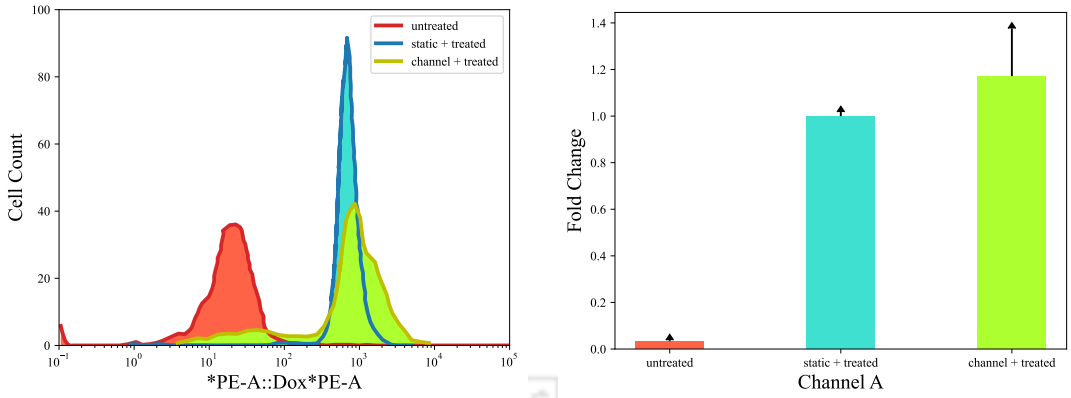

(a) (b)

Figure 6.4: (a) Flow-cytometric histograms of MCF-7 cells showing fluorescence of untreated MCF-7 cells, MCF-7 cells incubated with DOX in static condition, and MCF-7 cells incubated with DOX migration through a channel of 14.5 μm width (Channel A) of microcapillaries, (b) fold change in DOX uptake by MCF-7 cells while flowing through 14.5 μm (Channel A)

Table 6.1: Fold change in DOX uptake by MCF-7 cells flowing through Channel A

DOX uptake condition	Fold change
untreated	0.03
static + treated	1
channel + treated	1.17

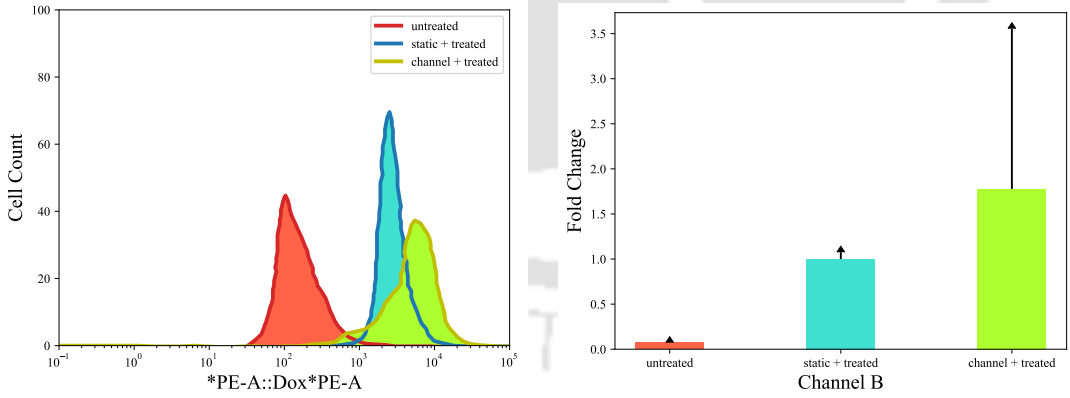

(a) (b)

Figure 6.5: Flow-cytometric histograms of MCF-7 cells showing fluorescence of untreated MCF-7 cells, MCF-7 cells incubated with DOX in static condition, and MCF-7 cells incubated with DOX migration through a channel of 22 μm width (Channel B) of microcapillaries, (b) fold change in DOX uptake by MCF-7 cells while flowing through 22 μm (Channel B)

The mixture of drug and cell solution obtained after their flow through branches of Channel A and Channel B were then collected at a single outlet in a single centrifuge tube. A flow cytometric study was done on the obtained mixture to

Table 6.2: Fold change in DOX uptake by MCF-7 cells flowing through Channel B

DOX uptake condition	Fold change
untreated	0.07
static + treated	1
channel + treated	1.78

estimate the amount of DOX uptake on MCF-7 cells. DOX uptake was estimated by observing its fluorescence in a flow cytometer. To discern an overall effect of channel configuration on DOX uptake on MCF-7 cells, the uptake results were compared with untreated MCF-7 cells and MCF-7 cells treated with DOX kept in a static centrifuge tube. The flow-cytometric histograms of MCF-7 cells showing fluorescence of untreated MCF-7 cells, MCF-7 cells incubated with DOX in a static tube, and MCF-7 cells with DOX flowing through channel A and Channel B are shown in Fig. 6.4a and Fig. 6.5a respectively. The plots (Fig. 6.4a) and (Fig. 6.5a) depict the fluorescence detected in channel *PE-A::Dox*PE-A of flow cytometer along the horizontal axis as a measure of DOX uptake by a number of cells represented along the vertical axis. The fluorescence data in green channels and red channels are collected by using a flow cytometer of BD Biosciences. The collected fluorescence data were extracted and analyzed using FlowJo software. The DOX uptake was observed for 1200 cells and the corresponding fluorescence intensity was reported. DOX manifests a characteristics green fluorescence, that is analysed and detected in a flow cytometer. Thus, observing its fluorescence through a flow cytometer can give a direct estimation of its uptake amount. It is to be noted that untreated cells showed fluorescence even without DOX in them. This is because MCF-7 cells also have a minute inherent fluorescent nature. Shift in mean DOX uptake by MCF-7 cells while flowing through Channel A from static centrifuge tube condition was observed (Fig. 6.4a). The observation suggested a significant shift in the amount of DOX uptake by MCF-7 cells when it is made to flow through blood capillaries alike microchannels. Moreover, along with the shift, the fold change in the amount of DOX uptake in Channel A was reported to be 1.17 times higher than the uptake in a static centrifuge tube as shown in Fig. 6.4b. Fold change represents how many times the DOX uptake by MCF-7 cells in the channel is greater than the uptake in static conditions. The values of fold change values of DOX uptake under different conditions and flowing through Channel A is shown in Table 6.1. The observation revealed astounding proof that the estimation of drug uptake by MCF-7 cells should be carried out in blood capillary-like microchannels. In the furtherance of the study, the uptake estimation was also observed in Channel B. A significant shift in mean DOX uptake by MCF-7 cells while flowing through Channel B was discerned (Fig. 6.5a). The fold change in DOX uptake in channel

B was 1.78 times higher than the uptake in static conditions (Fig. 6.5b). The values of fold change values of DOX uptake under different conditions and flowing through Channel B is shown in Table 6.2. Thus, it was observed that higher DOX uptake was achieved in both the Channels A and B. The value of mean DOX uptake was determined from 5 independent observations from two different sets of experiments for each channel configuration.

6.3.2 Effect of channel geometry on drug uptake on MCF-7 cells

In the previous section, it was observed that DOX uptake by MCF-7 cells in Channel B was better than in Channel A. Thus, it can be inferred that channel geometry and shear rate must significantly affect cell flow, allowing a shift in DOX uptake by cells. In order to investigate the effect of geometry on DOX uptake, the flow behavior of MCF-7 cells in the presence of a DOX solution inside branches and bifurcations of Channel A and Channel B was deciphered. The flow trajectories of the fore tip and tail end of MCF-7 cells, deformation, and variation of the speed ratio of the cell's fore tip and tail end along channel length were investigated. The flow trajectories were computed by using the point tracking method of the image processing application Phantom Camera Controller. The points selected for tracking were the cell fore tip along the flow direction and their tail end along the same direction. Deformation was calculated using the method adopted for calculating the deformation of viscoelastic drop given by Eq. 3.2. The speed ratio is defined as the ratio of speed of the cell's fore tip to the tail end while speed ratio was calculated according to the following relation (Eqs. 6.1 and 6.2).

$$\text{Speed} = \frac{x(t+\Delta t) - x(t)}{\Delta t} \tag{6.1}$$

$$\text{Speed Ratio} = \frac{\text{Cells' fore tip speed}}{\text{Cells' Tail End speed}} \tag{6.2}$$

where x was the distance traveled by fore tip/tail end of MCF-7 cells at time instant t, and Δt was the time interval between the two frames where the measurements were taken.

The sections and branches of Channel A taken for study are shown in Fig. 6.6. The channel length taken for study is divided into four regions named Bifurcation 1, Bifurcation 2, Bifurcation 3 , and Bifurcation 4. Bifurcation 2 divides into two daughter branches, BRANCH A and BRANCH B. The minimum width of BRANCH A and BRANCH B is 14.5 μm. Images captured from the high-speed

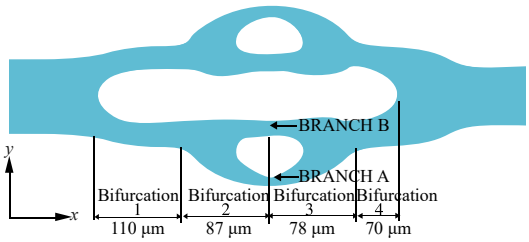

Figure 6.6: Section of the Channel A selected for studying MCF-7 cell's trajectory, deformation, and speed ratio

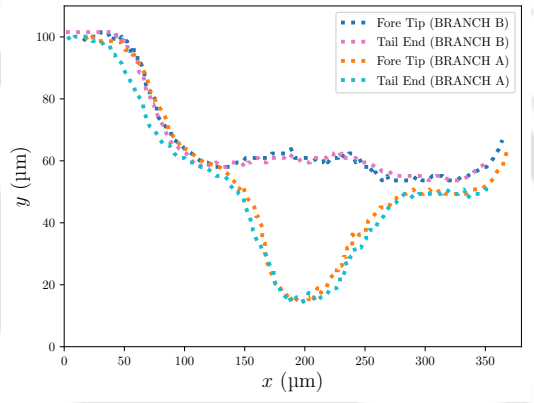

Figure 6.7: Trajectories of foretip and tail end of MCF-7 cells flowing through BRANCH A and BRANCH B of Channel A

camera were processed to find the transport behavior of the MCF-7 cells. The flow trajectories of MCF-7 cells along the Channel A length was visualized by tracking the position of the foretip and tail end of cells as shown in Fig. 6.7. The flow trajectories revealed that the fore tip and tail end of the cell followed similar trajectories with less tortuosity throughout each bifurcation of Channel A. An outcome of tortousity observed in BRANCH B was observed for both the fore tip and tail end of cells while a tortuous trajectory of the MCF-7 tail end was observed in BRANCH A. Observing the trajectories of the MCF-7 cell's foretip and tail end presented a clear picture of the effect of flow and confinement on cells' movement. It was suggested that cells are prone to undergo tortuous movement when they flow through narrower confinement.

In the furtherance of the study, variation of deformation of MCF-7 cells flowing through different bifurcations of Channel A via the path of BRANCH A was studied. The deformation study of MCF-7 cells revealed that there is a minor increase in the cell's deformation when it enters Bifurcation 1 (Fig. 6.8a). Cells were able to regain the original shape just after entry to the Bifurcation 1 suggesting a faster stress relaxation. The observation remained similar while flowing through Bifurcation

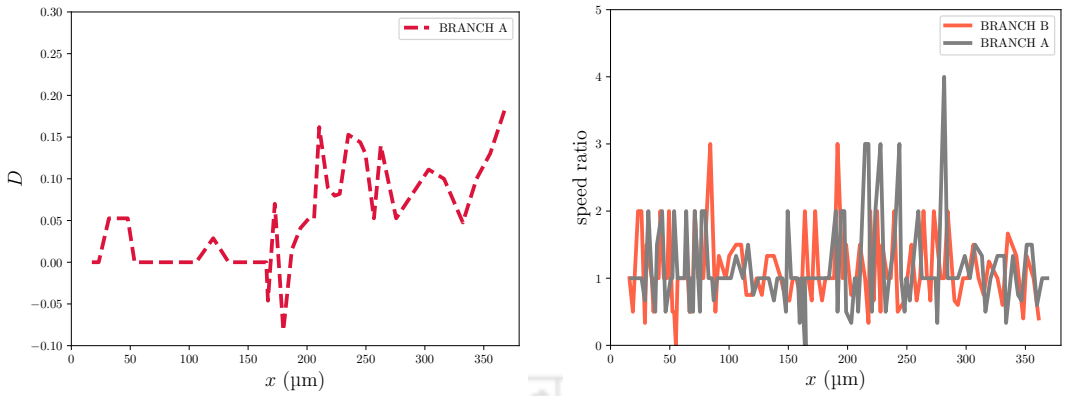

(a) (b)

Figure 6.8: (a) Plot showing the variation of deformation of MCF-7 cell along the axial length of of Channel A, flowing through BRANCH A, (b) plot showing the variation of speed ratio of MCF-7 cell along the axial length of Channel A flowing through BRANCH A and BRANCH B

2. A noticeable deformation was discerned when the cells flowed through the bend in Bifurcation 2 and later underwent deformation in a lateral direction after flowing out of the bend. The deformation later peaked when cells flowed through the narrowest confinement of BRANCH A. A sudden dip in deformation was observed at the exit of the narrow confinement but as it moved through the bend, the overshoot of deformation again appeared. Thus, a non-monotonic zig-zag pattern with a positive and negative value of deformation pattern prevailed in the Bifurcation 3 region. After leaving Bifurcation 3 the amplitude of the overshoot of deformation decreases and the frequency of the zig-zag deformation pattern also decreases till it reaches the exit of Bifurcation 4. However, a significant increase in the deformation parameter was observed at the exit of Bifurcation 4, where it experiences a sudden change in curvature and moves towards relatively lesser curved regions of the channel. The deformation study revealed interesting results on how cells stretch when they experience a change of curvature inside a microchannel. Furthermore, it was also discerned that cells are faster in stress relaxation when they undergo high shear flow inside extremely narrow confinement.

Furthermore, the variation of the cell's speed along the bifurcations of Channel A was investigated. To quantify the speed of the cells, a parameter speed Ratio was calculated. This parameter is the ratio of speed with which the cell's fore tip moved to the speed with which the cell's tail end moved. As the cell's sizes were comparable to the width of the channel, the speed of the cell's foretip and tail end should have been different while it flowed through the bifurcations and bends of Channel A. The speed ratio variation profile suggested that the cell's fore tip and tail end underwent periodic increases and decreases in speed. The

maximum increase in the speed ratio was observed in the Bifurcation 3 region of Channel A (Fig. 6.8b). A more significant increase and decrease in the speed ratio signified that the cells' fore tip and tail end moved at different speeds that can arise from the cell's response to stresses due to a change of channel curvature in narrow confinement. Interestingly, cells were observed to show a higher variation of deformation in the same region where there is a higher variation in the speed ratio. It was also observed that peak and decline of speed ratio values were less in the region (Bifurcation 4), where the cell's peak in deformation also started to decrease. The speed ratio profile of MCF-7 cells flowing through BRANCH A and BRANCH B was observed to be similar throughout each bifurcation of Channel A except for a noticeable difference in the junction of Bifurcation 2 and Bifurcation 3. The observation may arise due to differences in the stretching tendency of the cells passing through that region.

It is also important to discern the time variation of axial displacement of MCF-7 cells as they move through different bifurcations of Channel A. The variation of axial displacement with time for MCF-7 cells moving along different bifurcations of Channel A is shown in Fig. 6.9a. It was observed that the cells were observed to exhibit faster displacement in Bifurcation 1, 2, and 3. Faster displacements were observed in Bifurcation 2, and 4 as it includes the part of the channel when the cell enters into the narrower confinements. The average velocities through Bifurcations 1, 2, 3, and 4 are 78.51 mm/s, 99.15 mm/s, 81.78 mm/s, and 104.66 mm/s. The lines in the plot also include the error bands that represent the standard deviation in measuring the cell's axial displacement through each bifurcation. As the channel dimensions are very small, the deviation in displacement calculation also turned out to be lesser. The mean displacement profile with error bands is shown in Fig. 6.9b.

Furthermore, the flow behavior of MCF-7 cells flowing through different curves of Channel B was also studied. The section and curves of Channel B selected for study are shown in Fig. 6.10. The channel length taken for the study is divided into nine curves that bend in opposite directions periodically. The curves are named Curve 1, Curve 2, Curve 3, Curve 4, Curve 5, Curve 6, Curve 7, Curve 8, and Curve 9. The width of each curve was kept constant (22 μm), and the configuration has two branches named BRANCH I and BRANCH II. Similar to Channel A, the flow trajectories of MCF-7 cells along the Channel B length were visualized by tracking the position of the fore tip and tail end of cells as shown in Fig. 6.11. The flow trajectories revealed that the fore tip and tail end of the cell followed similar trajectories with less tortuosity throughout each curve of Channel B. The trajectories remained less tortuous for both branches. Interestingly, the appearance

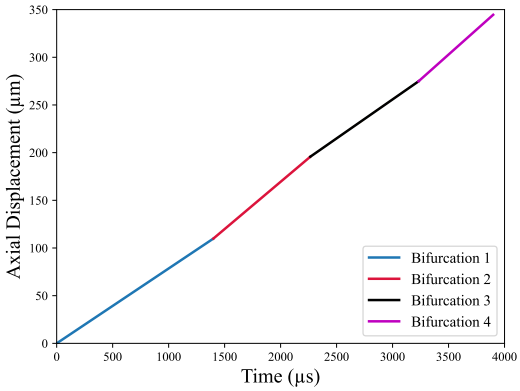

(a)

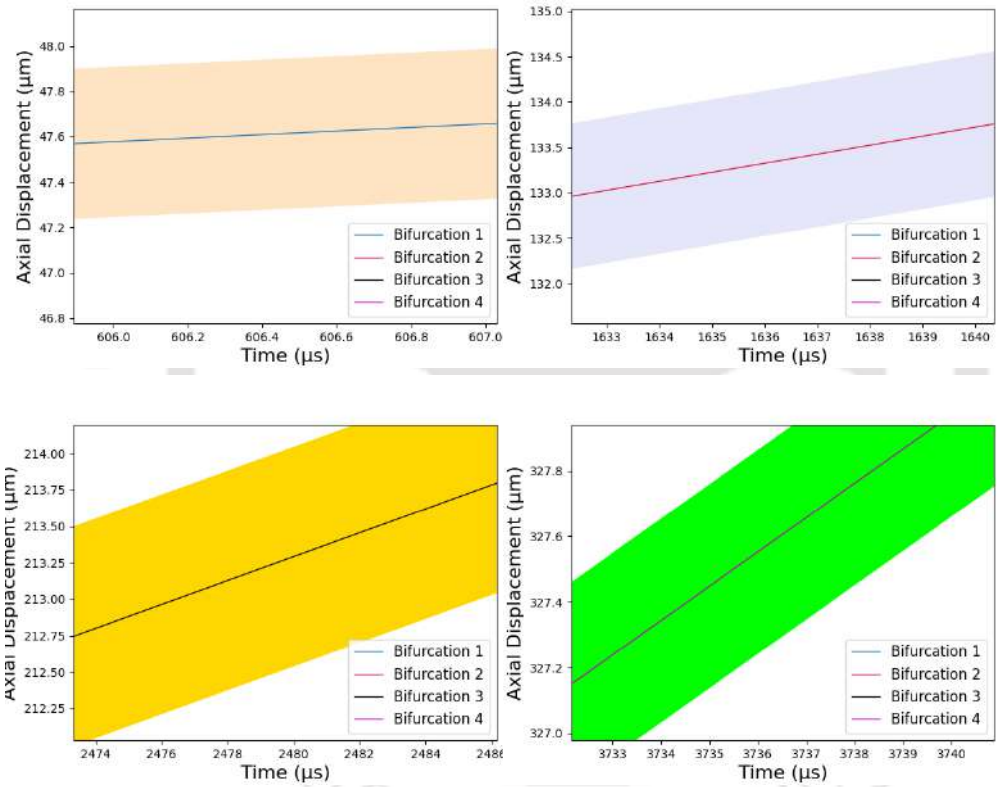

(b)

Figure 6.9: (a) Plot showing the variation of axial displacement with time for MCF-7 cells flowing through different bifurcations of Channel A via path of BRANCH A, (b) zoomed in view showing the error bands of axial displacement variation with time of MCF-7 cells flowing through different bifurcations of Channel A

of tortuosity was not observed during the MCF-7 cell's movement through different curves of Channel B. The observations suggested that the flow trajectories of cells are supposed to become tortuous when they experience a narrower confinement during their transport. As a result, the tortuous trajectory was observed in Channel A. In Channel B, cells undergo a less tortuous trajectory as they flow through the confinement of constant width.

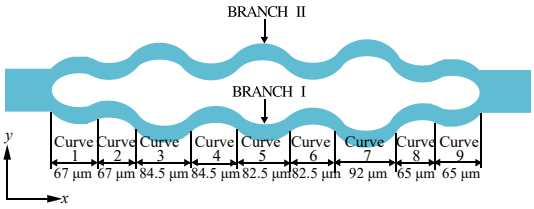

Figure 6.10: Section of the Channel B selected for studying MCF-7 cells trajectory, deformation, and speed ratio

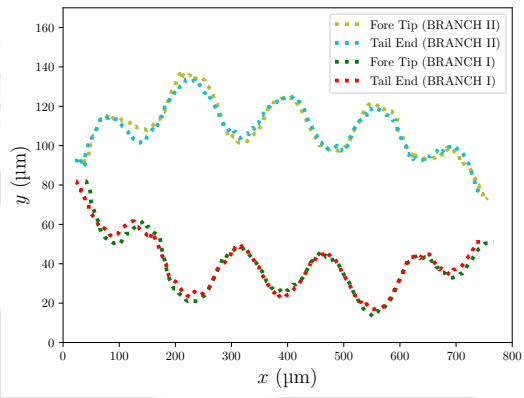

Figure 6.11: Trajectories of foretip and tail end of MCF-7 cells flowing through BRANCH I and II of Channel B

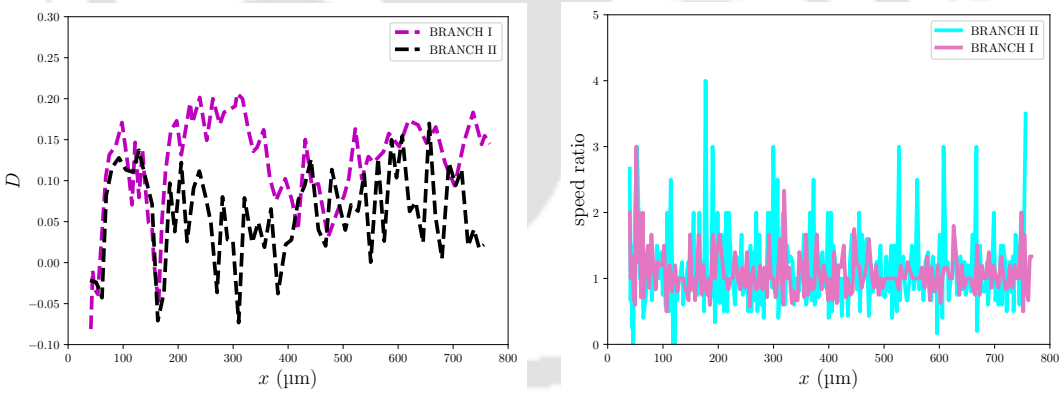

(a) (b)

Figure 6.12: (a) Plot showing the variation of deformation of MCF-7 cell along the axial length of Channel B, flowing through BRANCH I and II, (b) plot showing the variation of speed ratio of MCF-7 cell along the axial length of Channel B flowing through BRANCH I and II

In continuation of the study, variation of deformation of MCF-7 cells flowing through curves of Channel B was deciphered. The deformation study of MCF-7 cells revealed that there is a peak in a mechanical stretch of MCF-7 cells at the inflection where the curve changes its curvature as shown in Fig. 6.12a. The deformation later decreases till it reaches another inflection. The decrease in the deformation parameter in the non-inflection region of curves revealed that cells allow

themselves to deform in the cross-flow direction in order to release the mechanical stresses. Thus, a non-monotonic zig-zag deformation profile was delineated for cells flowing through Channel B. The resulting non-monotonic zig-zag deformation profile was more prominent in Channel B than in Channel A. Furthermore, it was investigated that the peak in deformation was highest when cells entered Curve 1, and it became highest while flowing through Curve 2, and Curve 3 in BRANCH II. Interestingly, negative deformation was also highest before reaching the inflection region of Curve 1, and Curve 2. The cell deformation later increases at the inflection region. The non-monotonic zig-zag nature of the deformation profile was observed for cells flowing through both BRANCH I and BRANCH II. However, the maximum stretch was observed in BRANCH II. The deformation study revealed an interesting observation of cells' ability to deform when they experience a change in curvature while flowing through different curves in the channel. Apart from this, the results also highlighted that cells were also fast in relaxing the stresses subjected to them by exhibiting deformation in a cross-flow direction.

In the furtherance of the study, the variation of the cell's speed along the different curves of Channel B was studied. Similar to the study presented for Channel A, speed ratio variation through BRANCH I and BRANCH II of Channel B was calculated. The speed ratio variation profile suggested that the cells exhibited a periodic increase and decrease in speed ratio values. The peak and drop of the speed ratio values were also observed to be different in each curve of the microchannel (Fig. 6.12b). The maximum increase in speed ratio was observed in the Curve 1 region of Channel B, while it was maximum in the Curve 3 region of the microchannel. Interestingly, it was observed that the peak and drop of the speed ratio values were higher in the region where significant non-monotonic zig-zag behavior of the deformation profile of cells was delineated. The observation further signified that in order to undergo faster stretching and healing, cells should flow with different foretip and tail-end speeds.

Similar to Channel A, the variation of axial displacement with time for MCF-7 cells moving along different curves of Channel B was also deciphered. The axial displacement was found for two branches of Channel B (BRANCH I and II) as shown in Fig. 6.13. It was observed that the cells exhibited faster displacement while flowing through the path of BRANCH I. The axial displacement profiles of MCF-7 cells flowing through BRANCH I and BRANCH II were observed to coincide till Curve 3 of Channel B. After exiting Curve 3, MCF-7 cells were observed to exhibit faster transport through BRANCH I. Faster displacement was observed at the middle section of the channel, that is Curve 5 of the Channel B.

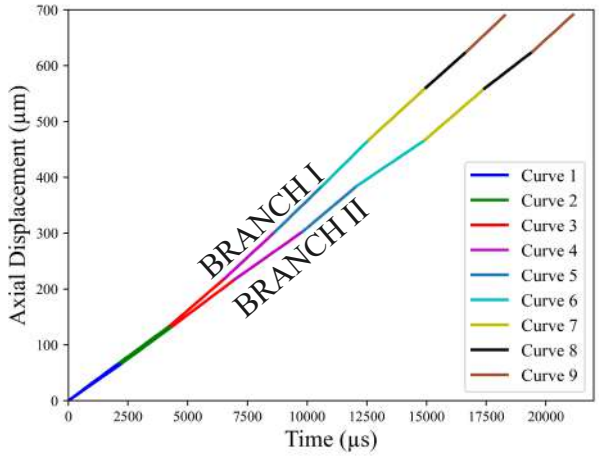

Figure 6.13: Plot showing the variation of axial displacement with time for MCF-7 cells flowing through different bifurcations of Channel B

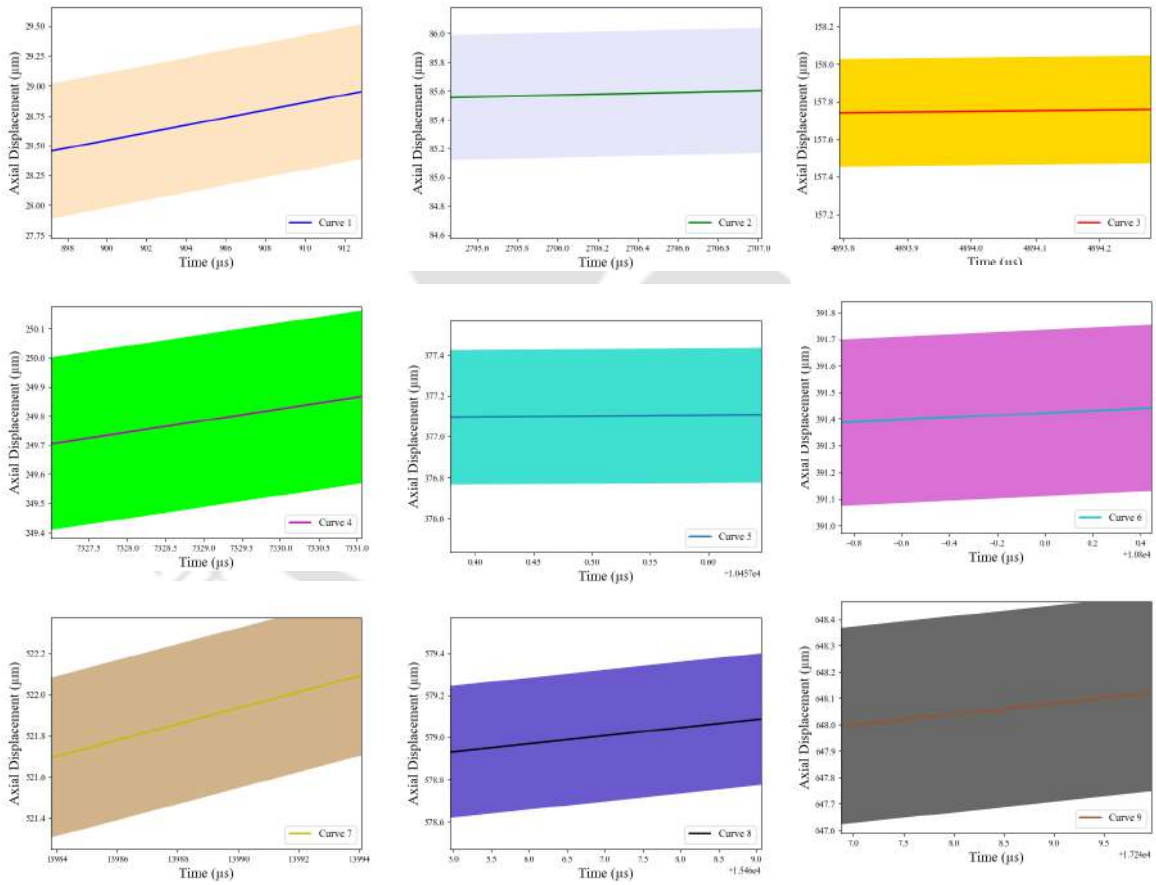

Figure 6.14: The zoomed in view of Fig. 6.13 showing the error bands of variation of axial displacement with time for MCF-7 cell flowing through different curves of BRANCH I of Channel B

The average velocities of MCF-7 cells flow through all the curves of Channel B flowing through BRANCH I and BRANCH II is mentioned in Table 6.3. The lines in the plot actually also include the error bands that represent the standard

deviation in measuring the cell's axial displacement through each curve. The mean displacement profile with error bands is shown in Fig. 6.14, and 6.15.

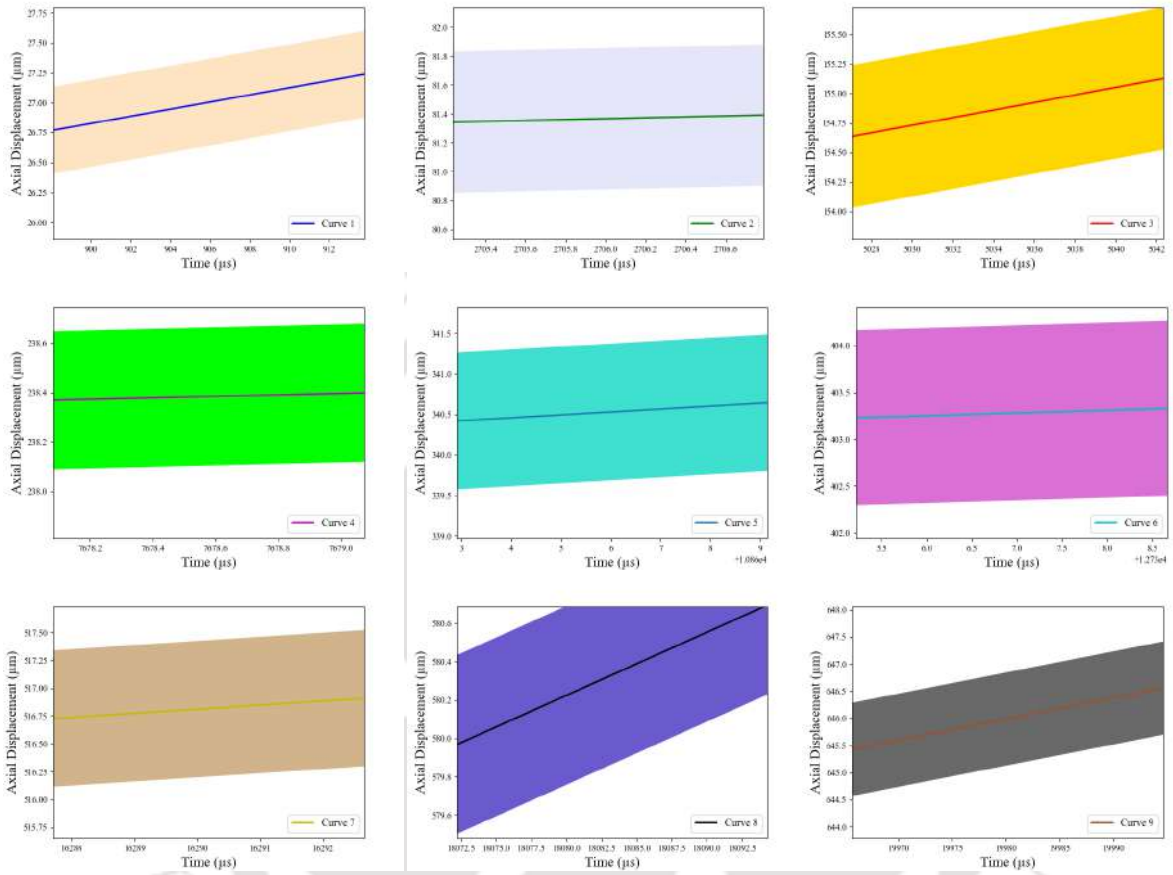

Figure 6.15: The zoomed in view of Fig. 6.13 showing the error bands of axial displacement of MCF-7 cell with time flowing through different curves of BRANCH II of Channel B

Table 6.3: Average velocities of MCF-7 cells flowing through different curves of Channel B

	BRANCH I	BRANCH II
Curve 1	31.71 mm/s	29.80 mm/s
Curve 2	31.33 mm/s	31.36 mm/s
Curve 3	36.92 mm/s	32.11 mm/s
Curve 4	39.65 mm/s	30.11 mm/s
Curve 5	41.46 mm/s	35.95 mm/s
Curve 6	42.44 mm/s	28.91 mm/s
Curve 7	38.97 mm/s	36.83 mm/s
Curve 8	37.98 mm/s	32.91 mm/s
Curve 9	40.42 mm/s	38.87 mm/s

6.3.3 Role of dean forces on cellular uptake of drugs

In the present experiment, a noticeable fold change in DOX uptake by MCF-7 cells was observed in Channel B. The hydrodynamic study revealed that MCF-7 cells underwent flow through successive curves with region of inflection. Other observations, such as non-monotonic zig-zag deformation patterns and speed ratio, were associated with increased fold change of DOX uptake. It has been reported earlier that stresses profoundly affect cell cytoskeleton and may cause cell death [229, 230]. However, even after flowing through high-shear regions in microchannels, MCF-7 cells were observed to exhibit better uptake while being alive. Thus, a further examination was done to understand the role of inertia, viscous, and dean forces on DOX uptake inside the microchannels. As cells flow through bifurcations and curves of Channel A and Channel B while doing so, they experience centrifugal force, or Dean force [231]. It has been observed that forces acting on the surface of the cells causes intracellular redistribution of mechanical responses based on its local structure [232]. Thus, estimating the role of Dean force can give better insight into the role of curvature and inflection on DOX uptake by MCF-7 cells.

For the analysis, the length scale (l_s = 14.5 μm) was taken as the narrowest dimension of the two channels (Channel A and Channel B). Meanwhile, a viscous time scale (t_s) was chosen for the analysis. The convective time scale was also calculated, but its order of magnitude was higher than the viscous time scale. The viscous time scale (t_s) is given by Eq. 6.3.

$$t_s = \frac{l_s^2}{\nu} \tag{6.3}$$

where ν is the kinematic viscosity, and it is the ratio of dynamic viscosity to the density of the fluid. The dynamic viscosity of the solution of MCF-7 cells with DOX was found by a rheometer. The standard fluid model was adopted to find the shear rate-dependent viscosity of the solution in Thermo Scientific HAAKE Viscotester. The variation of dynamic viscosity and shear stress with shear rate is shown in Fig. 6.16a and 6.16b. It was observed that with an increase in the shear rate, the viscosity of the solution decreased, indicating a shear-thinning behavior of the solution. Although, it was observed that viscosity variation ceased at higher shear rates. In the present study, the cells underwent high shear flow inside the microchannels. The dynamic viscosity of 3 cP corresponding to a shear rate of 1000 s^{-1} was chosen for the calculation of the viscous time scale. The density of the solution was found to be 1100 kg/m^3. Thus, the value of ν was found to be 2.73$\times$ 10^{-6} m^2/s. Thus, the viscous time scale (t_s) according to Eq. 6.3 came out to be 77 μs. Furthermore, the velocity scale (v_s) can be found from Eq. 6.4,

$$v_s = \frac{l_s}{t_s} \tag{6.4}$$

which gives, v_s as 0.19 m/s. Using these values, the Reynolds number (Re) for the present analysis was found to be 1. Furthermore, the Dean number can be found from the Eq. 6.5 [233]

$$Dn = Re\sqrt{\frac{l_s}{2r_c}} \tag{6.5}$$

where, r_c is the radius of the curvature of the channel. As the channels used in the present study had curves and bifurcations of varying radius of curvature, the smallest radius of curvature was chosen for the analysis. The r_c for the present analysis was taken to be 74 μm. The Dn for the present microfluidic system was found to be 0.31. Thus, it can be observed from the value of Dn that viscous forces dominate centrifugal forces. Thus, the presence of dean flow does not contribute to the drug uptake by MCF-7 cells. Interestingly, studies have shown that mixing is enhanced in curved microchannels [234]. But, in the present microchannels, drug uptake by cells was enhanced even when centrifugal forces were not dominant. The observation presented an interesting fact that drug uptake by MCF-7 cells can not be treated as a mixing phenomenon. The analysis suggested that the non-monotonic zig-zag pattern of the cell's deformation and speed ratio should be the primary region of increased DOX uptake in the microchannels. The observation can be further investigated by analyzing the effect of elastic forces on a cell's deformation and migration. The analysis will be part of the future extension of the work.

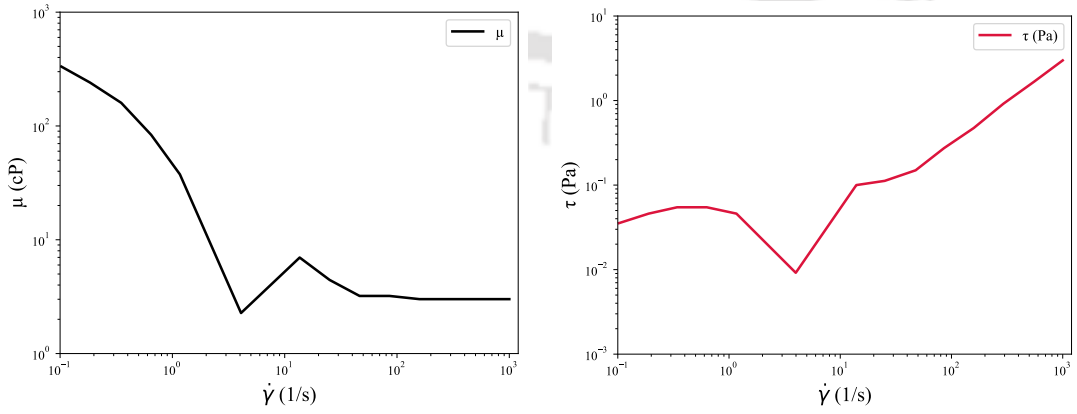

(a) (b)

Figure 6.16: (a) Plot showing the variation of viscosity of solution (MCF-7 cells with DOX) with shear rate, (b) plot showing the variation of shear stress of solution (MCF-7 cells with DOX) with shear rate

6.4 Summary

In the chapter, novel microfluidic devices for drug uptake study on MCF-7 cells were fabricated. Estimation of drug uptake by cells in vitro condition is widely determined in a static environment or in a centrifuge. Thus, it can be ascertained that this uptake study cannot give a correct estimation of drug uptake on cells as drug uptake by cells happens when both drug and cells are flowing inside blood capillaries. Considering this as a motivation, the microchannels were fabricated to decipher the drug uptake on breast cancer cells (MCF-7 cells) when they flow through conditions similar to the blood capillary network. The drug uptake in Channel A was observed to be 1.17 times higher than the static condition. At the same time, the drug uptake in Channel B was 1.78 times higher than the static condition. The inflection region where channel curvature changed caused MCF-7 cells to deform, which may lead to the weakening of the membrane, thus allowing a better drug uptake by cells. Furthermore, it was observed that the MCF-7 cells showed noticeable deformation at the entry of the bifurcations and at the inflection region. The MCF-7 cells were also able to exhibit faster stress relaxation in the region of higher stresses. The fore tip and tail end of the cells were observed to move at different speeds during stress relaxation. The microfluidic channels fabricated in the study offered a fresh and effective platform for the thorough evaluation of drug uptake by the cells.

7 Conclusions and Scope for future work

7.1 Conclusions

It can be discerned from the experimental and numerical investigations discussed in the thesis that various unknown aspects of the transport behavior of the drug carriers inside constricted microchannels were revealed. These carriers and cells should possess viscoelasticity to overcome inevitable adversities during migration through constricted microcapillaries. Furthermore, the surface property of these carriers and drug particles should be modified to restrict complications arising from aggregations, margination, and adhesion. In addition, a novel microfluidic platform for correct estimation of drug uptake on cancer cells was also presented in the thesis. The major conclusions from the present thesis can bring significant outcomes in targeted drug delivery in cancer therapeutics. The conclusions from each chapter of the thesis are discussed in subsequent paragraphs of the current sections.

At first, in a numerical investigation, the effect of parameters like solvent viscosity ratio (β), capillary number (Ca), viscosity ratio (θ), and channel confinement (CR) on the deformation of FENE-P drop migrating through the microchannel was observed. The deformation under channels with $CR = 6$ and 3 with sudden contraction/expansion was investigated. The deformation was found to depend on solvent viscosity ratio at unity Deborah number when drop flows through higher confinement. Drop deformation was observed to get enhanced with the increase in β values. However, the drop with a lesser β value was reported to exhibit faster stress relaxation. Drop showed more considerable deformation at higher capillary numbers. It was also reported that viscoelastic stress distribution gets convected faster at a higher capillary number when the strain rate inside drop reduces. Drop deformation was observed to vary non-monotonically with an increase in viscosity ratios. The drop deformation was reported to be at its

maximum in the later portion of the constricted region of the microchannel at viscosity ratios greater than 5. The droplet breakup was also observed at different viscosity ratios. Variations of critical capillary numbers with Deborah numbers, viscosity ratios, and confinement ratios were also discussed. The observation suggested that elastic stress growth due to the elongation of polymeric dumbbells resists droplet breakup in viscoelastic drops. A viscoelastic drop with a non-isolated arrangement and a higher concentration of polymer molecules can delay and resist droplet breakup inside the contraction/expansion microchannel. The drop breakup behavior of the FENE-P drop was compared with the breakup of the Oldroyd-B drop under similar conditions. The FENE-P drop breakup was characterized by forming two daughter droplets from its tail end. While Oldroyd-B drop only produced a single daughter droplet after the breakup. Drop breakup assessment can be utilized to design nanocarrier assembly for on-demand burst release of anti-cancer drugs at the selected site. The following results can also generate monodispersed emulsion by executing a controlled droplet breakup inside a confined microchannel. Furthermore, effects on deformation can provide valuable insights into the high-shear migrations of biological molecules inside blood vessels.

In the second work, an experimental and numerical investigation was conducted to decipher the self-healing properties of hydrogel particles that underwent migration through a constricted microchannel without adhering to the channel walls. The particles regained their physical structure after undergoing migration. The study revealed self-healing hydrogel nanocarriers' high load-carrying and elastic recovery characteristics. The aggregation of hydrogel particles restricted the decay of nanocarriers. The nanocarriers demonstrated longer retention of doxorubicin with sustained drug release. The mathematical model of the shear-thinning nanocarriers manifested remarkable insight into particle-squeezing inside microcapillaries. The numerical results can be further employed for designing complex microfluidic devices for studying drug delivery through brain capillaries, blood-brain barriers, and other intricate human body areas. Furthermore, the flow behavior and deformation of the cellular nanovesicles were also observed through branches of contraction/expansion microchannels designed to mimic the human blood capillary networks. An earlier study observed that nanovesicles could transport through the polymer matrix network to mimic the extra-cellular matrix. They reported that the combination of stress relaxation and matrix stiffness deformed the nanovesicles, which squeezed through the microchannels. However, the study failed to consider the lack of mechanical strength, which resulted in the nanovesicle accumulation. Also, their study could not provide a relative quantification of the nanovesicle deformities. Therefore, the study aimed to prove the relative quantification of the

nanovesicle deformities, which was a gap in their research. It was reported that the aggregated nanovesicles migrated in a high mechanical stress environment, making it flow through the microchannel blockages and branched contraction/expansion channels. The aggregated nanovesicles were observed to flow successfully through the microblockages and contraction/expansion microchannels. The nanovesicles were also observed to show higher deformation when subjected to higher stress in smaller square blockages. An interesting observation was made when nanovesicles underwent deformation in cross flow direction when stresses were removed from them. Additionally, the nanovesicles exhibiting faster migration showed slower elastic recovery. Moreover, a slower elastic recovery might lead to premature drug release by nanovesicles, resulting in lesser therapeutic efficiency. Nanovesicles are derived from cancer cell membranes, so they lack mechanical strength. In addition to better circular uptake and higher circulation time, it is also essential to consider the mechanical strength of nanovesicles for drug delivery applications, which is successfully portrayed in this study.

The third study investigated the transport of a commercially available chemotherapeutic drug, Paclicad, undergoing high shear flow inside a constricted microchannel. The particles were reported to transport without aggregation up to the flow rate of 50 μl/hr. However, the particle aggregation was observed at higher flow rates, causing capillary obstruction at a flow rate of 100 μl/hr. The experimental observation revealed the dominant role of shear rate in causing particle aggregation. The presence of aggregated particles in the flow field can lead to tortuous particle trajectory even in the advection dominant flow regime. The particle mobility was also discerned to decrease in the presence of varying channel cross-sections. A numerical model was also suggested for the Paclicad particles. The viscoelastic and Newtonian models closely predicted the experiment results, but the viscoelastic drop model showed better deformation and elastic recovery than the Newtonian model. The work provided valuable insight into the transport of a commercial drug inside an extremely confined flow that mimics a similar situation of human blood capillaries.

Lastly, with the knowledge and skills gathered from the previous studies, an attempt was made to devise a microchannel for a complete and practical assessment of drug uptake on MCF-7 cells. Novel microchannels with two different configurations were fabricated to replicate a network of branches in human blood capillaries. A noticeable shift in the DOX uptake by MCF-7 cells was observed when cells flowed through the fabricated microchannels compared to DOX uptake by MCF-7 cells in a static centrifuge tube. The fold change in DOX uptake was observed to be 1.17 times higher in a channel with bifurcation of varying width (Channel A).

Meanwhile, a remarkable fold change of 1.78 times was observed in a microchannel with different curves of constant width with periodic changes in curvature (Channel B). Various hydrodynamic conditions attributed to higher DOX uptake in the fabricated microchannel. One reason is the deformation of cells when they enter the channel bifurcations. The deformations of cells were observed to be higher when they entered the channel bifurcations. The cells exhibited a non-monotonic zig-zag pattern of deformation inside microchannels. The deformation was observed to increase at the region where the curvature of the microchannels changed. MCF-7 cells could undergo faster stress relaxation after flowing through the high shear zone of narrow confinement of 14.5 μm. The cell's foretip and tail end were observed to move at different speeds due to the cells' response to stresses brought about by changes in curvature. There was periodic increase and decrease of the cell's fore tip and tail end speed. The peak of speed ratio was higher in the region where cells showed maximum deformation. In addition, it was also observed that flow trajectory became tortuous in the narrowest confinement. Furthermore, it was evident that the cell's deformation was greatly affected by a change in curvature. As a result, a higher deformation was observed in the inflection regions of Channel B, leading to a higher DOX uptake in that configuration. The fabricated channel can open a new efficient method for assessing uptake of drugs on cells.

Various useful information was unraveled in the thesis. However, there are still certain limitations that can be addressed for immediate application of the research findings of the present study. In terms of numerical modeling, Newtonian fluid was assumed to model the carrier fluid, but in real intravenous flow, drug particles flow in blood as a carrier fluid. As blood exhibits a non-Newtonian behavior, a shear-thinning carrier fluid model should be selected for the numerical simulations. Besides, the presence of blood cells can also affect the transport of drug particles. A multiparticle model should be adopted for a closer estimation of the simultaneous transportation of blood cells and drug particles. Furthermore, fabrication of the cell-laden microchannel walls should be done to mimic the cellular environment prevailing in the blood capillaries. The replication of the cellular environment with a controlled pH level is required to increase the acceptability in the area of drug delivery through blood vessels.

7.2 Scope for future work

The present thesis presented an experimental and numerical investigation of the flow of viscoelastic drug carriers and drug uptake on MCF-7 cells in constricted microchannels designed to mimic the blood capillary network. In addition to the

present investigations, more insight can be obtained by carrying out the following study as a future extension of the work.

- An experimental setup can be designed to find the critical capillary number for viscoelastic drop breakup in a constricted microchannel. The information obtained from the numerical results reported in the thesis can be used to design the experimental setup. A microchannel can be fabricated to generate a larger drop and flow through a constricted microchannel to achieve an on-demand drop breakup. The solution of CMC (carboxymethyl cellulose) can be used for generating viscoelastic drop.
- A more complex microchannel design can be designed to replicate the complex network of human blood capillaries. Organ on-chip can be designed to understand the inter-organ transport of drug particles. The complex microchannel should be able to replicate the organs of the body. The cell laden microchannel wall can be fabricated for replicating the walls of the blood capillaries wall. A shear-thinning carrier fluid can be used for experimental and numerical study for modelling the intravenous blood flow.
- A drug-release device that can achieve zero-order release kinetics can be developed to develop drug delivery systems efficiently. The drug release device, together with the drug uptake microfluidic device discussed in the study, can be a potent drug delivery microdevice. The drug delivery device is required to achieve a controlled and targeted drug release for a more extended period.

References

[1] D. J. Beebe, G. A. Mensing, and G. M. Walker, "Physics and applications of microfluidics in biology," *Annual review of biomedical engineering*, vol. 4, no. 1, pp. 261–286, 2002.

[2] S. Chakraborty *et al.*, *Microfluidics and microfabrication*. Springer, 2010, vol. 1.

[3] P. Tabeling, *Introduction to microfluidics*. OUP Oxford, 2005.

[4] N. Convery and N. Gadegaard, "30 years of microfluidics," *Micro and Nano Engineering*, vol. 2, pp. 76–91, 2019.

[5] Z. Khazaei, S. M. Namayandeh, R. Beiranvand, H. Naemi, S. M. Bechashk, and E. Goodarzi, "Worldwide incidence and mortality of ovarian cancer and human development index (hdi): Globocan sources and methods 2018," *Journal of preventive medicine and hygiene*, vol. 62, no. 1, p. E174, 2021.

[6] B. A. Chabner and T. G. Roberts Jr, "Chemotherapy and the war on cancer," *Nature Reviews Cancer*, vol. 5, no. 1, p. 65, 2005.

[7] V. T. DeVita and E. Chu, "A history of cancer chemotherapy," *Cancer research*, vol. 68, no. 21, pp. 8643–8653, 2008.

[8] W. Zhang, Z. Zhang, and Y. Zhang, "The application of carbon nanotubes in target drug delivery systems for cancer therapies," *Nanoscale research letters*, vol. 6, no. 1, p. 555, 2011.

[9] S. S. Ahmad, M. A. Reinius, H. M. Hatcher, and T. V. Ajithkumar, "Anti-cancer chemotherapy in teenagers and young adults: managing long term side effects," *Bmj*, vol. 354, p. i4567, 2016.

[10] K. Nooter and G. Stoter, "Molecular mechanisms of multidrug resistance in cancer chemotherapy," *Pathology-Research and Practice*, vol. 192, no. 7, pp. 768–780, 1996.

[11] X. Liang, C. Chen, Y. Zhao, and P. Wang, "Multi-drug resistance in cancer," 2010.

[12] K. O. Alfarouk, C.-M. Stock, S. Taylor, M. Walsh, A. K. Muddathir, D. Verduzco, A. H. Bashir, O. Y. Mohammed, G. O. Elhassan, S. Harguindey *et al.*, "Resistance to cancer chemotherapy: failure in drug response from adme to p-gp," *Cancer cell international*, vol. 15, no. 1, p. 71, 2015.

[13] S. Senapati, A. K. Mahanta, S. Kumar, and P. Maiti, "Controlled drug delivery vehicles for cancer treatment and their performance," *Signal transduction and targeted therapy*, vol. 3, no. 1, pp. 1–19, 2018.

[14] H. Maeda, J. Wu, T. Sawa, Y. Matsumura, and K. Hori, "Tumor vascular permeability and the epr effect in macromolecular therapeutics: a review," *Journal of controlled release*, vol. 65, no. 1-2, pp. 271–284, 2000.

[15] H. Koo, M. S. Huh, I.-C. Sun, S. H. Yuk, K. Choi, K. Kim, and I. C. Kwon, "In vivo targeted delivery of nanoparticles for theranosis," *Accounts of chemical research*, vol. 44, no. 10, pp. 1018–1028, 2011.

[16] Y. H. Bae and K. Park, "Targeted drug delivery to tumors: myths, reality and possibility," *Journal of controlled release*, vol. 153, no. 3, p. 198, 2011.

[17] C. Ding, L. Tong, J. Feng, and J. Fu, "Recent advances in stimuli-responsive release function drug delivery systems for tumor treatment," *Molecules*, vol. 21, no. 12, p. 1715, 2016.

[18] K. S. Soppimath, T. M. Aminabhavi, A. R. Kulkarni, and W. E. Rudzinski, "Biodegradable polymeric nanoparticles as drug delivery devices," *Journal of controlled release*, vol. 70, no. 1-2, pp. 1–20, 2001.

[19] J. Su, F. Chen, V. L. Cryns, and P. B. Messersmith, "Catechol polymers for ph-responsive, targeted drug delivery to cancer cells," *Journal of the American Chemical Society*, vol. 133, no. 31, pp. 11 850–11 853, 2011.

[20] M. S. Shim and Y. J. Kwon, "Stimuli-responsive polymers and nanomaterials for gene delivery and imaging applications," *Advanced drug delivery reviews*, vol. 64, no. 11, pp. 1046–1059, 2012.

[21] S. Kumar, S. Singh, S. Senapati, A. P. Singh, B. Ray, and P. Maiti, "Controlled drug release through regulated biodegradation of poly (lactic acid) using inorganic salts," *International journal of biological macromolecules*, vol. 104, pp. 487–497, 2017.

[22] R. Mo, T. Jiang, and Z. Gu, "Recent progress in multidrug delivery to cancer cells by liposomes," *Nanomedicine*, vol. 9, no. 8, pp. 1117–1120, 2014.

[23] Y. Dong, A. A. Eltoukhy, C. A. Alabi, O. F. Khan, O. Veiseh, J. R. Dorkin, S. Sirirungruang, H. Yin, B. C. Tang, J. M. Pelet *et al.*, "Lipid-like nanomaterials for simultaneous gene expression and silencing in vivo," *Advanced healthcare materials*, vol. 3, no. 9, pp. 1392–1397, 2014.

[24] H. Shih and C.-C. Lin, "Photoclick hydrogels prepared from functionalized cyclodextrin and poly (ethylene glycol) for drug delivery and in situ cell encapsulation," *Biomacromolecules*, vol. 16, no. 7, pp. 1915–1923, 2015.

[25] Y. Li, D. Maciel, J. Rodrigues, X. Shi, and H. Tomas, "Biodegradable polymer nanogels for drug/nucleic acid delivery," *Chemical reviews*, vol. 115, no. 16, pp. 8564–8608, 2015.

[26] W. Sun and Z. Gu, "Engineering dna scaffolds for delivery of anticancer therapeutics," *Biomaterials science*, vol. 3, no. 7, pp. 1018–1024, 2015.

[27] F. X. Gu, R. Karnik, A. Z. Wang, F. Alexis, E. Levy-Nissenbaum, S. Hong, R. S. Langer, and O. C. Farokhzad, "Targeted nanoparticles for cancer therapy," *Nano today*, vol. 2, no. 3, pp. 14–21, 2007.

[28] D. Lombardo, M. A. Kiselev, and M. T. Caccamo, "Smart nanoparticles for drug delivery application: development of versatile nanocarrier platforms in biotechnology and nanomedicine," *Journal of Nanomaterials*, vol. 2019, 2019.

[29] L. Sun, H. Liu, Y. Ye, Y. Lei, R. Islam, S. Tan, R. Tong, Y.-B. Miao, and L. Cai, "Smart nanoparticles for cancer therapy," *Signal Transduction and Targeted Therapy*, vol. 8, no. 1, p. 418, 2023.

[30] A. Rana, M. Adhikary, P. K. Singh, B. C. Das, and S. Bhatnagar, ""smart" drug delivery: A window to future of translational medicine," *Frontiers in Chemistry*, vol. 10, p. 1095598, 2023.

[31] D. Peer, J. M. Karp, S. Hong, O. C. Farokhzad, R. Margalit, and R. Langer, "Nanocarriers as an emerging platform for cancer therapy," *Nature nanotechnology*, vol. 2, no. 12, p. 751, 2007.

[32] B. K. Lee, Y. H. Yun, and K. Park, "Smart nanoparticles for drug delivery: Boundaries and opportunities," *Chemical engineering science*, vol. 125, pp. 158–164, 2015.

[33] D. Liu, F. Yang, F. Xiong, and N. Gu, "The smart drug delivery system and its clinical potential. theranostics 6: 1306–1323," 2016.

[34] A. Abuchowski, J. R. McCoy, N. C. Palczuk, T. van Es, and F. F. Davis, "Effect of covalent attachment of polyethylene glycol on immunogenicity and circulating life of bovine liver catalase." *Journal of Biological Chemistry*, vol. 252, no. 11, pp. 3582–3586, 1977.

[35] S. M. Moghimi and J. Szebeni, "Stealth liposomes and long circulating nanoparticles: critical issues in pharmacokinetics, opsonization and protein-binding properties," *Progress in lipid research*, vol. 42, no. 6, pp. 463–478, 2003.

[36] S. M. Moghimi, A. C. Hunter, and J. C. Murray, "Long-circulating and target-specific nanoparticles: theory to practice," *Pharmacological reviews*, vol. 53, no. 2, pp. 283–318, 2001.

[37] K. Knop, R. Hoogenboom, D. Fischer, and U. S. Schubert, "Poly (ethylene glycol) in drug delivery: pros and cons as well as potential alternatives," *Angewandte chemie international edition*, vol. 49, no. 36, pp. 6288–6308, 2010.

[38] J. J. Verhoef and T. J. Anchordoquy, "Questioning the use of pegylation for drug delivery," *Drug delivery and translational research*, vol. 3, no. 6, pp. 499–503, 2013.

[39] I. Wong and C.-M. Ho, "Surface molecular property modifications for poly (dimethylsiloxane)(pdms) based microfluidic devices," *Microfluidics and nanofluidics*, vol. 7, no. 3, p. 291, 2009.

[40] B. Huang, H. Wu, S. Kim, and R. N. Zare, "Coating of poly (dimethylsiloxane) with n-dodecyl-β-d-maltoside to minimize nonspecific protein adsorption," *Lab on a Chip*, vol. 5, no. 10, pp. 1005–1007, 2005.

[41] R. Toy, E. Hayden, C. Shoup, H. Baskaran, and E. Karathanasis, "The effects of particle size, density and shape on margination of nanoparticles in microcirculation," *Nanotechnology*, vol. 22, no. 11, p. 115101, 2011.

[42] H. Ye, Z. Shen, L. Yu, M. Wei, and Y. Li, "Manipulating nanoparticle transport within blood flow through external forces: An exemplar of mechanics in

nanomedicine," *Proceedings of the Royal Society A: Mathematical, Physical and Engineering Sciences*, vol. 474, no. 2211, p. 20170845, 2018.

[43] E. M. Ahmed, "Hydrogel: Preparation, characterization, and applications: A review," *Journal of advanced research*, vol. 6, no. 2, pp. 105–121, 2015.

[44] S. H. Kim, Y. Sun, J. A. Kaplan, M. W. Grinstaff, and J. R. Parquette, "Photo-crosslinking of a self-assembled coumarin-dipeptide hydrogel," *New Journal of Chemistry*, vol. 39, no. 5, pp. 3225–3228, 2015.

[45] A. S. Hoffman, "Hydrogels for biomedical applications," *Advanced drug delivery reviews*, vol. 64, pp. 18–23, 2012.

[46] T. Billiet, M. Vandenhaute, J. Schelfhout, S. Van Vlierberghe, and P. Dubruel, "A review of trends and limitations in hydrogel-rapid prototyping for tissue engineering," *Biomaterials*, vol. 33, no. 26, pp. 6020–6041, 2012.

[47] X. Yu, X. Cao, X. Chen, N. Ayres, and P. Zhang, "Triplet–triplet annihilation upconversion from rationally designed polymeric emitters with tunable inter-chromophore distances," *Chemical Communications*, vol. 51, no. 3, pp. 588–591, 2015.

[48] M. C. Koetting, J. F. Guido, M. Gupta, A. Zhang, and N. A. Peppas, "ph-responsive and enzymatically-responsive hydrogel microparticles for the oral delivery of therapeutic proteins: Effects of protein size, crosslinking density, and hydrogel degradation on protein delivery," *Journal of controlled release*, vol. 221, pp. 18–25, 2016.

[49] Z. Jin, X. Liu, S. Duan, X. Yu, Y. Huang, T. Hayat, and J. Li, "The adsorption of eu (iii) on carbonaceous nanofibers: batch experiments and modeling study," *Journal of Molecular Liquids*, vol. 222, pp. 456–462, 2016.

[50] Q. Chai, Y. Jiao, and X. Yu, "Hydrogels for biomedical applications: their characteristics and the mechanisms behind them," *Gels*, vol. 3, no. 1, p. 6, 2017.

[51] M. McKenzie, D. Betts, A. Suh, K. Bui, L. D. Kim, and H. Cho, "Hydrogel-based drug delivery systems for poorly water-soluble drugs," *Molecules*, vol. 20, no. 11, pp. 20 397–20 408, 2015.

[52] E. Larrañeta, S. Stewart, M. Ervine, R. Al-Kasasbeh, and R. F. Donnelly, "Hydrogels for hydrophobic drug delivery. classification, synthesis and applications," *Journal of functional biomaterials*, vol. 9, no. 1, p. 13, 2018.

[53] I. K. Herrmann, M. J. A. Wood, and G. Fuhrmann, "Extracellular vesicles as a next-generation drug delivery platform," *Nature nanotechnology*, vol. 16, no. 7, pp. 748–759, 2021.

[54] M. W. Tibbitt, J. E. Dahlman, and R. Langer, "Emerging frontiers in drug delivery," *Journal of the American Chemical Society*, vol. 138, no. 3, pp. 704–717, 2016.

[55] K. B. Johnsen, J. M. Gudbergsson, M. N. Skov, L. Pilgaard, T. Moos, and M. Duroux, "A comprehensive overview of exosomes as drug delivery vehicles—endogenous nanocarriers for targeted cancer therapy," *Biochimica et Biophysica Acta (BBA)-Reviews on Cancer*, vol. 1846, no. 1, pp. 75–87, 2014.

[56] S. Kamerkar, V. S. LeBleu, H. Sugimoto, S. Yang, C. F. Ruivo, S. A. Melo, J. J. Lee, and R. Kalluri, "Exosomes facilitate therapeutic targeting of oncogenic kras in pancreatic cancer," *Nature*, vol. 546, no. 7659, pp. 498–503, 2017.

[57] W.-H. Chang, R. A. Cerione, and M. A. Antonyak, "Extracellular vesicles and their roles in cancer progression," in *Cancer Cell Signaling*. Springer, 2021, pp. 143–170.

[58] D. K. Jeppesen, A. M. Fenix, J. L. Franklin, J. N. Higginbotham, Q. Zhang, L. J. Zimmerman, D. C. Liebler, J. Ping, Q. Liu, R. Evans *et al.*, "Reassessment of exosome composition," *Cell*, vol. 177, no. 2, pp. 428–445, 2019.

[59] B. Escudier, T. Dorval, N. Chaput, F. André, M.-P. Caby, S. Novault, C. Flament, C. Leboulaire, C. Borg, S. Amigorena *et al.*, "Vaccination of metastatic melanoma patients with autologous dendritic cell (dc) derived-exosomes: results of thefirst phase i clinical trial," *Journal of translational medicine*, vol. 3, no. 1, pp. 1–13, 2005.

[60] E. Karnas, P. Dudek, and E. Zuba-Surma, "Stem cell-derived extracellular vesicles as new tools in regenerative medicine: immunomodulatory role and future perspectives," *Frontiers in Immunology*, 2023.

[61] Y. Wen, Q. Fu, A. Soliwoda, S. Zhang, M. Zheng, W. Mao, and Y. Wan, "Cell-derived nanovesicles prepared by membrane extrusion are good substitutes for natural extracellular vesicles," *Extracellular vesicle*, vol. 1, p. 100004, 2022.

[62] Q.-V. Le, J. Lee, H. Lee, G. Shim, and Y.-K. Oh, "Cell membrane-derived vesicles for delivery of therapeutic agents," *Acta pharmaceutica Sinica B*, vol. 11, no. 8, pp. 2096–2113, 2021.

[63] Q. Li, J. Shen, L. Wu, S. Lei, Y. Yang, W. Xu, K. Hao, Y. Zhang, F. Kong, W. Yang *et al.*, "Functional targeted therapy for glioma based on platelet membrane-coated nanogels," *Cancer Nanotechnology*, vol. 14, no. 1, p. 12, 2023.

[64] C. Xu, D. Ju, and X. Zhang, "Cell membrane-derived vesicle: A novel vehicle for cancer immunotherapy," *Frontiers in Immunology*, p. 3573, 2022.

[65] T. D. Clemons, R. Singh, A. Sorolla, N. Chaudhari, A. Hubbard, and K. S. Iyer, "Distinction between active and passive targeting of nanoparticles dictate their overall therapeutic efficacy," *Langmuir*, vol. 34, no. 50, pp. 15 343–15 349, 2018.

[66] D.-M. Zhu, L. Wu, M. Suo, S. Gao, W. Xie, M.-H. Zan, A. Liu, B. Chen, W.-T. Wu, L.-W. Ji *et al.*, "Engineered red blood cells for capturing circulating tumor cells with high performance," *Nanoscale*, vol. 10, no. 13, pp. 6014–6023, 2018.

[67] J.-Y. Zhu, D.-W. Zheng, M.-K. Zhang, W.-Y. Yu, W.-X. Qiu, J.-J. Hu, J. Feng, and X.-Z. Zhang, "Preferential cancer cell self-recognition and tumor self-targeting by coating nanoparticles with homotypic cancer cell membranes," *Nano letters*, vol. 16, no. 9, pp. 5895–5901, 2016.

[68] A. P. Bidkar, P. Sanpui, and S. S. Ghosh, "Red blood cell-membrane-coated poly (lactic-co-glycolic acid) nanoparticles for enhanced chemo-and hypoxia-activated therapy," *ACS Applied Bio Materials*, vol. 2, no. 9, pp. 4077–4086, 2019.

[69] K. D. Nyberg, K. H. Hu, S. H. Kleinman, D. B. Khismatullin, M. J. Butte, and A. C. Rowat, "Quantitative deformability cytometry: rapid, calibrated measurements of cell mechanical properties," *Biophysical journal*, vol. 113, no. 7, pp. 1574–1584, 2017.

[70] C. Lim, E. Zhou, and S. Quek, "Mechanical models for living cells—a review," *Journal of biomechanics*, vol. 39, no. 2, pp. 195–216, 2006.

[71] E. Evans and A. Yeung, "Apparent viscosity and cortical tension of blood granulocytes determined by micropipet aspiration," *Biophysical journal*, vol. 56, no. 1, pp. 151–160, 1989.

[72] R. Tran-Son-Tay, D. Needham, A. Yeung, and R. Hochmuth, "Time-dependent recovery of passive neutrophils after large deformation," *Biophysical journal*, vol. 60, no. 4, pp. 856–866, 1991.

[73] G. Schmid-Schonbein, Y. Y. Shih, and S. Chien, "Morphometry of human leukocytes," *Blood*, vol. 56, no. 5, pp. 866–875, 1980.

[74] F. Guilak, J. R. Tedrow, and R. Burgkart, "Viscoelastic properties of the cell nucleus," *Biochemical and biophysical research communications*, vol. 269, no. 3, pp. 781–786, 2000.

[75] N. Caille, O. Thoumine, Y. Tardy, and J.-J. Meister, "Contribution of the nucleus to the mechanical properties of endothelial cells," *Journal of biomechanics*, vol. 35, no. 2, pp. 177–187, 2002.

[76] C. Dong, R. Skalak, and K.-L. P. Sung, "Cytoplasmic rheology of passive neutrophils," *Biorheology*, vol. 28, no. 6, pp. 557–567, 1991.

[77] R. Hochmuth, H. Ting-Beall, B. Beaty, D. Needham, and R. Tran-Son-Tay, "Viscosity of passive human neutrophils undergoing small deformations," *Biophysical journal*, vol. 64, no. 5, pp. 1596–1601, 1993.

[78] F. Y. Leong, Q. Li, C. T. Lim, and K.-H. Chiam, "Modeling cell entry into a micro-channel," *Biomechanics and modeling in mechanobiology*, vol. 10, no. 5, pp. 755–766, 2011.

[79] Z. Luo, F. Xu, T. Lu, and B. Bai, "Direct numerical simulation of single leukocyte deformation in microchannel flow for disease diagnosis," *Journal of medical systems*, vol. 35, no. 5, pp. 869–876, 2011.

[80] S. Osher and J. A. Sethian, "Fronts propagating with curvature-dependent speed: algorithms based on hamilton-jacobi formulations," *Journal of computational physics*, vol. 79, no. 1, pp. 12–49, 1988.

[81] I. L. Ahmad and M. R. B. Ahmad, "A two component red blood cell model for single cell mechanic," 2015.

[82] M. A. Tsai, R. S. Frank, and R. E. Waugh, "Passive mechanical behavior of human neutrophils: power-law fluid," *Biophysical journal*, vol. 65, no. 5, pp. 2078–2088, 1993.

[83] W. Wang, Y. Huang, and D. B. Chrisey, "Numerical study of cell droplet and hydrogel coating impact process in cell direct writing," *Trans. NAMRI/SME*, vol. 35, pp. 217–223, 2007.

[84] S. H. Au, B. D. Storey, J. C. Moore, Q. Tang, Y.-L. Chen, S. Javaid, A. F. Sarioglu, R. Sullivan, M. W. Madden, R. O'Keefe *et al.*, "Clusters of circulating tumor cells traverse capillary-sized vessels," *Proceedings of the National Academy of Sciences*, vol. 113, no. 18, pp. 4947–4952, 2016.

[85] A. Raj and A. Sen, "Entry and passage behavior of biological cells in a constricted compliant microchannel," *RSC advances*, vol. 8, no. 37, pp. 20 884–20 893, 2018.

[86] S. M. Mijailovich, M. Kojic, M. Zivkovic, B. Fabry, and J. J. Fredberg, "A finite element model of cell deformation during magnetic bead twisting," *Journal of Applied Physiology*, vol. 93, no. 4, pp. 1429–1436, 2002.

[87] J. Barber and L. Zhu, "Two-dimensional finite element model of breast cancer cell motion through a microfluidic channel," *Bulletin of mathematical biology*, vol. 81, no. 4, pp. 1238–1259, 2019.

[88] T. Ye, H. Shi, N. Phan-Thien, C. T. Lim, and Y. Li, "Numerical design of a microfluidic chip for probing mechanical properties of cells," *Journal of biomechanics*, vol. 84, pp. 103–112, 2019.

[89] X. Wang and Y. Qu, "Dissipative particle dynamics simulation of cells deformation under tensile loading," in *2019 IEEE International Conference on Mechatronics and Automation (ICMA)*. IEEE, 2019, pp. 2257–2261.

[90] C. Dong, R. Skalak, K.-L. P. Sung, G. Schmid-Scho¨ nbein, and S. Chien, "Passive deformation analysis of human leukocytes," 1988.

[91] C. Zhou, P. Yue, and J. J. Feng, "Simulation of neutrophil deformation and transport in capillaries using newtonian and viscoelastic drop models," *Annals of biomedical engineering*, vol. 35, no. 5, pp. 766–780, 2007.

[92] S. J. Hymel, H. Lan, H. Fujioka, and D. B. Khismatullin, "Cell trapping in y-junction microchannels: A numerical study of the bifurcation angle effect in inertial microfluidics," *Physics of Fluids*, vol. 31, no. 8, p. 082003, 2019.

[93] H. Giesekus, "Carried along on a pathline in modelling constitutive equations of viscoelastic fluids," *Rheologica Acta*, vol. 29, no. 6, pp. 500–511, 1990.

[94] C. Simoncini, T. Lecomte, R. Thibeaux, N. Guillen, A. Dufour, and J.-C. Olivo-Marin, "Fluid dynamics modeling of cell and membrane deformations," in *2014 IEEE 11th International Symposium on Biomedical Imaging (ISBI)*. IEEE, 2014, pp. 262–265.

[95] F. Garner and A. H. Nissan, "Rheological properties of high-viscosity solutions of long molecules," *Nature*, vol. 158, no. 4018, pp. 634–635, 1946.

[96] S. Pundir, A. Badola, D. Sharma *et al.*, "Sustained release matrix technology and recent advance in matrix drug delivery system: a review," *Int J Drug Res Tech*, vol. 3, no. 1, pp. 12–20, 2013.

[97] J. Jagur-Grodzinski, "Polymers for targeted and/or sustained drug delivery," *Polymers for Advanced Technologies*, vol. 20, no. 7, pp. 595–606, 2009.

[98] S. Sershen and J. West, "Implantable, polymeric systems for modulated drug delivery," *Advanced drug delivery reviews*, vol. 54, no. 9, pp. 1225–1235, 2002.

[99] S. H. Lee, M. Park, C. G. Park, J. E. Lee, M. R. Prausnitz, and Y. B. Choy, "Microchip for sustained drug delivery by diffusion through microchannels," *Aaps Pharmscitech*, vol. 13, pp. 211–217, 2012.

[100] S. H. Lee, M. Park, C. G. Park, B.-H. Kim, J. Lee, S. Choi, S.-r. Nam, S.-H. Park, and Y. B. Choy, "Implantable micro-chip for controlled delivery of diclofenac sodium," *Journal of Controlled Release*, vol. 196, pp. 52–59, 2014.

[101] R. Vadlapatla, E. Y. Wong, and S. G. Gayakwad, "Electronic drug delivery systems: An overview," *Journal of Drug Delivery Science and Technology*, vol. 41, pp. 359–366, 2017.

[102] A. N. Khan, A. Ermakov, G. Sukhorukov, and Y. Hao, "Radio frequency controlled wireless drug delivery devices," *Applied Physics Reviews*, vol. 6, no. 4, 2019.

[103] H. B. Ji, S.-N. Kim, S. H. Lee, B. K. Huh, B. H. Shin, C. Lee, Y. C. Cho, C. Y. Heo, and Y. B. Choy, "Soft implantable device with drug-diffusion channels for the controlled release of diclofenac," *Journal of Controlled Release*, vol. 318, pp. 176–184, 2020.

[104] D. Izbassarov and M. Muradoglu, "A front-tracking method for computational modeling of viscoelastic two-phase flow systems," *Journal of Non-Newtonian Fluid Mechanics*, vol. 223, pp. 122–140, 2015.

[105] N. Desai, V. Trieu, Z. Yao, L. Louie, S. Ci, A. Yang, C. Tao, T. De, B. Beals, D. Dykes *et al.*, "Increased antitumor activity, intratumor paclitaxel concentrations, and endothelial cell transport of cremophor-free, albumin-bound paclitaxel, abi-007, compared with cremophor-based paclitaxel." *Clinical cancer research*, vol. 12, no. 4, pp. 1317–1324, 2006.

[106] S. Banerjee, A. K. Sahoo, A. Chattopadhyay, and S. S. Ghosh, "Hydrogel nanocarrier encapsulated recombinant iκbα as a novel anticancer protein therapeutics," *RSC advances*, vol. 3, no. 33, pp. 14 123–14 131, 2013.

[107] M. Saha, A. P. Bidkar, and S. S. Ghosh, "Developing membrane-derived nanocarriers for ex vivo therapy of homologous breast cancer cells," *Nanomedicine*, vol. 16, no. 21, pp. 1843–1856, 2021.

[108] W. Kern, "The evolution of silicon wafer cleaning technology," *Journal of the Electrochemical Society*, vol. 137, no. 6, p. 1887, 1990.

[109] A. J. Chorin, "On the convergence of discrete approximations to the navier-stokes equations," *Mathematics of computation*, vol. 23, no. 106, pp. 341–353, 1969.

[110] J. B. Bell, P. Colella, and H. M. Glaz, "A second-order projection method for the incompressible navier-stokes equations," *Journal of computational physics*, vol. 85, no. 2, pp. 257–283, 1989.

[111] A. S. Almgren, J. B. Bell, and W. Y. Crutchfield, "Approximate projection methods: Part i. inviscid analysis," *SIAM Journal on Scientific Computing*, vol. 22, no. 4, pp. 1139–1159, 2000.

[112] E. Aulisa, S. Manservisi, R. Scardovelli, and S. Zaleski, "Interface reconstruction with least-squares fit and split advection in three-dimensional cartesian geometry," *Journal of Computational Physics*, vol. 225, no. 2, pp. 2301–2319, 2007.

[113] R. B. DeBar, "Fundamentals of the kraken code. [eulerian hydrodynamics code for compressible nonviscous flow of several fluids in two-dimensional (axially symmetric) region]." [Online]. Available: https://www.osti.gov/biblio/7227630

[114] J. Hao and T.-W. Pan, "Simulation for high weissenberg number: viscoelastic flow by a finite element method," *Applied mathematics letters*, vol. 20, no. 9, pp. 988–993, 2007.

[115] C. Chung, J. M. Kim, M. A. Hulsen, K. H. Ahn, and S. J. Lee, "Effect of viscoelasticity on drop dynamics in 5: 1: 5 contraction/expansion microchannel flow," *Chemical engineering science*, vol. 64, no. 22, pp. 4515–4524, 2009.

[116] N. Aggarwal and K. Sarkar, "Deformation and breakup of a viscoelastic drop in a newtonian matrix under steady shear," *Journal of Fluid Mechanics*, vol. 584, pp. 1–21, 2007.

[117] F. Khalkhal and S. Muller, "Analyzing flow behavior of shear-thinning fluids in a planar abrupt contraction/expansion microfluidic geometry," *Physical Review Fluids*, vol. 7, no. 2, p. 023303, 2022.

[118] S. Hazra, L. Malik, S. Mitra, and A. Sen, "Interaction between droplets and co-flow interface in a microchannel: Droplet migration and interfacial deformation," *Physical Review Fluids*, vol. 7, no. 5, p. 054201, 2022.

[119] H. Lan and D. B. Khismatullin, "Numerical simulation of the pairwise interaction of deformable cells during migration in a microchannel," *Physical Review E*, vol. 90, no. 1, p. 012705, 2014.

[120] Z. Zhang, J. Xu, B. Hong, and X. Chen, "The effects of 3d channel geometry on ctc passing pressure–towards deformability-based cancer cell separation," *Lab on a Chip*, vol. 14, no. 14, pp. 2576–2584, 2014.

[121] P. Yue, J. J. Feng, C. Liu, and J. Shen, "Viscoelastic effects on drop deformation in steady shear," *Journal of Fluid Mechanics*, vol. 540, pp. 427–437, 2005.

[122] S. Ramaswamy and L. Leal, "The deformation of a newtonian drop in the uniaxial extensional flow of a viscoelastic liquid," *Journal of non-newtonian fluid mechanics*, vol. 88, no. 1-2, pp. 149–172, 1999.

[123] L. Ferrás, A. Afonso, M. Alves, J. Nóbrega, and F. Pinho, "Newtonian and viscoelastic fluid flows through an abrupt 1: 4 expansion with slip boundary conditions," *Physics of Fluids*, vol. 32, no. 4, p. 043103, 2020.

[124] C. Chung, M. A. Hulsen, J. M. Kim, K. H. Ahn, and S. J. Lee, "Numerical study on the effect of viscoelasticity on drop deformation in simple shear and 5: 1: 5 planar contraction/expansion microchannel," *Journal of Non-Newtonian fluid mechanics*, vol. 155, no. 1-2, pp. 80–93, 2008.

[125] C. Chung, K. H. Ahn, and S. J. Lee, "Numerical study on the dynamics of droplet passing through a cylinder obstruction in confined microchannel flow," *Journal of Non-Newtonian fluid mechanics*, vol. 162, no. 1-3, pp. 38–44, 2009.

[126] H. Zolfaghari, D. Izbassarov, and M. Muradoglu, "Simulations of viscoelastic two-phase flows in complex geometries," *Computers & Fluids*, vol. 156, pp. 548–561, 2017.

[127] D. Zhou, P. Yue, and J. J. Feng, "Viscoelastic effects on drop deformation in a converging pipe flow," *Journal of Rheology*, vol. 52, no. 2, pp. 469–487, 2008.

[128] A. Gupta and M. Sbragaglia, "Deformation and breakup of viscoelastic droplets in confined shear flow," *Physical Review E*, vol. 90, no. 2, p. 023305, 2014.

[129] H. Li and U. Sundararaj, "Experimental investigation of viscoelastic drop deformation in newtonian matrix at high capillary number under simple shear flow," *Journal of non-newtonian fluid mechanics*, vol. 165, no. 19-20, pp. 1219–1227, 2010.

[130] N. Aggarwal and K. Sarkar, "Effects of matrix viscoelasticity on viscous and viscoelastic drop deformation in a shear flow," *Journal of Fluid Mechanics*, vol. 601, pp. 63–84, 2008.

[131] S. Mukherjee and K. Sarkar, "Effects of viscosity ratio on deformation of a viscoelastic drop in a newtonian matrix under steady shear," *Journal of Non-Newtonian Fluid Mechanics*, vol. 160, no. 2-3, pp. 104–112, 2009.

[132] H. Li and U. Sundararaj, "Does drop size affect the mechanism of viscoelastic drop breakup?" *Physics of fluids*, vol. 20, no. 5, p. 053101, 2008.

[133] R. Poole, "The deborah and weissenberg numbers," *Rheol. Bull*, vol. 53, no. 2, pp. 32–39, 2012.

[134] M. Xiao, W. Lai, F. Wang, L. Li, C. Fan, and H. Pei, "Programming drug delivery kinetics for active burst release with dna toehold switches," *Journal of the American Chemical Society*, vol. 141, no. 51, pp. 20 354–20 364, 2019.

[135] D. Izbassarov and M. Muradoglu, "A computational study of two-phase viscoelastic systems in a capillary tube with a sudden contraction/expansion," *Physics of Fluids*, vol. 28, no. 1, p. 012110, 2016.

[136] V. Sibillo, G. Pasquariello, M. Simeone, V. Cristini, and S. Guido, "Drop deformation in microconfined shear flow," *Physical review letters*, vol. 97, no. 5, p. 054502, 2006.

[137] A. Vananroye, P. Van Puyvelde, and P. Moldenaers, "Effect of confinement on droplet breakup in sheared emulsions," *Langmuir*, vol. 22, no. 9, pp. 3972–3974, 2006.

[138] A. Hooper and W. Boyd, "Shear-flow instability at the interface between two viscous fluids," *Journal of Fluid Mechanics*, vol. 128, pp. 507–528, 1983.

[139] V. Tirtaatmadja, G. H. McKinley, and J. J. Cooper-White, "Drop formation and breakup of low viscosity elastic fluids: Effects of molecular weight and concentration," *Physics of fluids*, vol. 18, no. 4, p. 043101, 2006.

[140] B. Nath, A. Raza, V. Sethi, A. Dalal, S. S. Ghosh, and G. Biswas, "Understanding flow dynamics, viability and metastatic potency of cervical cancer (hela) cells through constricted microchannel," *Scientific Reports*, vol. 8, no. 1, p. 17357, 2018.

[141] D. Wang, D. S. Tan, B. C. Khoo, Z. Ouyang, and N. Phan-Thien, "A lattice boltzmann modeling of viscoelastic drops' deformation and breakup in simple shear flows," *Physics of Fluids*, vol. 32, no. 12, p. 123101, 2020.

[142] W. Lerdwijitjarud, R. G. Larson, A. Sirivat, and M. J. Solomon, "Influence of weak elasticity of dispersed phase on droplet behavior in sheared polybutadiene/poly (dimethyl siloxane) blends," *Journal of Rheology*, vol. 47, no. 1, pp. 37–58, 2003.

[143] S. Peng, Y.-L. Xiong, X.-Y. Xu, and P. Yu, "Numerical study of unsteady viscoelastic flow past two side-by-side circular cylinders," *Physics of Fluids*, vol. 32, no. 8, p. 083106, 2020.

[144] M. C. Operti, Y. Dölen, J. Keulen, E. A. van Dinther, C. G. Figdor, and O. Tagit, "Microfluidics-assisted size tuning and biological evaluation of plga particles," *Pharmaceutics*, vol. 11, no. 11, p. 590, 2019.

[145] A. Chyzy, M. Tomczykowa, and M. E. Plonska-Brzezinska, "Hydrogels as potential nano-, micro-and macro-scale systems for controlled drug delivery," *Materials*, vol. 13, no. 1, p. 188, 2020.

[146] X. Li, H. Qin, X. Zhang, and Z. Guo, "Triple-network hydrogels with high strength, low friction and self-healing by chemical-physical crosslinking," *Journal of colloid and interface science*, vol. 556, pp. 549–556, 2019.

[147] M. Guvendiren, H. D. Lu, and J. A. Burdick, "Shear-thinning hydrogels for biomedical applications," *Soft matter*, vol. 8, no. 2, pp. 260–272, 2012.

[148] Y. Liu and S.-h. Hsu, "Synthesis and biomedical applications of self-healing hydrogels," *Frontiers in chemistry*, vol. 6, p. 449, 2018.

[149] Y. Pang, J. Liu, Z. L. Moussa, J. E. Collins, S. McDonnell, A. M. Hayward, K. Jajoo, R. Langer, and G. Traverso, "Endoscopically injectable shear-thinning hydrogels facilitating polyp removal," *Advanced Science*, vol. 6, no. 19, p. 1901041, 2019.

[150] J. Jin and Z. M. Bhujwalla, "Biomimetic nanoparticles camouflaged in cancer cell membranes and their applications in cancer theranostics," *Frontiers in Oncology*, vol. 9, p. 1560, 2020.

[151] J. Yoo, C. Park, G. Yi, D. Lee, and H. Koo, "Active targeting strategies using biological ligands for nanoparticle drug delivery systems," *Cancers*, vol. 11, no. 5, p. 640, 2019.

[152] E. J. Comparetti, P. M. Lins, J. V. Quitiba, and V. Zucolotto, "Cancer cell membrane-derived nanoparticles improve the activity of gemcitabine and paclitaxel on pancreatic cancer cells and coordinate immunoregulatory properties on professional antigen-presenting cells," *Materials Advances*, vol. 1, no. 6, pp. 1775–1787, 2020.

[153] H. He, C. Guo, W. Liu, S. Chen, X.-Y. Wang, and H. Yang, "Engineering nanostructured pure cancer cell membrane-derived vesicles as a novel therapeutic cancer vaccine," *MedComm–Biomaterials and Applications*, vol. 1, no. 2, p. e22, 2022.

[154] Y. Yu, Q. Cheng, X. Ji, H. Chen, W. Zeng, X. Zeng, Y. Zhao, and L. Mei, "Engineered drug-loaded cellular membrane nanovesicles for efficient treatment of postsurgical cancer recurrence and metastasis," *Science Advances*, vol. 8, no. 49, p. eadd3599, 2022.

[155] S. Wadhwa, V. Garg, M. Gulati, B. Kapoor, S. K. Singh, and N. Mittal, "Nanovesicles for nanomedicine: theory and practices," *Pharmaceutical Nanotechnology: Basic Protocols*, pp. 1–17, 2019.

[156] K. Müller, D. A. Fedosov, and G. Gompper, "Margination of micro-and nano-particles in blood flow and its effect on drug delivery," *Scientific reports*, vol. 4, no. 1, pp. 1–8, 2014.

[157] V. Tirtaatmadja and T. Sridhar, "Comparison of constitutive equations for polymer solutions in uniaxial extension," *Journal of Rheology*, vol. 39, no. 6, pp. 1133–1160, 1995.

[158] S. Lenzini, R. Bargi, G. Chung, and J.-W. Shin, "Matrix mechanics and water permeation regulate extracellular vesicle transport," *Nature nanotechnology*, vol. 15, no. 3, pp. 217–223, 2020.

[159] M. S. B. Husain, A. Gupta, B. Y. Alashwal, and S. Sharma, "Synthesis of pva/pvp based hydrogel for biomedical applications: a review," *Energy Sources, Part A: Recovery, Utilization, and Environmental Effects*, vol. 40, no. 20, pp. 2388–2393, 2018.

[160] P. Rees, J. W. Wills, M. R. Brown, C. M. Barnes, and H. D. Summers, "The origin of heterogeneous nanoparticle uptake by cells," *Nature communications*, vol. 10, no. 1, pp. 1–8, 2019.

[161] R. Narayanaswamy and V. P. Torchilin, "Hydrogels and their applications in targeted drug delivery," *Molecules*, vol. 24, no. 3, p. 603, 2019.

[162] H. Xu, A. Clarke, J. Rothstein, and R. Poole, "Viscoelastic drops moving on hydrophilic and superhydrophobic surfaces," *Journal of colloid and interface science*, vol. 513, pp. 53–61, 2018.

[163] G. J. Tortora and B. Derrickson, "The cardiovascular system: blood vessels and hemodynamics," *Principles of anatomy and physiology*, pp. 610–635, 2012.

[164] R. P. Shank, D. R. Doose, A. J. Streeter, and M. Bialer, "Plasma and whole blood pharmacokinetics of topiramate: the role of carbonic anhydrase," *Epilepsy research*, vol. 63, no. 2-3, pp. 103–112, 2005.

[165] E. A. Swabb, J. Wei, and P. M. Gullino, "Diffusion and convection in normal and neoplastic tissues," *Cancer research*, vol. 34, no. 10, pp. 2814–2822, 1974.

[166] M. S. Aapro and G. Von Minckwitz, "Molecular basis for the development of novel taxanes in the treatment of metastatic breast cancer," *European Journal of Cancer Supplements*, vol. 6, no. 10, pp. 3–11, 2008.

[167] E. K. Rowinsky, L. A. Cazenave, and R. C. Donehower, "Taxol: a novel investigational antimicrotubule agent," *JNCI: Journal of the National Cancer Institute*, vol. 82, no. 15, pp. 1247–1259, 1990.

[168] D. M. Sze, K. Miller, and B. Neilan, "Development of taxol and other endophyte produced anti-cancer agents," *Recent Patents on Anti-Cancer Drug Discovery*, vol. 3, no. 1, pp. 14–19, 2008.

[169] E. P. Winer, D. A. Berry, S. Woolf, D. Duggan, A. Kornblith, L. N. Harris, R. A. Michaelson, J. A. Kirshner, G. F. Fleming, M. C. Perry *et al.*, "Failure of higher-dose paclitaxel to improve outcome in patients with metastatic breast cancer: cancer and leukemia group b trial 9342," *Journal of clinical oncology*, vol. 22, no. 11, pp. 2061–2068, 2004.

[170] J. Kloover, M. Den Bakker, H. Gelderblom, and J. Van Meerbeeck, "Fatal outcome of a hypersensitivity reaction to paclitaxel: a critical review of premedication regimens," *British journal of cancer*, vol. 90, no. 2, pp. 304–305, 2004.

[171] Y. Okamoto, K. Taguchi, S. Imoto, V. T. G. Chuang, K. Yamasaki, and M. Otagiri, "Cell uptake and anti-tumor effect of liposomes containing encapsulated paclitaxel-bound albumin against breast cancer cells in 2d

and 3d cultured models," *Journal of Drug Delivery Science and Technology*, vol. 55, p. 101381, 2020.

[172] A. S. Azmi, H. Y. Khan, I. Muqbil, A. Aboukameel, J. E. Neggers, D. Daelemans, A. Mahipal, G. Dyson, M. Kamgar, M. N. Al-Hallak *et al.*, "Preclinical assessment with clinical validation of selinexor with gemcitabine and nab-paclitaxel for the treatment of pancreatic ductal adenocarcinoma," *Clinical Cancer Research*, vol. 26, no. 6, pp. 1338–1348, 2020.

[173] X. Xiao, W. Chen, Z.-W. Wei, W.-W. Chu, X.-F. Lu, B. Li, H. Chen, S.-J. Meng, T.-F. Hao, J.-T. Wei *et al.*, "The anti-tumor effect of nab-paclitaxel proven by patient-derived organoids," *OncoTargets and therapy*, vol. 13, p. 6017, 2020.

[174] B. Karger, Y. Chu, and F. Foret, "Capillary electrophoresis of proteins and nucleic acids," *Annual review of biophysics and biomolecular structure*, vol. 24, no. 1, pp. 579–610, 1995.

[175] D. Y. Zhang, C. Dmello, L. Chen, V. A. Arrieta, E. Gonzalez-Buendia, J. R. Kane, L. P. Magnusson, A. Baran, C. D. James, C. Horbinski *et al.*, "Ultrasound-mediated delivery of paclitaxel for glioma: A comparative study of distribution, toxicity, and efficacy of albumin-bound versus cremophor formulations," *Clinical Cancer Research*, vol. 26, no. 2, pp. 477–486, 2020.

[176] Z. Hu, B. Zheng, J. Xu, S. Gao, and W. Lu, "An albumin-bound drug conjugate of paclitaxel and indoleamine-2, 3-dioxygenase inhibitor for enhanced cancer chemo-immunotherapy," *Nanotechnology*, vol. 31, no. 29, p. 295101, 2020.

[177] V. Hlady and J. Buijs, "Protein adsorption on solid surfaces," *Current opinion in biotechnology*, vol. 7, no. 1, pp. 72–77, 1996.

[178] C. A. Ross and M. A. Poirier, "Protein aggregation and neurodegenerative disease," *Nature medicine*, vol. 10, no. 7, pp. S10–S17, 2004.

[179] M. Tominaga, M. J. Caterina, A. B. Malmberg, T. A. Rosen, H. Gilbert, K. Skinner, B. E. Raumann, A. I. Basbaum, and D. Julius, "The cloned capsaicin receptor integrates multiple pain-producing stimuli," *Neuron*, vol. 21, no. 3, pp. 531–543, 1998.

[180] I. Firkowska-Boden, X. Zhang, and K. D. Jandt, "Controlling protein adsorption through nanostructured polymeric surfaces," *Advanced healthcare materials*, vol. 7, no. 1, p. 1700995, 2018.

[181] J. D. Andrade, *Surface and Interfacial Aspects of Biomedical Polymers: Volume 1 Surface Chemistry and Physics*. Springer Science & Business Media, 2012.

[182] A. Cooper, "Conformational fluctuation and change in biological macromolecules," *Science Progress (1933-)*, pp. 473–497, 1980.

[183] S. Clarke, "The hydrophobic effect: Formation of micelles and biological membranes, (tanford, charles)," 1981.

[184] M. Rabe, D. Verdes, and S. Seeger, "Understanding protein adsorption phenomena at solid surfaces," *Advances in colloid and interface science*, vol. 162, no. 1-2, pp. 87–106, 2011.

[185] K. C. Dee, D. A. Puleo, and R. Bizios, *An introduction to tissue-biomaterial interactions*. John Wiley & Sons, 2003.

[186] A. Brüning and J. Jückstock, "Misfolded proteins: from little villains to little helpers in the fight against cancer," *Frontiers in oncology*, vol. 5, p. 47, 2015.

[187] J. Tyedmers, A. Mogk, and B. Bukau, "Cellular strategies for controlling protein aggregation," *Nature reviews Molecular cell biology*, vol. 11, no. 11, pp. 777–788, 2010.

[188] F. G. D. Felice, M. N. Vieira, M. N. L. Meirelles, L. A. Morozova-Roche, C. M. Dobson, and S. T. Ferreira, "Formation of amyloid aggregates from human lysozyme and its disease-associated variants using hydrostatic pressure," *The FASEB journal*, vol. 18, no. 10, pp. 1099–1101, 2004.

[189] Y. Fung, B. W. Zweifach, and M. Intaglietta, "Elastic environment of the capillary bed," *Circulation research*, vol. 19, no. 2, pp. 441–461, 1966.

[190] S. Byun, S. Son, D. Amodei, N. Cermak, J. Shaw, J. H. Kang, V. C. Hecht, M. M. Winslow, T. Jacks, P. Mallick *et al.*, "Characterizing deformability and surface friction of cancer cells," *Proceedings of the National Academy of Sciences*, vol. 110, no. 19, pp. 7580–7585, 2013.

[191] P. M. Davidson, C. Denais, M. C. Bakshi, and J. Lammerding, "Nuclear deformability constitutes a rate-limiting step during cell migration in 3-d environments," *Cellular and molecular bioengineering*, vol. 7, no. 3, pp. 293–306, 2014.

[192] B. Nath, A. P. Bidkar, V. Kumar, A. Dalal, M. K. Jolly, S. S. Ghosh, and G. Biswas, "Deciphering hydrodynamic and drug-resistant behaviors of

metastatic emt breast cancer cells moving in a constricted microcapillary," *Journal of clinical medicine*, vol. 8, no. 8, p. 1194, 2019.

[193] S. Hazra, A. Nath, S. Mitra, and A. Sen, "Dynamics of rigid particles in a confined flow of viscoelastic and strongly shear-thinning fluid at very small reynolds numbers," *Physics of Fluids*, vol. 33, no. 5, p. 052001, 2021.

[194] E. M. Hotze, T. Phenrat, and G. V. Lowry, "Nanoparticle aggregation: challenges to understanding transport and reactivity in the environment," *Journal of environmental quality*, vol. 39, no. 6, pp. 1909–1924, 2010.

[195] D. Pasias, A. Passos, G. Constantinides, S. Balabani, and E. Kaliviotis, "Surface tension driven flow of blood in a rectangular microfluidic channel: Effect of erythrocyte aggregation," *Physics of Fluids*, vol. 32, no. 7, p. 071903, 2020.

[196] Z. Y. Luo and B. F. Bai, "Retardation of droplet transport in confined microchannel by interfacial jamming of nanoparticles," *Physics of Fluids*, vol. 32, no. 8, p. 087110, 2020.

[197] J. Landau and E. Davis, "Capillary thinning and high capillary blood-pressure in hypertension," *The Lancet*, vol. 269, no. 6983, pp. 1327–1330, 1957.

[198] R. D'Apolito, G. Tomaiuolo, F. Taraballi, S. Minardi, D. Kirui, X. Liu, A. Cevenini, R. Palomba, M. Ferrari, F. Salvatore *et al.*, "Red blood cells affect the margination of microparticles in synthetic microcapillaries and intravital microcirculation as a function of their size and shape," *Journal of Controlled Release*, vol. 217, pp. 263–272, 2015.

[199] R. D'Apolito, F. Taraballi, S. Minardi, X. Liu, S. Caserta, A. Cevenini, E. Tasciotti, G. Tomaiuolo, and S. Guido, "Microfluidic interactions between red blood cells and drug carriers by image analysis techniques," *Medical engineering & physics*, vol. 38, no. 1, pp. 17–23, 2016.

[200] N. Doshi, B. Prabhakarpandian, A. Rea-Ramsey, K. Pant, S. Sundaram, and S. Mitragotri, "Flow and adhesion of drug carriers in blood vessels depend on their shape: a study using model synthetic microvascular networks," *Journal of Controlled Release*, vol. 146, no. 2, pp. 196–200, 2010.

[201] M. Baaden and S. J. Marrink, "Coarse-grain modelling of protein–protein interactions," *Current opinion in structural biology*, vol. 23, no. 6, pp. 878–886, 2013.

[202] S. V. Sokolov, E. Katelhon, and R. G. Compton, "A thermodynamic view of agglomeration," *The Journal of Physical Chemistry C*, vol. 119, no. 44, pp. 25 093–25 099, 2015.

[203] E. J. W. Verwey, "Theory of the stability of lyophobic colloids." *The Journal of Physical Chemistry*, vol. 51, no. 3, pp. 631–636, 1947.

[204] H. C. Hamaker, "The london—van der waals attraction between spherical particles," *physica*, vol. 4, no. 10, pp. 1058–1072, 1937.

[205] S. Bhattacharjee, M. Elimelech, and M. Borkovec, "Dlvo interaction between colloidal particles: Beyond derjaguin's approximation," *Croatica Chemica Acta*, vol. 71, no. 4, pp. 883–903, 1998.

[206] A. Zaccone, H. Wu, D. Gentili, and M. Morbidelli, "Theory of activated-rate processes under shear with application to shear-induced aggregation of colloids," *Physical Review E*, vol. 80, no. 5, p. 051404, 2009.

[207] L. Sicignano, G. Tomaiuolo, A. Perazzo, S. P. Nolan, P. L. Maffettone, and S. Guido, "The effect of shear flow on microreactor clogging," *Chemical Engineering Journal*, vol. 341, pp. 639–647, 2018.

[208] H. Zhao, E. S. Shaqfeh, and V. Narsimhan, "Shear-induced particle migration and margination in a cellular suspension," *Physics of Fluids*, vol. 24, no. 1, p. 011902, 2012.

[209] K. Vahidkhah and P. Bagchi, "Microparticle shape effects on margination, near-wall dynamics and adhesion in a three-dimensional simulation of red blood cell suspension," *Soft Matter*, vol. 11, no. 11, pp. 2097–2109, 2015.

[210] B. Derjaguin and L. Landau, "Theory of the stability of strongly charged lyophobic sols and of the adhesion of strongly charged particles in solutions of electrolytes," *Progress in Surface Science*, vol. 43, no. 1-4, pp. 30–59, 1993.

[211] M. Rosen, "Surfactants and interfacial phenomena, 3rd edn. newyork: John-wiley and sons," 2004.

[212] M. Radhakrishna and S. K. Kumar, "Surface-mediated protein disaggregation," *Langmuir*, vol. 30, no. 12, pp. 3507–3512, 2014.

[213] A. Van Heel, M. Hulsen, and B. Van den Brule, "On the selection of parameters in the fene-p model," *Journal of non-newtonian fluid mechanics*, vol. 75, no. 2-3, pp. 253–271, 1998.

[214] J. Feng and L. Leal, "Numerical simulations of the flow of dilute polymer solutions in a four-roll mill," *Journal of non-newtonian fluid mechanics*, vol. 72, no. 2-3, pp. 187–218, 1997.

[215] R. Zhang, X. Qin, F. Kong, P. Chen, and G. Pan, "Improving cellular uptake of therapeutic entities through interaction with components of cell membrane," *Drug Delivery*, vol. 26, no. 1, pp. 328–342, 2019.

[216] D. B. Kell and S. G. Oliver, "How drugs get into cells: tested and testable predictions to help discriminate between transporter-mediated uptake and lipoidal bilayer diffusion," *Frontiers in pharmacology*, vol. 5, p. 231, 2014.

[217] K. Derakhshandeh, G. Hochhaus, and S. Dadashzadeh, "In-vitro cellular uptake and transport study of 9-nitrocamptothecin plga nanoparticles across caco-2 cell monolayer model," *Iranian journal of pharmaceutical research: IJPR*, vol. 10, no. 3, p. 425, 2011.

[218] L. C. Nelemans and L. Gurevich, "Drug delivery with polymeric nanocarriers—cellular uptake mechanisms," *Materials*, vol. 13, no. 2, p. 366, 2020.

[219] S. Ahn, E. Seo, K. Kim, and S. J. Lee, "Controlled cellular uptake and drug efficacy of nanotherapeutics," *Scientific reports*, vol. 3, no. 1, p. 1997, 2013.

[220] J. Mosquera, I. García, and L. M. Liz-Marzán, "Cellular uptake of nanoparticles versus small molecules: a matter of size," *Accounts of chemical research*, vol. 51, no. 9, pp. 2305–2313, 2018.

[221] S. R. MacEwan, D. J. Callahan, and A. Chilkoti, "Stimulus-responsive macromolecules and nanoparticles for cancer drug delivery," *Nanomedicine*, vol. 5, no. 5, pp. 793–806, 2010.

[222] B. Sebastian and P. S. Dittrich, "Microfluidics to mimic blood flow in health and disease," *Annual review of fluid mechanics*, vol. 50, pp. 483–504, 2018.

[223] Q. Guo, S. J. Reiling, P. Rohrbach, and H. Ma, "Microfluidic biomechanical assay for red blood cells parasitized by plasmodium falciparum," *Lab on a Chip*, vol. 12, no. 6, pp. 1143–1150, 2012.

[224] H. Xia, B. C. Strachan, S. C. Gifford, and S. S. Shevkoplyas, "A high-throughput microfluidic approach for 1000-fold leukocyte reduction of platelet-rich plasma," *Scientific reports*, vol. 6, no. 1, p. 35943, 2016.

[225] A. Jain, A. Graveline, A. Waterhouse, A. Vernet, R. Flaumenhaft, and D. E. Ingber, "A shear gradient-activated microfluidic device for automated

monitoring of whole blood haemostasis and platelet function," *Nature communications*, vol. 7, no. 1, p. 10176, 2016.

[226] M. Tsai, A. Kita, J. Leach, R. Rounsevell, J. N. Huang, J. Moake, R. E. Ware, D. A. Fletcher, W. A. Lam *et al.*, "In vitro modeling of the microvascular occlusion and thrombosis that occur in hematologic diseases using microfluidic technology," *The Journal of clinical investigation*, vol. 122, no. 1, 2011.

[227] J. T. Egaña, A. Condurache, J. A. Lohmeyer, M. Kremer, B. M. Stöckelhuber, S. Lavandero, and H.-G. Machens, "Ex vivo method to visualize and quantify vascular networks in native and tissue engineered skin," *Langenbeck's archives of surgery*, vol. 394, pp. 349–356, 2009.

[228] A. M. Talkington, R. B. Davis, N. C. Datto, E. R. Goodwin, L. A. Miller, and K. M. Caron, "Dermal lymphatic capillaries do not obey murray's law," *Frontiers in Cardiovascular Medicine*, vol. 9, p. 840305, 2022.

[229] S. L. DeMeester, J. P. Cobb, R. S. Hotchkiss, D. F. Osborne, I. E. Karl, K. W. Tinsley, and T. G. Buchman, "Stress-induced fractal rearrangement of the endothelial cell cytoskeleton causes apoptosis," *Surgery*, vol. 124, no. 2, pp. 362–371, 1998.

[230] C. Born, Z. Zhang, M. Al-Rubeai, and C. Thomas, "Estimation of disruption of animal cells by laminar shear stress," *Biotechnology and bioengineering*, vol. 40, no. 9, pp. 1004–1010, 1992.

[231] D. P. Taylor, P. Mathur, P. Renaud, and G. V. Kaigala, "Microscale hydrodynamic confinements: shaping liquids across length scales as a toolbox in life sciences," *Lab on a Chip*, vol. 22, no. 8, pp. 1415–1437, 2022.

[232] B. P. Helmke and P. F. Davies, "The cytoskeleton under external fluid mechanical forces: hemodynamic forces acting on the endothelium," *Annals of biomedical engineering*, vol. 30, pp. 284–296, 2002.

[233] W. R. Dean, "Xvi. note on the motion of fluid in a curved pipe," *The London, Edinburgh, and Dublin Philosophical Magazine and Journal of Science*, vol. 4, no. 20, pp. 208–223, 1927.

[234] P. Mashaei, S. Asiaei, and S. Hosseinalipour, "Mixing efficiency enhancement by a modified curved micromixer: A numerical study," *Chemical Engineering and Processing-Process Intensification*, vol. 154, p. 108006, 2020.

List of Publications

Journal Publications

- **Prasad, N. K.**, Shome, R., Biswas, G., Ghosh, S. S., & Dalal, A. (2021). Discerning the self-healing, shear-thinning characteristics and therapeutic efficacy of hydrogel drug carriers migrating through constricted microchannel resembling blood microcapillary. Colloids and Surfaces A: Physicochemical and Engineering Aspects, 626, 127070.
- **Prasad, N. K.**, Shome, R., Biswas, G., Ghosh, S. S., & Dalal, A. (2022). Transport Behavior of Commercial Anticancer Drug Protein-Bound Paclitaxel (Paclicad) in a Micron-Sized Channel. Langmuir, 38(6), 2014-2025.
- **Prasad, N. K.**, Ghosh, S. S., & Dalal, A. (2023). Understanding Deformation and Breakup Tendency of Shear-Thinning Viscoelastic Drops in Constricted Microchannels. Langmuir, 39(34), 11975-11991.
- **Prasad, N. K.**, Sen, P., Ghosh, S. S., & Dalal, A. Understanding the migration tendency of cancer cell membrane-derived nanovesicles through network of micron sized channels , Submitted to Biomicrofluidics (Under Review).
- **Prasad, N. K.**, Arora, A., Ghosh, S. S., & Dalal, A. A Heuristic approach to assess the drug uptake by MCF-7 cells inside microfluidic channel designed to mimic the blood capillary networks. (Manuscript under preparation).

Publications from Collaborative Works

- Agnihotry, A., **Prasad, N. K.**, & Dalal, A. (2023). Numerical study of bubble rise in a three-dimensional sinusoidal channel. Physics of Fluids, 35(9).
- Neogi, A., **Prasad, N. K.**, Ghosh, S. S., & Dalal, A. "Achieving Complete Separation of Circulating Tumor Cells Inside Grooved Microchannel Under Effect Of Dielectrophoretic Forces" Manuscript under preparation.

International Conference Publications

- **Prasad, N. K.**, Shome, R., Biswas, G., Ghosh, S. S., & Dalal, A. (2020). Transport behaviour of commercial anti-cancer drug protein-bound paclitaxel (Nanopacli) in blood capillary sized microchannel, Paper No. FMFP2020

– 245, Proceedings of the 8th International and 47th National Conference on Fluid Mechanics and Fluid Power (FMFP), December 09-11, 2020, IIT Guwahati, Guwahati-781039, Assam, India.

- **Prasad, N. K.**, Ghosh, S. S., & Dalal, A.. (2021). Numerical Study of Deformation of Viscoelastic Drop Migrating Through Microchannel With Sudden Constriction, Paper No. IMECE2021-71401, Proceedings of the ASME 2021, International Mechanical Engineering Congress and Exposition (IMECE2021), November 1-5, 2021, Virtual, Online.

- **Prasad, N. K.**, Ghosh, S. S., & Dalal, A.. (2021). Computational Study of Deformation of Viscoelastic (Oldroyd-B) Drop Flowing Through Microchannel With Sudden Constriction, Paper No. IHMTC2021–038, Proceedings of the 26th National and 4th International ISHMT-ASTFE Heat and Mass Transfer Conference, December 17-20, 2021, IIT Madras, Chennai-600036, Tamil Nadu, India, Virtual, Online.

- **Prasad, N. K.**, Dalal, A., & Ghosh, S. (2022). Computational study on the breakup of FENE-P drop migrating through microconfinement with gradual entry and exit. Bulletin of the American Physical Society.

National Conference Publications

- **Prasad, N. K.**, Dalal, A., & Ghosh, S. (2023). Assessment of The Viscoelastic Normal Stress Difference Distribution Inside Shear-Thinning Viscoelastic Drop Migrating Through Constricted Microchannel' in the 1st Indian Conference on Micro Nano Fluidics (ICOM 2023) held during 29th Sep. to 1st Oct. 2023 at IIT Madras India.